SCHOOL OF MEDICINE

FACULTY OF HEALTH SCIENCES

On the Properties and Behaviour of Single Neurons in the Cortex

Minh-Son To

Bachelor of Mathematical and Computer Sciences (Hons)

Bachelor of Pharmacy (Hons)

Supervisors

Prof Greg Stuart

Prof Damien Keating

June 2016

Thesis submitted in partial fulfilment of the requirements for the degree of Doctor of Philosophy

Declaration

I certify that this thesis does not incorporate without acknowledgment any material previously submitted for a degree or diploma in any university; and that to the best of my knowledge and belief it does not contain any material previously published or written by another person except where due reference is made in the text.

Minh-Son To

Author contributions

The contributions of the author and other individuals to the results chapters (Chapters 2 to 6) are as follows.

- Chapter 2: Fabio Longordo and Kaori Ikeda performed the experimental work shown in the chapter (Figures 2.1 and 2.3). The author performed all numerical simulations. Analyses were performed jointly with Fabio Longordo.
- Chapter 3: The author performed all numerical simulations and analyses presented in the chapter.
- Chapter 4: The author performed all numerical simulations and analyses presented in the chapter.
- Chapter 5: Vince Daria and Ann Go along with the author conceived the microscopy design incorporating the digital micro-mirror device. Ann Go performed the calibration experiments shown in Figures 5.3 and 5.4. The author together with Ann Go performed the integration experiments shown in Figure 5.5.
- Chapter 6: The behavioural paradigm was conceived with Diego Gutnisky. The two-photon microscope, behavioural apparatus and imaging software were configured in conjunction with Vijay Iyer and Nick Sofroniew. Animal surgeries and viral transfections were performed by Bryan MacLennan. The author performed all the behavioural experiments and analyses presented in the chapter, with advice from Simon Peron regarding analysis of imaging data.

Acknowledgements

Many individuals have contributed in some way to this body of work and it is a delight to acknowledge them here. First of all, I am indebted to my research supervisor, Greg Stuart, who has supported me throughout my candidature and provided timely guidance and advice when they were needed the most. His patience invariably outlasted my questioning and his wisdom has been a beacon in times of confusion. It has been a great privilege to work in Canberra with Greg over the past few years.

Closer to home in Adelaide, Damien Keating as my supervisor at Flinders University has remained a constant presence over the years. He has kept me on track and has been ever-willing to lend an ear.

My collaboration with Fabio Longordo and Kaori Ikeda led to the work presented in Chapter 2. Discussions with Jonathan Victor provided the initial inspiration to develop the 4D uncaging system presented in Chapter 5 and much of that work would not have been possible either without contributions from Vince Daria and Ann Go. I am also immensely grateful to Garry Rodda, who kept us in order and made sure things ran smoothly in the department. Chapter 6 is the result of my time at the Howard Hughes Medical Institute's Janelia Farm Research Campus in Karel Svoboda's lab, where I worked closely with Diego Gutnisky in planning and conducting the research. The year-long experience in Virginia, USA was undoubtedly a highlight of the past 5 years, and opened my eyes up to a whole new world of neuroscience I never knew existed. Nick Sofroniew, Simon Peron, Vijay Iyer, Bryan MacLennan and Heather Davies all contributed and were instrumental in making the experience a success.

Much of the PhD experience is defined by the friendships that are forged by the hardships and successes shared by those around you. During my time at the John Curtin School of Medical Research in Canberra, my colleagues in the Stuart lab, including Fabio, Kaori, JD, Scott, Tobi, Stephen, Gui, Bill and Jay provided good company and comic relief, and we share many memories of our exploits both in and out of the lab. While in Virginia, I was also fortunate to meet new friends from the George Washington University Vietnamese Student Association and VietVelo. My adventures on the bike with VietVelo kept me sane and only added positively to the overseas experience.

The opportunities I have been granted over the years were made possible by the support of various foundations and fellowships. For the greater part of my candidature I was funded by the MF & MH Joyner Scholarship in Medicine. My time at Janelia Farm was in part supported by an Endeavour Research Fellowship as well as sponsorship from Janelia Farm itself. During the latter part of my candidature I was supported by an Australian Postgraduate Award and following that, by my supervisor Greg.

A special mention must go to Trinh Phuong Anh, who is now my beloved wife. We first met in Adelaide not long before I departed for Canberra to undertake my research. We endured much over the years, and despite facing her own trials she has been unwavering in her commitment and steadfast in her support. My efforts have paled in comparison to hers, and she remains an endless source of strength.

My sisters, To Bao Hien and To Chieu Duong, along with my brother-in-law Tran Tuong Thanh, deserve my heartfelt thanks, for sticking with me through the good and the bad.

Lastly, and most importantly, I would not be here if not for my parents To Minh Tuan and Tran Thi Thien. They began looking after me from before I was born and to this day continue to do so. They raised and educated me, and provided everything I ever needed to reach for my dreams. Although words alone are not enough, I wish to thank them for their boundless love and encouragement.

Tô Minh Sơn

Abstract

Neurons are the building blocks of the nervous system, and the computations they perform underlie our thoughts, emotions and behaviour. The thesis begins *in vivo* in the mouse binocular visual cortex. This system provides a convenient setting for studying how different inputs are combined in single neurons. We investigate the mechanisms underlying sublinear summation of visual information in pyramidal neurons of the binocular visual cortex and reveal the critical role of balanced excitation and inhibition. Our methods involve use of the somatic voltage-clamp technique. However, we show that distortions due to poor space-clamp affect the estimation of excitatory and inhibitory conductances. We therefore next use numerical simulations *in silico* to determine how space-clamp errors affect the measurement of combined excitatory and inhibitory inputs, including the estimated temporal relationship between excitation and inhibition. We also explore how the somatic or dendritic location of inhibition affects neuronal output. These simulations show that the site and nature of excitatory synaptic input to a neuron play a fundamental role in how inhibition modulates the input-output relationship. These findings motivated the development of a two-photon microscope to allow arbitrary activation of distributed synaptic inputs in three-dimensions with high temporal precision. Such a tool provides unprecedented flexibility in dissecting how synaptic inputs are processed in single neurons, but can also be extended to explore network properties including connectivity. Finally the thesis arrives back where it began, *in vivo*, where we develop a behavioural paradigm involving operant conditioning of single neuron activity recorded *in vivo* using two-photon microscopy. This system will enable the future study of the mechanisms underlying synaptic plasticity and neuroprosthetic learning *in vivo*, as well as help to understand how single neurons contribute to behaviour.

Contents

Chapter 1

Introduction

This thesis focuses on the types of computations performed in single neurons with a strong emphasis on the role of dendrites. As we shall see, dendrites are indispensable for neuronal function and hence we devote much of the thesis to studying how dendrites operate as well as developing tools for investigating information processing in dendrites and single neurons. In this Introduction we will review the properties of dendrites and how they relate to the computations performed by neurons. We first provide a brief historical account of research on dendrites, followed by a discussion of the various anatomical and physiological features of dendrites that contribute to their function. Since the neocortex is responsible for higher level brain functions, we focus much of our attention to cortical pyramidal neurons but we will also draw on informative examples from other neuron types as necessary. For authoritative reviews on dendritic properties and physiology, we refer the reader to [Sjöström et al., 2008, Stuart et al., 2008, Stuart and Spruston, 2015].

1.1 Literature review

The Neuron Doctrine, originally formulated by Ramon Y Cajal, hypothesised that the neuron forms the fundamental unit of the nervous system, and that information flows from the dendrites as the input site, through the soma and towards the axon, which delivers the output to other neurons. Decades earlier, Golgi had developed the silver stain which permitted the visualisation of individual neurons under a light microscope [Golgi, 1873]. The staining technique was especially remarkable given that only a small fraction of neurons are stained at random and in their entirety. This revolutionary development paved the way for Cajal to undertake his heroic cataloguing of neurons in the central nervous system, a monumental contribution to neuroanatomy which was later acknowledged by the Nobel Prize in Physiology or Medicine in 1906. During the course of his valiant work, Cajal produced many detailed drawings of dendrites and

while a description of dendritic physiology largely eluded him, his extensive descriptions of dendritic structure provided much inspiration for future generations of neuroscientists striving to understand dendritic function. Despite Cajal's groundbreaking work on the anatomy of dendrites, many decades passed before significant inroads in dendritic physiology were made.

Initially, limitations in experimental technique hindered the ability to obtain electrical recordings from dendrites. As a result early work on understanding the physiology of dendrites was based on theoretical approaches. By applying cable theory to dendrites, work by Wilfred Rall laid out the mathematical framework for understanding signal propagation in passive dendrites [Rall, 1959, Rall et al., 1995]. While the dogma at the time was that dendrites were passive and did not possess the mechanisms to support active conduction of electrical signals, direct micro-electrode recordings from dendrites of Purkinje cells [Fujita, 1968, Llinás et al., 1968, Llinás and Hess, 1976], hippocampal neurons [Wong and Prince, 1978, Wong et al., 1979] and neocortical cells [Houchin, 1973] revealed active electrical events occurring in the dendrites and provided the evidence necessary to shift the prevailing thought.

Our current understanding of dendritic physiology has since evolved and has been punctuated by a series of key technical advances dating from the early 1990s. The breakthrough in dendritic physiology, building on the pioneering work of Erwin Neher and Bert Sakmann over a decade earlier [Sakmann and Neher, 1984] was the ability to obtain patch-clamp recordings from visually identified dendrites of neurons in brain slices [Stuart et al., 1993, Stuart et al., 1994]. This technical feat led to an explosion in the field of dendritic physiology research, allowing exploration of hitherto largely unchartered domains of dendritic function such as ion channel density [Migliore and Shepherd, 2002], dendritic excitability, synaptic integration and plasticity [Sjöström et al., 2008], to name a few.

More recently, optical approaches for studying dendrites have risen to the fore. Developments in imaging techniques, notably two-photon microscopy [Svoboda and Yasuda, 2006] offer the ability to observe fine dendritic structures and estimate electrical activity in regions inaccessible to patch electrodes such as spines and thin, distal dendrites *in vivo*. Most recently, the optogenetics revolution has witnessed a great expansion in the number of tools available for manipulating neural activity [Yizhar et al., 2011]. The combination of light and genetics allows targeting of light-sensitive opsin proteins to genetically defined subpopulations of neurons, and achieves selective activation or inactivation of those neurons with millisecond precision. The use of optogenetic manipulations has contributed significantly to our understanding of dendritic physiology, by enabling manipulation of the circuit elements involved in producing

and regulating dendritic signals [Lovett-Barron et al., 2012, Palmer et al., 2012b]. Combinations of these techniques have also emerged. For example, two-photon targeted patch recordings from neurons *in vivo* [Komai et al., 2006, Margrie et al., 2003] extends the advantages afforded by patch-clamp recordings to *in vivo* settings and also allows electroporation of DNA in single, identified neurons [Kitamura et al., 2008]. With closed-loop integration of genetically encoded reporters of neural activity and optogenetics [Hochbaum et al., 2014], all-optical electrophysiology is rapidly becoming feasible and may soon supercede conventional electrophysiology [Scanziani and Häusser, 2009].

Dendritic morphology and passive properties

Most neurons consist of a soma, axon, and dendrites. Dendritic morphology is highly variable and even among pyramidal neurons, there is heterogeneity in branching structure depending on location e.g. layer 2/3 versus layer 5 cortical pyramidal neurons, hippocampal CA1 versus CA3 pyramidal neurons (Figure 1.1). Dendrites are thin, relative to the cell body, and significantly increase surface area while occupying a small volume. It is thought that this enables neurons to receive more inputs, and indeed, the dendritic membrane is where the majority of postsynaptic inputs arrive [Gray, 1959]. While the dendritic tree can be very elaborate, it only receives synaptic inputs locally. In contrast, axons can travel long distances to synapse in the opposite hemisphere, and in the case of cortical inputs to motor neurons that innervate distal limbs can be over a metre in length.

Alongside morphology, the passive biophysical properties of dendrites are the greatest factors that shape electrical signals in the dendrites. At the most elemental descriptive level, the plasma membrane acts as an insulative barrier to current flow across the membrane. Accordingly, the membrane has capacitance and resistance. Furthermore, axial current flows within dendrites also experience a resistance as a result of dendrites being tubes and the presence cytosolic components. The combined effect of resistive and capacitive elements produces filtering effects that sculpt synaptic responses and signal propagation within dendrites, forming the basis of the Rall model. Contributions of the model include a description of action potential propagation including branch-point failures, characterisation of the impact of synaptic inputs at different locations along a dendrite, as well predictions as to the electrical properties of spines.

Figure 1.1: Heterogeneity of pyramidal neuron structure. Examples of structures of pyramidal neurons from different cortical areas are shown. Dendritic morphology exhibits notable differences between the pyramidal neurons shown. Compared to layer 2/3 pyramidal neurons, layer 5 pyramidal neurons have longer apical dendrites and fewer oblique apical dendrites. Branching of the apical dendrites of hippocampal CA3 pyramidal neurons occurs closer to the soma compared to CA1 pyramidal neurons. Adapted from [Spruston, 2008].

Ion channels in dendrites

The large surface area of the dendritic membrane also accommodates an array of ion channels. Through interactions with the passive membrane properties, ion channels play an integral role in shaping the membrane potential changes that occur and how they propagate throughout dendrites. Following the first demonstration that dendrites contained voltage-gated Na^+ channels that supported active back-propagation of action potentials [Stuart et al., 1994], many other classes of dendritic ion channels have been described. This work indicates that dendritic ion channels show cell-type specific expression, as well as dendrite specific distributions [Migliore and Shepherd, 2002, Lai and Jan, 2006, Vacher et al., 2008] and contribute to a variety of dynamic phenomena. For instance, apart from supporting action potential back-propagation, dendritic Na^+ channels also enable dendritic action potential initiation [Stuart et al., 1997a, Golding and Spruston, 1998, Gasparini et al., 2004] and can amplify synaptic responses [Magee and Johnston, 1995, Stuart and Häusser, 2001].

Voltage-gated Ca^{2+} channels are another group of ion channels found in dendrites and are comprised of several subtypes, so-called L-, N-, P/Q-, R-, and T-types, which are distinguished by their voltage-dependent properties and dendritic distributions. Like Na^+ channels, Ca^{2+} channels typically enhance dendritic excitability and different dendritic Ca^{2+} channels make various contributions to neuronal function. Dendritic T-type channels for example are involved in burst firing [Magee and Carruth, 1999, Williams and Stuart, 1999] and synaptic plasticity [Isomura et al., 2002] in pyramidal neurons. Since these channels have a low threshold for activation, they are also thought to amplify synaptic responses [Markram and Sakmann, 1994, Magee et al., 1995]. The high-voltage activated Ca^{2+} channels (L-, N-, P/Q-, and R-type) play similar roles in amplification of synaptic responses [Schiller et al., 1997, Sabatini and Svoboda, 2000] and action potential burst firing [Womack and Khodakhah, 2004], while also contributing to the generation of dendritic spikes [Schiller et al., 1997, Larkum et al., 1999b, Pérez-Garci et al., 2013]. Under some circumstances, Ca^{2+} channels may also serve as a calcium source for dendritic transmitter release [Simmons et al., 1995], synaptic plasticity [Yasuda et al., 2003, Froemke et al., 2005] and modulation of other Ca^{2+}-dependent mechanisms such as Ca^{2+}-activated K^+ channels [Faber and Sah, 2003].

Potassium channels are the largest and most diverse group of ion channels, with over 100 subunits of distinct K^+ channels identified [Coetzee et al., 1999]. The vast array of K^+ channels have been divided into four families according to their genetic homology, structure and function: voltage-gated K^+ channels, Ca^{2+}-activated K^+ channels, inward rectifier K^+ channels, and leak K^+ channels [Coetzee et al., 1999]. The effect of dendritic K^+ channels on dendritic excitability has been well-studied for a number of

channel subtypes [Yuan and Chen, 2006]. Since the K^+ current has a hyperpolarising effect on membrane potential, K^+ channels have an inhibitory action on dendritic excitability, which depends on the individual properties of the channels. The A-type K^+ channel (reviewed in [Jerng et al., 2004]), for example, produces a number of interesting effects on dendritic signals related to the activation and inactivation kinetics of the channel. The current, which is normally inactivated at rest, shows rapid subthreshold activation, relatively rapid development of inactivation as well as rapid recovery from inactivation at hyperpolarised membrane potentials. Owing to these properties, the current enhances attenuation of the back-propagating action potential and increases the threshold for dendritic spike generation under resting conditions [Hoffman et al., 1997, Gasparini et al., 2004]. However, pairing a back-propagating action potential with excitatory synaptic input reduces the attenuation of the back-propagating action potential, since the excitatory input leads to rapid inactivation of the A-type current [Magee and Johnston, 1997]. Thus, the action of the A-type current in gating back-propagating action potentials provides a mechanism for coincidence detection and may have significant consequences for synaptic plasticity [Watanabe et al., 2002].

Another subset of K^+ channels, the Ca^{2+}-activated K^+ channels, are widely distributed throughout the central nervous system and are typified by their activation following increases in cytosolic calcium [Faber and Sah, 2003]. These channels are responsible for the prolonged after-hyperpolarisation (AHP) observable in many neurons following action potentials as a consequence of the calcium influx via voltage-gated Ca^{2+} channels that are activated during spiking. Three subfamilies of Ca^{2+}-activated K^+ channels have been identified according to their biophysical and pharmacological properties; small-conductance (SK), large-conductance (BK), and intermediate-conductance (IK) Ca^{2+}-activated K^+ channels [Sah, 1996, Vergara et al., 1998, Faber and Sah, 2003]. Pharmacological manipulations have revealed that BK and SK channels underlie different components of the AHP [Sah, 1996, Vogalis et al., 2003]. Of the Ca^{2+}-activated K^+ channels, SK channels in particular have been implicated in dendritic signalling and plasticity [Kim and Hoffman, 2008]. These channels are involved in hippocampal synaptic plasticity [Blank et al., 2003, Hammond et al., 2006], and pharmacological blockade enhances both neural excitability and LTP induction [Stackman et al., 2002, Tzounopoulos and Stackman, 2003]. In the dendrites of pyramidal neurons, SK channels are localised to dendritic spines, where they interact with NMDA receptors and voltage-gated Ca^{2+} channels to regulate dendritic integration [Cai et al., 2004], synaptic excitability [Ngo-Anh et al., 2005, Faber, 2010] and plasticity [Lin et al., 2008, Faber, 2010, Ohtsuki et al., 2012].

The hyperpolarisation-activated cation current (I_h) is a mixed Na^+ and K^+ current also found in dendrites. The current is encoded by the hyperpolarisation-activated cyclic nucleotide-gated channel gene family (HCN1-HCN4) [Ludwig et al., 1998, Santoro and Tibbs, 1999] and underlies many functions in neurons [Robinson and Siegelbaum, 2003, Biel et al., 2009]. The presence of I_h can be detected by a characteristic "sag" in the voltage response to a constant hyperpolarising current step (as a depolarising current becomes activated with hyperpolarisation). Both patch-clamp [Magee, 1998, Williams and Stuart, 2000, Berger et al., 2001, Kole et al., 2006, Harnett et al., 2015] and immunogold labelling [Lörincz et al., 2002, Notomi and Shigemoto, 2004] studies have demonstrated that I_h density increases along the apical dendrites of hippocampal CA1 and layer 5 neocortical pyramidal neurons. Since the current is activated at rest, I_h affects resting membrane potential, input resistance and consequently membrane time constant. The distance-dependent expression of I_h also normalises the effective input resistance along the length of the apical dendrite of cortical layer 5 pyramidal neurons [Williams and Stuart, 2002]. The current affects synaptic integration, by shortening the width of excitatory postsynaptic events [Magee, 1998] and inhibits generation of distal dendritic calcium spikes [Tsay et al., 2007]. Upregulation of the channel with the anticonvulsant lamotrigine also decreases dendritic excitability [Poolos et al., 2002]. Lastly, dendritic I_h enforces temporal fidelity of dendritic coincidence detection [Berger et al., 2003, Migliore et al., 2004] as well as enhancing timing precision of action potential output [Kole et al., 2006].

Active dendrites

The ion channels described in the previous section that are present in dendritic compartments enable dendrites to elicit various phenomena. In this section we will discuss two well-known behaviours supported by dendritic ion channels, namely action potential back-propagation and dendritic spikes.

Action potential back-propagation Action potentials are initiated in the axon, before propagating back into the soma and invading the dendritic tree [Stuart et al., 1994, Kole et al., 2008]. The efficacy of action potential back-propagation into the dendritic tree can be assessed by simultaneously recording from the soma and a dendritic location and differs markedly among the various neuronal types [Stuart et al., 1997b, Häusser et al., 2000, Waters et al., 2005]. At one extreme, back-propagation in cerebellar Purkinje cells is weak and largely passive [Llinás and Sugimori, 1980, Stuart et al., 1994]. At the other, action potentials in dopaminergic substantia nigra neurons [Häusser et al., 1995] and hippocampal interneurons [Martina et al., 2000] actively back-propagate with minimal attenuation. In between these extremes, back-propagation is active but decremental, as in the apical dendrites of layer 5 pyramidal cells [Larkum et al., 2001, Stuart and Häusser, 2001] and hippocampal CA1 pyramidal cells [Andreasen and Lambert, 1995, Magee and Johnston, 1995, Spruston et al., 1995].

The extent and reliability of action potential back-propagation depends on a number of factors. Several active conductances distributed throughout the dendritic tree greatly influence back-propagation [Migliore and Shepherd, 2002]. The density of Na^+ channels is strongly related to the degree of back-propagation. As shown by single-channel recordings, cerebellar Purkinje dendrites have a low density of Na^+ channels [Stuart and Häusser, 1994], while pyramidal dendrites have intermediate densities of the channel [Stuart et al., 1994]. This corresponds to the extent of back-propagation in these neurons; back-propagation is more reliable in pyramidal neurons than in Purkinje neurons. K^+ channels also play an important role. A-type K^+ channels act to limit the extent of back-propagation in hippocampal CA1 [Hoffman et al., 1997] and neocortical layer 5 pyramidal neurons, whereas pharmacological inactivation of these channels enhances back-propagation [Bekkers, 2000, Korngreen and Sakmann, 2000]. Similar results have also been reported in interneurons [Goldberg et al., 2003].

Aside from voltage-gated conductances, dendritic morphology and branching also have a significant impact on action potential back-propagation. For instance, dendritic patch recordings have shown a tendency for back-propagation failure at branch points in hippocampal CA1 pyramidal dendrites [Spruston et al., 1995]. Computer simulations have shown that the impact of morphology can be profound, such that even with the same profile of ion channels, different dendritic morphologies can produce markedly varying back-propagation [Vetter et al., 2001]. Furthermore, interactions between morphology and ion channels can also modulate back-propagation. For example, varying ion channel densities in the dendrites of Purkinje neurons has little effect on back-propagation reliability while ion channel density has much greater influence on back-propagation in layer 5 pyramidal neurons [Vetter et al., 2001]. Other numerical simulations have even suggested a role for dendritic spines in enhancing back-propagation in layer 5 pyramidal neurons, by recruiting high densities of Na^+ channels clustered in spines [Tsay and Yuste, 2002].

As to the role of back-propagation, several ideas have been put forward. Since the back-propagating action potential provides a depolarisation to the dendritic tree following an axo-somatic spike, it may serve as a relatively global signal that the neuron has been brought to threshold. This has important implications in synaptic plasticity, particularly for spike-timing dependent plasticity (STDP) where timing-dependent interactions between synaptic inputs and the back-propagating spike determines the sign and magnitude of the changes in synaptic efficacy [Bi and Poo, 1998, Linden, 1999]. In layer 5 cortical pyramidal neurons, the back-propagating action potential also enables coupling of the two spike initiation zones in the axo-somatic and apical dendritic regions. We elaborate on this interesting feature in the following section on dendritic spikes. Observations that the back-propagating action potential can trigger neurotransmitter release from the dendrites reveal another role for back-propagation [Ludwig et al., 2002, Kuczewski et al., 2008], which we will not discuss further here (for a review on dendritic neurotransmitter release, see [Ludwig and Pittman, 2003]).

Dendritic spikes Dendrites are also capable of generating all-or-nothing events similar to somatic action potentials. These events propagate forward from the dendrites to the soma and have attracted significant interest since they can be generated independently of axonal action potentials. The factors that influence forward propagation of dendritic spikes are related to those that affect action potential back-propagation, although forward propagation of dendritic spikes is typically less reliable than back-propagation of somatic action potentials [Golding and Spruston, 1998, Mehta, 2004]. We will discuss three types of dendritic spikes that have been described extensively, namely calcium, NMDA and sodium spikes.

Regenerative calcium spikes in layer 5 pyramidal neurons are initiated near the main apical bifurcation and contribute to burst firing in these neurons. These calcium action potentials are mediated by voltage-gated Ca^{2+} channels and can be evoked by intense distal synaptic stimulation (corresponding to upper layer 2 and layer 1 inputs) [Schiller et al., 1997]. Calcium electrogenesis in the distal apical and basal dendrites can also be generated by a burst of back-propagating action potentials [Larkum et al., 1999a, Kampa and Stuart, 2006]. Furthermore, the combination of subthreshold synaptic input in the distal apical dendrite together with a single back-propagating axosomatic action potential leads to a large calcium spike in the distal dendrite and subsequent burst firing [Larkum et al., 1999b]. Taken together, these results suggest multiple roles for calcium spikes in pyramidal neurons, including coincidence detection of synaptic input, amplification of distal dendritic inputs, and coupling of signals in the distal dendrites with the soma.

The second type of dendritic spike, the NMDA spike, is generated by activation of the NMDA subtype of glutamate receptor (NMDARs), and occurs in the thin, basal [Schiller et al., 2000, Nevian et al., 2007], oblique [Polsky et al., 2004] and apical tuft [Larkum et al., 2009] dendrites of pyramidal neurons that are densely innervated by glutamatergic inputs. Synchronous activation of nearby (10-50) glutamatergic synapses can trigger an NMDA spike, which is characterised by a large, local depolarisation (40-50 mV) of extended duration (up to several hundred milliseconds). NMDA spikes initiated in the proximal basal dendrites can also also produce a sustained depolarisation in the soma resembling a cortical Up state [Milojkovic et al., 2005b].

Simultaneous somatic and dendritic patch recordings from the primary apical dendrites of layer 5 pyramidal neurons and hippocampal CA1 pyramidal neurons have demonstrated the existence of fast dendritic spikes *in vitro* mediated by voltage-gated Na^{+} channels [Stuart et al., 1997a, Golding and Spruston, 1998]. Similar dendritic spikes have also been recorded *in vivo* [Kamondi et al., 1998]. Although dendritic sodium spikes propagate to the soma with variable reliability, they can influence axonal action potential

initiation [Stuart et al., 1997a, Golding and Spruston, 1998, Gasparini et al., 2004]. There is also evidence for their existence in basal dendrites of cortical pyramidal neurons [Milojkovic et al., 2005a, Nevian et al., 2007].

From our brief survey of dendritic spikes, several features shared between the different dendritic spikes are apparent. Firstly, dendritic spikes are all-or-nothing events that enable coincidence detection of multiple synaptic inputs. Activation of synapses close together in time and location on the dendritic tree favours generation of a dendritic spike. This in turn may enable temporally precise integration of synaptic inputs [Ariav et al., 2003]. Secondly, distal inputs that normally do not propagate to the soma can modify neuronal output when they contribute to generation of a dendritic spike. This provides a means to gate inputs and specific stimuli [Helmchen et al., 1999], or selectively couple the somatic and dendritic domains [Larkum et al., 1999b]. Thirdly, dendritic spikes can be evoked in the absence of axonal action potentials and back-propagation. An important consequence is that dendritic spikes alone can trigger synaptic plasticity, since the large local depolarisation can generate sufficient calcium entry to drive plasticity [Golding et al., 2002, Gambino et al., 2014]. In short, these examples demonstrate the compartmentalised nature of dendritic integration and encapsulate the view that dendrites themselves serve as discrete computational units.

Dendritic physiology in vivo

While *in vitro* brain slice studies have contributed enormously to our understanding of dendritic physiology, it is unclear which of the diverse phenomena observed *in vitro* also occur *in vivo*, in particular, during awake behaviour. Although *in vivo* recordings of dendritic spikes have dated back to almost half a century ago [Llinás et al., 1968], the relative lack of *in vivo* recordings of dendritic activity is in part due to the difficulty of obtaining direct electrical access to dendrites *in vivo* compared to *in vitro*. Despite this, *in vivo* studies of dendritic signalling have been accumulating in recent times, in part due to developments in two-photon microscopy [Komai et al., 2006]. Two key differences exist between *in vitro* and *in vivo* preparations which potentially have profound implications on the nature of dendritic signalling. Firstly, spontaneous activity in slices under normal incubation conditions is typically rare, although certain modifications aimed at better replicating *in vivo* conditions have been reported to reproduce *in vivo*-like activity [Sanchez-Vives and McCormick, 2000, Shu et al., 2003b]. The presence of spontaneous synaptic activity is thought to modify dendritic signalling [Destexhe et al., 2003] through both presynaptic [Shu et al., 2006, Kole et al., 2007b] and postsynaptic mechanisms [Waters et al., 2003]. Secondly, the vast neuromodulatory drive present in the intact brain is virtually entirely absent in slice preparations since most long-range

connections are severed during the slicing procedure. These include processes from monoaminergic and cholinergic neurons in the brainstem and basal forebrain that project throughout the brain. Thus, the subcortical neuromodulatory nuclei involved in attention and arousal no longer provide modulatory input in brain slices, which may otherwise be involved in regulating neuronal and dendritic excitability [Seamans and Yang, 2004, Gulledge and Stuart, 2005]. Importantly, much of the early work *in vivo* took place under anaesthetised conditions, but the advent of head-fixation has since enabled awake behaviours to be studied (see [Schwarz et al., 2010] for a review of head-fixed behaviour in rats).

Earlier recordings of dendritic activity *in vivo*, performed by Kamondi et al. (1998, Buzsaki lab), suggested that dendritic spikes were enhanced during synchronous population activity. In this study, dendritic events were observed by combining sharp electrode recordings from the apical dendrites of hippocampal area CA1 pyramidal neurons with extracellular local field potential (LFP) recordings during sharp-wave ripple (SWR) activity. SWRs comprise of synchronous discharges in area CA3 that propagate to area CA1 via the Schaeffer colaterals, which in turn arrive on the proximal apical dendrites of CA1 pyramidal neurons [Buzsáki et al., 1983]. In the study by Kamondi et al., both fast and slow dendritic events were observed, presumably sodium spikes and calcium spikes, respectively, consistent with what has been observed *in vitro* [Golding and Spruston, 1998, Golding et al., 1999].

Back-propagating action potentials have also been investigated *in vivo*. A recent study [Waters et al., 2003] reported that the apical dendrites of layer 2/3 pyramidal neurons contained Na^+ channels that supported active back-propagation of action potentials both *in vitro* and *in vivo*. Furthermore, supralinear calcium events in the tuft region could be initiated by pairing a somatic action potential with local synaptic input. A subsequent study by the same group investigated action potential back-propagation during neocortical Up and Down states *in vivo* [Waters and Helmchen, 2004]. Using whole-cell recordings combined with two-photon imaging of calcium activity in layer 2/3 pyramidal neurons, this study revealed not only that back-propagation was maintained *in vivo*, it was in fact enhanced during neocortical Up states, as reflected by augmented dendritic calcium influx when action potentials occurred during Up states. This contrasts with the notion that during Up states the local input resistance of the dendrites is reduced due to synaptic bombardment, which would increase attenuation of the back-propagating action potential [Destexhe et al., 2003]. Extracellular recordings and current source density analysis have also shown action potential back-propagation in neocortical pyramidal neurons is robust and relatively uniform across different brain states [Bereshpolova et al., 2007].

The impact of supralinear dendritic events on representation of sensory inputs, perception and behaviour has also been explored. Several *in vivo* patch-clamp recording studies have directly implicated a role for supralinear dendritic activity in sensory coding. In the rat barrel cortex for example, it has been shown that NMDA spikes in the dendrites of layer 4 spiny stellate cells contribute to angular tuning of these neurons [Lavzin et al., 2012]. Similarly, NMDA spikes in apical dendrites of layer 2/3 pyramidal neurons in the mouse primary visual cortex enhance orientation tuning [Smith et al., 2013]. Two-photon imaging during an active sensing behaviour [Xu et al., 2012] have corroborated these findings of nonlinear dendritic integration *in vivo*. Since supralinear dendritic activity is highly voltage-dependent, injection of hyperpolarising current into the recorded neuron is often used to confirm the presence of dendritic spikes *in vivo* [Lavzin et al., 2012, Smith et al., 2013]. In the case of NMDA spikes, hyperpolarisation acts to maintain the magnesium block of the receptor, preventing initiation of the spike. For calcium spikes, hyperpolarisation reduces the voltage-dependent activation of calcium channels. With this in mind, another study obtained patch-clamp recordings from hippocampal CA1 cells during navigatory behaviour and characterised the place-field tuning of subthreshold and spiking activity [Lee et al., 2012a]. Place-field spiking in neurons was abolished with hyperpolarising current injection. However, and remarkably, depolarisation of silent cells gave rise to a spatially-tuned subthreshold response along with place-field spiking. This result not only strongly hints at the involvement of voltage-dependent dendritic mechanisms in the generation of place-fields, which in many ways is analogous to tuning in the sensory cortices, but also gives much greater importance to intracellular mechanisms, specifically dendritic, over synaptic connectivity in the determination of spatial tuning in the hippocampus. These studies along with others [Murayama and Larkum, 2009, Xu et al., 2012, Palmer et al., 2014] implicate the involvement of active dendritic events in a wide range of activities *in vivo* and tenuously establish their relevance in producing behaviour.

Synaptic modulation of dendritic excitability

One of the most influential factors involved in the modulation of dendritic excitability is synaptic input provided by inhibitory interneurons (reviewed in [Palmer et al., 2012a]). GABAergic neurotransmission can evoke fast inhibition via $GABA_A$ receptor-mediated anionic conductances (Cl^- and HCO_3^-) and slow inhibition via G protein-coupled $GABA_B$ receptors that open inwardly rectifying K^+ (GIRK) channels [Lüscher et al., 1997]. Despite only comprising a minority of cells in the cortex, inhibitory interneurons demonstrate an exquisite ability to finely tune the output of cortical pyramidal neurons. This ability in part stems from their morphological, molecular, physiological and synaptic diversity [Markram et al., 2004], and indeed such diversity has presented various challenges in developing a systematic nomenclature

for interneurons [Ascoli et al., 2008, DeFelipe et al., 2013]. The vast majority of neocortical inhibitory interneurons can be classified as one of three types, depending on the molecular markers they express, namely parvalbumin, somatostatin or the serotonin receptor 5HT3a [Rudy et al., 2011]. Interneurons in these classes show class-specific connectivity to other neurons and are differentially active during behaviour [Kepecs and Fishell, 2014]. Even within a molecular class, different interneuron subtypes may exist that are distinguished from one another by how they modulate activity in their post-synaptic targets. For example, parvalbumin-expressing interneurons include basket cell and chandelier cell subtypes. Basket cells innervate the soma and proximal dendrites of pyramidal neurons while chandelier cells target the axon initial segment [Somogyi et al., 1998], and such differential targeting provides a potential mechanism for independently regulating the integration of inputs and production of spikes in pyramidal neurons. While describing interneuron diversity in detail extends beyond the scope of this thesis, we will revisit how this diversity influences dendritic integration in later chapters of this thesis.

Individual neurons in the cortex receive barrages of synaptic inputs from hundreds and thousands of other neurons, involving inhibitory neurons working in concert with excitatory neurons. A feature of this synaptic drive is that excitatory input is balanced by inhibitory input, such that temporal fluctuations in excitation are closely matched by fluctuations in inhibition [Haider et al., 2006, Shu et al., 2003b]. The resulting high conductance state of neurons in the cortex impacts on dendritic excitability and neuronal integration by modifying input resistance [Destexhe et al., 2003] (but see also [Waters and Helmchen, 2004]) and introducing membrane potential variability with consequences on the temporal precision of neuronal output [Shadlen and Newsome, 1998]. Many studies that have contributed to these findings have relied on the voltage-clamp technique to dissect the excitatory and inhibitory components of synaptic input in the cortex [Borg-Graham et al., 1998, Shu et al., 2003b, Wehr and Zador, 2003, Haider et al., 2006]. Despite being one of the only methods available for directly measuring synaptic conductances, the utility of the method is limited by space-clamp errors [Spruston et al., 1993], which are compounded by branching dendritic morphology. These issues will be explored in further detail throughout this thesis.

Spines

A review of dendritic integration would be incomplete without a discussion on spines. Here we will provide only a brief overview of spine physiology and some results relevant to dendritic information processing. For authoritative reviews on the structure and function of dendritic spines, we refer the reader to [Hering and Sheng, 2001, Nimchinsky et al., 2002, Rochefort and Konnerth, 2012]. Dendritic spines are small membrane protrusions on dendrites that form the post-synaptic component of the vast majority of excitatory synapses in the brain. Spines come in different shapes and sizes, and have been classified as stubby, thin, or mushroom based on their morphology [Peters and Kaiserman-Abramof, 1970] (Figure 1.2), with different spine morphologies found along the same dendrite [Harris and Stevens, 1988, Harris and Stevens, 1989]. Spines are dynamic structures [Bhatt et al., 2009] and can undergo rapid morphological changes observable on the timescale of minutes to hours in activity-dependent and activity-independent manners [Maletic-Savatic et al., 1999, Engert and Bonhoeffer, 1999, Toni et al., 1999, Matsuzaki et al., 2004, Lang et al., 2004, Zhou et al., 2004, Nägerl et al., 2004, Bastrikova et al., 2008, Yasumatsu et al., 2008]. On the other hand, spines also show remarkable stability *in vivo*, and can persist for months and even up to the lifetime of animals [Holtmaat et al., 2005, Zuo et al., 2005, Yang et al., 2009, Xu et al., 2009, Hofer et al., 2009]. For these reasons, dendritic spines are thought to be a key structural substrate for learning and long-term memory storage [Holtmaat and Svoboda, 2009, Kasai et al., 2010].

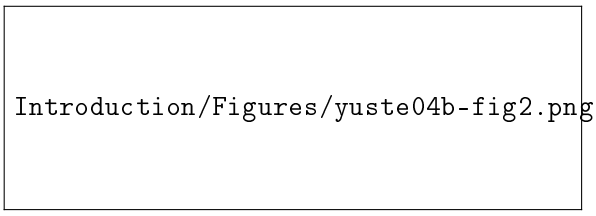

Figure 1.2: Spines have a variety of morphologies. Classification of spines as 'stubby', 'thin' or 'mushroom' is based on their structural appearance [Peters and Kaiserman-Abramof, 1970]. Adapted from [Yuste and Bonhoeffer, 2004].

Many interesting properties of spines arise from their peculiar morphology, which enables compartmentalisation of chemical and electrical signals. The spine head is separated from the dendrite by a thin neck, and owing to this geometry, spines readily isolate biochemical signals and in particular, act as calcium compartments [Svoboda et al., 1996, Yuste et al., 2000]. The calcium dynamics in spines, aided by biochemical compartmentalisation, is thought to be an important driver of input-specific and activity-dependent synaptic plasticity [Nevian and Sakmann, 2006, Higley and Sabatini, 2008]. Early studies established that changes in calcium in the spine heads were not necessarily coupled to the calcium dy-

namics in the dendritic shafts, thus demonstrating the isolation of biochemical signals to individual spines [Guthrie et al., 1991, Müller and Connor, 1991]. Increases in spine calcium can be induced by subthreshold synaptic stimulation and back-propagating action potentials initiated in the axo-somatic region [Yuste and Denk, 1995, Koester and Sakmann, 1998]. Several sources of calcium have also been elucidated, including calcium influx through voltage-gated Ca^{2+} channels [Yuste and Denk, 1995, Majewska et al., 2000] and NMDA-receptors [Yuste et al., 1999, Mainen et al., 1999, Kovalchuk et al., 2000], as well as calcium release from intracellular stores [Takechi et al., 1998, Emptage et al., 1999, Wang et al., 2000]. These studies, together, paint a complex picture of the various players involved in shaping calcium signals in spines.

The geometric configuration that allows biochemical compartmentalisation in spines also shapes electrical signals. The spine neck has a high resistance relative to the dendritic shaft and consequently filters membrane potential changes such that voltage changes in the spine head are attenuated when they reach the shaft, whereas voltage changes in the shaft are virtually unfiltered as they invade the spine head [Araya et al., 2006, Palmer and Stuart, 2009]. Owing to the high impedance of the spine neck, depolarising synaptic inputs within the spine head are passively amplified to membrane potentials significantly higher than what would be reached by those inputs occurring on the dendritic shaft, leading to activation of nonlinear voltage-gated conductances which in turn promotes cooperativity of synaptic inputs in spines [Harnett et al., 2012]. Some of the ion channels found in spines include voltage-gated Ca^{2+} channels [Sabatini and Svoboda, 2000, Jones and Stuart, 2013], voltage-gated Na^{+} channels [Araya et al., 2007], Ca^{2+}-activated K^{+} channels [Ngo-Anh et al., 2005, Bloodgood and Sabatini, 2007, Jones and Stuart, 2013] as well as NMDA-receptors [Ngo-Anh et al., 2005, Bloodgood and Sabatini, 2007].

Neuronal computation and behaviour

As we have seen, dendrites are endowed with an assortment of mechanisms that enable them to process inputs in complex ways and produce a wide range of dynamic phenomena. Due to the intricacies of these mechanisms, understanding the rules governing dendritic computation and untangling the contribution of single neurons to information processing in networks is immensely challenging. Many common approaches describe dendritic transformations in terms of abstract operations in order to simplify the interpretation. To this end, by using a combination of passive properties and active mechanisms dendrites of layer 5 pyramidal neurons have been broadly described as performing a wide range of computations, such as low-pass filtering of voltage responses, logical operations with excitatory and inhibitory inputs, segregation and amplification of synaptic inputs, and coincidence detection of distal synaptic input with somatic

action potentials [London and Häusser, 2005].

Given the compartmentalised and localised nature of synaptic integration in dendrites [Polsky et al., 2004], including their ability to generate spikes, it is appropriate to view dendritic branches as the basic computational unit of a neuron [Branco and Häusser, 2010]. The dendritic tree, being comprised of many individual dendrites, can therefore be seen as a network of such units. In this vein, synaptic integration in a pyramidal neuron model can be approximated by a two-layer neural network [Poirazi et al., 2003], where incident synaptic inputs are integrated by dendrites in the first layer, and the summated output of the first layer is then integrated by a single output unit in the second layer that then drives firing of the axon (Figure 1.3A). Furthermore, dendritic computations can be classified as sublinear, linear, supralinear, or a combination of these (e.g. sigmoidal), depending on the shape of the input-output transformations performed by the dendrites. According to this abstraction, integration in separate branches is independent of other branches and the combined output of the first layer is summed linearly. Such an abstraction is consistent with experimental observations, by reproducing, for example, nonlinear within-branch summation and linear between-branch summation (Figure 1.3B). One important feature this feedforward model lacks however, is action potential back-propagation and interaction thereof with dendritic nonlinearities [Larkum et al., 1999b].

Extending this framework of dendritic computation to deciphering the contribution of neurons to information processing at the behavioural level is significantly more difficult, since behaviour typically involves numerous neurons that interact with one another in complex ways. Thus the impact of dendritic integration in a single neuron on behaviour, let alone the impact of spiking in a single neuron, may not be observable (although see [Brecht et al., 2004]). Nevertheless there are several instructive examples that eloquently demonstrate how dendritic information processing may be relevant for guiding behaviour. Below we choose two examples of this from the literature, and briefly discuss directional selectivity in retinal ganglion cells (RGCs) and sound localisation in mammals and birds.

Figure 1.3: Two-stage dendritic integration in pyramidal neurons. (**A**) Modelling a pyramidal neuron as a two-layer neural network. A schematic representing the mapping of synaptic inputs on thin terminal dendrites (left) onto independent subunits of a two-layer neural network (right). The number of dendritic subunits is denoted n_i, for subunits indexed i, and the coupling weight of each subunit is denoted by α_i and represented by the size of the solid circles. The nonlinear dendritic input-output function is denoted $s(n_i)$, and the somatic nonlinear input-output function is denoted g, which produces a firing rate output y. Adapted from [Poirazi et al., 2003]. (**B**) Within-branch summation is nonlinear and between-branch summation is linear. Basal dendrites of a layer 5 pyramidal neuron were stimulated by two electrodes to mimic synaptic input. Stimulation was delivered separately and then simultaneously, and the somatic EPSP response was recorded. The expected peak EPSP was calculated by summing the individual responses. The coloured circles demonstrate the strongly nonlinear response when the same dendrite was stimulated twice, while the green diamonds show close to linear summation of inputs delivered to different branches. The dashed line indicates exact linear summation. Adapted from [Polsky et al., 2004].

Direction-selective RGCs are ganglion cells in the retina that respond to stimuli in the visual field that move in a specific direction [Barlow et al., 1964, Barlow and Levick, 1965]. The direction in which the spiking response is greatest is known as the "preferred direction"; the opposite direction, which produces no response, is referred to as the "null direction". Many lines of evidence including electrophysiological and imaging studies indicate a role for both presynaptic and postsynaptic mechanisms in producing direction selectivity (Figure 1.4A). A simple model for understanding the dendritic origin of direction selectivity can be developed by delivering consecutive synaptic inputs along the length of a passive dendrite [Rall, 1964]. An input sequence that begins proximally and ends distally will produce a smaller somatic response compared to a sequence that begins distally and ends proximally. In the latter case, since distal synaptic inputs are filtered and delayed as they propagate towards the soma, the somatic response from distal stimulation coincides with the response to proximal inputs, leading to stronger summation at the soma. Others have suggested that asymmetries in excitatory and inhibitory inputs are responsible for directional selectivity, whereby excitatory inputs are delivered ahead of inhibition in the preferred direction, while inhibition interrupts excitation in the null direction [Taylor and Vaney, 2002]. More recently, direct electrical recordings from the dendrites of direction-selective ganglion cells have also revealed the involvement of active dendritic processing. Sodium-dependent dendritic spikes generated by light bars moving in the preferred direction enable distal dendritic inputs to overcome severe dendritic filtering and influence somatic spiking [Sivyer and Williams, 2013]. While there is no consensus as to the mechanisms underlying directional selectivity, the postsynaptic mechanisms described above are likely to be involved and draw parallels with input sequence discrimination found in pyramidal neurons [Branco et al., 2010] (Figure 1.4B). The ability to detect input sequences expands the repertoire of integrative abilities of pyramidal neurons and may represent a widespread computational tool the brain employs.

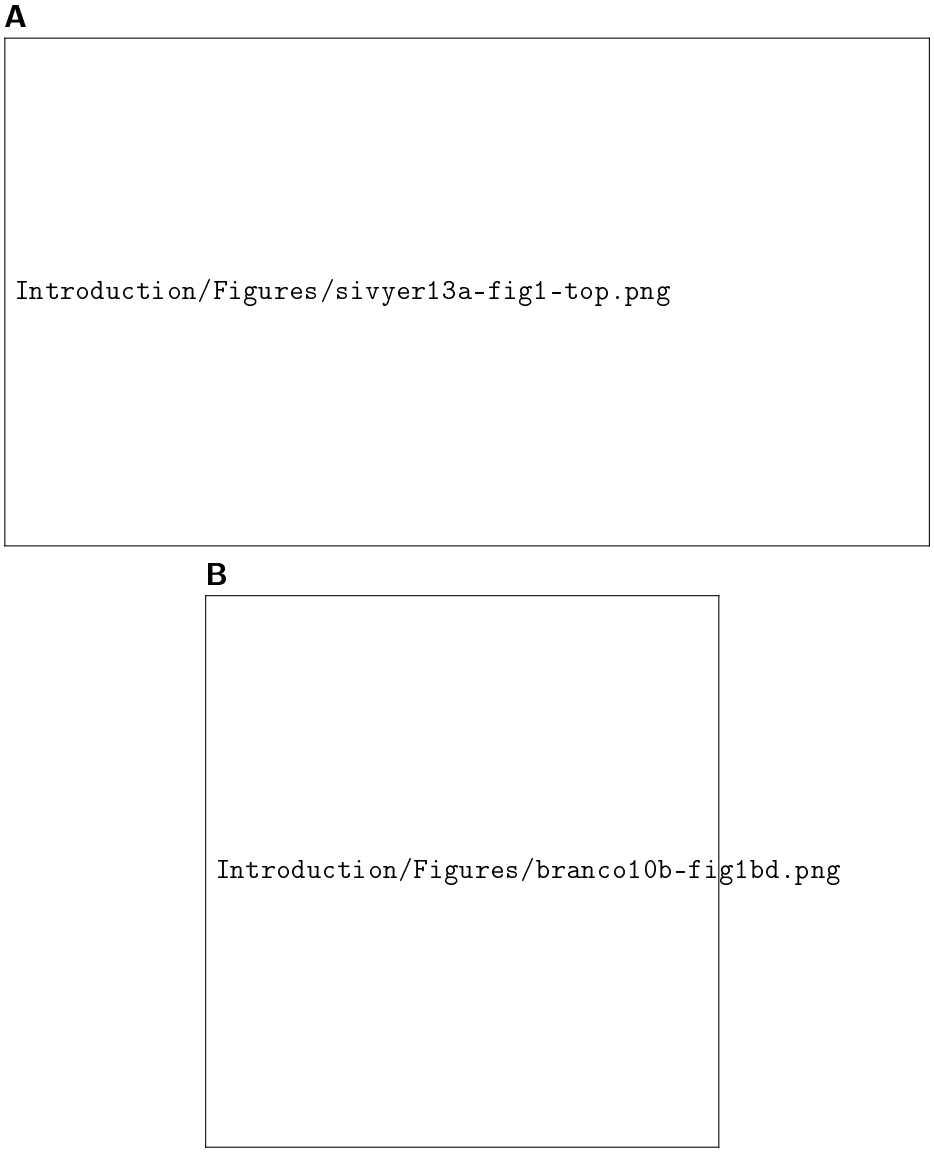

Figure 1.4: Directional selectivity and discrimination of input sequence mediated by dendrites. (**A**) Dendritic spikes are generated in direction-selective retinal ganglion cells in response to moving visual stimuli. Reconstructions of direction-selective ganglion cells showing the position of recording electrodes and the preferred-direction movement of a light bar (yellow). The recorded dendritic subtree is coloured in red. Voltage traces (right) show example simultaneous recordings from somatic (black) and dendritic (red) electrodes. Traces are aligned to the peak of the somatic action potential. Dendritic spikes are evoked and precede somatic action potentials when a moving light bar stimulus is presented on the preferred side of the dendritic tree (positions 1 and 2). When the light bar is presented on the null side (position 4), dendritic spikes are no longer observed before the somatic action potential. Adapted from [Sivyer and Williams, 2013]. (**B**) Individual dendrites can discriminate the direction of synaptic input patterns. A single dendrite of a layer 2/3 pyramidal neuron filled with Alexa 594 dye is stimulated by two-photon glutamate uncaging (top) and the somatic membrane potential response is recorded (bottom). Uncaging locations along the dendrite are indicated by yellow dots. The uncaging locations are stimulated either in a distal to proximal sequence (IN) or proximal to distal sequence (OUT) (middle). The IN direction produces a larger membrane potential response at the soma compared to the OUT direction. Adapted from [Branco et al., 2010].

Another example of dendritic computation relevant to behaviour is sound localisation in mammals and birds, which involves detection of differences in arrival time of sounds at the two ears. The neurons involved in sound localisation respond only to very specific interaural time differences and have several peculiar features that suggest a role for dendritic integration. These neurons have bipolar dendrites, with each dendrite receiving inputs from one ear only [Stotler, 1953, Smith and Rubel, 1979]. Furthermore, the dendritic length is inversely related to the preferred frequency of the neurons [Parks and Rubel, 1975, Smith and Rubel, 1979]. These neurons act as coincidence detectors, such that their firing is maximal when inputs onto both dendrites arrive simultaneously. In these neurons, segregation of binaural inputs across the two dendrites enhances coincidence detection by reducing sublinear summation that would occur if binaural inputs were colocalised to the same dendrite [Agmon-Snir et al., 1998]. Although likely to serve different computational roles, coincidence detection mechanisms also exist in cortical pyramidal neurons, such as burst firing following pairing of back-propagating action potentials with EPSPs in the distal apical dendrites [Larkum et al., 1999b, Stuart and Häusser, 2001] (Figure 1.5A). Such a mechanism is likely to be at play *in vivo* in the generation of dendritic plateau potentials in layer 5 pyramidal neuron of the barrel cortex when vibrissal sensory input is coincident with activity in the primary motor cortex [Xu et al., 2012] (Figure 1.5B). Thus coincidence detection enabled by dendrites appears to be a ubiquitous computation that exists in many different guises throughout the nervous system.

Figure 1.5: Dendritic coincidence detection *in vitro* and during *in vivo* behaviour. (**A**) Temporal coincidence of a somatic action potential with an EPSP produces amplification of the back-propagating action potential. EPSPs were evoked at different times relative to a somatic action potential. Dendritic recording from distal apical dendrite of a layer 5 pyramidal neuron, 480 μm from the soma (top). The amplitude of the peak dendritic response versus the time difference between the EPSP and onset of the somatic action potential (bottom). Zero time denotes the time of the somatic action potential peak and the smooth line is the fit with a skewed Gaussian. The peak dendritic response shows maximal amplitude when the EPSP arrives in a short time window prior to initiation of the somatic action potential. Adapted from [Stuart and Häusser, 2001] (**B**) Nonlinear dendritic integration of a sensory and motor input during active whisking behaviour in mice. **i.** Head-fixed mice were trained to perform a whisker-dependent object-localisation task under a two-photon microscope. Imaging was performed over the superficial barrel cortex, on distal dendrites of deep-layer neurons expressing GCaMP3 (top right). Mice were required to actively whisk to locate a pole, and respond by licking (go) or withholding licking (no go). High-speed videography enabled determination of the time when whisker-pole contacts occurred (bottom). N.A., numerical aperture. **ii.** The fluorescence signals (reported as $\Delta F/F$, bottom) reflecting changes in intracellular Ca^{2+} in the tuft branches (top and middle). **iii.** Fluorescence signals from trials during which the whisker touched the pole. The sampling interval is denoted by the vertical blue bars. **iv.** Imaging performed on a C2 barrel neuron showing averaged Ca^{2+} signals during C2 whisker touch (Touch C2), touches from non-C2 whiskers (Touch non-C2) and no whisker touches. Large-amplitude Ca^{2+} transients are preferentially generated during whisker touch events in neurons belonging to the corresponding whisker barrel. Such responses were absent during passive whisker deflection (data not shown), suggesting a role for whisking during sensation in producing these regenerative dendritic Ca^{2+} events. Adapted from [Xu et al., 2012].

Single neurons and network computation

Just as dendrites are the computational subunits of individual neurons, neurons are regarded as the basic computational unit of the brain. As we have discussed previously, dendrites subserve many facets of neuronal function by expanding the computational capabilities of individual neurons and enabling them to engage in a range of behaviourally-relevant tasks [Lavzin et al., 2012, Xu et al., 2012, Smith et al., 2013, Bittner et al., 2015]. The complexity of these tasks invites the question, what is the contribution of individual neurons to the surrounding network activity or even behaviour [Wolfe et al., 2010]? Experimental evidence has demonstrated that a single cell can exert detectable effects on behaviour, from generation of whisker deflections [Brecht et al., 2004], sensory perception [Voigt et al., 2008, Houweling and Brecht, 2008, Doron et al., 2014], to modification of brain state [Cheng-Yu et al., 2009]. Attempts to quantify the influence of a single neuron's activity on the subsequent firing of nearby neurons *in vivo* have also revealed measurable effects. One study relying on existing anatomical data on neuron-neuron connectivity used *in vivo* whole-cell patch clamp recordings to arrive at the estimate that a single additional spike in an excitatory neuron causes 28 ± 13 extra spikes among its postsynaptic targets [London et al., 2010]. In this study, the increase in local network activity was measured by an extracellular multichannel silicon probe. A similar study investigated the effect of pyramidal neuron burst spiking on target excitatory and inhibitory neurons estimated that each burst spiking event recruits approximately 14 pyramidal neurons and 3-9 SOM interneurons within a radius of $\sim$100 μm [Kwan and Dan, 2012]. Collectively, these studies indicate that the activity of individual neurons can significantly modify the dynamics of the local network and even generate a measurable behavioural response.

How have networks evolved to acquire such exquisite sensitivity to the activity of individual neurons? A number of studies have revealed important insights as to how behavioural learning is effected at the single-cell and even the single-spine level. Motor learning in mice leads to rapid formation of dendritic spines on pyramidal neurons in the motor cortex [Xu et al., 2009], while spines, once formed, may persist for years, suggesting a role in long-term memory storage [Yang et al., 2009]. In monkeys, a learning task involving a repetitive motor behaviour induced formation of spines in clusters, mostly as neighbouring spine pairs [Fu et al., 2012]. Neurons also show a remarkable ability to compartmentalise learning, with branch-specific dendritic calcium spikes mediating long-term plasticity and segregation of different learning experiences to individual dendrites [Cichon and Gan, 2015]. While such studies hint that behavioural plasticity is executed with remarkable precision within single neurons, a common feature of these studies is that there are no constraints on the temporal structure of neural activity. This is in direct contrast to classical *in vitro* STDP studies, for example, where the relative timing between a spike in the pre-synaptic neuron

and a spike in the post-synaptic neuron is controlled with millisecond precision [Markram et al., 1997, Bi and Poo, 1998]. Since the structure of neural activity is not constrained, the precise role of the activity in driving plasticity is unclear.

Pathology

Although neuropathology is beyond the scope of this thesis, we conclude this chapter by providing a very brief account of various pathologies involving changes to dendritic function to highlight the importance of normal functioning dendrites. Pathological change to dendrites can occur in many ways, and can feature alterations to dendritic structure, such as branching [Baloyannis, 2009], or alterations to dendritic excitability, which is typically also associated with changes in ion channel function or expression [Poolos and Johnston, 2012]. Given that spines are very delicate structures and play a central role in synaptic integration as sites of excitatory synaptic inputs, it is not surprising that changes in spine number or structure are also commonly observed in neurological disorders [Fiala et al., 2002, Blanpied and Ehlers, 2004, Penzes et al., 2011].

Some of the most well-studied syndromes with known dendritic pathologies are associated with mental retardation; Down, Rett and fragile-X syndromes [Kaufmann and Moser, 2000]. Down syndrome, also known as trisomy 21, is a genetic disorder associated with abnormal physical growth and intellectual disability. Brain growth is also affected, with reductions in brain size and weight observed at the macroscopic level [Wisniewski, 1990], while at the microscopic level, reductions in spine densities in neurons [Suetsugu and Mehraein, 1980, Takashima et al., 1981] and age-dependent abnormalities in dendritic branching in various cortical areas have been documented [Becker et al., 1986, Schulz and Scholz, 1991]. Rett syndrome, another genetic disorder that almost exclusively affects young females, is characterised by regression of language and motor skills, seizures, and development of stereotypical hand movements [Hagberg et al., 1983]. Neurologically, the syndrome is associated with a low brain weight, reduced dendritic branching, and a decrease in dendritic spines [Armstrong, 2005]. Fragile X syndrome is an inherited cause of intellectual disability that predominantly affects males and involves the Fragile X mental retardation 1 (FMR1) gene on the X chromosome. Studies of Fragile X syndrome patients have provided several observations of immature, long, and tortuous spines across different cortical areas [Hinton et al., 1991, Irwin et al., 2000, Irwin et al., 2001], pointing to a failure of normal spine maturation and/or pruning during development. Dendritic channelopathies have also been implicated in Fragile X syndrome, in particular dendritic HCN and BK channels, which play a role in producing sensory hyperexcitability in Fmr1-/y mice [Zhang et al., 2014].

The epilepsy disorders, which are characterised by a disturbance to the balance of excitatory and inhibitory activity resulting in a hyperexcitable state, provide another instructive example of dendritic pathology. This imbalance can arise in various ways, including alterations in (voltage-gated) ion channels and synaptic transmission [Mulley et al., 2003, Heron et al., 2007], with pathologies involving dendrites in some cases [Poolos and Johnston, 2012]. Various dendritic ion channels have been implicated in different forms of epilepsy. For example in absence epilepsy, it is thought that impaired dendritic HCN channels contribute to enhanced neuronal excitability and burst firing by amplifying dendritic calcium electrogenesis [Shah et al., 2004, Strauss et al., 2004, Kole et al., 2007a]. Similarly, reduced availability of dendritic I_A in temporal lobe epilepsy leads to increased dendritic excitability in CA1 pyramidal neurons [Bernard et al., 2004]. Altered GABAergic neurotransmission can also be involved. For example, in an experimental model of temporal lobe epilepsy, dendritic GABAergic inhibition is impaired while somatic inhibition is enhanced [Cossart et al., 2001, Wendling et al., 2002]. Structural derangements of dendrites have also been noted in epilepsy, such as spine loss [Jiang et al., 1998, Swann et al., 2000] along with changes in dendritic branching [Multani et al., 1994], although it is less clear if these changes are a cause or consequence of epilepsy.

The examples above provide a small glimpse into how dendritic pathologies can contribute to altered neurological function. The manifestations of these pathologies are varied and in many cases devastating to those individuals affected, underscoring the importance of maintaining the integrity of dendritic structure and function for ensuring the normal neurological status of the brain.

1.2 Thesis outline

The purpose of this Introduction was to provide an overview of dendritic properties, and how they contribute to the computational processes performed by neurons *in vitro* and *in vivo*. These issues are central to the topic of this thesis, which is structured as follows. In Chapter 2 we summarise experiments demonstrating sublinear dendritic integration in layer 2/3 pyramidal neurons of the binocular visual cortex, and employ a reconstructed multi-compartment neuron model to explore the mechanisms underlying this observation. In Chapters 3 and 4, we consider several issues that arise from Chapter 2. In Chapter 3 we explore how voltage- and space-clamp errors affect the estimation of synaptic conductances in a simple two-compartment neuron model. In Chapter 4, we investigate how the location of synaptic inhibition affects neuronal integration and action potential generation. The focus of Chapter 5 is the description of a novel method for 3D photo-stimulation with millisecond precision using two-photon microscopy and its application for studying dendritic integration. Chapter 6 describes the development of a closed-loop two-photon microscope system and demonstrates operant conditioning of single neuron activity, allowing investigation of the population dynamics underlying behavioural learning. Finally, in Chapter 7, we summarise the findings of the thesis and discuss their broader implications.

Chapter 2

Sublinear binocular integration in layer 2/3 pyramidal neurons

2.1 Introduction

Neurons in the brain typically receive thousands of synaptic inputs, which are integrated in time and space to generate an output signal. As most of these inputs are made on the dendritic tree, research over many years has focused on understanding how the passive and active properties of dendrites influence synaptic integration. A range of forms of synaptic integration have been described, from sublinear, as seen in passive dendrites [Koch et al., 1983], to supralinear due to generation of dendritic spikes [Larkum et al., 1999b, Losonczy and Magee, 2006, Schiller et al., 2000, Schiller et al., 1997, Stuart et al., 1997a]. More subtle modifications of synaptic integration have also been described, due to activation of potassium, HCN and persistent sodium channels [Hoffman et al., 1997, Magee and Johnston, 1995, Stuart and Sakmann, 1995, Magee, 1999]. Evidence for these different forms of synaptic integration is based largely on experiments conducted *in vitro*. Much less is known about how neurons process synaptic inputs while embedded in their network *in vivo*.

The cortex provides an ideal brain region where this issue can be addressed. Single neurons in sensory cortical areas integrate inputs with defined spatial and temporal patterns depending on the characteristics of the stimulus. These early computations are thought to be crucial to the processing of sensory information. While there is emerging evidence that somatosensory stimulation can evoke active forms of dendritic integration *in vivo* [Murayama et al., 2009, Xu et al., 2012, Lavzin et al., 2012, Palmer et al., 2014], to what extent this can be generalised across different sensory modalities is unclear. *In vitro* work indicates that supralinear forms of synaptic integration require correlated activity clustered

onto the same dendritic location or branch [Losonczy and Magee, 2006, Polsky et al., 2004]. In contrast, when inputs are dispersed onto different branches or activated at different times, linear or sublinear forms of synaptic integration usually occur [Polsky et al., 2004, Cash and Yuste, 1998, Cash and Yuste, 1999]. It is only now becoming apparent how synaptic inputs, encoding specific sensory information, are distributed at the dendritic level. Some evidence indicates that sensory information is processed by dendrites in a dispersed manner [Chen et al., 2011, Varga et al., 2011], which is less likely to recruit active dendritic processing, whereas other evidence supports clustered activation of synaptic inputs onto the same dendrite [Kleindienst et al., 2011, Takahashi et al., 2012].

Here we use a combination of *in vivo* experiments and numerical simulations to examine the integration of synaptic inputs in the binocular region of the primary visual cortex of the mouse. By definition, binocular neurons encode information from the two eyes, providing a model system in which to study how two defined sensory inputs are integrated at the single-cell level. In mice, it is thought that visual input from the two eyes are separate until they converge in the binocular cortex [Coleman et al., 2009] (but see also [Howarth et al., 2014]). Visual information from each eye passes from the retina along the retinogeniculate projection to separate groups of neurons in the dorsal lateral geniculate nucleus (dLGN) of the thalamus. These neurons then transmit the retinal input to layer 4 neurons in the primary visual cortex. Neurons in the so-called binocular cortex respond to visual input to both eyes. Although extracellular recording has provided a basic understanding of how simple and complex cells integrate binocular information [Ohzawa and Freeman, 1986a, Ohzawa and Freeman, 1986b], this analysis is based exclusively on the firing output of neurons and therefore lacks information on the integration of the underlying synaptic responses. Using whole-cell patch-clamp recording *in vivo*, in this Chapter we demonstrated that small synaptic inputs from the two eyes are integrated linearly, whereas large inputs are integrated sublinearly [Longordo et al., 2013]. Based on voltage-clamp data and compartmental modelling, we show that sublinear binocular integration cannot be explained solely by nonlinear integration of excitatory inputs but requires balanced recruitment of inhibition.

2.2 Methods

In vivo physiology

The numerical simulations presented in this Chapter are based on experimental data obtained by Fabio Longordo and Kaori Ikeda. Experimental procedures are detailed in [Longordo et al., 2013]. Briefly, *in vivo* whole-cell current-clamp and voltage-clamp recordings were obtained from layer 2/3 neurons in the binocular region of C57BL/6 mice (8-10 weeks of age) during presentation of visual stimuli to each eye separately or to both eyes together. Mice were maintained under urethane or isoflurane anaesthesia (0.5 to 1%) throughout the experiment. Visual stimuli were generated in MATLAB using the Psychophysics Toolbox extension and consisted of sinusoidal gratings. A sliding median filter of 10 ms width was applied to voltage traces to selectively remove action potentials while preserving the overall subthreshold membrane potential dynamics. Currents evoked by the presentation of sinusoidal gratings were recorded during somatic whole-cell voltage-clamp without compensation for series resistance at two holding potentials. Excitatory and inhibitory conductances were estimated as previously described [Borg-Graham et al., 1998, Cruikshank et al., 2007], after correction for the junction potential ($\sim$10 mV) and series resistance and assuming reversal potentials for excitation and inhibition of 0 mV and -80 mV, respectively.

Model

Computer simulations were performed using the NEURON simulation environment on a Linux desktop computer running Ubuntu 12.04 LTS. A multicompartment model was obtained by reconstructing a biocytin-filled layer 2/3 pyramidal neuron. The reconstructed neuronal model consisted of 136 compartments, subdivided into a total of 1,021 segments. All dendritic branch diameters were scaled by a factor of 1.3 to account for cell shrinkage. Specific membrane resistance (R_m), capacitance (C_m; 1 μF/cm^2) and internal resistance (100 Ω cm) were uniformly distributed throughout the model. Spines were incorporated into the model by decreasing R_m and increasing C_m by a factor of 2 in distal dendritic compartments (>40 μm from the soma). In current clamp simulations the resting membrane potential was set to -70 mV and R_m to 8,000 Ω/cm^2, giving an apparent membrane time constant (8 ms) and input resistance (80 MΩ) similar to those observed for this cell at the resting membrane potential *in vivo*. In voltage-clamp simulations the resting membrane potential was set to -52 mV to match holding currents recorded at hyperpolarised and depolarised potentials in these experiments, which used a caesium-based internal solution. No voltage-gated ion channels were included in the model. The series resistance of the somatic voltage-clamp 'electrode' in voltage-clamp simulations was set to 35 MΩ to match the average series resistance in experimental voltage-clamp recordings.

To simulate synaptic input excitatory and inhibitory inputs were placed on the soma and dendrites in different configurations. In models with only excitatory input, synapses were distributed on basal dendrites in different spatial configurations. In the dispersed configuration, contralateral and ipsilateral inputs were randomly distributed onto all dendritic branches. In the partitioned configuration, contralateral and ipsilateral inputs were distributed onto different dendritic branches such that no single branch contained both inputs. In the clustered configuration, all contralateral and ipsilateral inputs were positioned on the same, single dendritic branch. The number of synapses in the different models was 500 (dispersed), 550 (partitioned) and 700 (concentrated), and their activation was varied at rates between 1 Hz (trough) and 80 Hz (peak). Temporal correlations between synaptic inputs were introduced by using a common Poisson input train to drive sets of 50 synapses. This was the highest temporal correlation possible while still maintaining modulated responses similar to those seen experimentally. Common input trains were either restricted to within the contralateral and ipsilateral pools (monocular correlation) or shared between the pools (binocular correlation). In these simulations, the number and distribution of excitatory synapses was identical to that in the dispersed configuration.

In models with dendritic inhibition, 1000 excitatory and 300 inhibitory synapses were distributed randomly throughout the basal dendrites, with the density of inputs on a selected segment proportional to its surface area. Models with somatic inhibition contained 800 excitatory synapses distributed throughout the basal dendrites plus 180 inhibitory synapses at the soma. Excitatory inputs representing contralateral and ipsilateral inputs were sampled from the same pool (common pool model) or segregated into two pools with 60% classified as contralateral and 40% classified as ipsilateral (segregated model). As seen in the Results, there was essentially no difference between common pool and segregated models. The conductance change at excitatory synapses had an exponential rise and decay of 0.2 and 2 ms, respectively, a peak of 150 pS and a reversal potential of 0 mV. Using these parameters, the average unitary EPSP amplitude at the soma during activation of inputs randomly distributed throughout basal dendrites was 0.164 ± 0.018 mV, consistent with previous experimental findings [Silver et al., 2003]. The conductance change at inhibitory synapses had an exponential rise and decay of 0.2 and 10 ms, respectively, a peak of 150 pS and a reversal potential of -80 mV. In simulations with current-based synapses, 'excitatory' inputs had an amplitude of -2.8 pA, whereas 'inhibitory' inputs had an amplitude of $+1.1$ pA in the models with dendritic inhibition and $+0.7$ pA in models with somatic inhibition, with only excitatory inputs activated at hyperpolarised potentials and only inhibitory inputs activated at depolarised potentials. To simulate the response to drifting gratings, synapses were activated in a sinusoidal manner (2 Hz modulation) by independent, nonhomogeneous Poisson processes to match experimentally recorded currents and voltages

during visual input. In the common pool model, excitatory inputs were activated at rates between 0.54 (trough) and 27.54 Hz (peak) during contralateral input, between 0.36 and 18.36 Hz during ipsilateral input, and between 0.9 and 45.9 Hz during binocular input. In the segregated pool model, the different sets of contralateral and ipsilateral synapses were activated at rates between 0.9 and 45.9 Hz. The effective probability of release was 1.

2.3 Results

Binocular synaptic inputs sum sublinearly

We first summarise the key experimental results relevant to the numerical simulations conducted, which represent the candidate's main contribution to this study. Integration of binocular inputs was investigated by performing *in vivo* whole-cell current-clamp recordings from layer 2/3 pyramidal neurons in primary visual cortex of anaesthetised adult mice. Visual stimuli consisting of sinusoidal drifting gratings were generated on a monitor and presented individually to each eye alone or to both eyes together using computer-controlled motorised eye shutters (Figure 2.1A). To extract the underlying synaptic response, voltage traces were median-filtered to remove action potentials. Median-filtered voltage responses were averaged across trials, as well as over a single cycle of the visual stimulus, fitted with a sinusoidal function and the peak (V_{peak}), mean (V_{mean}), and amplitude of sinusoidal modulation ($V_{\text{modulation}}$) quantified (Figure 2.1B). Inputs from the contralateral and ipsilateral eyes added linearly in cells where the expected linear sum was small; however, they added sublinearly in cells where the expected linear sum was large (Figure 2.1C,D). Overall, at the preferred orientation, we observed sublinear integration of binocular synaptic inputs when the peak of the expected linear sum was larger than approximately 15 mV (Figure 2.1E), with the extent of sublinear integration increasing with the amplitude of the expected linear sum. This was also the case when we pooled all the data across all grating directions (Figure 2.1F).

Modelling sublinear binocular integration

We first simulated binocular integration of synaptic inputs in a morphologically realistic model of a layer 2/3 pyramidal neuron to determine the extent with which nonlinear interactions between ipsilateral and contralateral excitatory inputs alone contributes to sublinear integration of binocular inputs. As the extent of sublinear summation depends on the relative location of synaptic inputs, we generated models with different spatial distributions of excitatory input: either dispersed randomly throughout the entire basal dendritic tree, partitioned into different basal dendritic regions or concentrated onto a single dendritic branch (Figure 2.2A). As observed experimentally, small contralateral and ipsilateral responses summed linearly, whereas larger responses summed sublinearly (Figure 2.2B,C). The extent of sublinear binocular integration was greatest when contralateral and ipsilateral synapses were concentrated onto a single dendritic branch; however, even in this extreme case, sublinear integration was substantially less than that observed experimentally (Figure 2.2C).

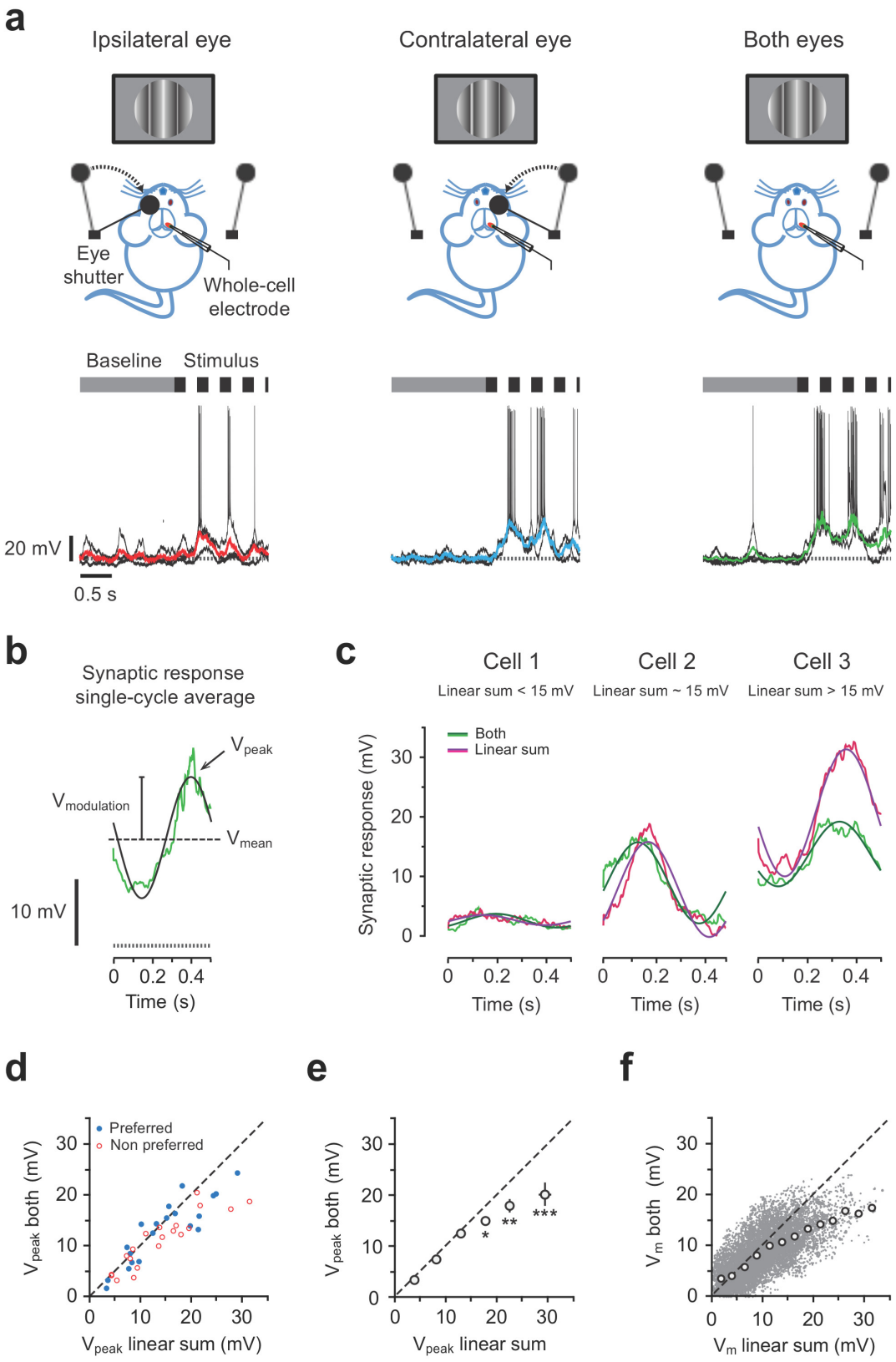

Figure 2.1: (Caption next page.)

Figure 2.1: Summation of binocular inputs at the preferred orientation. (**A**) Top: the experimental setup during presentation of the same visual stimulus selectively to each eye alone or to both eyes together, using eye shutters. Bottom: overlaid trials ($n = 3$) of membrane potential during baseline (grey bar, top) and in response to drifting gratings at the preferred orientation (dotted bars, top) during stimulation of the ipsilateral (left) or contralateral eye (middle) and both eyes together (right) with corresponding colour-coded median-filtered average responses. Dashed grey line indicates average membrane potential during baseline. (**B**) Single-cycle average of a median-filtered synaptic response (light green) fitted with a sinusoidal function (black). The peak (V_{peak}), mean (V_{mean}) and modulation component ($V_{\text{modulation}}$) are indicated. (**C**) Single-cycle synaptic response to stimulation of both eyes (light green) superimposed with the linear sum of contralateral and ipsilateral responses (pink) for three cells with different expected linear sums. Data fitted with sinusoids (dark green and purple). (**D**) V_{peak} of synaptic responses to stimulation of both eyes at the preferred orientation at either the preferred or non-preferred direction versus the corresponding expected linear sum (40 responses, $n = 20$ cells). Dashed diagonal line indicates linear summation. (**E**) Same data as in **D** in 5-mV bins for the expected linear sum and expressed as an average ± s.e.m. ($n = 20$ cells; $*P < 0.05$, $**P < 0.01$, $***P < 0.001$, two-way ANOVA, Bonferroni post-test). (**F**) Pooled data during stimulation of both eyes together. V_{m} binned in 10-ms epochs; 12,000 time bins from 240 averaged responses to 12 stimulus directions in 20 simple cells. Small grey symbols indicate individual data points. Large open symbols indicate average ± s.e.m. after binning in 2.5 mV increments. Dashed diagonal line indicates linear summation.

Next, we tested the impact of temporal correlations between excitatory inputs. Temporal correlations were made either within (monocular correlation) or between (binocular correlation) contralateral and ipsilateral inputs by using the same Poisson input train to drive multiple sets of synapses in the dispersed model (Figure 2.2D). We characterised the extent of these correlations by comparing the number of activated excitatory inputs in different time windows (Figure 2.2E). As expected, the introduction of temporal correlations increased the proportion of synapses that were simultaneously activated; however, the difference between uncorrelated and correlated models rapidly decayed when we considered correlations over longer time windows, still relevant for nonlinear interactions (Figure 2.2E,F). As a result, introduction of temporal correlations either within or between contralateral and ipsilateral inputs did not appreciably affect the degree of sublinear integration of excitatory inputs (Figure 2.2G). Together, these simulations reveal that nonlinear interactions between excitatory inputs alone are not sufficient to explain the extent of sublinear binocular integration observed experimentally. This suggests that other factors are likely to be involved in producing sublinear integration, such as inhibitory synaptic input.

The role of inhibition in sublinear binocular integration

Since excitatory input alone in our model could not produce the same degree of sublinear integration we observed experimentally, we next investigated the role of synaptic inhibition. Summation of excitatory and inhibitory postsynaptic currents (EPSCs and IPSCs) during binocular stimulation was investigated using somatic whole-cell voltage-clamp recordings. EPSCs recorded at the predicted reversal potential for inhibition (−80 mV) during stimulation of both eyes were orientation tuned (Figure 2.3A,B), consistent with previous data in mice during monocular stimulation [Tan et al., 2011, Atallah et al., 2012]. Notably, EPSCs evoked by stimulation of both eyes together were similar in magnitude to the linear sum of EPSCs evoked during stimulation of each eye alone (Figure 2.3C). Similarly, IPSCs recorded at depolarized potentials during stimulation of both eyes together were well predicted by the linear sum of IPSCs evoked by stimulation of each eye alone (Figure 2.3D). These data indicate that inhibitory and excitatory conductance changes sum essentially linearly, arguing against the idea that sublinear integration of voltage responses during binocular stimulation is presynaptic, resulting from reduced excitation or increased inhibition.

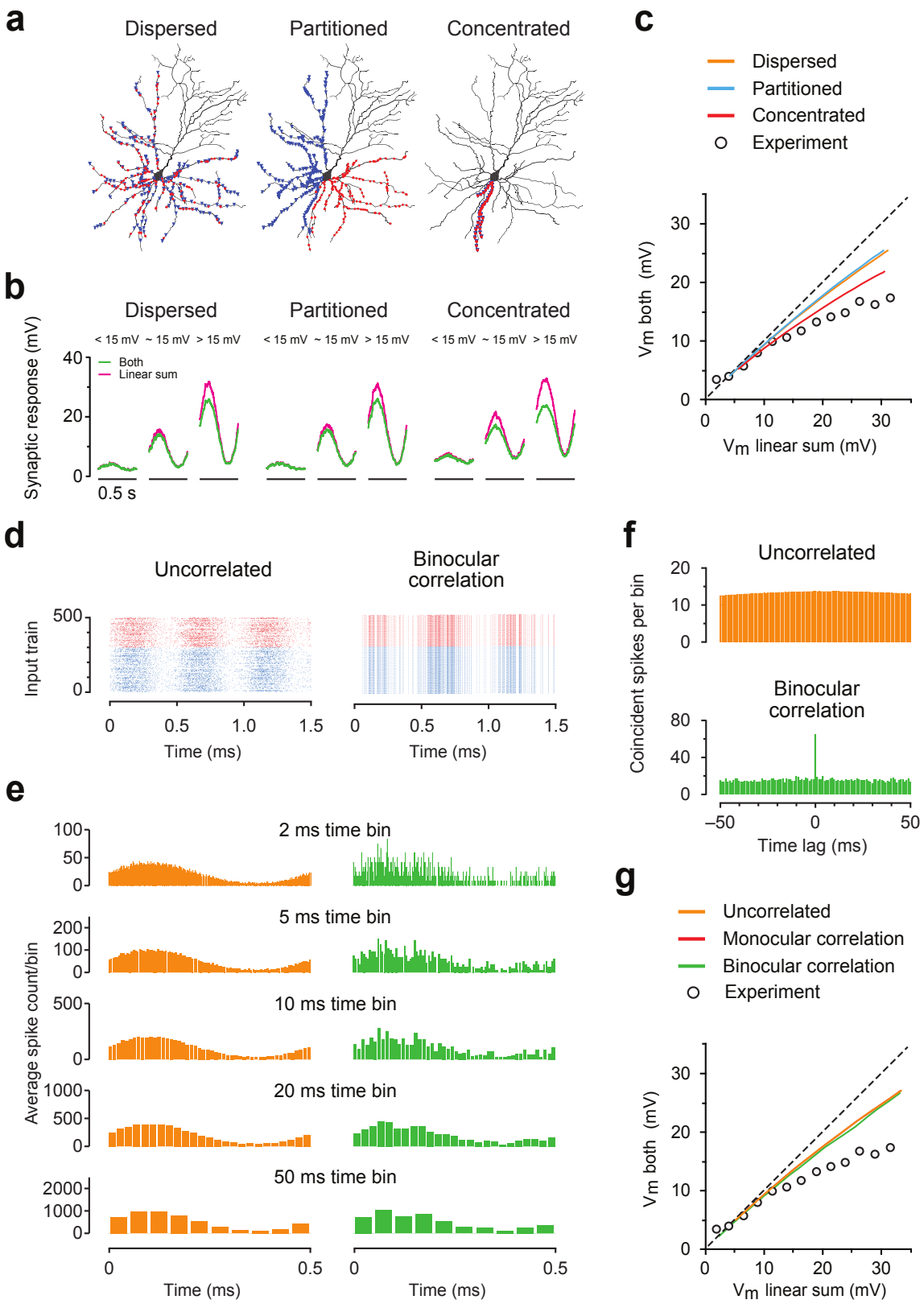

Figure 2.2: (Caption next page.)

Figure 2.2: Interactions between excitatory synapses alone cannot account for sublinear integration of binocular inputs. (**A**) Dendritic location of contralateral (blue symbols) and ipsilateral (red symbols) excitatory synapses on the basal dendrites of the layer 2/3 pyramidal neuron model. Synapses were distributed in three different spatial configurations. (**B**) Somatic current-clamp simulations of synaptic responses during activation of contralateral and ipsilateral inputs together at different intensities to evoke responses of different amplitude (linear sum $<$15 mV, $\sim$15 mV and $>$15 mV) for the different configurations. Corresponding expected linear sums are superimposed. (**C**) Simulated synaptic response amplitude during activation of contralateral and ipsilateral inputs together plotted versus the linear sum for the different models together with experimental data (open symbols, from Figure 2.1F). (**D**) Raster plots of uncorrelated (left) and correlated (right) spike trains driving contralateral (blue) and ipsilateral (red) sets of synapses during binocular stimulation. Correlations were introduced by using common Poisson trains to drive sets of 50 synapses. (**E**) Peristimulus time histograms (PSTHs) of the spike trains shown in d averaged over six stimulation cycles for the indicated time windows for uncorrelated (left) and binocularly correlated (right) inputs. (**F**) Cross-correlogram (1-ms bins) averaged across all pairs of input spike trains for uncorrelated and binocularly correlated spike trains. (**G**) Simulated synaptic response amplitude during activation of contralateral and ipsilateral sets of inputs in the dispersed model versus the corresponding expected linear sums for the uncorrelated, monocularly correlated and binocularly correlated models, together with the experimental data (open symbols, from Figure 2.1F). Orange, red and green lines are essentially superimposed.

The relationship between excitation and inhibition in single cells during binocular stimulation at the preferred orientation was studied by estimating excitatory (g_e) and inhibitory (g_i) conductances using published methods [Borg-Graham et al., 1998, Cruikshank et al., 2007]. This analysis revealed that g_e and g_i in individual neurons increased in a proportional manner during stimulation of both eyes together (Figure 2.3E; average correlation $= 0.95 \pm 0.01$, $n = 9$ cells; $P < 0.01$). The ratio of inhibition to excitation (g_i/g_e), estimated from the slope of linear fits to data from different cells, indicated that inhibition and excitation were recruited in a balanced manner, with an average ratio close to 1 (1.12 ± 0.18; $n = 9$). Consistent with this analysis, the average reversal potential of evoked synaptic currents during binocular stimulation was approximately halfway between the predicted reversal potential for excitation and inhibition (-45.8 ± 3.7 mV; $n = 9$). These data indicate that excitation and inhibition are recruited in a balanced manner during binocular visual input.

As one would expect owing to space-clamp errors associated with voltage-clamping neurons with complex dendritic trees [Williams and Mitchell, 2008], the real excitatory and inhibitory conductances required to match the experimental data were substantially larger than that estimated from somatic voltage-clamp, particularly in models with dendritic inhibition (Figure 2.4). For example, in the dendritic inhibition models, the real excitatory and inhibitory conductances (Figure 2.4B,F) were significantly greater than the corresponding measured conductances (Figure 2.4A,E). In contrast, in the somatic inhibition models, the real inhibitory conductances were closely matched to the measured inhibitory conductances, while the real excitatory conductances were again greater than the measured excitatory conductances (Figure 2.4C,D,G,H). There was essentially no difference between the common pool (Figure 2.4B,D) and segregated models (Figure 2.4F,H) in terms of the amount of excitation and inhibition required to match the experimental observations. Proportionally more inhibition was required to simulate the experimentally recorded inhibitory-to-excitatory conductance ratio ($g_i/g_e = 1.12$) in models with dendritic inhibition ($g_i/g_e = 1.22 - 1.23$, Figure 2.4B,F), whereas the opposite situation was observed in models with somatic inhibition ($g_i/g_e = 0.92$, Figure 2.4D,H). This is presumably because the impact of inhibition, as recorded from the soma, is greater when the inhibition is located at the soma. These simulations highlight issues with the interpretation of excitatory and inhibitory conductance estimates from somatic voltage-clamp data in neurons with dendrites. We will explore this further in Chapter 3.

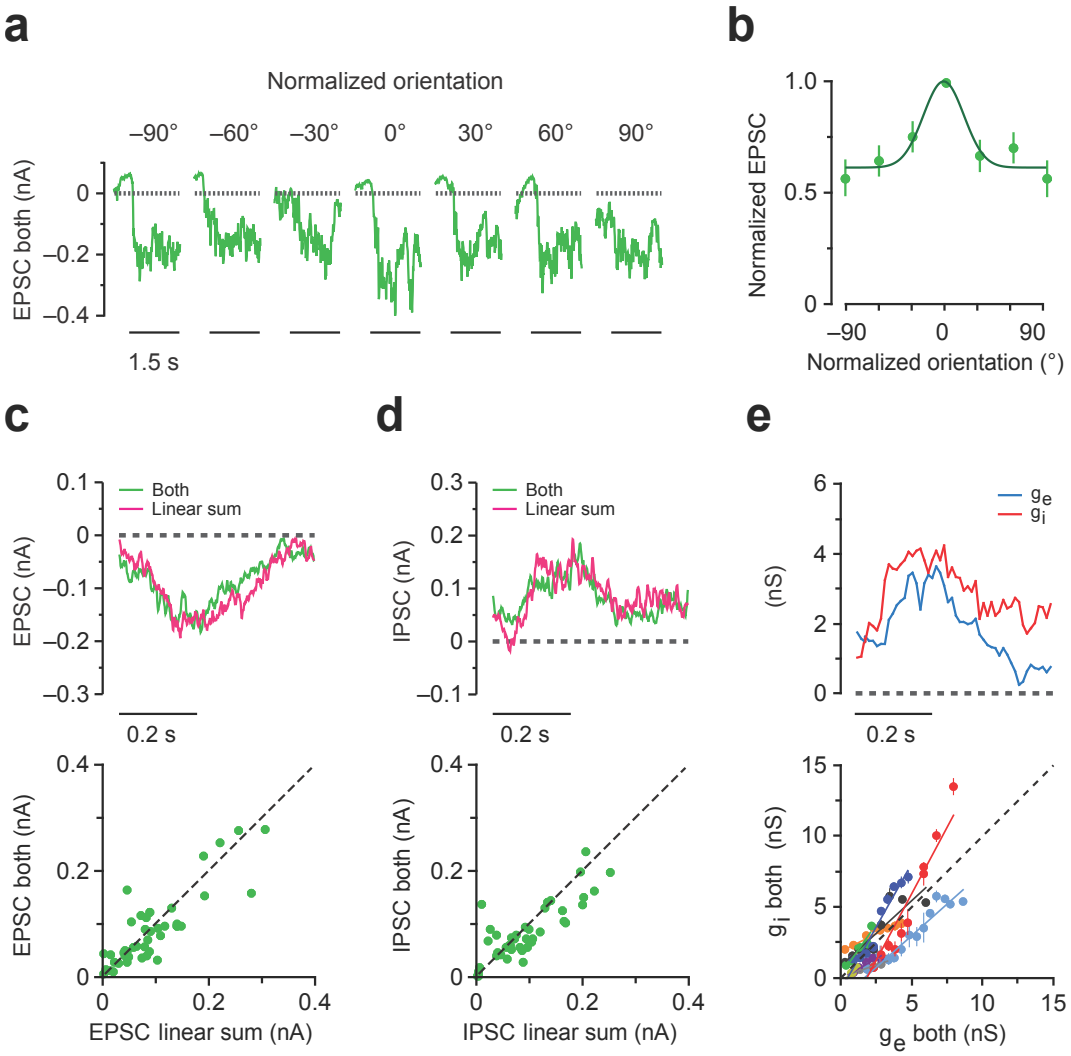

Figure 2.3: Recruitment and summation of excitation and inhibition during binocular integration. (**A**) EPSCs recorded at −80 mV in response to stimulation of both eyes with drifting gratings at six different orientations. (**B**) Normalized EPSC amplitude (± s.e.m.; averaged over the duration of the stimulus) during stimulation of both eyes versus stimulus orientation (preferred orientation defined as 0°; $n = 12$ cells). Data fitted with a Gaussian. (**C**,**D**) Top: single-cycle EPSC (**C**; recorded at −80 mV) and IPSC (**D**; recorded at +20 mV) in response to stimulation of both eyes at the preferred orientation together with the linear sum of EPSCs (**C**) and IPSCs (**D**) evoked by stimulation of each eye alone. Bottom: peak EPSC (**C**; $n = 44$ responses, $n = 11$ cells) and IPSC (**D**; $n = 40$ responses, $n = 10$ cells) amplitude evoked by stimulation of both eyes with gratings at four different orientations (preferred, +30°, +60°, +90°) versus the corresponding linear sum. (**E**) Top: single-cycle average of estimated excitatory (g_e) and inhibitory (g_i) conductance changes in a single cell in response to gratings at the preferred orientation. Bottom: g_i versus g_e ($n = 9$ cells). Data from individual cells (represented by different colours) binned at 0.5 nS increments for g_e and expressed as average ± s.e.m. Coloured lines represent linear fits to each data set.

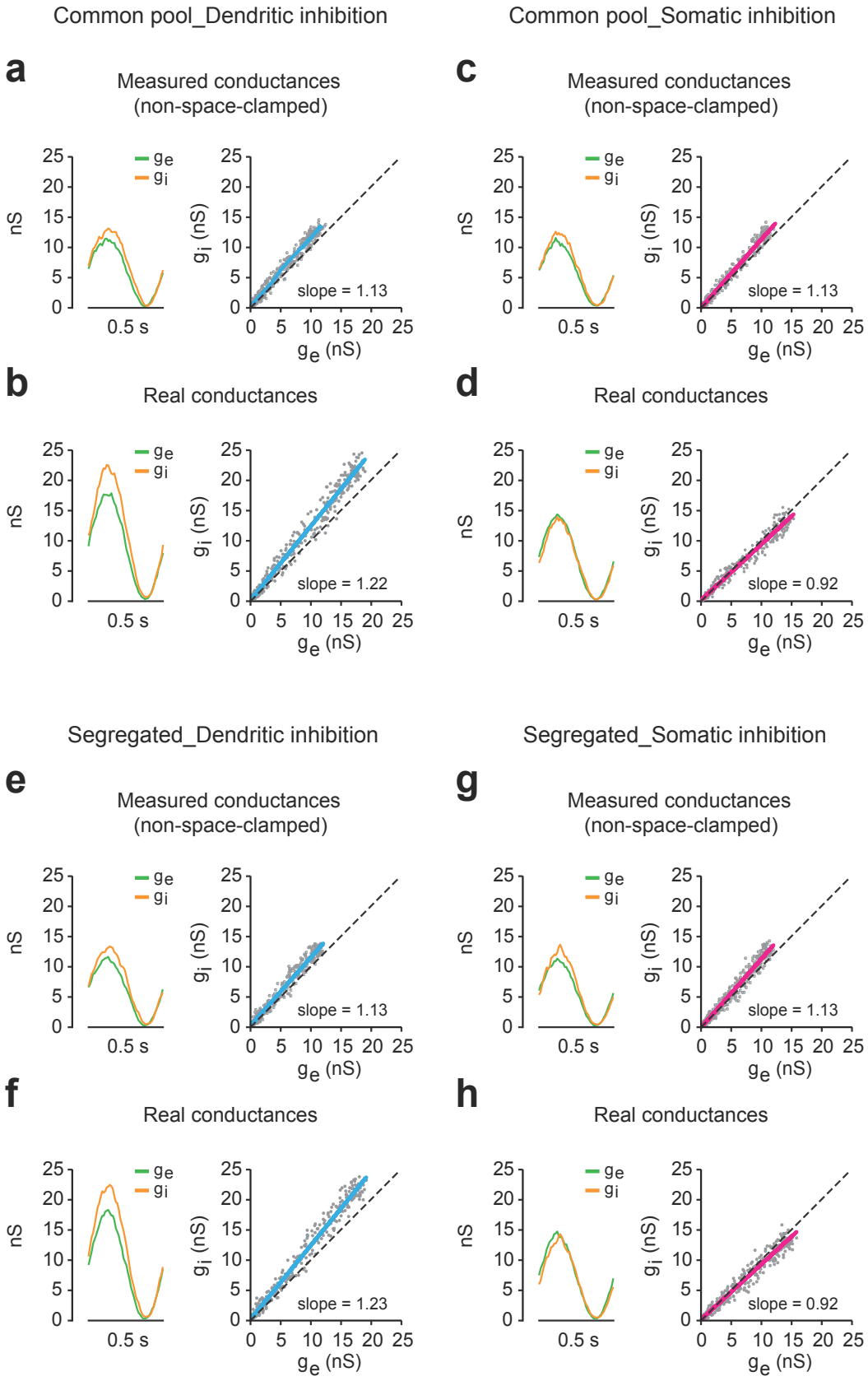

Figure 2.4: (Caption next page.)

Figure 2.4: Errors associated with somatic voltage clamp estimates of the inhibition to excitation ratio (g_i/g_e) (**A**) Left: Estimate of excitatory (g_e, green trace) and inhibitory (g_i, orange trace) conductance changes during a single cycle of binocular visual stimulation in the common-pool model with dendritic inhibition. Right: Plot of g_i versus g_e estimated from voltage-clamp simulation in the common-pool model with dendritic inhibition. Data fitted with a linear regression (light blue line, slope = 1.13). (**B**) Left: The real g_e (green trace) and g_i (orange trace) used in the common-pool model with dendritic inhibition during a single cycle of binocular visual stimulation. Right: Plot of real g_i versus g_e used in the common-pool model with dendritic inhibition. Data fitted with a linear regression (light blue line, slope = 1.22). (**C**) As for **A**, but for the common-pool model with somatic inhibition. Data fitted with a linear regression (pink line, slope = 1.13). (**D**) As for **B**, but for the common-pool model with somatic inhibition. Data fitted with a linear regression (pink line, slope = 0.92). (**E**) As for **A**, but for the segregated model with dendritic inhibition. Data fitted with a linear regression (light blue line, slope = 1.13). (**F**) As for **B**, but for the segregated model with dendritic inhibition. Data fitted with a linear regression (light blue line, slope = 1.23). (**G**) As for **C**, but for the segregated model with somatic inhibition. Data fitted with a linear regression (pink line, slope = 1.13). (**H**) As for **D**, but for the segregated model with somatic inhibition. Data fitted with a linear regression (pink line, slope = 0.92).

That EPSCs and IPSCs sum essentially linearly during binocular stimulation suggests that sublinear integration of binocular synaptic potentials has a postsynaptic origin. To investigate this further, we simulated visual responses in which contralateral and ipsilateral excitatory and inhibitory inputs were recruited linearly in a balanced manner, to match our experimental observations (Figure 2.3E). We envisaged two alternate scenarios. In one scenario, contralateral and ipsilateral inputs converged upstream from layer 2/3, for example in layer 4 (Figure 2.5A, left). In the second scenario, separate contralateral and ipsilateral inputs converged onto layer 2/3, but originated from layer 4 neurons with different ocular dominance (Figure 2.5A, middle) [Medini, 2011], whereas in the third scenario they arise via different thalamic or hemispheric pathways (Figure 2.5, right) [Restani et al., 2009]. We simulated these two scenarios by sampling ipsilateral and contralateral excitatory inputs either from a common pool or from two segregated pools of synapses distributed randomly onto basal dendrites (Figure 2.5B, top). Inhibition was modelled by distributing inhibitory inputs randomly onto the basal dendrites or placed at the soma (Figure 2.5B, bottom). We simulated our voltage-clamp data (Figure 2.3) using a realistic value of the somatic series resistance (35 MΩ) and adjusted the resting membrane properties of the model to match the average holding currents recorded at hyperpolarised and depolarised potentials. Excitatory and inhibitory inputs were randomly activated by means of sinusoidally modulated independent Poisson processes in a balanced manner. The number of activated excitatory and inhibitory synapses was adjusted in the different models so that the magnitude and ratio of inhibitory to excitatory synaptic conductances estimated from these somatic voltage-clamp simulations was similar to that observed experimentally (Figure 2.6; compare with Figure 2.3).

Linear recruitment of ipsilateral and contralateral excitatory inputs, separately or together in a balanced manner with inhibition, generated excitatory and inhibitory currents that summed in a manner similar to that observed experimentally (Figure 2.6A). Essentially no difference in voltage-clamp responses at the soma was observed in models with common compared to segregated ipsilateral and contralateral excitatory inputs (Figure 2.6A). These simulations predicted a small amount of sublinear summation of excitatory and inhibitory currents during large responses, which was absent in models with current-based synapses (Figure 2.6B), indicating that it results from poor voltage or space clamp. The capacity of this linear recruitment model to accurately predict our voltage-clamp data further substantiates our conclusion that sublinear integration of voltage responses arises postsynaptically and is not due to a decrease in excitatory drive or an increase in inhibitory drive during large binocular responses.

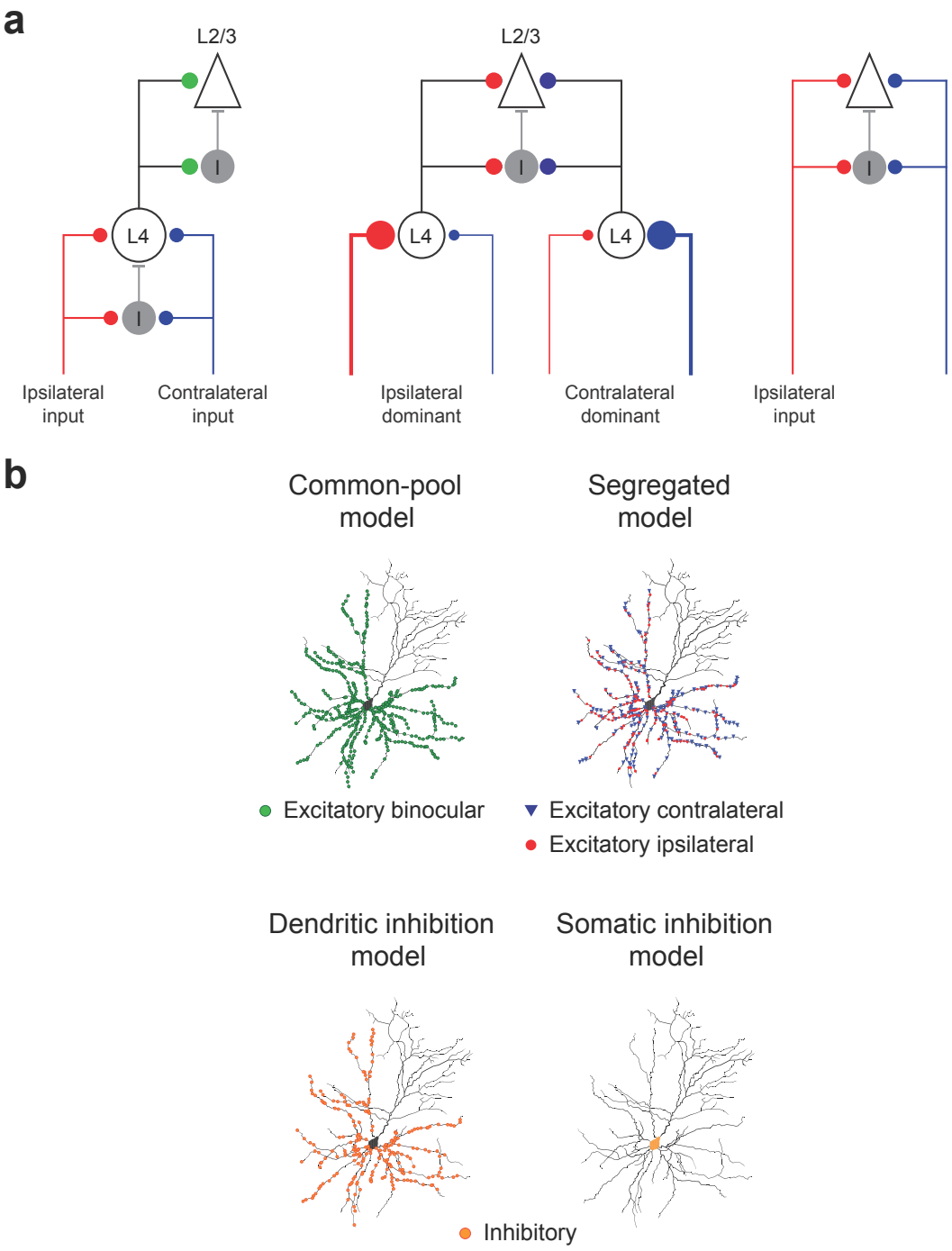

Figure 2.5: Balanced recruitment of excitation and inhibition explains sublinear integration of binocular synaptic inputs. (**A**) Models of binocular integration in layer 2/3 (L2/3) pyramidal neurons in which contralateral (blue) and ipsilateral (red) inputs converge upstream from layer 2/3, for example in layer 4 (L4, left) or arise via separate inputs from layer 4 neurons with different ocular dominance (middle) or from different thalamic/hemispheric pathways (right). Putative feed-forward interneurons (I) are shown in grey. (**B**) Distribution of excitatory and inhibitory synapses on layer 2/3 pyramidal neurons in the different models.

We next used these models to simulate voltage responses at the soma during stimulation of contralateral and ipsilateral inputs alone or together. As in the simulations using only excitatory synapses, the passive properties of the model were matched to those observed experimentally at the resting membrane potential during current-clamp recordings. These simulations accurately predicted the extent of sublinear integration of voltage responses observed experimentally during binocular stimulation (Figure 2.6C,D). Notably, we were not able to distinguish between models with common or segregated ipsilateral and contralateral input, indicating either model is valid. Furthermore, we could not distinguish between models with somatic or dendritic inhibition.

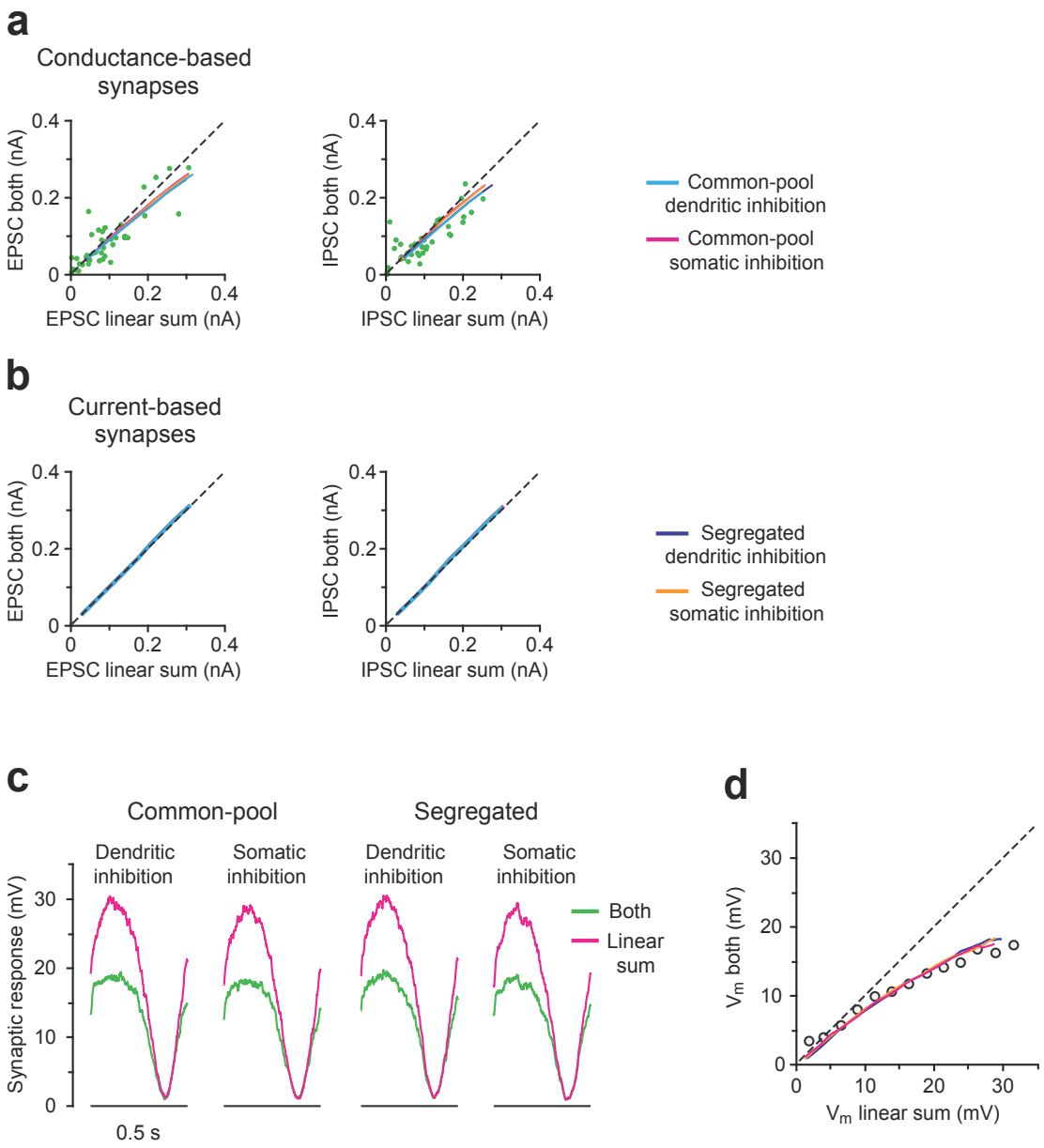

Figure 2.6: Balanced recruitment of excitation and inhibition explains sublinear integration of binocular synaptic inputs. (**A,B**) Somatic voltage-clamp simulations of EPSC (top) and IPSC (bottom) amplitude during activation of contralateral and ipsilateral inputs together compared to their linear sum using either conductance (**A**) or current synapses (**B**) for common-pool and segregated models with somatic or dendritic inhibition (lines essentially superimposed). Experimental data (from Figure 2.3C,D) shown as green symbols. (**C**) Somatic current-clamp simulations of the single-cycle synaptic responses to activation of contralateral and ipsilateral inputs together compared to their linear sum in the different models. (**D**) Simulated synaptic response amplitude during activation of contralateral and ipsilateral inputs together plotted versus the linear sum for the different models (lines essentially superimposed; same color code as in **C**). Experimental data (from Figure 2.1F) shown as open symbols.

2.4 Discussion

Here we describe the integration of binocular synaptic inputs in layer 2/3 pyramidal neurons from mouse primary visual cortex. The main experimental finding is that small inputs from the two eyes are integrated linearly, whereas large inputs are integrated sublinearly [Longordo et al., 2013]. Sublinear integration depends solely on the amplitude of the incoming inputs and is not restricted to information encoding particular aspects of the visual stimulus, such as orientation, direction, contrast or binocular phase disparity. Furthermore, sublinear binocular integration is not a result of network interactions upstream from layer 2/3 pyramidal neurons but occurs postsynaptically owing to nonlinear interactions between excitatory and inhibitory inputs recruited in a balanced manner. These experimental findings formed the basis of our numerical simulations.

Previous work *in vitro* has indicated that neurons can integrate inputs in sublinear, linear and supralinear regimes [Larkum et al., 1999b, Losonczy and Magee, 2006, Polsky et al., 2004, Williams and Stuart, 2002, Cash and Yuste, 1999, Cash and Yuste, 1998, Branco and Häusser, 2011, Krueppel et al., 2011, Enoki et al., 2002]. Synaptic inputs in these studies were activated using non-physiological stimuli under artificial conditions. How the different types of integration observed in these *in vitro* studies relate to synaptic integration *in vivo* during encoding of physiologically relevant information is unclear. Integration of binocular visual input in the visual cortex provides an ideal system for studying this issue. In mice, as in higher mammals including humans, visual inputs from the two eyes terminate in distinct and well-defined areas of the thalamus before passing on to primary visual cortex, where they converge onto single neurons [Jaubert-Miazza et al., 2005, Muir-Robinson et al., 2002, Ziburkus and Guido, 2006]. By presenting the two eyes with independently controlled visual stimuli, it is possible to see how distinct aspects of visual information are integrated at the single-cell level. Under the experimental conditions described in [Longordo et al., 2013], it was found that binocular inputs were integrated either linearly or sublinearly even with small amplitude responses, but not supralinearly, suggesting that active dendritic mechanisms are not recruited during binocular integration. Notably, sublinear integration of binocular inputs depended exclusively on the amplitude of the incoming monocular responses and was not related to specific aspects of the visual information. It therefore represents a general mode of integration in these neurons that is likely to occur under a range of stimulus conditions. The linear and sublinear modes of dendritic integration that we observed are consistent with data showing that integration of visual information in layer 2/3 pyramidal neurons occurs by means of summation of distributed rather than clustered inputs [Jia et al., 2010]. In contrast, more recent studies have demonstrated the existence

of supralinear dendritic integration in layer 2/3 pyramidal neurons *in vivo* [Smith et al., 2013, Palmer et al., 2014]. Dendritic NMDA receptor-mediated and Na^+ spikes are generated in monocular layer 2/3 pyramidal neurons by visually-evoked synaptic inputs, which in turn enhance the orientation selectivity of these neurons [Smith et al., 2013]. Similar dendritic NMDA spikes in the tufts of layer 2/3 pyramidal neurons *in vivo* occur spontaneously and can be evoked by somatosensory stimulation [Palmer et al., 2014]. Evidence also exists for supralinear dendritic integration of somatosensory information in the dendrites of cortical layer 5 pyramidal [Murayama et al., 2009, Palmer et al., 2014, Xu et al., 2012] and layer 4 spiny stellate neurons [Lavzin et al., 2012]. Our results along with previous studies indicate that while sublinear and supralinear dendritic integration modes exist *in vivo* and may be widespread phenomena in the cortex, it remains unclear the conditions under which different integration modes are utilised. While at the soma binocular integration was sublinear, it is possible that supralinear forms of integration generated by dendritic spikes occur at dendritic locations during both monocular and/or binocular synaptic input.

Although it is well documented that the convergence of the inputs from the two eyes first happens at the level of the cortex [Jaubert-Miazza et al., 2005, Muir-Robinson et al., 2002, Ziburkus and Guido, 2006], whether this convergence happens at the level of layer 2/3 pyramidal neurons is not known. Preprocessing of binocular input upstream of layer 2/3 pyramidal neurons could, in principle, explain the observed sublinear integration. This could occur through a decrease in excitatory input from layer 4 during strong binocular input, as a result of increased inhibition within layer 4. Alternatively, there could be an increase in inhibitory input to layer 2/3 neurons during large binocular responses, as a result of enhanced recruitment of feed-forward inhibition. The voltage-clamp data argue against these possibilities by showing that during binocular integration both excitatory and inhibitory currents sum linearly (Figure 2.3C,D). Furthermore, the voltage clamp data were well described by models using linear recruitment of excitatory and inhibitory input (Figure 2.6A). The capacity of this 'postsynaptic' model to accurately reproduce the extent of sublinear binocular integration observed experimentally (Figure 2.6C,D) strengthens the conclusion that sublinear integration is due to nonlinear interactions within layer 2/3 pyramidal neurons. Notably, this mechanism depends exclusively on the number of activated inputs and not on their origin. Indeed, our simulations showed that the extent of sublinear integration observed experimentally was independent of whether binocular inputs were integrated upstream of layer 2/3 neurons (common pool model) or arose through segregated ipsilateral and contralateral inputs (segregated model).

During binocular stimulation, inhibition was recruited in a proportional manner with excitation, with

an inhibitory-to-excitatory conductance ratio close to 1. Models with only excitatory synapses could not reproduce the extent of sublinear integration observed experimentally, even when we pushed these models using extreme scenarios with all excitatory inputs concentrated on the same branch or activated with high instantaneous temporal correlations. We conclude, therefore, that the recruitment of balanced inhibition is an essential component of binocular sublinear integration. Addition of inhibition makes the net reversal potential of the binocular response more hyperpolarized than with excitation alone. This increases the impact of changes in membrane potential on the driving force for current flow and thereby enhances sublinear integration. Together with other data [Haider and McCormick, 2009, Yizhar et al., 2011], these findings provide further evidence that balanced recruitment of excitation and inhibition is critical for sensory processing. Moreover, our simulations show that postsynaptic sublinear integration is a robust mechanism that, in comparison to supralinear dendritic computations, is not dependent on the precise location of incoming excitatory and inhibitory inputs

Future directions One of the key observations in our study is that inhibition is critical for sublinear integration of binocular inputs. Recent findings in mouse primary visual cortex have suggested that distinct subclasses of cortical interneurons, targeting specific neuronal compartments, are responsible for mediating different transformations of the input/output relationship of pyramidal neurons [Atallah et al., 2012, Lee et al., 2012b, Wilson et al., 2012]. Although our simulations do not allow us to identify the location of inhibition recruited during binocular integration, the observed impact of binocular sublinear integration on orientation tuning is very similar to that found during optogenetic activation of parvalbumin-expressing interneurons [Atallah et al., 2012]. This may suggest that inhibition recruited during binocular integration is largely somatic in origin. Future studies will be required to resolve the specific interneuron subtypes recruited during binocular integration and the role of these neurons in depth perception and stereopsis.

Chapter 3

Voltage- and space-clamp errors in the estimation of synaptic conductances

3.1 Introduction

Understanding the synaptic conductances driving action potential generation in neurons provides a window into the dynamics of the surrounding network. There are a number of challenges associated with accurately estimating synaptic conductances using the voltage clamp technique. The majority of synaptic inputs to neurons occur on their dendrites, distant from the typical somatic location of electrophysiological recordings. Owing to a leaky membrane and filtering effects, voltage changes do not propagate with full fidelity between the dendrites and the soma resulting in inadequate voltage- and space-clamp. In an intact cortical network, inhibitory inputs are also dynamically balanced by excitatory inputs, which means that inhibition and excitation need to be estimated concurrently. This presents further challenges as the presence of additional conductances produces a shunting effect, not dissimilar from the effect of increasing the leak conductance.

Despite these obstacles, the somatic voltage-clamp has become one of the most popular methods for investigating the dynamics of synaptic responses both *in vitro* and *in vivo* [Borg-Graham et al., 1998, Shu et al., 2003b, Wehr and Zador, 2003, Haider et al., 2006, Monier et al., 2008]. In comparison, there is a relative scarcity of studies that have investigated the impact of poor voltage-control due to cable-filtering, or so-called *space-clamp errors*, on conductance estimates obtained. One *in vitro* study directly measured the quality of dendritic voltage control obtained by somatic voltage clamp and reported that 50% of voltage control can be lost at distances as close as just 60 μm from the soma at room temperature [Williams and Mitchell, 2008]. These errors are only expected to worsen in *in vivo* settings, owing to

the lower quality of whole-cell recordings obtained and associated higher series resistance, as well as the higher conductance state of neurons in an intact brain [Destexhe et al., 2003], which compounds dendritic filtering.

Given the widespread use of the voltage-clamp technique for dissecting the synaptic conductances underlying cortical activity, we set out to clarify how voltage- and space-clamp errors affect the estimation of coincident excitatory and inhibitory synaptic inputs.

Estimating synaptic conductances

Here we review two different approaches for estimating synaptic conductances - the Borg-Graham method [Borg-Graham et al., 1998] and a class of statistical methods [Pospischil et al., 2009]. Both approaches begin with a biophysical description of the membrane potential dynamics of a single compartment, passive neuron model

$$I_{\mathrm{m}} = C\frac{dV}{dt} + g_{\mathrm{pas}}\left(V - E_{\mathrm{pas}}\right) + I_{\mathrm{syn}}, \tag{3.1.1}$$

where V is the membrane potential, C is the membrane capacitance, g_{pas} is the leak conductance, E_{pas} is the leak reversal potential and I_{m} is the total membrane current. The synaptic current, I_{syn}, is given by $I_{\mathrm{syn}} = g_{\mathrm{syn}}\left(V - E_{\mathrm{syn}}\right)$, where g_{syn} and E_{syn} are the net conductance and net reversal potential of the synaptic current, respectively. The synaptic conductance can be further decomposed into an excitatory (g_{e}) and an inhibitory (g_{i}) component, such that

$$\begin{aligned} g_{\mathrm{syn}}(t)(V - E_{syn}) &= g_{\mathrm{e}}(t)(V - E_{\mathrm{e}}) + g_{\mathrm{i}}(t)(V - E_{\mathrm{i}}), & (3.1.2)\\ g_{\mathrm{syn}}(t) &= g_{\mathrm{e}}(t) + g_{\mathrm{i}}(t), & (3.1.3)\\ E_{\mathrm{syn}}(t) &= \frac{g_{\mathrm{e}}(t)E_{\mathrm{e}} + g_{\mathrm{i}}(t)E_{\mathrm{i}}}{g_{\mathrm{e}}(t) + g_{\mathrm{i}}(t)}. & (3.1.4) \end{aligned}$$

where E_{e} and E_{i} are the reversal potentials of the excitatory and inhibitory inputs, respectively.

Using these equations and given values for E_{e} and E_{i}, we can derive expressions for g_{e} and g_{i} as functions of g_{syn} and E_{syn}

$$\begin{aligned} g_{\mathrm{i}}(t) &= \frac{g_{\mathrm{syn}}(t)[E_{\mathrm{e}} - E_{\mathrm{syn}}(t)]}{E_{\mathrm{e}} - E_{\mathrm{i}}}, & (3.1.5)\\ g_{\mathrm{e}}(t) &= g_{\mathrm{syn}}(t) - g_{\mathrm{i}}(t). & (3.1.6) \end{aligned}$$

The Borg-Graham method [Borg-Graham et al., 1998]

In voltage-clamp, the membrane potential is held at a constant voltage (V_{hold}), hence $\frac{dV}{dt} = 0$. As a result, the current through the electrode (I_{hold}) is given by

$$I_{\text{hold}} = I_{\text{pas}} + I_{\text{syn}} = g_{pas}\left(V_{\text{hold}} - E_{\text{pas}}\right) + g_{\text{syn}}\left(V_{\text{hold}} - E_{\text{syn}}\right), \tag{3.1.7}$$

where $I_{\text{pas}} = g_{\text{pas}}\left(V_{\text{hold}} - E_{\text{pas}}\right)$ and $I_{\text{syn}} = g_{\text{syn}}\left(V_{\text{hold}} - E_{\text{syn}}\right)$ are the passive and synaptic contributions to I_{hold}, respectively.

In the baseline state, where it is assumed there is no synaptic activity ($I_{\text{syn}} = 0$), the holding current is made up entirely of the passive component

$$I_{\text{hold,rest}} = I_{\text{pas}} = g_{\text{pas}}V_{\text{hold}} - g_{\text{pas}}E_{\text{pas}}. \tag{3.1.8}$$

Thus, g_{pas} is the slope of the ($I_{\text{hold,rest}}$ vs V_{hold}) relationship, which has a vertical intercept $-g_{\text{pas}}E_{\text{pas}}$. That is, g_{pas} and E_{pas} are easily determined by the linear relationship between $I_{\text{hold,rest}}$ and V_{hold}.

In the active state, when synapses are being stimulated, the holding current includes the synaptic component as well

$$I_{\text{hold,act}} = I_{\text{pas}} + I_{\text{syn}} = \left(g_{\text{pas}} + g_{\text{syn}}\right)V_{\text{hold}} - \left(g_{\text{pas}}E_{\text{pas}} + g_{\text{syn}}E_{\text{syn}}\right). \tag{3.1.9}$$

Here, $\left(g_{\text{pas}} + g_{\text{syn}}\right)$ is the slope of the ($I_{\text{hold,act}}$ vs V_{hold}) relationship, which has vertical intercept $-\left(g_{\text{pas}}E_{\text{pas}} + g_{\text{syn}}E_{\text{syn}}\right)$. Since g_{pas} was determined from the linear relation in Equation (3.1.8), g_{syn} is obtained by subtracting g_{pas} from the slope of Equation (3.1.9), and E_{syn} is subsequently calculated from the vertical intercept of Equation (3.1.9). Once g_{syn} and E_{syn} are known, g_{i} and g_{e} are obtained from Equations (3.1.5) and (3.1.6).

The Borg-Graham method has been used extensively to estimate the excitatory and inhibitory synaptic conductances underlying spontaneous and evoked network activity both *in vitro* and *in vivo*, for example during cortical Up and Down states [Shu et al., 2003b, Haider et al., 2006] and visual stimulation [Anderson et al., 2000a, Longordo et al., 2013].

Statistical methods [Pospischil et al., 2009]

Statistical methods in general (reviewed in [Pospischil et al., 2009]), take as their starting point Equation (3.2.1) i.e. a cell in current-clamp configuration. Then by making certain assumptions about the statistical form of $g_e(t)$ and $g_i(t)$, it is possible to estimate the parameters of the statistical model from $V(t)$. For example, a classic statistical model used to describe variability in synaptic input that gives rise to membrane potential fluctuations is the Ornstein-Uhlenbeck process (OUP; [Uhlenbeck and Ornstein, 1930])

$$\frac{dg_{\{e,i\}}}{dt} = \frac{1}{\tau_{\{e,i\}}}\left[g_{\{e,i\}}(t) - g_{\{e,i\},0}\right] + \sqrt{\frac{2\sigma^2_{\{e,i\}}}{\tau_{\{e,i\}}}}\chi_{\{e,i\}}(t), \tag{3.1.10}$$

where $g_{e,0}$ and $g_{i,0}$ are the average conductances, τ_e and τ_i are time constants, σ_e and σ_i are the standard deviation of the excitatory and inhibitory noise, and $\chi_e(t)$ and $\chi_i(t)$ are independent Gaussian white noise processes with mean zero and standard deviation one [Destexhe et al., 2001]. The utility of the OUP is in its simplicity, and the existence of numerical methods for solving the stochastic equations [Gillespie, 1996]. For each conductance $g_{\{e,i\}}(t)$, there are three parameters, $\{g_{\{e,i\},0}, \sigma_{\{e,i\}}, \tau_{\{e,i\}}\}$. Usually, the time constants τ_e and τ_i are taken to reflect the decay of the synaptic conductances, and hence are assumed to be known. Thus the unknown parameters are the mean and standard deviation $\{g_{\{e,i\},0}, \sigma_{\{e,i\}}\}$ of the synaptic conductances.

One approach for estimating $\{g_{\{e,i\},0}, \sigma_{\{e,i\}}\}$, the so-called VmD method [Rudolph et al., 2004], relies on the observation that the probability density function of V, $\rho(V)$, can be approximated by a Gaussian distribution characterised by two parameters, $(\overline{V}, \sigma_V)$ [Rudolph and Destexhe, 2003],

$$\rho(V) \approx \exp\left[-\frac{(V-\overline{V})^2}{2\sigma_V^2}\right]. \tag{3.1.11}$$

Furthermore, the parameters, $(\overline{V}, \sigma_V)$ can be expressed in terms of the synaptic conductance parameters $\{g_{\{e,i\},0}, \sigma_{\{e,i\}}\}$. However, there are four unknown parameters to be estimated (two each for excitatory and inhibitory conductances) and only two measurable quantities $(\overline{V}, \sigma_V)$. To render the solution tractable, two different distributions of V need to be considered, at two different levels of constant current injection.

An advantage of the VmD method over the Borg-Graham method is that in addition to providing estimates for the mean conductances, $\{g_{\{e,i\},0}\}$, the VmD method also estimates the magnitude of the variability in synaptic input, $\{\sigma_{\{e,i\}}\}$. Unlike the VmD method described previously, which requires two voltage traces,

the VmT approach ([Pospischil et al., 2007, Pospischil et al., 2008]) requires a single voltage trace to estimate the four synaptic parameters $\{g_{\{e,i\},0}, \sigma_{\{e,i\}}\}$. The way the VmT method achieves this is by employing a maximum-likelihood estimation.

These statistical methods and other related approaches [Lansky et al., 2006, Lansky et al., 2010] require relative stationarity of the statistical process (e.g. the plateau phase of an Up state) and so are not suited for dissecting events which rapidly change (e.g. a Down to Up state transition or evoked responses).

Single-trial estimation

The Borg-Graham and the VmD methods described above require multiple trials to estimate both excitatory and inhibitory conductances. In contrast, the VmT method is able to extract the statistical parameters of the synaptic conductances in a single trial. However, the statistical methods typically require relative stationarity of the synaptic inputs for robust estimation (on the order of 100's of ms). Consequently, these approaches are unsuitable for studying the interplay between excitatory and inhibitory conductances that occur on shorter time scales (i.e. millieseconds).

Several single trial methods have been proposed for resolving non-stationary synaptic conductances. One approach is to oversample the membrane potential, allowing extraction of several variables (i.e. synaptic conductance parameters) from a single measurement [Bédard et al., 2012]. Another approach is a variant on the Borg-Graham method that involves rapidly alternating the holding voltage, so that the excitatory and inhibitory conductances are measured pseudo-simultaneously [Cafaro and Rieke, 2010]. Related methods include periodically probing the neuron with hyperpolarising current pulses [Douglas et al., 1988] or action potentials [Chizhov et al., 2014]. In general, these methods are only appropriate when the time-scale of the synaptic conductance fluctuations is significantly slower than the alternating frequency used to change the membrane potential, which in turn is limited by the time taken for the cell to reach steady-state voltage. In [Cafaro and Rieke, 2010], the method was applied to midget ganglion cells in the retina, which are small, compact and have short time constants, and the alternating frequency of 100 Hz was significant faster than the kinetics of the measured synaptic response. In contrast, cortical pyramidal neurons are much larger and have longer time constants, and therefore would require a slower alternating frequency while the time scale of synaptic conductance changes (e.g. in response to sensory input) is also faster (on the order of milliseconds to tens of milliseconds). An altogether different approach takes advantage of correlated synaptic inputs between nearby cortical neurons *in vivo* [Okun and Lampl, 2008]. Since nearby neurons receive similar synaptic inputs, reflected by highly synchronous membrane potential

fluctuations [Lampl et al., 1999, Petersen et al., 2003, Hasenstaub et al., 2005], excitatory and inhibitory conductances can be estimated concurrently by simultaneously recording from two nearby neurons.

Single compartment versus multiple compartments

It is important to note that all of these methods view a neuron as a single compartment and to our knowledge, none have adequately addressed the multi-compartment extension. The key challenge in estimating synaptic conductances in a two or multi-compartment model is the presence of space-clamp errors. Electrodes act as a point source of current. The combination of resistance to current flow along the axis of dendrites, as well as the inherent leakiness of cell membranes means that current passing through the electrode exerts little influence distal from the recording location. Similarly, synaptic currents that enter the cell distally can be significantly attenuated by the time they reach the soma. These effects together prevent accurate estimation of synaptic conductances, in both current-clamp and voltage-clamp recordings.

3.2 Methods

To elucidate the basic features of voltage- space-clamp errors and how they affect the estimation of synaptic conductances, we performed numerical simulations on one- and two-compartment neuron models in the NEURON environment. The models were purely passive and did not contain any voltage-gated conductances. The only membrane conductances present in the models were a leak conductance and excitatory and inhibitory synaptic conductances.

The single compartmental model

The single compartment model, depicted in Figure 3.1A, consists of a membrane capacitance, leak conductance, and excitatory and inhibitory synaptic conductances. The compartment has length 10 μm and diameter 10 μm and consisted of a single segment only. The membrane potential (V) changes in the compartment are governed by the differential equation

$$C\frac{dV}{dt} = -g_{\text{pas}}(V - E_{\text{pas}}) - g_{\text{e}}(t)(V - E_{\text{e}}) - g_{\text{i}}(t)(V - E_{\text{i}}) + I_{\text{ext}} \tag{3.2.1}$$

The specific membrane resistance ($R_{\text{m}} = 1/g_{\text{pas}}$) was set to 10000 Ω cm^2 and the leak reversal potential (E_{pas}) was -70 mV. The specific membrane capacitance (C) was 1 μF cm^{-2}. Voltage-clamp recordings were performed by a single "electrode" at the soma. The current injected by the electrode at this site is I_{ext}; in voltage-clamp mode, this corresponds to the holding current.

The two compartmental model

We extend the one-compartment model described in the previous section by adding an additional dendritic compartment governed by the same biophysical equations (Figure 3.1B). The somatic (s) and dendritic (d) compartments are connected by an axial resistance (R_{axial}), and the membrane potential dynamics are described by the following differential equations

$$C_{\text{s}}\frac{dV_{\text{s}}}{dt} = -g_{\text{s}}(V_{\text{s}} - E_{\text{s,rev}}) - \frac{V_{\text{d}} - V_{\text{s}}}{R_{\text{axial}}} + I_{\text{ext}}, \tag{3.2.2}$$

$$C_{\text{d}}\frac{dV_{\text{d}}}{dt} = -g_{\text{d}}(V_{\text{d}} - E_{\text{d,rev}}) - \frac{V_{\text{s}} - V_{\text{d}}}{R_{\text{axial}}}, \tag{3.2.3}$$

where $C_{\text{s,d}}$ represents the specific membrane capacitance, $V_{\text{s,d}}$ the membrane potential, $g_{\text{s,d}}$ the net conductance of all membrane currents, and $E_{\text{s,d}}$ the net reversal potential of all membrane conductances, in the respective compartments. In the two-compartment model, the somatic compartment had length 10 μm and diameter 10 μm, while the dendritic compartment had length 1000 μm and diameter 2.5

μm. Both compartments consisted of a single segment only. The default value of the axial resistance (R_{axial}) was 100 Ω cm, but was varied in a number of the experiments. Values for the other biophysical properties were the same as for the one compartment model. The current injected by the electrode at this soma is I_{ext}.

Synapses

In simulations with the one compartment model, a single excitatory and inhibitory synapse was located in the somatic compartment. In simulations with the two compartment model, excitatory and inhibitory synapses was located in both compartments or in the dendritic compartment only, as indicated in the relevant sections. The time course of excitatory and inhibitory synaptic conductance changes had exponential rise ($\tau_{\text{rise,e}} = 0.2$ ms and $\tau_{\text{rise,i}} = 0.3$ ms) and fall ($\tau_{\text{fall,e}} = 2$ ms and $\tau_{\text{fall,i}} = 5$ ms), and reversal potentials $E_{\text{e}} = 0$ mV and $E_{\text{i}} = -80$ mV, respectively. The conductance change at excitatory synapses had a peak of 250 pS while inhibitory synapses had a peak of 100 pS. Synapses were stimulated randomly by independent Poisson processes.

Estimating cell capacitance

In the single compartment (iso-potential) model the effective cell capacitance was estimated by measuring the area under the curve of the voltage response to a current step as follows. After adjusting for the baseline voltage, the voltage response to a step current is given by

$$V = V_0 e^{-t/R_{\text{in}}C} \tag{3.2.4}$$

where V_0 is the initial voltage, t is time, R_{in} is input resistance, and C is effect cell capacitance. The integral of the voltage response is then

$$\begin{aligned} \int_0^\infty V\,dt &= \int_0^\infty V_0 e^{-t/R_{\text{in}}C}\,dt \\ &= V_0 R_{\text{in}} C \end{aligned}$$

Hence

$$C = \frac{\text{AUC}}{V_0 R_{\text{in}}} \tag{3.2.5}$$

where $\text{AUC} = \int_0^\infty V\,dt$ is the area under the voltage response curve.

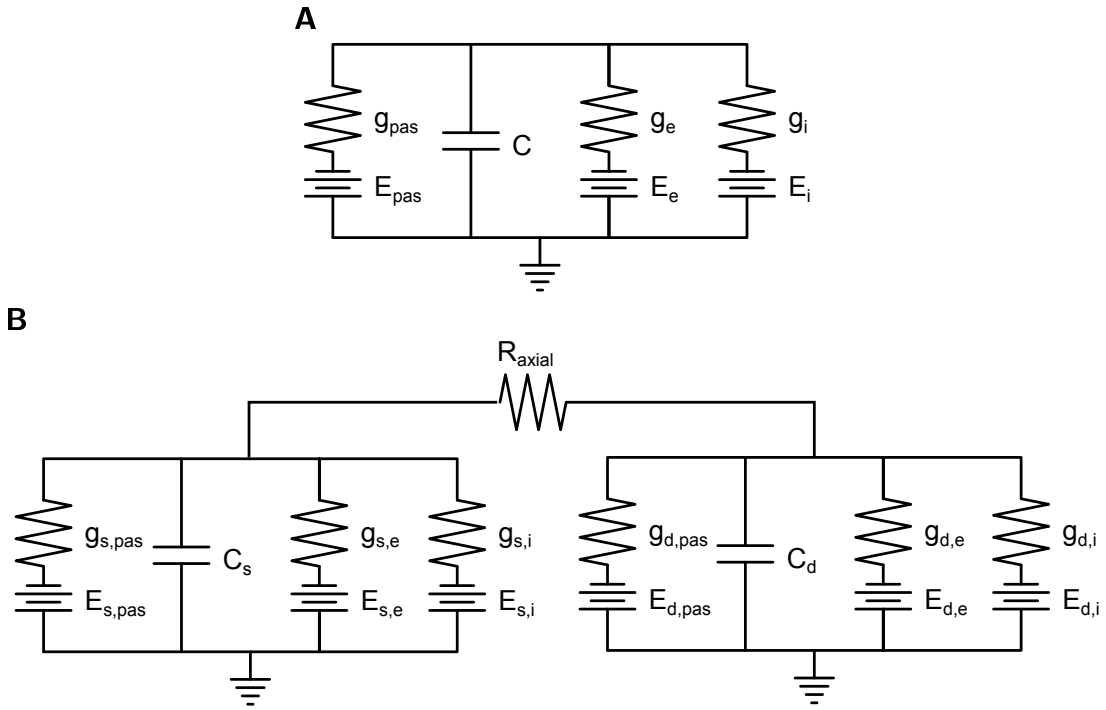

Figure 3.1: Circuit diagrams for neuron models. (**A**) Equivalent circuit diagram of single compartment neuron model. Circuit elements are the leak conductance, g_{pas}; leak reversal potential, E_{pas}; membrane capacitance, C; excitatory synaptic conductance, g_{e}; excitatory synaptic reversal potential, E_{e}; inhibitory synaptic conductance, g_{i}; inhibitory synaptic reversal potential, E_{i}. (**B**) Equivalent circuit diagram of two-compartment neuron model. Circuit elements are the leak conductance, $g_{\text{x,pas}}$; leak reversal potential, $E_{\text{x,pas}}$; membrane capacitance, C_{x}; excitatory synaptic conductance, $g_{\text{x,e}}$; excitatory synaptic reversal potential, $E_{\text{x,e}}$; inhibitory synaptic conductance, $g_{\text{x,i}}$; inhibitory synaptic reversal potential, $E_{\text{x,i}}$; where $x = \{\text{s}, \text{d}\}$ for the somatic and dendritic compartments, respectively.

3.3 Results

Series resistance errors

In our first set of simulations we consider the impact of electrode series resistance errors on the estimation of synaptic conductances in a single compartment neuron (Figure 3.1A). Excitatory and inhibitory synapses were stimulated at a rate of 5000 Hz. This resulted in an average excitatory conductance of 3.2 nS and an average inhibitory conductance of 3.0 nS. The impact of electrode series resistance was determined by using dynamic clamp reinjection of the conductances estimated from voltage clamp simulations and comparing the resultant change in membrane potential with the change in membrane potential during the actual synaptic conductance. The mean squared error (MSE) of the difference between the actual synaptic voltage change and the voltage recorded during dynamic clamp re-injection of the estimated synaptic conductances was used to quantify the accuracy of the predicted conductance estimations.

The resistance across the electrode (referred to as the "series resistance", R_s) causes a voltage drop across the electrode of iR_s, where i is the current recorded by the electrode. Without series resistance compensation, there are two important implications for single electrode voltage-clamp recordings

1. the cell is held at a voltage different from the command voltage, and
2. the cell is no longer clamped at a constant voltage.

Regarding the first point, the difference between the command voltage and the actual membrane potential is simply the voltage drop across the electrode; $\Delta V = iR_s$. The second point requires further elaboration. Referring to Equation (3.2.1), if the cell's membrane potential is no longer constant, then $\frac{dV}{dt}$ does not vanish to zero in the derivation of the Borg-Graham method. That means that the holding current, I_{hold}, in Equation 3.1.7 contains a capacitive term. That is

$$I_{hold} = I_{pas} + I_{syn} = g_{pas}\,(V_{hold} - E_{pas}) + g_{syn}\,(V_{hold} - E_{syn}) + C\frac{dV}{dt}. \tag{3.3.1}$$

Therefore, two corrections need to be applied sequentially to account for the series resistance.

1. the holding voltage is $\tilde{V}_{hold} = V_{hold} - iR_s$, and
2. the holding current corrected for the capacitative term is $\tilde{I}_{hold} = I_{hold} - C\frac{dV}{dt}$.

Using these expressions, the series resistance corrected current-voltage relationships become

$$\tilde{I}_{\text{hold,rest}} = g_{\text{pas}}\tilde{V}_{\text{hold}} - g_{\text{pas}}E_{pas}, \tag{3.3.2}$$

$$\tilde{I}_{\text{hold,act}} = (g_{\text{pas}} + g_{\text{syn}})\,\tilde{V}_{\text{hold}} - (g_{\text{pas}}E_{\text{pas}} + g_{\text{syn}}E_{\text{syn}})\,, \tag{3.3.3}$$

and the linear relationship between $\tilde{I}$ and $\tilde{V}$ allows extraction of the synaptic conductance parameters.

We demonstrate these ideas in Figure 3.2. We first fit a single exponential (with time constant $\tau = 10.02$ ms) by extracting the capacitance from the area under the curve of the voltage response to a current step (Figure 3.2B). By knowing the amplitude of the current step we can recover the input resistance of the compartment, and using Equation (3.2.5) we derive the value of the capacitance used for the capacitive current correction.

We consider a series of scenarios. First, we simulate recordings obtained with different series resistance levels, and we estimate the synaptic conductances without any series resistance compensation (Figure 3.2C,D). We then reinject the estimated synaptic conductances and record the membrane potential response (Figure 3.2E). From these traces it is apparent that estimates obtained under a high series resistance poorly reproduce the current-clamp recordings. The MSE of the predicted traces increase markedly for high series resistance levels (Figure 3.2F). In addition to calculating the MSE, we also compute the cross-covariance of the predicted traces with the actual current-clamp recordings. While the normalised cross-covariances have the same shape, there is an appreciable time lag that worsens with increasing series resistance (Figure 3.2G). This lag reflects filtering effects in the estimation of synaptic conductances when the series resistance is high.

Using the same synaptic conductance time courses, we perform the same estimation procedure but we now compensate for the voltage drop across the series resistance and adjust the holding voltage of the cell accordingly. In this case, the synaptic conductances are estimated much more reliably (Figure 3.2H,I) and dynamic clamp reinjection of the estimated conductances reproduces the current-clamp trace more precisely (Figure 3.2J), as indicated by smaller MSEs (Figure 3.2K) and smaller lags in the cross-covariance (Figure 3.2L). Finally, we estimate the synaptic conductances and correct for both the voltage drop across the series resistance and the capacitive current. Under these conditions, the synaptic conductances are estimated almost exactly (Figure 3.2M-Q). For example, in the absence of series resistance correction, the MSE of the predicted voltage response with 100 MΩ series resistance is

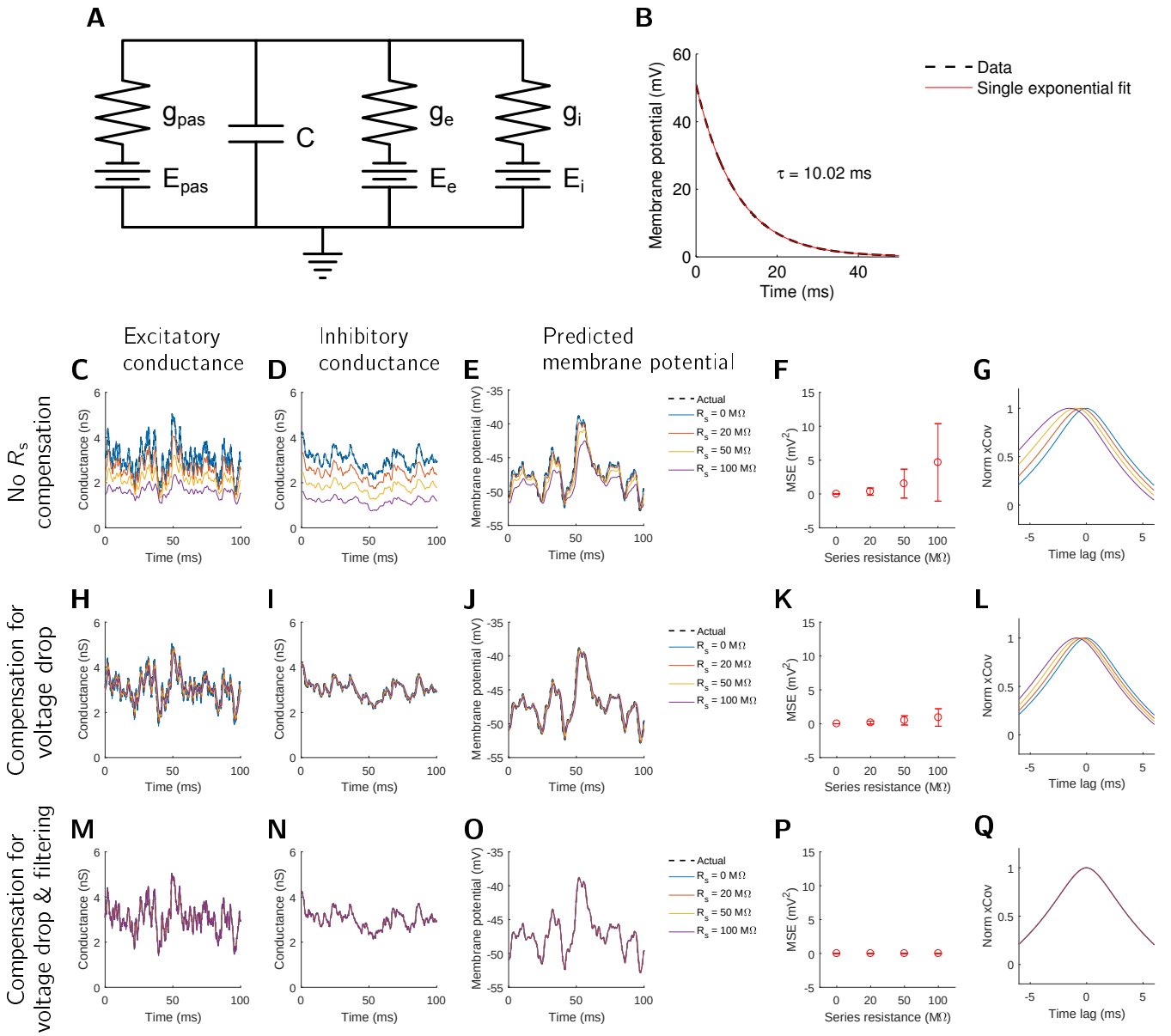

Figure 3.2: Series resistance and capacitive compensation in a single compartment neuron model. (**A**) Circuit diagram of one compartment model. (**B**) Voltage response to current step, adjusted for steady state and single exponential fit. Time constant of the fit is 10.02 ms. Second row (**C-G**), no series resistance compensation; third row (**H-L**), correction for the voltage drop across the series resistance; fourth row (**M-Q**), correction for both the voltage drop and the capacitive current. First column (**C,H,M**), the actual and estimated excitatory conductances. Second column (**D,I,N**), the actual and estimated inhibitory conductances. Third column (**E,J,O**), the membrane potential response to dynamic clamp reinjection of the estimated conductances. Fourth column (**F,K,P**), the mean squared error (MSE) between the actual membrane potential and dynamic clamp conductance reinjection. Fifth column (**G,L,Q**), the cross covariance between the actual membrane potential and dynamic clamp conductance reinjection of estimated conductances.

4.66 mV^2. Correcting for the voltage drop, this improves markedly to 0.92 mV^2, an 80.3% reduction in MSE. The addition of capacitance correction to series resistance compensation virtually eliminates the MSE, which is 5.29×10^{-4} mV^2 (Figure 3.2F,K,P).

Taken together, these results indicate that when applying the Borg-Graham method to extract the synaptic conductances in a single compartment neuron model, the cell does not need to be held at a constant voltage with series resistance compensation applied. Since the command voltage and current are known, and the series resistance and cell capacitance can be estimated, the actual membrane potential of the cell can be calculated. This procedure allows estimation of the synaptic conductances even when the series resistance is not compensated. Furthermore, in our model, compensating for the voltage drop across the series resistance accounted for most of the error, while the capacitive current only contributes to a smaller fraction of the error.

Series resistance correction in a two compartment neuron model

Series resistance compensation in a single compartment model as discussed in the previous section does not address issues that arise due to space-clamp errors in neurons with dendrites. To investigate problems associated with poor space-clamp we performed the same simulations using a two-compartment model (Figure 3.3A). Excitatory and inhibitory synapses were located on both somatic and dendritic compartments and stimulated at a rate of 5000 Hz. This resulted in an average total excitatory conductance of 6.4 nS and an average total inhibitory conductance of 6.0 nS. Under all conditions the excitatory and inhibitory conductances, which both contain somatic and dendritic components, are significantly underestimated compared to the actual conductances. In the absence of series resistance compensation, the greater the series resistance, the more the conductances are underestimated (Figure 3.3C,D). In contrast to the single compartment case, even with series resistance compensation, the synaptic conductances remain severely underestimated (Figure 3.3H,I,M,N). The predicted membrane potential is also affected by increasing series resistance (Figure 3.3E,F), however the MSE is markedly reduced by series resistance compensation (Figure 3.3K,K,P). In the absence of series resistance compensation or capacitance correction, the MSE of the predicted voltage response with 100 MΩ series resistance is 36.0 mV^2. With series resistance correction, this improves markedly to 0.45 mV^2, a 98.7% reduction. The addition of capacitance correction to series resistance compensation, despite the fact that estimation of the capacitance based on the area under the exponential fit is wrong (see poor fit in Figure 3.3B), improves the MSE slightly to 0.34 mV^2, a further 25.2% reduction (Figure 3.3F,K,P). Correcting for the capacitive current does not correct the conductance underestimation, however, and only has a small impact on

the predicted membrane potential even with series resistance compensation. Capacitance correction also does not eliminate the filtering effects, unlike the single compartment case. Importantly in the two compartment case, low MSEs achieved by dynamic clamp reinjection of the estimated conductances in the soma only reflects the ability of the voltage-clamp to estimate the net effect of synaptic conductances on the somatic membrane potential. It does not indicate good space-clamp since the total synaptic conductances remain significantly underestimated.

We explain these observations by considering the circuit description of the two compartment model (Figure 3.3A), given by Equations (3.2.2) and (3.2.3) (see Methods for further details). Suppose under steady-state conditions (i.e. temporal derivatives are zero), the somatic membrane potential is held at some voltage $V_{\mathrm{s,hold}}$ with holding current I_{hold}. Then Equations (3.2.2) and (3.2.3) become

$$0 = -g_{\mathrm{s}}\left(V_{\mathrm{s,hold}} - E_{\mathrm{s,rev}}\right) - \frac{V_{\mathrm{d}} - V_{\mathrm{s,hold}}}{R_{\mathrm{axial}}} + I_{\mathrm{hold}}, \tag{3.3.4}$$

$$0 = -g_{\mathrm{d}}\left(V_{\mathrm{d}} - E_{\mathrm{d,rev}}\right) - \frac{V_{\mathrm{s,hold}} - V_{\mathrm{d}}}{R_{\mathrm{axial}}}. \tag{3.3.5}$$

Then from Equation (3.3.5), if $V_{\mathrm{s,hold}} = V_{\mathrm{d}}$, it follows that $V_{\mathrm{s,hold}} = E_{\mathrm{d,rev}}$. In other words, the dendritic compartment is only held at the same voltage as the somatic compartment when the holding voltage of the somatic compartment is equal to the net reversal potential of the membrane currents in the dendritic compartment. This condition is never met when the membrane currents in the dendritic compartment are varying. In this case, the dendritic membrane potential also fluctuates and therefore produces a capacitive current. As a result, the current that flows through the axial resistance contributes to the currents measured by the somatic electrode, and this axial current contains both a capacitive component as well as synaptic components that cannot be dissociated. Moreover, since the model is not isopotential, the capacitance is distributed and cannot be compensated for by a point electrode. Thus, while we have attempted to correct for the capacitive component based on a single exponential time course for the voltage decay (see Methods), which assumes a single compartment RC model, in reality the voltage response contains a mixture of exponential time courses. This complicates the estimation of the cell capacitance.

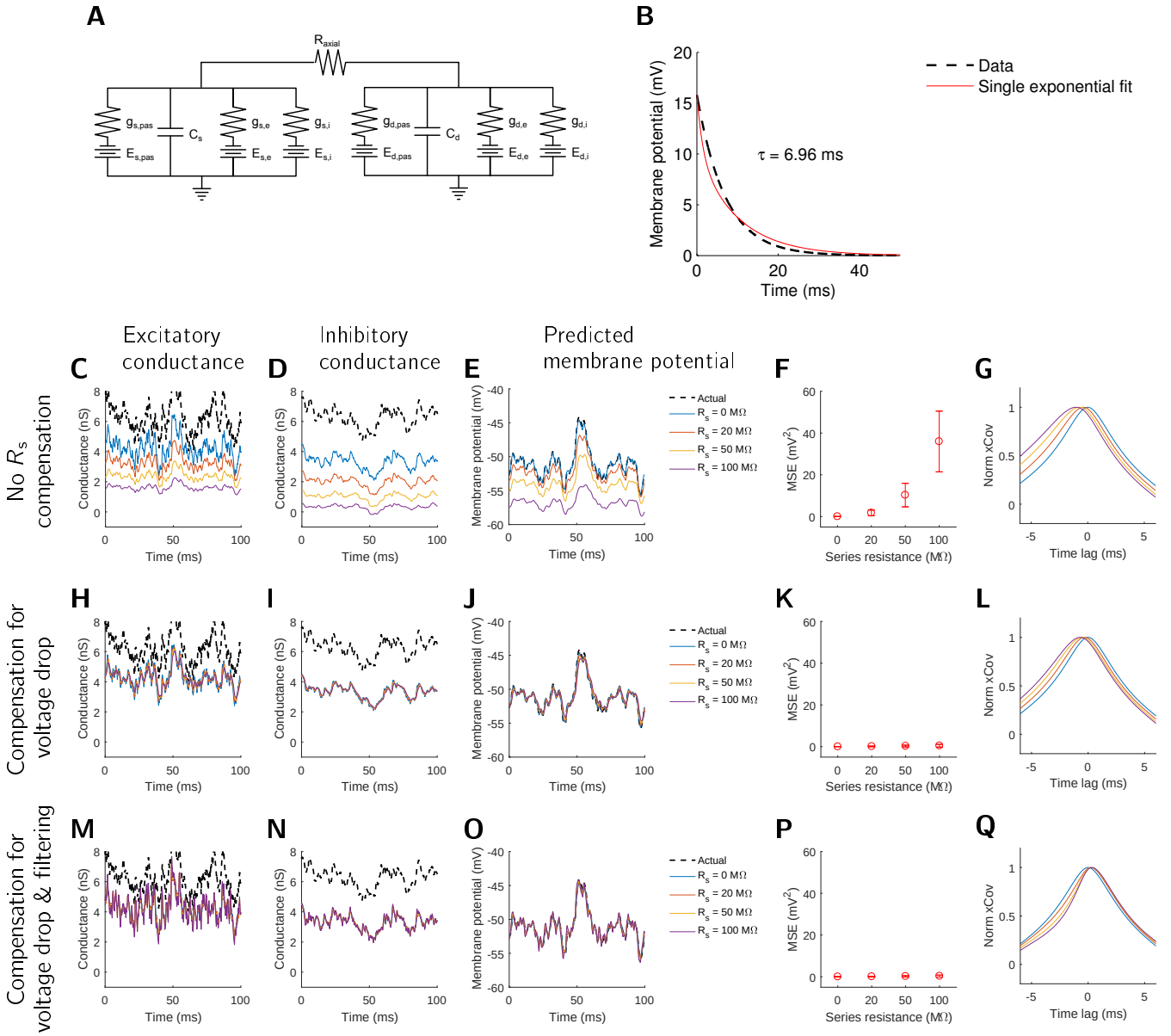

Figure 3.3: Series resistance and capacitive compensation in a two compartment neuron model. (**A**) Circuit diagram of one compartment model. (**B**) Voltage response to current step, adjusted for steady state and single exponential fit. Time constant of the fit is 6.96 ms. Second row (**C-G**), no series resistance compensation; third row (**H-L**), correction for the voltage drop across the series resistance; fourth row (**M-Q**), correction for both the series resistance and the capacitive current First column (**C,H,M**), the actual and estimated excitatory conductances. Second column (**D,I,N**), the actual and estimated inhibitory conductances. Third column (**E,J,O**), the membrane potential response to dynamic clamp reinjection of the estimated conductances. Fourth column (**F,K,P**), the mean squared error (MSE) between the actual membrane potential and dynamic clamp conductance reinjection. Fifth column (**G,L,Q**), the cross covariance between the actual membrane potential and dynamic clamp conductance reinjection of estimated conductances.

The impact of axial resistance on conductance estimation

Given how the presence of an axial current impairs our ability to estimate synaptic conductances, we explored the effect of axial resistance in further detail. In our two-compartment model (Figure 3.3A), synaptic currents entering the dendritic compartment can either leak out of the dendritic membrane or travel through the axial resistance to enter the somatic compartment. The greater the axial resistance encountered, the less current flows through this axial resistance and the more leaks out of the dendritic membrane. A similar situation occurs in real neurons. The cumulative intrinsic resistance provided by the cytoplasm and other intracellular structures provides a barrier to current flow. The presence of any other open membrane conductances (e.g. leak, voltage-gated channels) offers an alternative conduit for current flow, but across the cell membrane. The axial resistance, together with the leaky membrane, are effectively the cause of space-clamp errors.

To investigate the impact of the axial resistance on the estimation of excitatory and inhibitory conductances we varied the axial resistance up to 500 MΩ (R_{axial} in Figure 3.1B) and estimated the synaptic conductances. To ensure that conductances measured arose from the distal compartment, we restricted synaptic conductances to the dendritic compartment only. The excitatory and inhibitory synapses were stimulated randomly at a rate of 5000 Hz, resulting in an average ratio of excitation to inhibition ($g_e : g_i$) of 1.08. For these and all remaining simulations the series resistance was set to 0. With increasing axial resistance, the estimated mean excitatory, inhibitory, and consequently total synaptic conductances decreased, reflecting a deterioration in space-clamp (Figure 3.4A). Interestingly, the estimated inhibitory conductance was actually negative for higher axial resistance values. We also calculated the fraction of synaptic conductance estimated, and noted that estimation of the excitatory conductance was consistently superior compared to the inhibitory conductance (Figure 3.4B). As a result, the estimated excitatory-to-inhibitory ratio markedly deviated from the actual ratio of the conductances (Figure 3.4C). The maximum positive deviation was a $g_e : g_i$ ratio of 8.1 (at 140 MΩ), while the maximum negative deviation a $g_e : g_i$ ratio of -9.0 (at 180 MΩ). For greater values of R_{axial}, the ratio remained negative and tended towards -1.9 (at 500 MΩ). The hyperbolic nature of the estimated excitatory-to-inhibitory ratio arises as the estimated inhibitory conductance passes very close to zero when it transitions from positive to negative (Figure 3.4A). Finally, with dynamic clamp reinjection of the estimated conductances at the soma the MSE of the predicted membrane potential showed a peak at a value of R_{axial} at 190 MΩ (Figure 3.4D, blue). The improvement in the predicted membrane potential for high values of R_{axial} likely occurs because as the axial resistance increases the amplitude of the synaptic response at the soma decreases, which alone reduces the MSE. When the MSE is normalised, by first taking the square-root

and then dividing by the mean amplitude of the actual synaptic responses, the normalised error shows a steady increase with increasing axial resistance (Figure 3.4D, red).

Masking of synaptic conductances

When clamping at the excitatory reversal potential to estimate the inhibitory conductance, the current measured has a component of the inhibitory current (which is outward), and a component of excitatory current (which is inward) since the voltage control at the synapse is poor when there is poor space-clamp. The combination of an outward (positive) current with an inward (negative) current results in a diminished outward current; that is, the inhibitory conductance is underestimated. Similarly, when clamping at the inhibitory reversal potential to estimate the excitatory conductance, mixing of these conductances due to poor space-clamp leads to an underestimation of the excitatory conductance. These so-called conductance masking effects can also be viewed as mixing of conductances; a fraction of the estimated g_e is mixed with the estimated g_i, and vice versa.

We examined how well excitatory and inhibitory conductances are estimated when their relative strength differs (Figure 3.5), by again restricting synaptic conductances to the dendritic compartment and independently varying the stimulation frequency of the excitatory and inhibitory synapses from 0 to 20000 Hz (Figure 3.5A,B). Keeping g_e fixed but increasing g_i caused a subtle reduction in the fraction g_e estimated (Figure 3.5H). Similarly, keeping g_i fixed but increasing g_e also caused a reduction in the fraction g_i estimated (Figure 3.5I). However, the fraction of the overall conductance estimated did not depend on a specific combination of g_e/g_i intensity, but rather the total of g_e and g_i (Figure 3.5J). To verify this, we calculated the fraction of the total conductance estimated and plotted against the mean total conductance for all combinations of g_e and g_i (Figure 3.5K). This figure shows that the fraction of the real conductance estimated depends only on the mean conductance, and not on the relative balance between g_e and g_i.

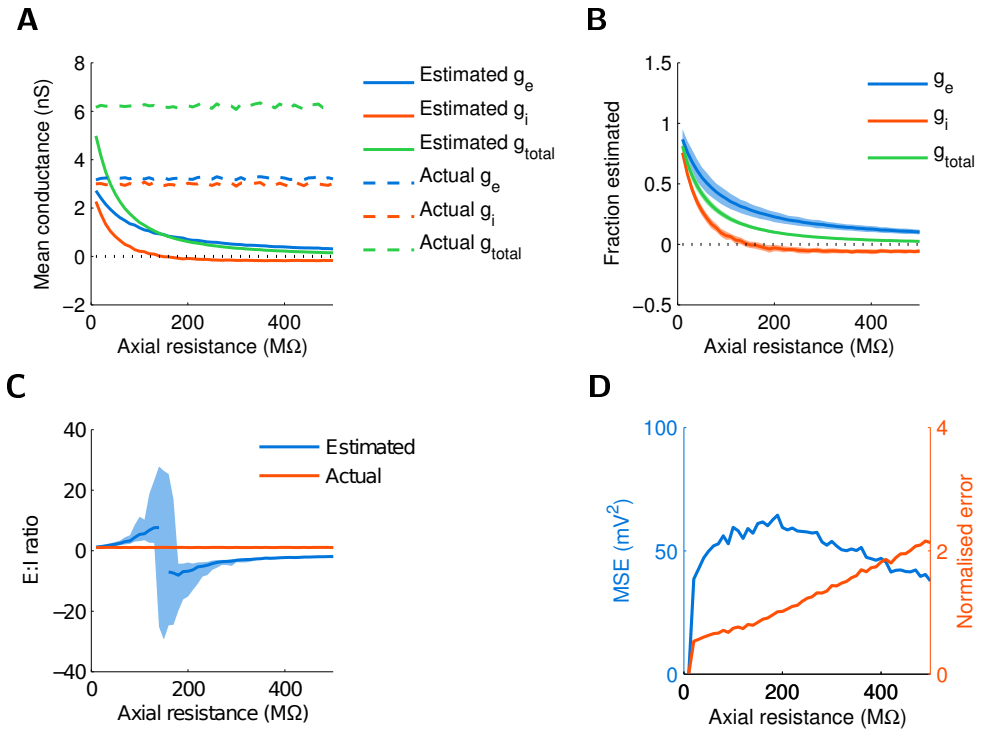

Figure 3.4: The impact of axial resistance on conductance estimation. (**A**) The mean estimated conductance decreases with increasing axial resistance. The estimated excitatory, inhibitory and total conductances are shown as solid lines, and the actual conductances are shown as broken lines. The estimated inhibitory conductance is negative for moderate to high levels of axial resistance. (**B**) The fraction conductance estimated (estimated conductance/actual conductance) decreases with axial resistance. The fraction inhibitory conductance is negative for moderate to high levels of axial resistance. (**C**) The estimated E:I ratio as a function of axial resistance. The estimated ratio deviates significantly from the actual ratio over the entire range of axial resistance, and is particularly unstable where the estimated inhibitory conductance is close to zero. The solid line represents the mean estimated E:I ratio, while the shading represents the distribution of the estimated E:I ratio within two standard deviations of the mean. (**D**) The error in the predicted membrane potential response as a function of axial resistance. For intermediate levels of axial resistance the MSE is maximal but decreases thereafter (blue). The normalised error, derived by dividing the square-root of the MSE by the amplitude of the actual synaptic response, shows a continuous increase with increasing axis resistance (red).

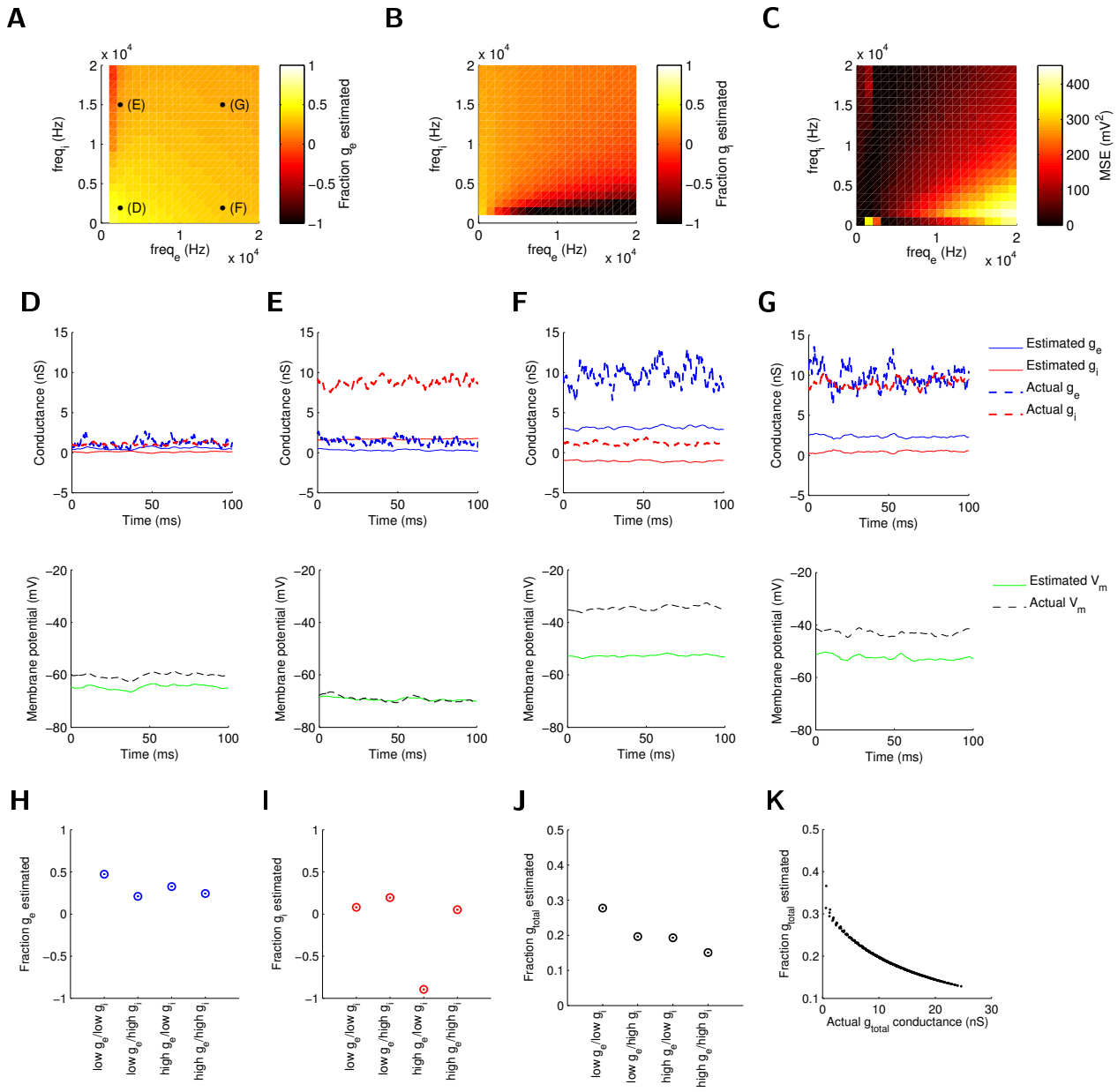

Figure 3.5: (Caption next page.)

Figure 3.5: Space-clamp errors introduce masking effects in conductance estimation. Synaptic conductances were only included in the dendritic compartment. The stimulation frequencies of the excitatory and inhibitory conductances were systematically varied between 0 and 20000 Hz. (**A**) The fraction of excitatory conductance estimated, calculated by dividing the mean estimated excitatory conductance by the mean actual excitatory conductance. Generally, keeping the excitation frequency fixed but increasing the inhibition frequency results in a reduction in the fraction of excitatory conductance estimated. (**B**) The fraction of inhibitory conductance estimated, calculated by dividing the mean estimated inhibitory conductance by the mean actual inhibitory conductance. Generally, keeping the inhibition frequency fixed but increasing the excitation frequency results in a reduction in the fraction of inhibitory conductance estimated. Note the large number of stimulation frequency combinations that lead to a negative fraction estimated. (**C**) MSE of predicted membrane potential for different stimulation frequency combinations. The MSE is worse for higher values of freq_e and lower values of freq_i. Four pairs of stimulation frequencies are shown in more detail; freq_e/freq_i: 2000 Hz/2000 Hz (**D**), 2000 Hz/15000 Hz (**E**), 15000 Hz/2000 Hz (**F**), 15000 Hz/15000 Hz (**G**). (**D**-**G**) Example estimated conductances (top) and predicted membrane potentials (bottom) for different combinations of stimulation frequencies. The average fraction of the actual excitatory conductance estimated (**H**), average fraction of the actual inhibitory conductance estimated (**I**) and average fraction of the total conductance estimated (**J**). (**K**) The fraction total synaptic conductance estimated decreases as the mean total synaptic conductance increases.

Temporal interactions

As the estimates of the excitatory and inhibitory conductances contain (negative) components of each other, correlations between the estimates are introduced. We demonstrate these effects in Figure 3.6. Excitatory and inhibitory synapses were restricted to the dendritic compartment and were stimulated at a rate of 5000 Hz, resulting in an average excitatory conductance of 3.2 nS and an average inhibitory conductance of 3.0 nS. This was carried out for a model with 20 MΩ axial resistance (Figure 3.6A) and a model with 200 MΩ axial resistance (Figure 3.6B). We estimated the excitatory and inhibitory conductances with somatic voltage clamp (Figure 3.6A,B) and then calculated the cross-covariance of the actual conductances and compared with the cross-covariance of the estimated conductances for the two scenarios (Figure 3.6C,D). In the model with 20 MΩ axial resistance, the cross-covariance of the estimated conductances had a pronounced negative peak that was absent in the cross-covariance of the actual conductances (Figure 3.6C). The half-max width of this peak was 6.2 ms. We observed the emergence of similar peak in the model with 200 MΩ, however this peak was wider with half-max width of 10.9 ms, and the cross-covariance was also smoothed (Figure 3.6D). We repeated the analysis for an extended range of axial resistance, which reveals a widening of the cross-correlation half-width as the axial resistance increases (Figure 3.6E). Taken together, these results show that conductance masking due to space-clamp errors introduce anti-correlations between the estimated excitatory and inhibitory conductances that are not present in the actual conductances. The smoothing of the cross-covariance we observed also indicates that estimation of high-frequency changes in the synaptic conductances is subject to filtering effects which worsens as the space-clamp degrades.

The relative time courses of excitatory and inhibitory conductances have been well-studied to help shed light on the network mechanisms underlying cortical activity [Haider et al., 2006, Higley and Contreras, 2006]. In both spontaneous Down to Up state transitions and cortical responses to sensory inputs, the consensus view is that the increase in excitation precedes the rise in inhibition by several milliseconds [Isaacson and Scanziani, 2011]. Given that space-clamp errors introduce artifactual anti-correlations between estimated synaptic conductances, how do these anti-correlations affect the estimation of the temporal relationship between time-varying synaptic conductances? To answer this question, we considered conductance changes with a well-defined time course of the form

$$g(t) = \bar{g}\left(1 - \exp\left(-t/\tau\right)\right). \tag{3.3.6}$$

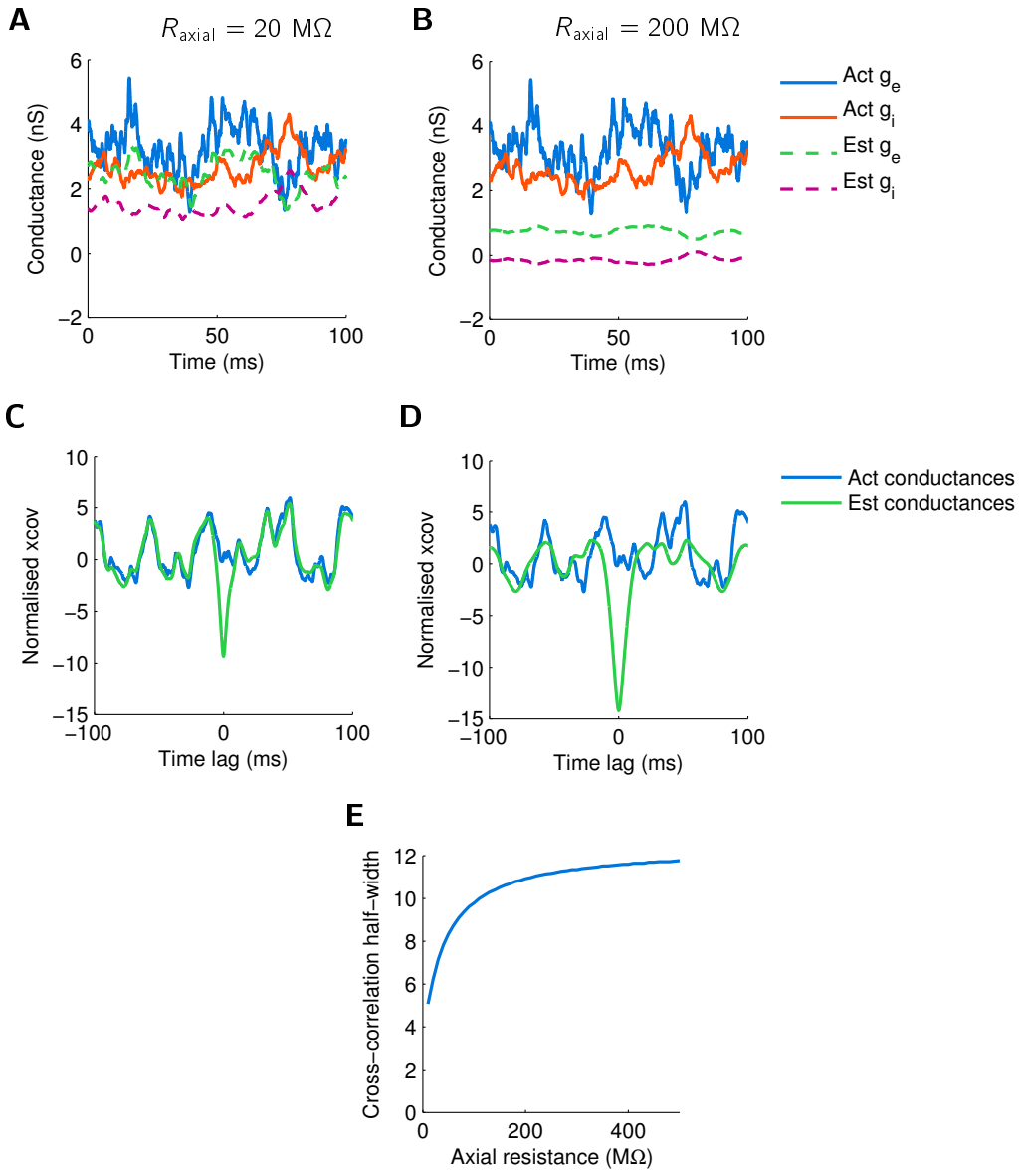

Figure 3.6: Space-clamp errors introduce anti-correlations between estimated synaptic conductances. (**A**,**B**) Uncorrelated excitatory and inhibitory synaptic conductance inputs were estimated at 20 MΩ (**A**) and 200 MΩ (**B**) axial resistance. (**C**,**D**) Example cross-covariance traces at 20 MΩ (**C**) and 200 MΩ (**D**) axial resistance. The cross-covariance of the estimated synaptic conductances reveals a prominent negative peak centred around 0 ms time lag that is absent in the cross-covariance of the actual conductances. (**E**) The width of the negative cross-covariance peak increases as the axial resistance increases.

Equation (3.3.6) describes a conductance that approaches a maximum $\bar{g}$ exponentially, with a time constant of τ. We considered a two-compartment model with excitatory and inhibitory conductances in the dendritic compartment only, and set $\bar{g}_e = 5$ nS, $\bar{g}_e = 5$ nS. We first fixed R_{axial} to 100 MΩ and simulated three combinations of τ_e and τ_i; 5 ms/5 ms, 4 ms/6 ms and 6 ms/4 ms. The second two combinations were chosen to mimic different time courses of the rise of inhibition relative to excitation. When τ_e and τ_i were the same (5 ms/5 ms), the normalised estimated excitatory and inhibitory conductances followed the same time course, but the estimate of the rise of the conductances was slightly delayed compared to the normalised actual conductances (Figure 3.7B). We also calculated the difference between the normalised excitatory and inhibitory conductance time courses, for both actual and estimated conductances, and observed no difference (Figure 3.7C). Thus, while the amplitude and time course of the estimated conductance are distorted, the temporal relationship is maintained when τ_e and τ_i are equal. What happens when τ_e and τ_i are not equal (Figure 3.7D,G)? When τ_e and τ_i were not equal, the difference in the time courses of the normalised estimated conductances becomes accentuated (Figure 3.7E,H) and the estimated peak difference between the normalised conductance change are delayed (Figure 3.7F,I). In the case where τ_e (4 ms) was shorter than τ_i (6 ms), the time of the peak difference was 4.88 ms for the actual conductances, compared to 7.6 ms for the estimated conductances (Figure 3.7F). Similarly when reversing the relative time courses such that τ_e (6 ms) was longer than τ_i (4 ms), the time of the peak difference was again 4.88 ms for the actual conductances, compared to 7.5 ms for the estimated conductances (Figure 3.7I). We systematically compared the mismatch for different combinations of τ_e and τ_i between 1 ms and 10 ms, and for different levels of R_{axial}, and observed an exaggeration of the mismatch between the estimated conductance time courses as the axial resistance increased (Figure 3.7J-L). Taken together, these simulations indicate that distortions arising from space-clamp errors can affect estimation of the temporal relationship between excitatory and inhibitory conductance changes.

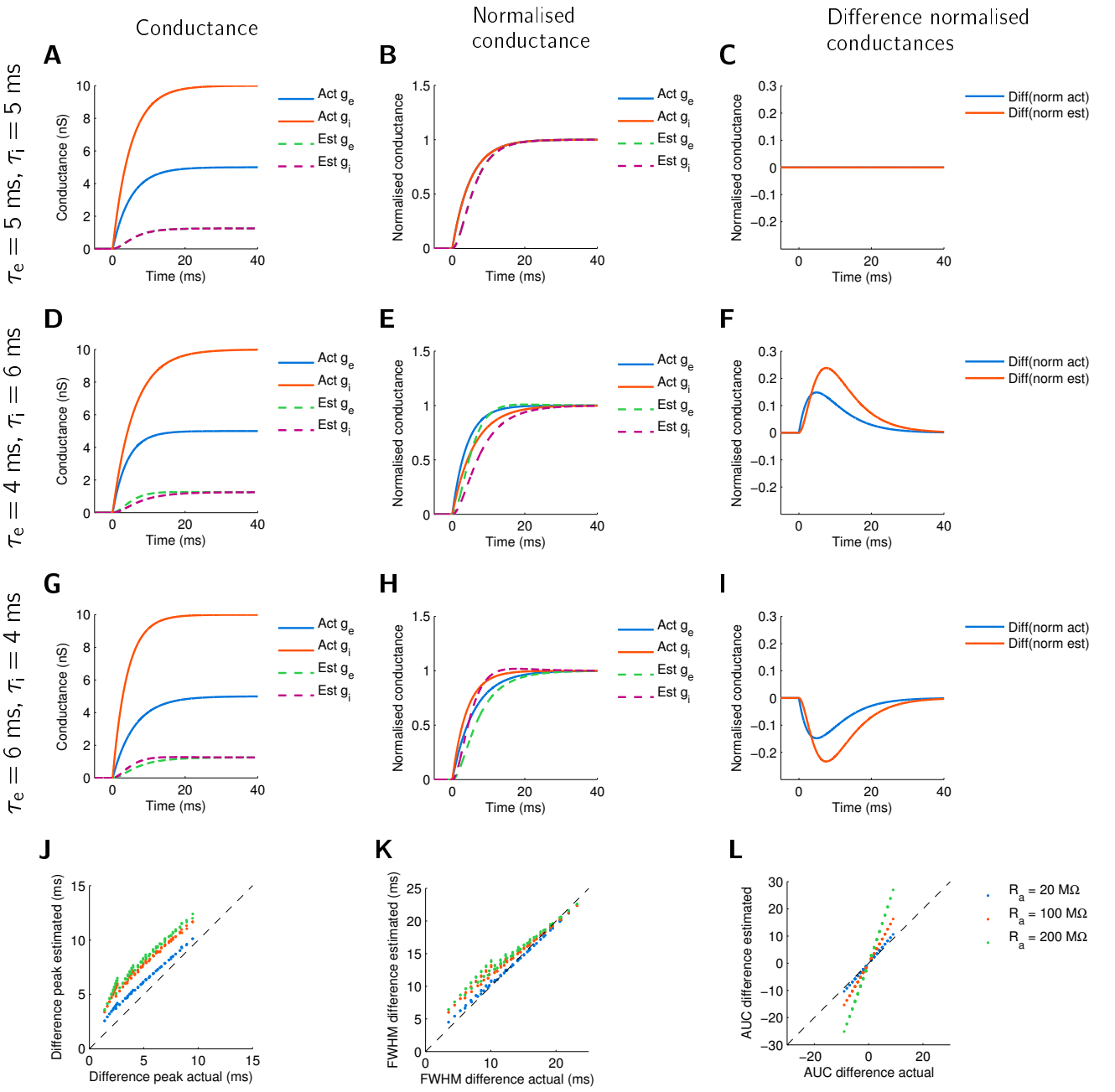

Figure 3.7: Interactions arising from conductance masking distort the temporal relationship between the time course of estimated conductances. The time course of the conductance changes is given by Equation (3.3.6). Keeping R_{axial} fixed at 100 MΩ, we used different combinations of τ_e/τ_i: 5 ms/5 ms (first row, **A**-**C**), second row, 4 ms/6 ms (**D**-**F**), third row, 4 ms/6 ms (**G**-**I**). The time courses of the actual and estimated excitatory and inhibitory conductances (**A**,**D**,**G**) were normalised to the steady state level (**B**,**E**,**H**). When the time courses of excitation and inhibition were different, the difference between the normalised estimated conductances are accentuated compared to the difference between the normalised actual conductances (**C**,**F**,**I**). A positive difference indicates a relative excess of excitation (**F**), while a negative difference indicates a relative excess of inhibition (**I**). The excitation and inhibition mismatch can be quantified by comparing the time of the peak in the difference of the normalised conductances (**J**), the full-width at half-maximum (FWHM) of the difference (**K**), as well as the area under the curve (AUC) of the difference (**L**). We evaluated these measurements for combinations of τ_e and τ_i between 1 ms and 10 ms, at three different levels of R_{axial}; 20 MΩ (blue), 100 MΩ (red) and 200 MΩ (green). The transient imbalance between excitation and inhibition is generally overestimated, and especially for increasing values of R_{axial}.

3.4 Discussion

We investigated how voltage- and space-clamp errors affect the Borg-Graham method for estimation of synaptic conductances [Borg-Graham et al., 1998]. Voltage-clamp errors occur from the voltage drop across the electrode series resistance. As a result, the membrane potential is not held at the command voltage. A second consequence of poor voltage-clamp is that with a fluctuating membrane potential, for instance due to barrages of synaptic input, a capacitive current is induced. This capacitive current contributes to a component of the current measured. While the first issue can be corrected for *post hoc* in single compartment models simply by calculating the voltage drop across the series resistance, accounting for the capacitive component is more complex and requires knowing the cell capacitance. Nevertheless, our simulations suggest that the capacitive current only contributes a small error, relative to the error caused by the voltage drop across the series resistance in this isopotential situation.

In a two-compartment model, the presence of the axial resistance introduces a space-clamp error in the compartment distal to the clamping electrode. Poor space-clamp contributes to three types of errors in the estimation of synaptic conductances. The first error is underestimation of the total synaptic conductance. Since estimates of the excitatory and inhibitory conductances depend on the estimated total synaptic conductance, both conductances are affected but more so inhibitory conductances as discussed below. The second error is masking effects arise, where changes in one synaptic conductance (excitatory or inhibitory) affects estimation of the other conductance. This occurs from mixing of excitatory and inhibitory conductances in the presence of poor space-clamp. The third type of error is temporal in nature. Due to conductance mixing, the estimated temporal relationships between fluctuating synaptic conductances is distorted.

Why are inhibitory conductances estimated more poorly than excitatory conductances (Figure 3.4B & 3.5B)? The reason is because the leak conductance impairs the ability of the somatic voltage clamp to hold the dendritic compartment at membrane potentials far from the leak reversal potential. As a result the voltage clamp is more effective at holding the potential close to the inhibitory reversal potential, as is required to measure excitatory conductances, than at the reversal potential of excitatory conductances, which is required to measure inhibitory conductances.

Several of these observations can be explained by considering how $g_{\text{syn}}(t)$ and $E_{\text{syn}}(t)$ are measured (Equations 3.1.3 and 3.1.4), and the subsequent derivation of the estimates for $g_{\text{e}}(t)$ and $g_{\text{i}}(t)$ (Equations

3.1.5 and 3.1.6). As mentioned previously, g_{pas} is the slope of the ($I_{hold,rest}$ vs V_{hold}) relationship and ($g_{pas} + g_{syn}$) is the slope of the ($I_{hold,act}$ vs V_{hold}) relationship (Figure 3.8a, left). While $E_{syn}(t)$ can be calculated from the vertical intercept of ($I_{hold,act}$ vs V_{hold}) relationship in Equation (3.1.9), $E_{syn}(t)$ is also where the curves ($I_{hold,pas}$ vs V_{hold}) and ($I_{hold,act}$ vs V_{hold}) intersect (Figure 3.8, left). Further, the expressions in Equations (3.1.3) and (3.1.4) for $g_{syn}(t)$ and $E_{syn}(t)$ can be rearranged to obtain $g_i(t)$ and $g_e(t)$

$$g_i(t) = \frac{g_{syn}(t)[E_e - E_{syn}(t)]}{E_e - E_i}, \quad (3.4.1)$$

$$g_e(t) = \frac{g_{syn}(t)[E_{syn}(t) - E_i]}{E_e - E_i}. \quad (3.4.2)$$

It is clear from Equations (3.4.1) and (3.4.2), that changes to either $g_{syn}(t)$ or $E_{syn}(t)$ will affect estimation of both $g_i(t)$ and $g_e(t)$. Masking effects arise from these interactions. Therefore, increasing the inhibitory conductance would cause an increased slope and a leftward shift in $E_{syn}(t)$ (Figure 3.8, middle), and as a result, less inward (excitatory) current would be measured at the inhibitory reversal potential while more outward (inhibitory) current would be measured at the excitatory reversal potential. Correspondingly, an increased inhibitory conductance estimate would be associated with a decreased excitatory conductance estimate. Similarly, increasing the excitatory conductance would also cause an increased slope but a rightward shift in $E_{syn}(t)$ (Figure 3.8, right), leading to an increased estimated excitatory conductance but a decreased inhibitory conductance estimate.

Predicting voltage changes While space-clamp errors cause synaptic conductances to be underestimated, the estimated conductances may still provide a prediction of the effect of the conductances at the soma [Monier et al., 2008, Wehr and Zador, 2003]. Reinjecting the estimated conductances at the soma by dynamic clamp produces membrane potential changes that are often close to those produced by the actual dendritic conductances. We emphasise that the ability to predict the somatic membrane potential is simply an indication that the voltage-clamp is relatively accurate at recovering the synaptic conductances 'visible' from the soma, but does not imply good voltage control throughout the cell. In a single compartment model, reinjecting the estimated conductances (with appropriate series resistance compensation and adjustment of the capacitive current) recovers the actual voltage response exactly (Figure 3.2O,P). In a two compartment model, distributed capacitive effects that cannot be adjusted for by a point electrode lead to small errors in the predicted membrane potential, even after series resistance compensation (Figure 3.3O,P). We see however, that when space-clamp errors become severe, even the estimated conductances do not predict the membrane potential changes very reliably (Figure 3.5C); thus,

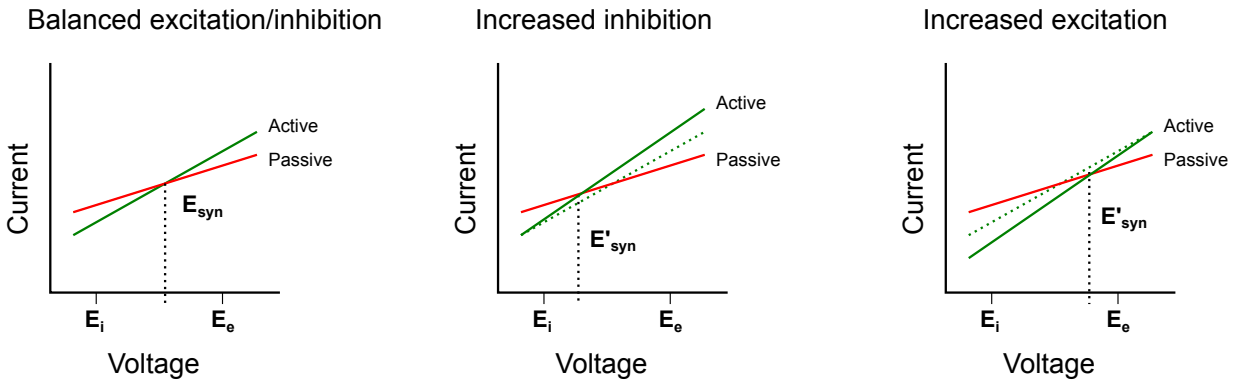

Figure 3.8: Masking interactions arise from space-clamp errors and affect the estimation of synaptic conductance parameters from the current-voltage response. In these plots, the current axis represents the current recorded for a given holding voltage and the voltage axis represents the holding voltage adjusted for series resistance. The slopes of the curves represent the total conductances, and the voltage at the intersection point of the two curves represents the reversal potential of the active conductance, which can be used to estimate the underlying excitatory and inhibitory conductances if their reversal potentials are known in a single compartment model. This intersection point is in between the inhibitory and excitatory reversal potentials (E_i and E_e) during balanced excitation/inhibition (left), and is shifted to the left or right during increases in inhibition (middle) and excitation (right). In the presence of space-clamp errors the required holding voltage for E_i and E_e is more negative and positive, respectively, than what is attained by the electrode. The current-voltage response is first recorded under passive conditions (red curves) and then under active conditions (green curves). The slopes of the curves represent the conductances, and the voltage at the intersection point of the two curves represents the reversal potential of the active conductance, which can be used to estimate the underlying excitatory and inhibitory conductances if their reversal potentials are known in a single compartment model. Increasing the amount of inhibition causes the current measured at E_i and the current measured at E_e to both become more positive. As a result, the increase in estimated inhibitory conductance is coupled to a decrease in estimated excitatory conductance (middle). Similarly, increasing the amount of excitation from initial (left) results in an increase in estimated excitatory conductance coupled to a decrease in inhibitory conductance (right). The dotted green lines (middle, right) represent the initial current-voltage response under active conditions (left).

a high MSE when this happens is consistent with poor space-clamp.

Relation to other work Simulations have been a popular approach to study the effects of space-clamp errors on the estimation of conductance properties [Joyner et al., 1975, White et al., 1995, Velte and Miller, 1996, Hartline and Castelfranco, 2003, Bar-Yehuda and Korngreen, 2008]. These studies have been accompanied by experimental measurements of space-clamp errors [Williams and Mitchell, 2008] and together have enabled an appreciation of the distortions that arise from voltage-clamp methods Little work, however, has been done on how voltage- and space-clamp errors impact on the estimation of synaptic conductances during combined excitatory and inhibitory input. Furthermore, despite well-documented evidence that space-clamp issues can significantly distort synaptic conductances the voltage-clamp technique is still commonly used to dissect the excitatory and inhibitory components underlying synaptic input [Haider et al., 2013, Longordo et al., 2013], primarily due to the lack of alternatives. One earlier simulation study investigated how excitatory and inhibitory synaptic conductances interact and are distorted in voltage-clamp recordings in morphologically realistic neurons [Poleg-Polsky and Diamond, 2011]. This study explored how morphology and dendritic branching contributes voltage-clamp distortions, showing how the complexity of realistic neurons greatly increases the dimensionality of the parameter space, making it difficult to delineate the precise contribution of different parameters to the distortions observed. We have adopted the other extreme by considering single and two-compartment models. This has allowed us to determine the mechanisms underlying the observed voltage- and space-clamp distortions during combined excitatory and inhibitory input.

[Wehr and Zador, 2003] argue using compartmental simulations that estimated delays between the time course of excitation and inhibition are unlikely to be affected by space-clamp errors. In their case, the same time courses were used for the excitatory and inhibitory conductance changes, but the onset of the conductance changes had a variable time offset. We investigated an alternate scenario, where the onset of the conductances were the same but the speed of the onset differed. Masking effects which lead to anti-correlations between the estimated conductances distorted the estimates such that the differences in the excitation and inhibition time course became accentuated (Figure 3.7). In contrast to [Wehr and Zador, 2003] we conclude therefore, that during combined excitation and inhibition it may be difficult to determine the time course of actual conductance changes especially when the estimated conductances (which are already distorted) have different time courses.

Future directions Our simulations with a two-compartment model reflect an extreme case in which the dendritic synaptic conductances are colocalised in the same compartment. In such a configuration, the dendritic synaptic conductances interact with each other maximally. Cortical neurons are better represented by multi-compartment models with synapses dispersed across different dendritic branches. This spatial complexity may lead to additional interactions, which may affect conductance estimation in different ways. For example, on a single dendritic branch, how are masking effects influenced by synapse location and the presence of other synapses more proximal or distal? To what extent do synapses on different branches interact? In general, while it is widely accepted that space-clamp errors distort synaptic conductance estimates, these distortions have not been explored in detail during combined excitatory and inhibitory synaptic input. To do so in real neurons requires a thorough understanding of the distribution and activation patterns of synaptic inputs [Chen et al., 2013b, Jia et al., 2010] or the ability to mimic synaptic barrages. Recent developments in optogenetics [Yizhar et al., 2011] and two-photon uncaging strategies [Kantevari et al., 2010] may permit such investigations in the future. We will encounter some of these strategies in Chapter 5.

Chapter 4

The impact of somatic versus dendritic inhibition on neuronal output

4.1 Introduction

In Chapter 2, we characterised the effect of balanced excitation and inhibition on synaptic integration in binocular layer 2/3 pyramidal neurons and showed that the presence of inhibition contributes to sublinear summation in these neurons. Inhibition in the cortex can exert a variety of effects, in part due to the anatomical and functional diversity of inhibitory neurons [Isaacson and Scanziani, 2011, Markram et al., 2004]. This complicates studying the contribution of inhibition to cortical computations, as the specific role of inhibition is likely to depend on the physiological and behavioural context it operates in. Nevertheless, a simple way to characterise the effect of inhibition is to assess how it alters the input-output (IO) relationship of a neuron (Figure 4.1). The slope of the IO relationship is called gain and provides a simple quantification of how the spiking response of a neuron varies with the strength of the input it receives. Gain control refers to the modulation of the slope of this IO relationship [Chance et al., 2002, Mitchell and Silver, 2003, Carvalho and Buonomano, 2009] and in this framework, inhibition is said to be additive/subtractive if it shifts the IO curve to the left/right, and multiplicative/divisive if it increases/reduces the slope of the IO curve (Figure 4.1B). Although simple in definition, this can be a powerful way to understand how inhibition affects information coding. For example, divisive gain control affects the responsiveness of a neuron but not how it represents a stimulus, as seen in contrast invariance of orientation tuning [Anderson et al., 2000b] and attentional scaling [Treue and Trujillo, 1999]. In contrast, subtractive inhibition has been shown to increase response discriminability of odour representations in the piriform cortex [Sturgill and Isaacson, 2015].

The mechanisms underlying gain modulation have been extensively studied by a variety of experiment and computational approaches and many different factors have been suggested to play a role. These include excitatory and inhibitory inputs [Murphy and Miller, 2003], background synaptic activity [Chance et al., 2002, Prescott and De Koninck, 2003, Shu et al., 2003a], synaptic depression [Rothman et al., 2009] and plasticity [Carvalho and Buonomano, 2009], dendritic saturation [Prescott and De Koninck, 2003], active dendrites [Larkum et al., 2004, Mehaffey et al., 2005], and the slow after-hyperpolarisation conductance [Higgs et al., 2006]. More recently, optogenetic strategies have allowed the contribution of defined interneuron populations to the IO relationship of neurons to be investigated *in vivo* [Lee et al., 2012b, Wilson et al., 2012, Atallah et al., 2012]. However no consensus on this matter has been reached [Lee et al., 2014, El-Boustani et al., 2014]. For example, parvalbumin-expressing (PV) interneurons that target the perisomatic region of layer 2/3 pyramidal neurons have been shown to exert predominantly divisive effects while somatostatin-expressing (SOM) interneurons that target the dendrites have subtractive effects [Wilson et al., 2012, Atallah et al., 2012]. Opposite results have also been demonstrated, whereby PV interneurons exert subtractive effects while SOM interneurons produce divisive effects [Lee et al., 2012b]. Interestingly, these studies have used very similar preparations and all studied the effect of inhibition on the tuning properties of superficial pyramidal neurons in the visual cortex.

Given the conflicting nature of these results, we set out to investigate the conditions under which subtractive or divisive effects may be produced, and the dependence of these effects on the location of inhibition.

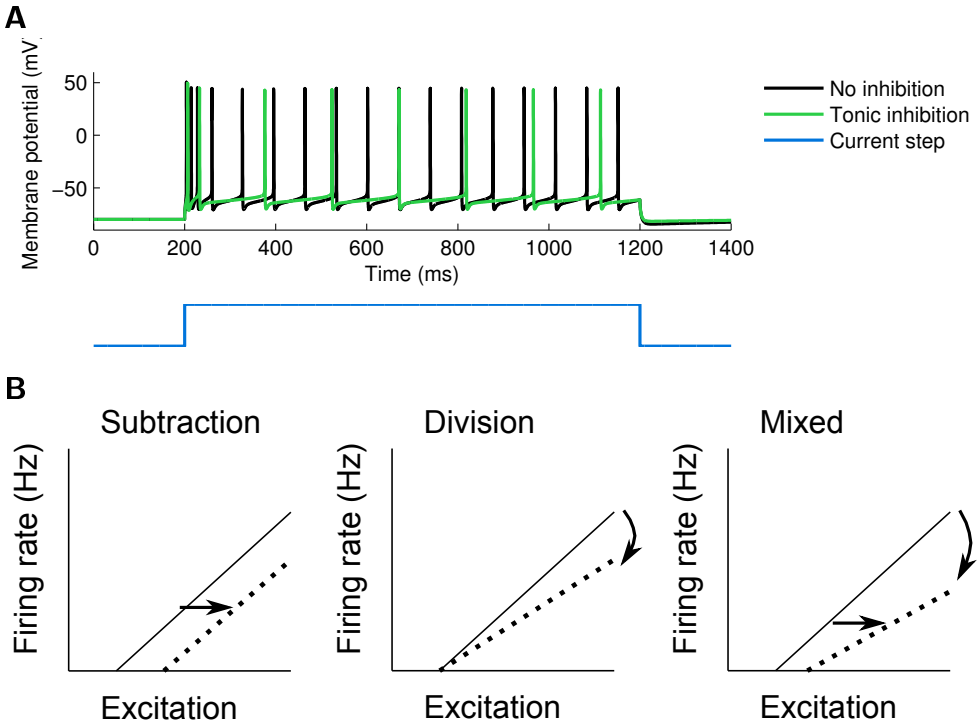

Figure 4.1: Effects of inhibition on the IO curve of a neuron. (**A**) The IO curve of a neuron is determined by the firing rate response to an excitatory stimulus (black), in this case a depolarising current step. The impact of inhibition is quantified by its effect on the firing rate response (green). (**B**) The effect of inhibition can be characterised by its effect on the IO curve on the neuron. Subtraction is seen as a rightward shift in the IO curve (left) while division is seen as a reduction in the slope of the IO curve (middle). Inhibition can also have mixed subtractive and divisive effects (right).

4.2 Methods

We used the NEURON simulation environment to simulate a reconstructed layer 2/3 pyramidal neuron with passive properties (obtained from [Longordo et al., 2013]; see Chapter 2). The biophysical parameters for the soma and dendrites are as follows: $C_m = 0.9$ μF cm^{-2}, $R_m = 12$ kΩ cm^2, $R_i = 105$ Ω cm, $E_{leak} = -80$ mV. The model also contained an axon with the same passive parameters except $R_m = 400$ Ω cm^2. Spines were incorporated into the model by decreasing R_m and increasing C_m by a factor of 2 in distal dendritic compartments (>40 μm from the soma). The neuron also included Hodgkin-Huxley Na^+ and K^+ channels in the soma and axon, to support action potential generation, together with K_m channels and an AHP mechanism in the soma, to enable spike firing adaptation. The simulation time step was 0.05 ms.

The firing rate of the neuron was calculated by counting the number of spikes generated by the neuron in response to a 1 second stimulus. We used a variety of ways to stimulate the neuron. The neuron was stimulated by steady-state somatic current injections, steady-state dendritic excitatory conductance changes, noisy somatic current injections or asynchronous and synchronous dendritic excitatory conductance changes together with either somatic or dendritic inhibition. The neuron included 1000 dendritic excitatory synapses located on basal dendrites >40 μm from the soma (Figure 4.2, left), 100 perisomatic inhibitory synapses located <40 μm of the soma (Figure 4.2, middle) and 100 dendritic inhibitory synapses located on basal dendrites >40 μm from the soma (Figure 4.2, right). Excitatory and inhibitory input was either applied as a constant change in conductance to a defined level, or as synapses randomly activated at different rates by independent, homogeneous Poisson processes. For these latter simulations, the conductance change at excitatory synapses had an exponential rise and decay of 0.2 and 2 ms, respectively, a peak of 100 pS and a reversal potential of 0 mV. The conductance change at inhibitory synapses had an exponential rise and decay of 0.2 and 10 ms, respectively, a peak of 100 pS and a reversal potential of -80 mV. In simulations with noisy current injections, current noise was modelled by an Ornstein-Uhlenbeck Process (OUP) [Uhlenbeck and Ornstein, 1930]. The OUP was described by the following differential equation

$$\frac{dI}{dt} = \frac{1}{\tau}\left[I(t) - I_{bias}\right] + \sqrt{\frac{2\sigma^2}{\tau}}\chi(t), \tag{4.2.1}$$

where σ is the standard deviation of the noise, $\chi(t)$ is a Gaussian white noise process with zero mean and unit standard deviation, and $I_{bias} = 0$ is the mean current, and $\tau = 2$ ms is the time constant of the fluctuations. The differential equation given by Equation (4.2.1) was solved using standard methods.

Data produced by the NEURON simulations were analysed in MATLAB. We assume the transformations to the IO curve are exclusively represented by a combination of subtractive or divisive effects. Suppose $f(I)$ is the firing rate response to a stimulus I. Then subtraction is expressed as

$$f(I) \rightarrow f(I - c), \tag{4.2.2}$$

for some constant c, while division is expressed as

$$f(I) \rightarrow kf(I), \tag{4.2.3}$$

for some constant k. Hence, a transformation containing both subtractive and divisive effects is given by

$$f(I) \rightarrow kf(I - c). \tag{4.2.4}$$

We quantified the extent of subtractive and divisive effects by fitting the control curve ($f(I)$) with a linear interpolation in the absence of inhibition and then determined the values of c and k required to fit the change in $f(I)$ in the presence of inhibition using a least-squares optimisation approach (Figure 4.3). The fit was performed using the MATLAB Optimization Toolbox.

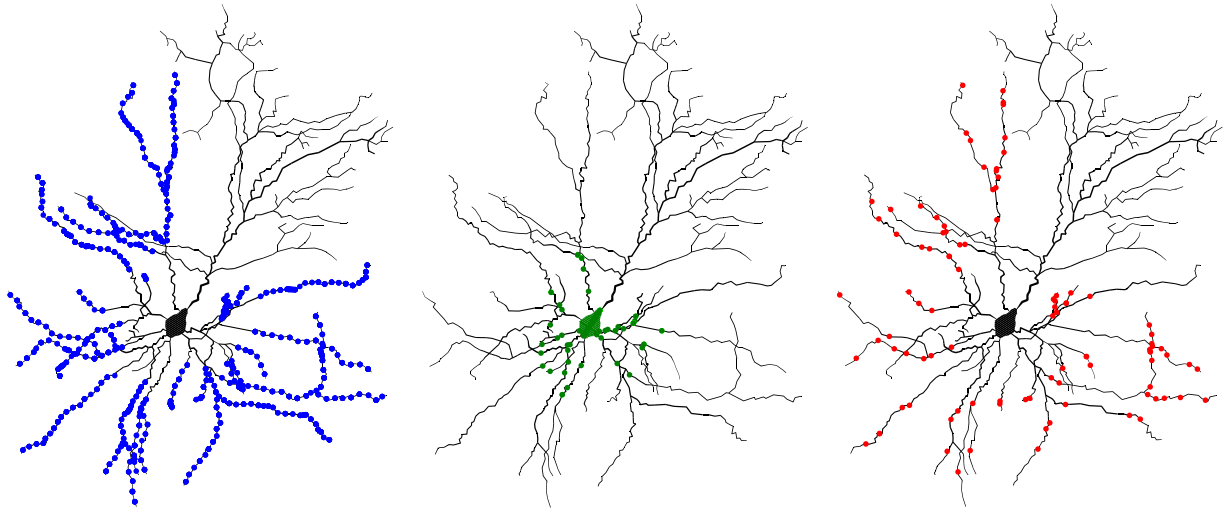

Figure 4.2: Distribution of excitatory and inhibitory synapses in the layer 2/3 pyramidal neuron model. 1000 excitatory synapses (blue) were located on basal dendrites >40 μm from the soma (left), 100 perisomatic inhibitory synapses (green) located <40 μm of the soma (middle) and 100 dendritic inhibitory synapses (red) located on basal dendrites >40 μm from the soma (right)

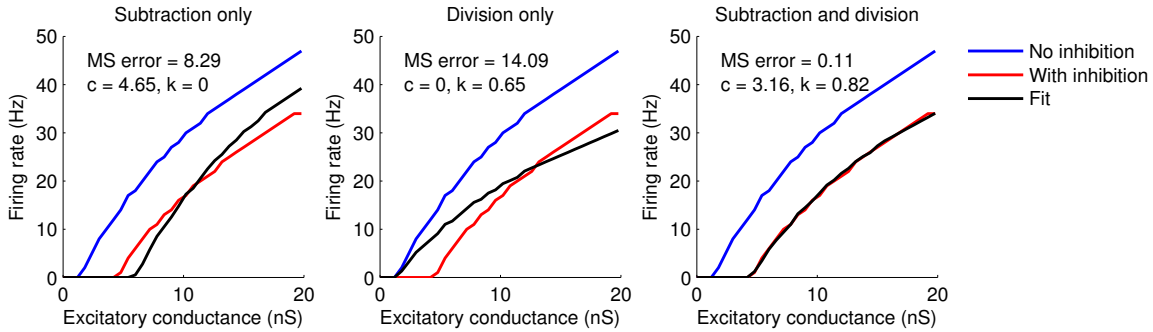

Figure 4.3: Fitting the subtractive and divisive effects of inhibition. The curve-fitting approach obtains the values of c and k that minimises the mean squared error (MSE) of the difference between the transformed control curve (no inhibition) and the target curve (with inhibition). In the example shown, the MSE of the difference between the control curve and target curve is 125.9. Fitting the subtractive (left) or divisive (middle)components only reduces the MSE to 8.29 and 14.09, respectively. Fitting both components obtains the superior fit (middle), with a MSE of only 0.11.

4.3 Results

Using a reconstructed layer 2/3 pyramidal neuron model [Longordo et al., 2013], we explored the dependence of the IO relationship on inhibition and how this varied under different stimulation conditions. The IO curve of the neuron was first obtained by injecting current through a somatic 'electrode' and measuring the firing rate of the neuron under current clamp conditions (Figure 4.4). The response curve was approximately linear (Figure 4.4C) and in our neuron model we did not observe saturation of spike firing when up to 1.5 nA of current was injected. To investigate the impact of inhibition on the IO curve we added inhibitory synapses to the model. Excitatory pyramidal neurons receive inhibitory inputs from several different interneuron types. Two major classes of cortical interneurons that have been described include parvalbumin (PV) expressing interneurons that mainly synapse onto the perisomatic region of their pyramidal neuron targets, and somatostatin (SOM) expressing interneurons that typically synapse more distally on the dendrites of pyramidal neurons [Markram et al., 2004]. To mimic these two sources of inhibitory inputs, two sets of inhibitory synapses were distributed perisomatically (Figure 4.2, middle) or throughout the distal basal dendrites (Figure 4.2, right) of the neuron model. These two sets of inhibitory synapses were activated separately. To model the conductance change associated with synaptic input in a noiseless situation, all inhibitory synapses were activated simultaneously and the conductance of these synapses was constant. Under these conditions, regardless of whether the site of inhibition was perisomatic (Figure 4.4A) or dendritic (Figure 4.4B), the presence of inhibition resulted in a rightward shift in the IO curve of the neuron (Figure 4.4C). The transformation in the IO curve was almost purely subtractive and divisive effects were largely absent (Figure 4.4D). The amount of subtraction observed was also proportional to the strength of the inhibition, and unsurprisingly, perisomatic inhibition had greater subtractive effects than dendritic inhibition (Figure 4.4D).

Having characterised the effects of inhibition on a neuron stimulated by depolarising current injection, we replaced the current injection with constant conductance excitatory input. Excitatory synapses were distributed throughout the basal dendritic tree (Figure 4.2, left), and in the next series of simulations activation of the excitatory synapses was modelled by a constant conductance (Figure 4.5A,B). Although somatic current injections are usually used to extract the IO curve of neurons (e.g. [Chance et al., 2002]), conductance input differs from current input in two key ways. Firstly, increasing the synaptic conductance reduces the input resistance of the neuron, effectively reducing the responsiveness of the neuron to further stimulation. Secondly, the depolarisation evoked by excitation brings the membrane potential of the neuron closer to the reversal potential of the excitatory synaptic current, thereby reducing

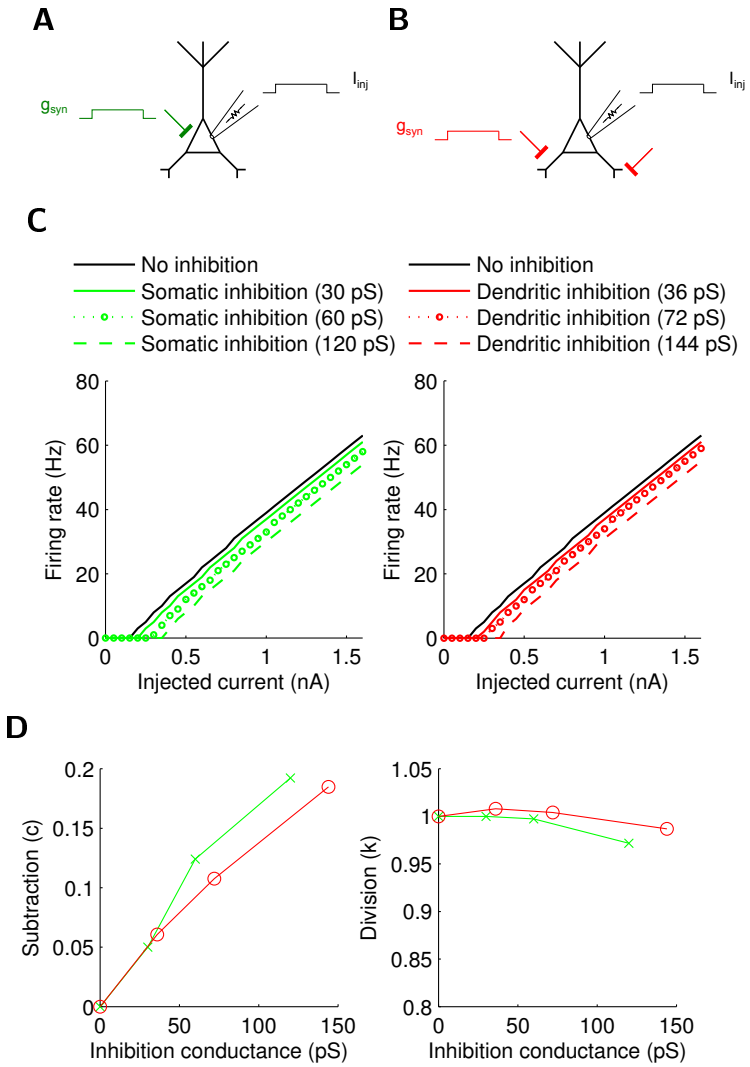

Figure 4.4: Somatic and dendritic inhibition can cause purely subtractive effects. Depolarising current injection was applied at the soma along with constant conductance inhibitory input in the perisomatic (**A**) and basal dendritic (**B**) regions. (**C**) The input-output curves showing the effect of somatic inhibition (left) and dendritic inhibition (right). (**D**) Both somatic and dendritic inhibition exerted subtractive effects which increased with increasing inhibitory conductance (left), but neither produced significant divisive effects (right).

the driving force for additional excitatory current. These two effects combined to produce a saturation in the IO curve, seen as a sublinear increase in firing rate in response to increasing excitatory conductance (Figure 4.5C). Constant conductance somatic and dendritic inhibition again both produced subtractive effects on the IO curve (Figure 4.5D, left), however, a divisive component also emerged (Figure 4.5D, right).

Up to this point, we have only considered constant current or constant conductance conditions. Neurons *in vivo* are bombarded by synaptic inputs and this barrage of synaptic activity leads to large fluctuations in the membrane potential [Steriade et al., 1993, Destexhe et al., 2003]. Even if the average membrane potential of the neuron is below threshold, sufficiently large fluctuations will cause the membrane potential to occasionally reach threshold. Thus, membrane potential variability is expected to have implications on the shape of the IO curve, particularly near threshold [Chance et al., 2002, Prescott and De Koninck, 2003]. We first investigated the impact of membrane potential variability on the IO curve in the absence of inhibition by measuring the response to depolarising current injections at the soma with different levels of added noise (Figure 4.6). The current noise was modelled by an Ornstein-Uhlenbeck Process (described in Methods) and superimposed on current steps. An increase in the amplitude of membrane potential fluctuations was associated with an increase in spiking rate and a smoothing of the IO relationship near threshold (Figure 4.6B). The current noise also produced membrane potential fluctuations reminiscent of the membrane potential variability observed *in vivo* and contributed to irregular spiking (Figure 4.6C).

We next introduced synaptic input with realistic activation and deactivation kinetics, and stimulated excitatory and inhibitory synapses with independent Poisson processes. IO curves were generated by increasing the frequency of dendritic excitation in the presence of increasing levels of somatic or dendritic inhibition (Figure 4.7A,B). As the EPSP response at each synapse is small and also subject to dendritic filtering effects, during asynchronous activation of excitatory and inhibitory inputs the summation of numerous randomly occurring EPSPs generates only small membrane potential fluctuations at the soma. This leads to IO curves generated in the absence of large membrane potential fluctuations (Figure 4.7C). In order to generate larger fluctuations in the membrane potential, excitatory synapses were stimulated in groups of 4 (Figure 4.7D), 10 (Figure 4.7E) and 25 (Figure 4.7F), where each group of synapses was driven by a common Poisson process, while the Poisson processes used to drive different groups were independent of one another. The size of the membrane potential fluctuations generated by this grouping increased with the number of synapses recruited simultaneously. Modifying the statistics of the synaptic stimulation by increasing the number of co-activated excitatory inputs reduced the subtractive

effects of inhibition without impacting divisive effects, and was similar in models with somatic inhibition and dendritic inhibition (Figure 4.7G,H). The finding that increasing levels of membrane voltage noise decrease the subtractive effects of inhibition is consistent with the simulations shown in Figure 4.6, which show that voltage noise acts to smooth the IO relationship near threshold (see also [Prescott and De Koninck, 2003]).

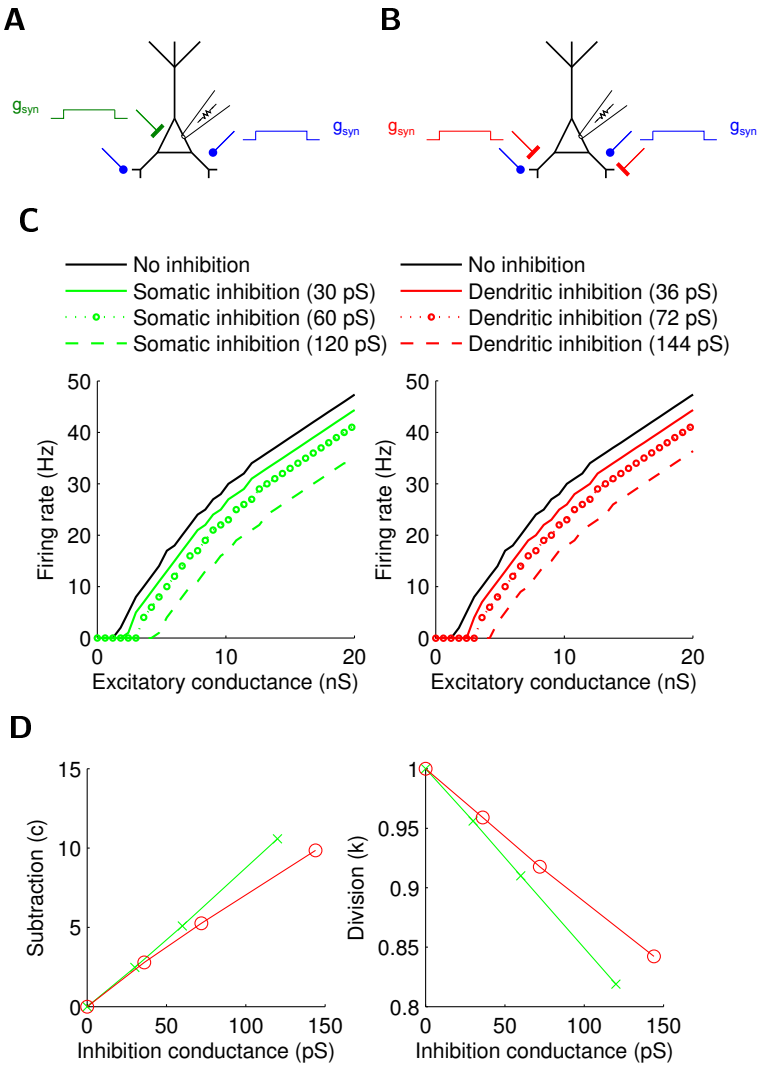

Figure 4.5: Somatic and dendritic inhibition can cause mixed subtractive and dendritic effects. Constant conductance excitatory input was applied at the soma along with constant conductance inhibitory input in the perisomatic (**A**) and basal dendritic (**B**) regions. (**C**) The IO curves showing the effect of somatic inhibition (left) and dendritic inhibition (right). Compared to current injection, these IO curves show a sublinearity with increasing excitatory conductance. (**D**) Both somatic (left) and dendritic (right) inhibition exerted subtractive and divisive effects which increased with increasing inhibitory conductance.

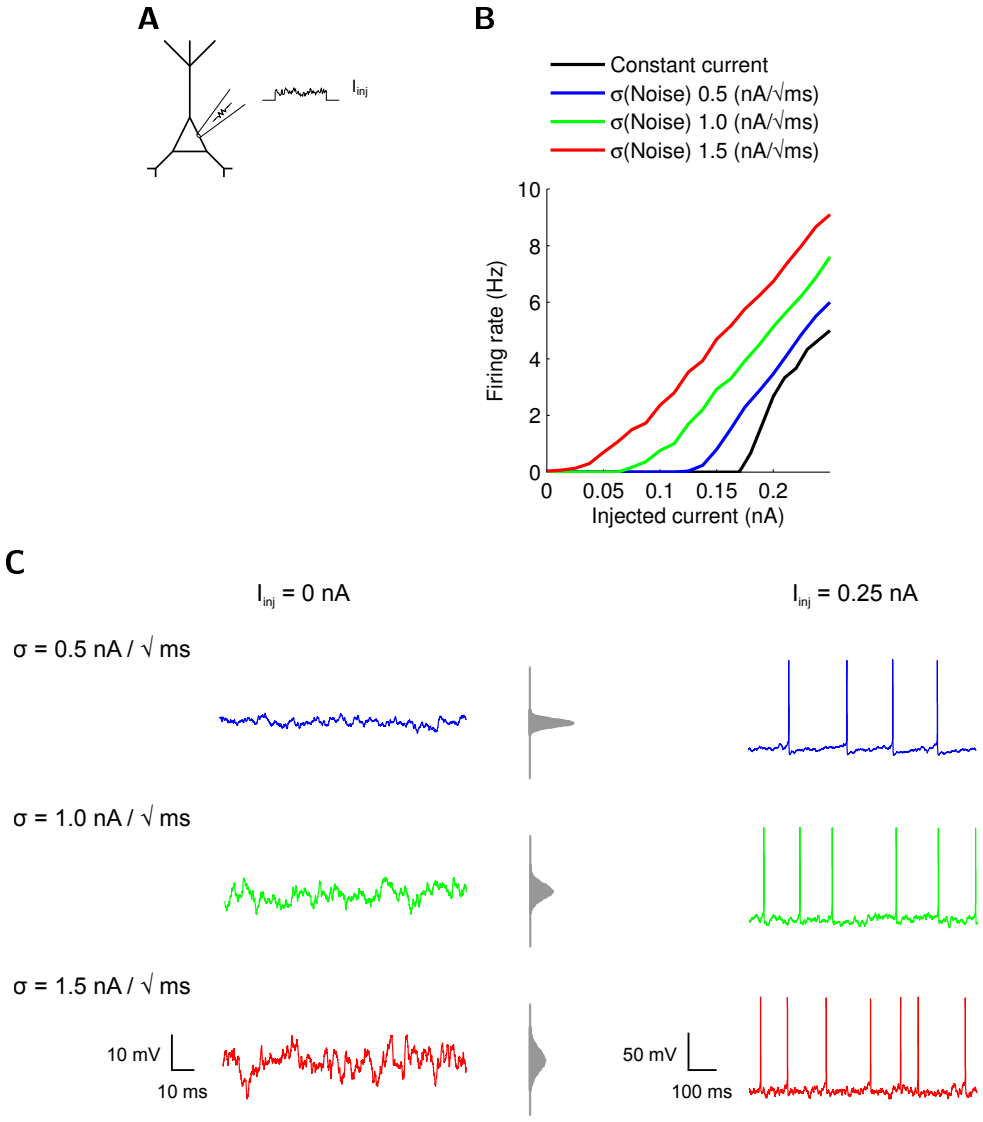

Figure 4.6: The impact of using noisy current injection to drive spiking. (**A**) Schematic of the recording configuration whereby a single electrode is used to deliver noisy current at the soma. (**B**) IO curve of the neuron with different levels of noise. Increasing noise smoothens the IO curve near threshold and shifts the IO curve to the left. (**C**) Increasing the standard deviation of the noise increases the magnitude of random fluctuations in the membrane potential at rest (mean $I_{inj} = 0$ nA; left column) and increases intensity of spiking(mean $I_{inj} = 0.25$ nA; right column). The histograms show the distribution of the resting membrane potential. Each row corresponds to a different level of noise (0.5, 1.0 and 1.5 nA/$\sqrt{\text{ms}}$).

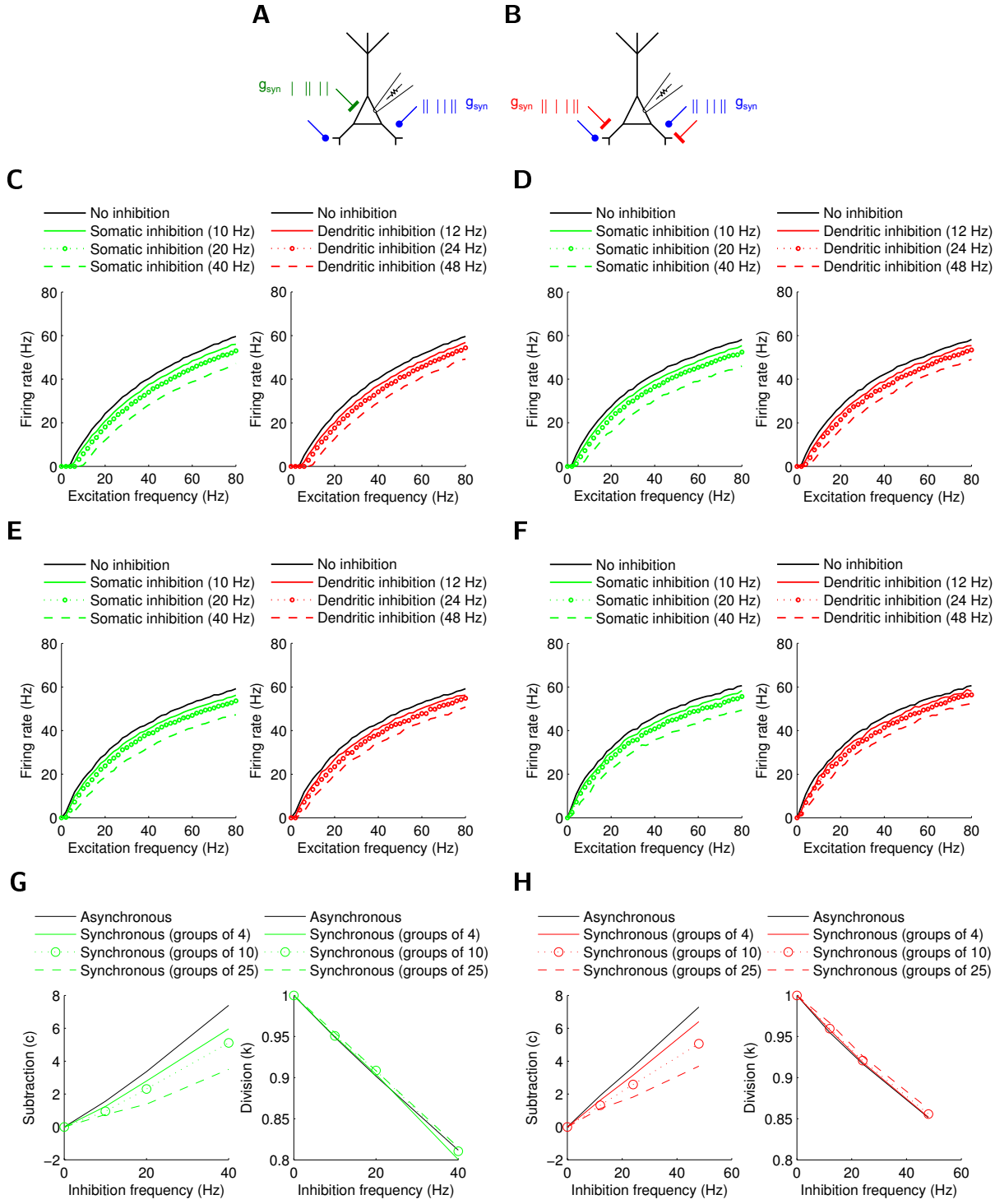

Figure 4.7: Conductance noise decreases subtractive effects without affecting division. Conductance-based excitatory synapses were stimulated in groups by Poisson inputs. Conductance-based inhibitory synapses in the perisomatic (**A**) and basal dendritic (**B**) regions were stimulated by independent Poisson processes. The IO curves showing the effect of somatic inhibition (left) and dendritic inhibition (right) when excitatory synapses were stimulated asynchronously (**C**), in groups of 4 (**D**), in groups of 10 (**E**) or in groups of 25 (**F**). Increasing the synchronicity of the excitatory synapses reduces the subtractive effects for both somatic (**G**) and dendritic (**H**) inhibition without altering the divisive effects.

4.4 Discussion

We have explored how the location of synaptic inhibition affects the input-output firing curve of a biophysically realistic layer 2/3 pyramidal neuron model. In our simulations, we investigated the IO relationship generated during depolarising somatic current injection and dendritic excitatory conductance input under noiseless and noisy conditions, and we compared the effect of perisomatic and dendritic inhibition on these different stimulation conditions. We show that the effect of inhibition, whether subtractive or divisive, was largely independent of the site of inhibition. Rather, the effect of inhibition depended more on the characteristics of the stimulus used to drive the neuron. When constant current injection was used to drive the neuron, inhibition was predominantly subtractive. On the other hand, replacing constant current stimulation with constant conductance excitation introduced a divisive component to the effect of inhibition on the IO relationship, which was observed during both somatic and dendritic inhibition. The purely subtractive effects of inhibition were further diminished when synapses with realistic activation and deactivation kinetics were used instead of constant conductance excitation. Under these conditions introducing correlations between excitatory inputs to increase membrane potential noise led to a further reduction in the subtractive effects of both somatic and dendritic inhibition without changing their divisive impact on the IO relationship.

The IO relationship of a neuron is influenced by the features of the excitatory stimulus used to drive the neuron and any other background activity [Chance et al., 2002, Prescott and De Koninck, 2003]. Unlike depolarising current injection (Figure 4.4), an excitatory conductance input exerts a shunting effect on the neuron as the input resistance decreases when the conductance increases (Figure 4.5). Since the excitatory current also saturates, the firing rate response curve of a neuron driven by excitatory conductance is sublinear, compared to that observed during current injection. In addition, synaptic activity, such as that found *in vivo*, leads to fluctuations in the membrane potential that can cause random excursions above threshold. This noise-induced spiking smoothens the IO relationship of a neuron near threshold, such that the onset to spiking with increasing stimulus intensity is less abrupt (Figure 4.6; see [Prescott and De Koninck, 2003]). As a result the shape of the IO curve of a neuron depends on the nature of the input used to drive the neuron (current or conductance, noisy or noiseless). While the IO response fitted with a parametric curve allows quantification and comparison of the subtractive and divisive components with appropriate model selection, the choice of curve depends on the shape of the IO response. To address this issue, for a given set of stimulation conditions, we took the IO response in the absence of inhibition as the reference curve, and then determined the subtractive and divisive

components (c and k) required to transform the response to that observed in the presence of inhibition (Figure 4.3). This circumvents the need to define the shape of the parametric curve used to describe the IO relationship.

Relation to other work Our results contrast with several recent experimental studies that have placed a much greater emphasis on the role of the site of inhibition in determining its effect on the IO relationship. For example, recent work *in vivo* has assigned subtractive effects to soma-targeting PV interneurons and divisive effects to dendrite-targeting SOM interneurons [Lee et al., 2012b, Atallah et al., 2012], although the opposite has also been reported [Wilson et al., 2012]. Based on the simulations presented in this Chapter we concluded that, in principle, both soma-targeting and dendrite-targeting interneurons are capable of generating both subtractive and divisive inhibition depending on the nature of the stimulation used to drive the neuron of interest.

These studies highlight how stimulus control *in vivo* can be particularly challenging for various reasons. Pyramidal neurons are recurrently connected with each other and highly interconnected with surrounding inhibitory interneurons. Cortical activity is known to depend on recurrent excitation [Petersen et al., 2003, Fiser et al., 2004]. Thus it is very difficult to isolate the manipulation of one subpopulation of neurons without inadvertently modifying the activity of other elements in the circuit in some way. Optogenetic up- or down-regulation of an inhibitory interneuron population, as performed in the studies cited above, not only affects the activity of the neurons receiving direct input from the activated or inhibited inhibitory population, but is likely to have downstream effects in the recurrently connected larger network. For example, SOM interneurons also inhibit PV interneurons in the visual cortex [Pfeffer et al., 2013]. In addition, the overall impact of optogenetic stimulation or inhibition of different interneuronal populations will depend on rhodopsin expression levels, light intensities and the timing and duration of optogenetic stimulation, making comparisons between different studies problematic. Furthermore, Cre driver lines for labelling PV and SOM interneurons are not entirely specific and label overlapping morphologically distinct types of interneurons, such that the separation of soma- and dendrite-targeting interneurons is not ensured by these labelling methods [Jiang et al., 2015]. For all of these reasons, selectively activating a genetically-defined population of interneurons does not necessarily allow unambiguous extraction of the divisive and subtractive effects attributable to that population alone.

To our knowledge, only one other study has provided a combined experimental and modelling approach to comparing somatic and dendritic inhibition [Pouille et al., 2013]. In these experiments excitation was delivered via dynamic clamp injection of an excitatory conductance into the apical dendritic trunk of CA1 pyramidal neurons, or via focal optogenetic stimulation of channelrhodopsin-2 expressing neocortical pyramidal neurons. Local somatic or dendritic inhibition was mimicked by focal application of muscimol (a $GABA_A$ agonist) delivered by picospritzer-controlled local applications through a micropipette. The conclusions drawn from these experiments was that colocalising excitation and inhibition led to subtractive effects, independent of whether inhibition was somatic or dendritic, whereas dendritic excitation combined with somatic inhibition resulted in a predominant divisive change which had a smaller subtractive component. Computer simulations in a simplified ball and stick model were presented that replicated these experimental observations. One criticism of this study is that the experimental conditions and computer simulations represent a relatively specific scenario. Excitatory input, both in the experiments as well as the simulations, was very focal and would likely lead to very high localised changes in input resistance. Similarly, inhibition was applied focally and would also have a very localised effect. These large, localised changes in input resistance and membrane potential due to focal excitatory input are unlikely to mimic the response to realistic, dispersed input. This questions the physiological relevance of the study. In our morphologically realistic model the effects of somatic and dendritic inhibition were far less disparate. As synaptic inputs in this model were distributed throughout the dendritic tree and activated in a dispersed manner, similar to that observed *in vivo* [Chen et al., 2013b, Jia et al., 2010], activation of individual inputs would be associated with localised conductance changes and smaller membrane potential changes, leading to less local shunting interactions between the conductances. This difference is likely to explain why in our simulations both divisive and subtractive effects of somatic and dendritic inhibition were observed.

Future directions The key result we have presented that dendritic and somatic inhibition can produce similar divisive and subtractive effects are derived from computer simulations and hence require experimental validation. As we have discussed, focal synaptic stimulation represents an unrealistic scenario and may produce misleading conclusions [Pouille et al., 2013]. Therefore the ideal *in vitro* experiment would involve controlled, diffuse but targeted activation of excitatory and inhibitory synapses to mimic the way synapses are activated *in vivo*, and could be implemented by the neurotransmitter uncaging strategies we will discuss in Chapter 5.

Since dendritic and somatic inhibition have very similar effects on neuronal output in our model, when is the location of inhibition important? We argue that the effect of inhibition is more dependent on the functional context that the inhibition operates in rather than the biophysical location of the inhibition itself. This is not to say that the location of inhibition does not play a role. The functional impact of inhibition is likely to depend critically on how it interacts with the local active properties of the region targeted. For example, in some circumstances dendritic inhibition very effectively shuts down cell spiking by suppressing dendritic electrogenesis and provides a powerful mechanism for divisive gain control [Miles et al., 1996]. In the hippocampus for example, *in vitro* silencing of SOM+ dendrite-targeting interneurons, but not PV+ perisomatic-targeting interneurons, dramatically increases the firing rate response of CA1 pyramidal neurons to CA3 input [Lovett-Barron et al., 2012]. In the cortex, various dendrite-targeting interneurons are also able to regulate dendritic electrogenesis and subsequent neuronal output [Murayama et al., 2009, Jiang et al., 2013], while interhemispheric inhibition mediated by $GABA_B$ receptors and delivered by layer 1 interneurons to the tuft region of layer 5 pyramidal neurons robustly shuts down firing for hundreds of milliseconds [Palmer et al., 2012b]. With regard to axosomatic inhibtion, chandelier cells, which target the axon initial segment of cortical pyramidal neurons, may be uniquely positioned to exert exquisite control over the output of these neurons [Howard et al., 2005, Woodruff et al., 2010]. The ability of chandelier cells to precisely control pyramidal neuron output is also demonstrated by their role in establishing oscillations and enforcing synchrony in the hippocampus [Somogyl, 1995]. Together, these examples serve to demonstrate how the effect of inhibition may be intimately related to the nature of the active properties of the recipient domain.

Beyond the local active properties of the neuron, *in vitro* and *in vivo* studies have also shown that different classes of interneurons may be recruited under different circumstances. In the hippocampus for example, basket, axo-axonic and oriens-lacunosum-moleculare cells, which innervate the perisomatic region, axon initial segment, and distal apical dendrites, respectively, show class-specific and distinct patterns of activity during behaviourally-relevant theta rhythms and sharp-wave ripples [Klausberger et al., 2003]. In the cortex, two inhibitory microcircuits which both target the apical dendrites of pyramidal neurons have been shown to be active under different circumstances. Namely, the deep layer Martinotti neurons which act via $GABA_A$-mediated neurotransmission [Murayama et al., 2009, Silberberg and Markram, 2007], and the layer 1 neurogliaform cells which act via $GABA_B$-mediated neurotransmission or volume transmission [Chu et al., 2003, Oláh et al., 2009]. The context-specific firing of interneurons in these examples also lend weight to the notion that the timing of inhibition is key, such as in the establishment and maintenance of hippocampal rhythms [Somogyi and Klausberger, 2005]. Indeed, somatic feed-forward

inhibition is known to impose a very narrow time window for EPSP integration in pyramidal neurons [Pouille and Scanziani, 2001].

These examples provide instructive guides for directing future investigations and also demonstrate the limited utility of characterising the effects of inhibition according to how the IO relationship of a neuron is modulated during somatic current injection. Characterisation of inhibition in this way does not distinguish other important features such as the timing of inhibition and its impact on active dendritic processes including dendritic spikes. Thus future efforts should be directed to further understand which interneuron populations are active and under what circumstances during behaviour.

Chapter 5

Four-dimensional multi-site photolysis of caged neurotransmitters

5.1 Introduction

Optical methods for studying neuronal integration have changed the landscape of studying neuronal function [Scanziani and Häusser, 2009] by enabling researchers to study the physiology of dendritic compartments not accessible to electrophysiological recordings. Light offers several advantages over electrodes. Optical methods are essentially non-invasive since light passes through cells, producing minimal trauma. Light also offers superior spatial characteristics, with the ability to precisely localise signals while recording from multiple locations. For example, with two-photon (2P) microscopy it is possible to image with cellular resolution across all depths of the cortex [Chia and Levene, 2009, Andermann et al., 2013] and even two distant cortical areas simultaneously [Lecoq et al., 2014]. For these reasons, light microscopy has become one of the most widely used tools for probing neurons and neural circuits.

Neurotransmitter uncaging, or photostimulation with caged neurotransmitters, has been an influential method for studying synaptic integration [Wang and Augustine, 1995, Pettit et al., 1997]. Uncaging approaches involve photolysis of caged compounds, which are molecules attached to a photolabile protecting group that renders the molecule biologically inert. Light is used to break the attachment to the protecting group, releasing the molecule in an active form. Many caged compounds have been developed [Adams and Tsien, 1993], including caged neurotransmitters such as glutamate [Matsuzaki et al., 2001], GABA [Wieboldt et al., 1994], and acetylcholine [Milburn et al., 1989]. Uncaging differs from optogenetics in that optogenetics relies primarily on genetic specificity for precise targeting, whereas uncaging relies on optical manipulation of light to achieve spatial precision. Furthermore, by uncaging with 2P

laser stimulation, it is possible to achieve sub-millisecond control with sub-micron resolution, allowing one to mimic the temporal and spatial dynamics of neurotransmitter release [Noguchi et al., 2011].

Laser-scanning systems utilising galvanometer mirrors [Matsuzaki et al., 2001, Gasparini and Magee, 2006, Branco et al., 2010] implemented in 2P laser-scanning microscopes provide quasi-simultaneous multi-site stimulation by scanning the laser beam at fast rates (∼10 kHz i.e. switching time of ∼100 μs). These two-dimensional scanning systems, however, are restricted to a single optical plane. A high-speed 3D scanning system has been described employing four acousto-optic modulators (AOMs) [Reddy et al., 2008]. This system has been used to monitor neuronal activity via calcium imaging [Reddy et al., 2008, Katona et al., 2012]. However, using four AOMs results in low optical throughput, and the dispersion through the AOM crystal significantly decreases 2P efficiency due to pulse broadening. Consequently, such a system has not been utilised for multi-site photolysis of caged neurotransmitters in 3D. Beam-shaping techniques using a spatial light modulator (SLM) can split a single laser beam into several beamlets and generate arbitrary illumination patterns. These techniques have been demonstrated for photostimulation with shaped illumination in single-photon (1P) [Lutz et al., 2008, Zahid et al., 2010] and 2P [Dal Maschio et al., 2010, Papagiakoumou et al., 2010], and for multi-foci photostimulation patterns in 1P [Anselmi et al., 2011, Yang et al., 2011] and 2P [Nikolenko et al., 2008]. 1P excitation exhibits poor resolution along the optical axis, due to scattering in brain tissue. While 2P photostimulation offers enhanced axial resolution, previous studies have only shown stimulation in a single plane.

Two-photon photolysis of caged neurotransmitters using holographic projection of an arbitrary 3D multi-foci uncaging pattern has recently been demonstrated [Go et al., 2012]. While holographic projection allows simultaneous multi-site photostimulation in 3D, the slow response of the SLM (∼10-30 ms) remains the limiting factor in achieving fast-switching light patterns within physiologically relevant timescales (∼1 ms). Here, we overcome this limitation by temporally gating the 3D multi-foci uncaging pattern generated by the SLM using a high-speed spatial light-switching array provided by a digital micro-mirror device (DMD). The programmable array of micro-mirrors can be used to independently control each beamlet in less than a millisecond (∼0.7 ms) allowing the multi-site pattern to be changed at submillisecond rates. Random spatial stimulation patterns in 3D are therefore possible at physiologically relevant timescales. In this Chapter we demonstrate the performance of this system as a tool for studying neuronal integration by uncaging glutamate at multiple foci with submillisecond resolution, stimulating activation of multiple dendritic spines on different dendritic branches. My contribution to this collaboration was the design of the software used to control the DMD as well as experimental testing of the system. Vince Daria and

Ann Go also made substantial contributions to this work, and are acknowledged throughout this chapter.

5.2 Methods

Microscope design

Our time-gated holographic microscope system employed a SLM, encoded with a phase hologram to generate a multi-focal excitation pattern of the incident laser beam, and a DMD, which acts as a spatial light switch allowing independent switching of the individual foci. The resulting spatio-temporal excitation pattern is used for glutamate uncaging. We also use galvanometer scanning mirrors to image the 3D morphology of the neuron. A schematic of the system is described in Figure 5.1A.

The microscope system consisted of a photostimulation arm and an imaging arm, with corresponding uncaging (720 nm) and imaging (800 nm) lasers. The two laser beams are split by a polarising beam splitter (PBS), and recombined ahead of the objective lens by a second PBS following reorientation of the polarisation of each laser using half-wave plates. The imaging arm includes a near infrared (NIR) Ti:S laser (MIRA 900, Coherent Inc) and galvanometer scanning mirrors that scan the linearly polarised imaging beam across the field of view. A photomultiplier tube (PMT) is used to detect photons collected from the sample under the objective. Photons are directed to the PMT via a second dichroic mirror, which reflects wavelengths below 650 nm into the PMT. For DIC imaging, infrared light from below the sample passes through the objective and the first dichroic mirror charge-coupled device (CCD) camera (Dage-MTI IR-1000EX). In DIC imaging mode, the dichroic mirror above the objective lens allows infrared light (>810 nm wavelength) to pass through and focus onto a charge-coupled device (CCD) camera (Dage-MTI IR-1000EX).

The two principle components of the photostimulation that enable fast spatiotemporal light modulation are a spatial light modulator (SLM), which generates a multi-focal three-dimensional excitation pattern from the incident laser beam, and a digital micro-mirror device (DMD), which serves as a two-dimensional light switch that enables rapid and independent switching of individual stimulation foci. The uncaging laser beam from a Ti:S laser (Coherent Inc. Chameleon) is expanded by a telescope to illuminate the 16×12 mm^2 area of a programmable phase-only SLM (Hamamatsu X10468-02), where the phase-only hologram is encoded. The hologram is computed using custom software based on the standard prism-lens superposition algorithm [Liesener et al., 2000, Curtis et al., 2002]. The DMD (DLP3000, Texas Instruments) is positioned at the Fourier plane with respect to the SLM and is interfaced to the microscope using $4f$ relay lenses, which position the DMD at the conjugate image plane with respect to the sample region. The DMD is used to individually switch each beamlet of the excitation pattern ON

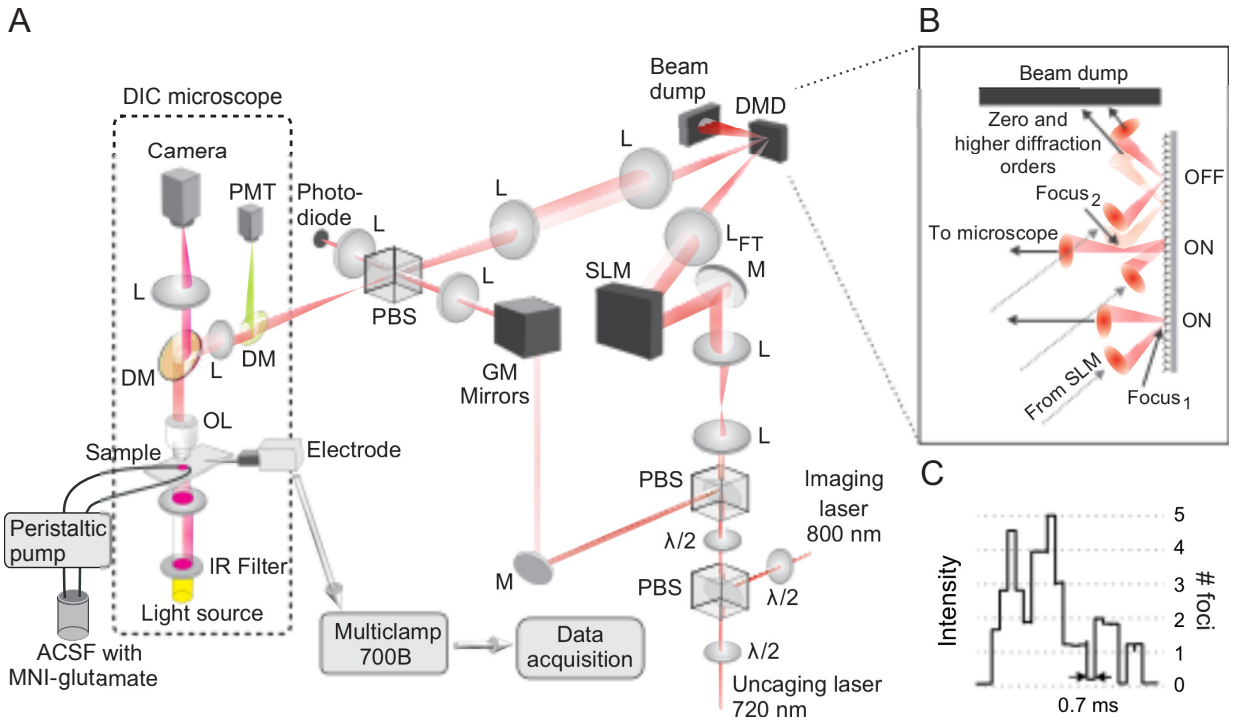

Figure 5.1: Optical design of 4D holographic microscope. (**A**) Light from a laser tuned to 800 nm is projected through two polarising beam splitters (PBS) onto two galvanometer (GM) scanning mirrors that scan the excitation beam across the sample for imaging. Fluorescence from the sample is collected by a photomultiplier tube (PMT). Light from another laser tuned to 720 nm is expanded, projected onto a spatial light modulator (SLM), focused onto a digital micro-mirror device (DMD) and imaged onto the sample. The SLM is encoded with a phase hologram that generates a multi-focal excitation pattern from the incident laser beam. The DMD acts as a spatial light switch allowing independent switching of the individual foci. The resulting spatio-temporal excitation pattern at the sample plane is used for uncaging glutamate. λ/2, half-wave plate; DM, dichroic mirror; M, mirror; L, lens; L_{FT}, Fourier transform lens; OL, objective lens; ACSF, artificial cerebrospinal fluid. (**B**) The DMD operates the micro-mirrors by changing their tilt between an ON and an OFF state. In the ON state, incident light is directed towards the objective, while in the OFF state, incident light is directed towards a beam dump. The micro-mirrors can all be operated independently from one another. For a given beam focus size, fewer micro-mirrors are required to switch a focus on the DMD that is confocal with the objective lens ($Focus_1$) than a focus that is above the DMD plan ($Focus_2$). (**C**) The intensity of light incident on the photodiode located in the conjugate Fourier plane reflects the number of foci switched ON. Micro-mirror states can be switched at 1440 Hz, corresponding to a period of approximately 0.7 ms. This microscope design was conceived with Vince Daria and Ann Go.

or OFF. In the ON state, the micro-mirrors direct the laser light to the sample (see Figure 5.1B). In the OFF state, the laser light is directed to a beam dump. The relay lenses are chosen to ensure that the back aperture of the objective lens is filled and that the area of the DMD encompasses the field of view of the objective lens (200 μm^2 for a 1.0 NA 40× objective).

The dimension of one micro-mirror in the DMD is smaller than the diffraction-limited focal spot of the Fourier transform (FT) lens, with an effective numerical aperture (NA) of ∼0.1. Hence, it takes a small set of micro-mirrors to switch a single beamlet of the multi-focal pattern ON and direct it to the sample for uncaging (see Figure 5.1). When the holographic focus generated by the SLM is either above or below the plane of the DMD, a larger subset of micro-mirrors is needed. The size of the subset of micro-mirrors is calculated based on the conical angle of the focus with respect to the NA of the FT lens and the operating wavelength (720 nm). Figure 5.1C shows the relative intensity in the sample plane as measured by a photo-diode located at the conjugate Fourier plane (see Figure 5.1A) for different numbers of focal spots turned ON by the DMD. The DMD receives 24-bit RGB data at 60 Hz per pixel, with each colour channel (RGB) having 8-bit depth i.e. 256 different intensity levels. At the level of the micro-mirrors, the RGB pixel intensity determines when each mirror is switched on and off during a 60 Hz cycle. The way the video input is used to turn individual mirrors on and off depends on the mode the DMD is operating in. We operated the DMD in 1-bit monochrome mode. In this mode, an image frame in a single 60 Hz cycle consists of 24 1-bit planes, which encode the micro-mirror state (ON or OFF) at 24 consecutive time epochs during that cycle. This allows temporal sequences to be read out at 1440 Hz. In Figure 5.2 we show how the temporal sequence of micro-mirror states is encoded in the RGB pixel intensities. The photostimulation pattern and video feed to the DMD were generated with a custom MATLAB routine running the Psychophysics Toolbox (PTB) package.

The setup is also equipped with a micromanipulator (Sutter Instruments), peristaltic pump (Gilson Minipuls 3) and amplifier (MultiClamp 700B, Molecular Devices) for electrophysiology. We use custom software developed in LabVIEW (National Instruments) to control the acquisition of 3D 2P images, the calculation of the appropriate hologram for projection of photostimulation sites, and the laser intensity via a polarising beam splitter and a half-wave plate on a motorised rotation mount.

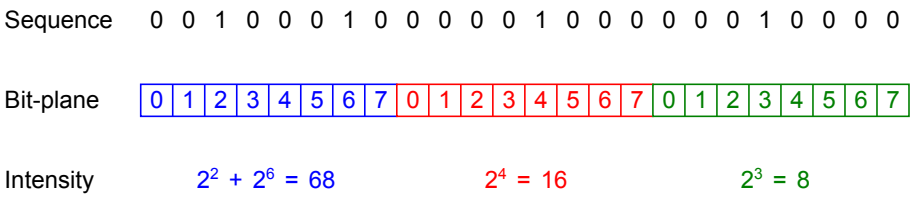

Figure 5.2: Encoding the temporal sequence of mirror states. A 24-bit RGB pixel encodes a single 60 Hz cycle consisting of 24 consecutive mirror states. To encode a sequence of 24 mirror states, the binary sequence is split into three groups corresponding each colour channel (blue, red and green). Thus each group consists of 8 elements. Each element is assigned to a different bit-plane, numbered from 0 to 7. To determine the intensity of each colour based on the sequence of mirror states, the bit-planes corresponding to non-zero (i.e. ON) states are exponentiated (base 2) and summed. For example in the figure shown, the first eight elements of the ON-OFF sequence, 00100010, corresponding to the blue channel, have non-zero states in bit-planes 2 and 6. Thus the intensity of the blue channel is calculated as $2^2 + 2^6 = 68$.

Slice preparation and electrophysiology

Wistar rats (3-5 weeks old) of either sex were anaesthetised with isoflurane and decapitated according to protocols approved by the Animal Ethics Committee of the Australian National University. Three hundred micrometer thick parasagittal brain slices of somatosensory cortex and hippocampus were made using a Leica VT1200S vibratome. During slice preparation, the brain tissue was submerged in ice-cold artificial CSF (ACSF) containing (in mM): 125.0 NaCl, 2.5 KCl, 1.25 NaH_2PO_4, 2.0 $CaCl_2$, 25.0 $NaHCO_3$, 1.0 $MgCl_2$, and 10.0 glucose, bubbled with 95% O_2/5% CO_2 (pH $\approx$ 7.4). Slices were transferred to a holding chamber containing ACSF bubbled with 95% O_2/5% CO_2 (pH $\approx$ 7.4) and incubated at 34°C for 30 minutes before being maintained at room temperature.

Somatic whole-cell recordings were made from visually identified layer 2/3 and 5 pyramidal neurons under differential interference contrast optics [Stuart et al., 1993] with a MultiClamp 700B amplifier. Recording electrodes were filled with a solution containing (in mM): 115 K-gluconate, 20 KCl, 10 HEPES, 10 phosphocreatine, 4 ATP-Mg, 0.3 GTP, 5.4 biocytin, and 0.1 Alexa-488 (Invitrogen). In some instances, neurons were injected with current to hold their resting membrane potential at -70 mV. For the experiments depicted in Figures 5.4D-F, the resting membrane potential was depolarised to -55mV to enable APs to be more easily generated. Data analysis was performed with AxoGraph X and MATLAB. We calculated peak currents and voltages by averaging 5-12 trials.

Two-photon imaging and glutamate uncaging

Neurons were filled with 0.1 mM Alexa-488 for 20-30 minutes before imaging at 800 nm with 12-22 mW of laser power. Image stacks measuring 800 $\times$ 800 pixels per image plane were acquired, with a separation of 1 μm between planes in the stack. ImageJ (National Institute of Health) was used for volume rendering and 3D visualisation. We determined the potential sites on the dendritic tree for photostimulation from the 3D image map of the fluorescently labelled neuron. The appropriate phase hologram for the desired multifocal pattern around the neuron was then calculated and encoded onto the SLM. The DMD was used to switch individual sites ON or OFF.

MNI-caged glutamate (3 mM in ACSF, Tocris Bioscience) was bath-applied with 0.1 mM cyclothiazide. Uncaging was performed at 720 nm using 9-30 mW power per uncaging spot. A closed recirculating system using a peristaltic pump was used to minimise the ACSF volume. A semi-automated drift detection algorithm was executed prior to every uncaging experiment to ensure that the photostimulation sites remained in the same positions.

5.3 Results

Time-gated holographic system

Our microscope design builds on an earlier 2P holographic microscope system capable of simultaneous multi-site photostimulation in 3D [Go et al., 2012] by incorporating a DMD element. The addition of the DMD offers several advantages over the original system. Firstly, the DMD is able to rapidly update photostimulation patterns at 1440 Hz (under 0.7 ms per frame), an order of magnitude faster than what the SLM is capable of, which has a response time of ∼10-30 ms. Since each pixel on the DMD array operates separately, stimulation foci can be switched independently of each other. This is in contrast to shutter systems that can also provide sub-millisecond switching, but cannot switch stimulation foci individually. Secondly, the DMD can eliminate spurious light patterns normally produced by phase-only holograms [Palima and Daria, 2006, Palima and Daria, 2007, Go et al., 2011], thereby reducing artifactual uncaging outside of the designated foci.

To visualise the different foci, we placed a reflective surface (e.g. glass slide) in the sample plane and imaged the reflected light leaked through the dichroic mirror directly above the objective lens (see Figure 5.1A). Figure 5.3A shows the photo- stimulation pattern produced by the SLM projected onto the sample with all DMD pixels in the ON position. Figure 5.3B shows the same photostimulation pattern with only the intended nine foci switched ON. Note that the undiffracted (i.e. zero-order; see image centre in Figure 5.3A) beam from the SLM is missing in the latter, as are other higher diffraction orders and mirror projections of the first orders. The DMD therefore provides an easy way of eliminating the zero-order beam, thus, reducing the risk of unintended uncaging, and gives independent control for switching each stimulation site.

Figure 5.3C shows how the power on one uncaging focus depends on the number of focal spots, N, produced by the SLM. The relationship is an inverse proportionality as reported earlier [Daria et al., 2009]. The error bar for $N = 1$ shows the variability in power among different non-central positions of the holographic spot which results from the spatial variation in the diffraction efficiency of the SLM. For $N = 2$ to 20, the ON focus was kept at a fixed position as the spot configuration for a fixed number of foci was varied. Note that the variability in power within a single position is much less than the spatial variability. The laser beam has a Gaussian intensity profile. Figure 5.3D shows the normalised power as a cumulative Gaussian function of DMD array size, defined as the length of the square array of micro-mirrors for gating the uncaging focus, averaged over different positions of the holographic spot. On average,

96% of the maximum intensity at each spot was recovered using a DMD array size of 21, whereas 90% was recovered with an array size of 15. Based on this information, for most of the experiments in this paper we used an array size of 15. Figures 5.3E,F show how the glutamate uncaging-evoked response varies with number of uncaging sites, N, and DMD array size, respectively. The quadratic intensity dependence of 2P absorption is reflected here with the peak voltage seen as a function of $1/N^2$ and a squared cumulative Gaussian function of DMD array size. As the total laser power was kept constant for the experiment in Figure 5.3E, data points for $N < 6$ were not investigated to preclude damaging the DMD with high laser power. Laser pulse duration for Figure 5.3E,F is 2 ms.

Figure 5.4A shows 11 foci positioned in a circular arrangement with z-axis positions ranging from 10 μm above (negative) to 10 μm below (positive) the nominal focus of the objective lens (0 μm). The point in the focal plane is in focus (i.e. sharpest) but the rest are out of focus with the points in the farthest away planes ($\pm$ 10 μm) the most out of focus. Figure 5.4B shows the same light pattern but with the objective lens focused in the plane $z = +$ 10 μm. Figure 5.4C shows the DMD array sizes for gating the different foci in the light pattern in Figure 5.4A. By scaling the micro-miror array size for gating the relevant site with distance from the nominal focal plane of the objective lens, we accommodate the increasing size of the out-of-focus projection of the beamlets and allow collection of light for points projected above and below the focal plane. The DMD array size puts a restriction on the minimum separation between two uncaging sites for independent gating. Figure 5.4D plots the minimum distance between two uncaging sites as a function of axial distance for an array size of 15 for the case where one spot is fixed while the other spot is moved away axially and for when both spots move together in the axial direction. The minimum separation for two uncaging sites in the same plane is 6.5 μm. As a result we refrained from positioning uncaging sites within 10 μm of the centre to avoid switching ON the zero-order beam and unnecessarily illuminating the sample. Technically, however, this minimum separation is a soft limit as independent uncaging at two sites, defined by the spatial resolution of glutamate uncaging, has a much narrower profile. Figures 5.4E,F show representative lateral and axial resolution profiles from uncaging-evoked voltage responses to 700 μs laser pulse duration. The responses were measured in current clamp as the uncaging site was moved orthogonally from the spine while the objective was kept fixed. The lateral profile has a full width at half maximum (FWHM) of 0.8 ± 0.1 μm. The axial profile was 1.3 ± 0.1 μm. The solid lines correspond to Gaussian curve fits. The final resolution depends on laser power, laser pulse duration and local MNI-glutamate concentration. For example, we earlier reported uncaging resolution with FWHM of 2.4 ± 0.2 μm and 3.7 ± 0.3 μm for the lateral and axial profiles, respectively, using 2 ms laser pulse duration [Go et al., 2012].

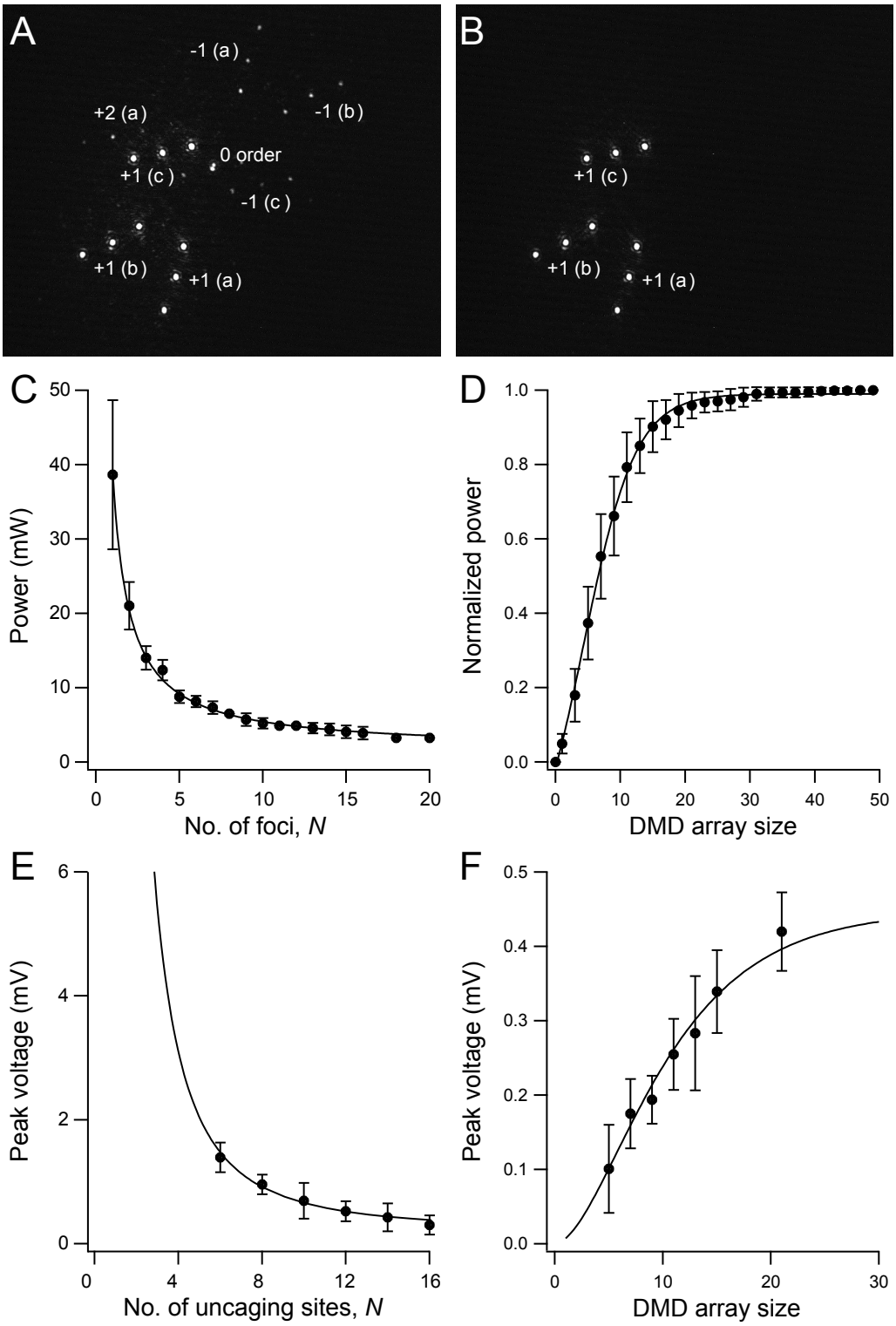

Figure 5.3: (Caption next page)

Figure 5.3: SLM-generated 3D photostimulation pattern with DMD gating. (**A**) Nine-foci light pattern produced by the SLM with all DMD pixels turned ON showing zero order (0 order), second order [+2 (a)] and mirror projections [-1 (a-c)] of the first diffraction order [+1 (a-c)]. (**B**) Same photostimulation pattern as in (**A**) but with only the nine desired foci gated by the DMD. All other light is eliminated by being directed to the beam dump. (**C**) Power on one ON focus as a function of number of foci, N ($n = 10$ different spot configurations), measured by a power meter under the objective lens. For $N = 2 - 20$ foci generated by the SLM, the DMD was configured to illuminate a single (ON) focus only. The ON focus was kept at a fixed position. Solid line is $1/N$ fit. (**D**) Normalised power as a function of DMD array size ($n = 10$ focal spot positions). The array size is defined as the length, in pixels, of the square array of micro-mirrors for gating each uncaging focus. Solid line is a cumulative Gaussian fit. (**E**,**F**) Peak of glutamate-evoked voltage from one ON uncaging site as a function of (**E**) number of uncaging sites and (**F**) DMD array size ($n = 8 - 10$ trials). In **F**, 10 foci were generated by the SLM. Solid lines are proportional to squares of curve fits in **C** and **D**, respectively. These experiments were performed by Ann Go.

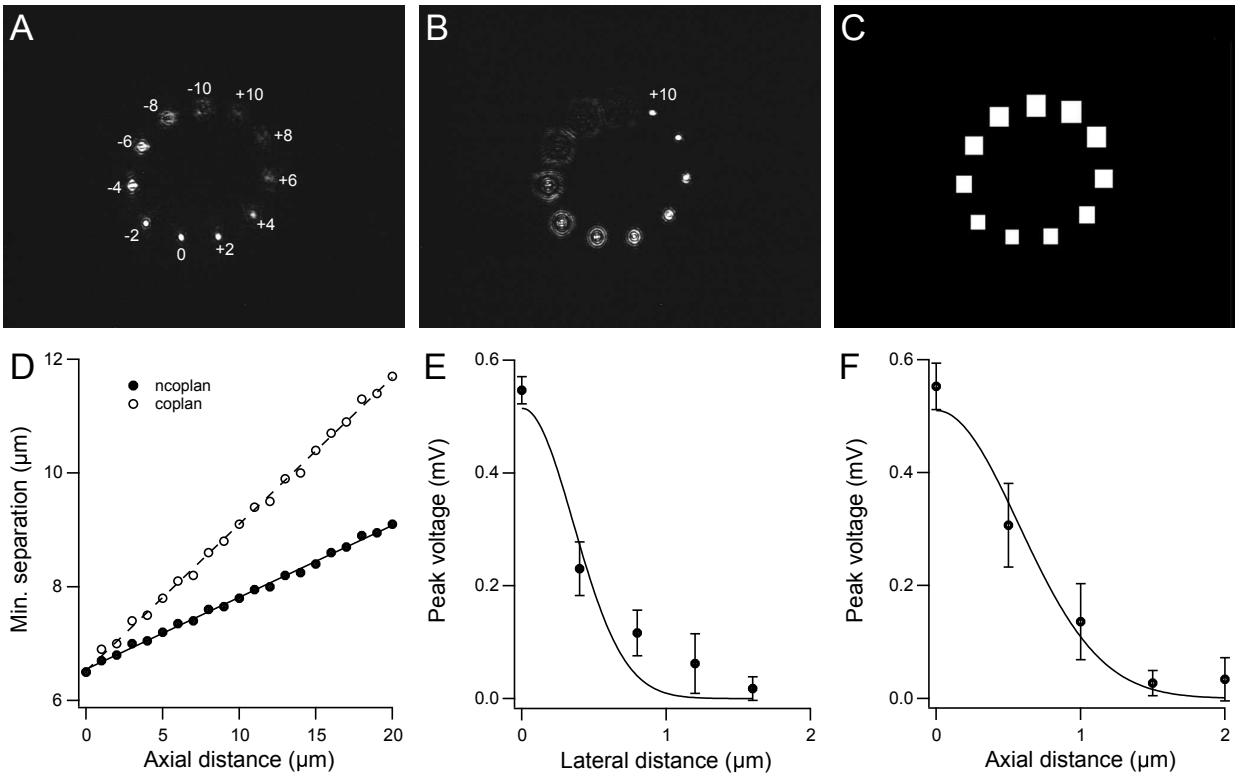

Figure 5.4: Spatial resolution of independent gating and uncaging. (**A**) 3D photostimulation pattern with objective lens focused in the reference plane $z = 0$ μm and the other 10 sites holographically projected either above (negative) or below (positive) the reference plane. (**B**) Same photostimulation pattern as in C but with objective lens focused in the plane $z = +10$ μm. (**C**) Sizes of micro-mirror arrays for switching foci shown in **A**. The array size scales with distance from the objective focal plane allowing collection of out-of-focus light. (**D**) Minimum separation for independent gating of two uncaging sites as a function of axial distance for the case when one spot is fixed while the other spot is moved away axially (ncoplan) and for when both spots move together in the axial direction (coplan). DMD array size is 15. Solid line is linear fit. (**E**) Peak voltage with varying lateral distance orthogonal to a spine. FWHM $= 0.8 \pm 0.1$ μm. (**F**) Peak voltage as a function of axial distance above the spine. FWHM $= 1.3 \pm 0.1$ μm. For E and F, solid lines are Gaussian fits. These experiments were performed by Ann Go.

Spatio-temporal patterned stimuli

The system offers access to the 3D dendritic arbor of the neuron for activating synaptic receptors. This enables the study of how neurons integrate multiple synaptic inputs on their dendritic trees. We illustrate such an experiment in Figure 5.5. A 2P fluorescence image of a layer 5 pyramidal neuron is shown in Figure 5.5A with the recording pipette at the soma and some basal dendrites either viewed from the top (xy) or side (yz). Four uncaging sites are chosen with two each projected onto two basal dendrites located 5 μm apart in the vertical direction. A static hologram for all four sites is generated with the SLM, and the DMD is used to switch ON one focus at a time. Figure 5.5B shows glutamate-evoked excitatory postsynaptic potentials (EPSPs) generated by individually uncaging glutamate at each site for a duration of 3 ms. Laser power was set to generate EPSPs consistent with single synaptic inputs (<0.5 mV) [Nevian et al., 2007, Fino et al., 2009]. Figure 5.5C summarises EPSP summation for all the possible combinations of the uncaging sites. Linearity is expressed as the ratio of the peak amplitude of the composite EPSP generated when all sites are simultaneously stimulated and the arithmetic sum of individual EPSPs. The blue bar corresponds to within-branch and the red to between-branch summation, respectively. No statistically significant difference is observed, indicating that the summation is largely linear (two inputs in one basal, $n = 2$; two inputs on two basal dendrites, $n = 4$; three inputs, $n = 4$; four inputs, $n = 1$; pooled data, $n = 11$ combinations). This observed linear within-branch summation is consistent with the observation by [Polsky et al., 2004] who showed that two EPSPs on the same layer 5 basal dendrite 20 μm apart summate linearly.

The DMD, by enabling independent switching of individual photostimulation sites, makes it possible to activate different combinations of sites without having to change the phase hologram i.e. the hologram remains static and sites are switched ON/OFF by the DMD. Moreover, to allow comparison of different stimulus combinations, it is critical that the laser power at each uncaging site is kept constant. Use of the DMD to switch sites on and off allows this and eliminates the need to adjust the total power for distribution among the uncaging sites when using different numbers of stimulus sites.

Using the DMD system we next investigated the impact of integrating different synaptic inputs located at different dendritic locations on AP output. Figure 5.5D shows five marked uncaging sites on three apical oblique dendrites of a layer 2/3 pyramidal neuron. The DMD is used to randomly switch uncaging sites ON or OFF for $0.7 - 4$ ms at a time for a total period of 4 s. Figure 5.5E shows the relative intensity at the sample, indicating the number of stimulus sites at which glutamate is uncaged, together with the membrane potential at the soma for two trials of identical time-varying uncaging patterns. Several

peaks of the APs during the two trials align in time indicating that the APs are not randomly evoked, but are triggered by specific uncaging patterns. Figure 5.5F shows a magnified view of sections of the membrane potential trajectory and laser intensity 60 ms before to 20 ms after the peak for four of the APs generated by this uncaging pattern. Integration of several inputs is required prior to AP generation. This information can be used to determine the glutamate uncaging profile leading to AP generation. Figure 5.5G shows the average membrane potential and laser intensity ($n = 53$ APs) 60 ms preceding AP generation to 20 ms after. This analysis indicates that on average, an AP is driven by a significant increase in laser intensity ∼23 ms before its peak.

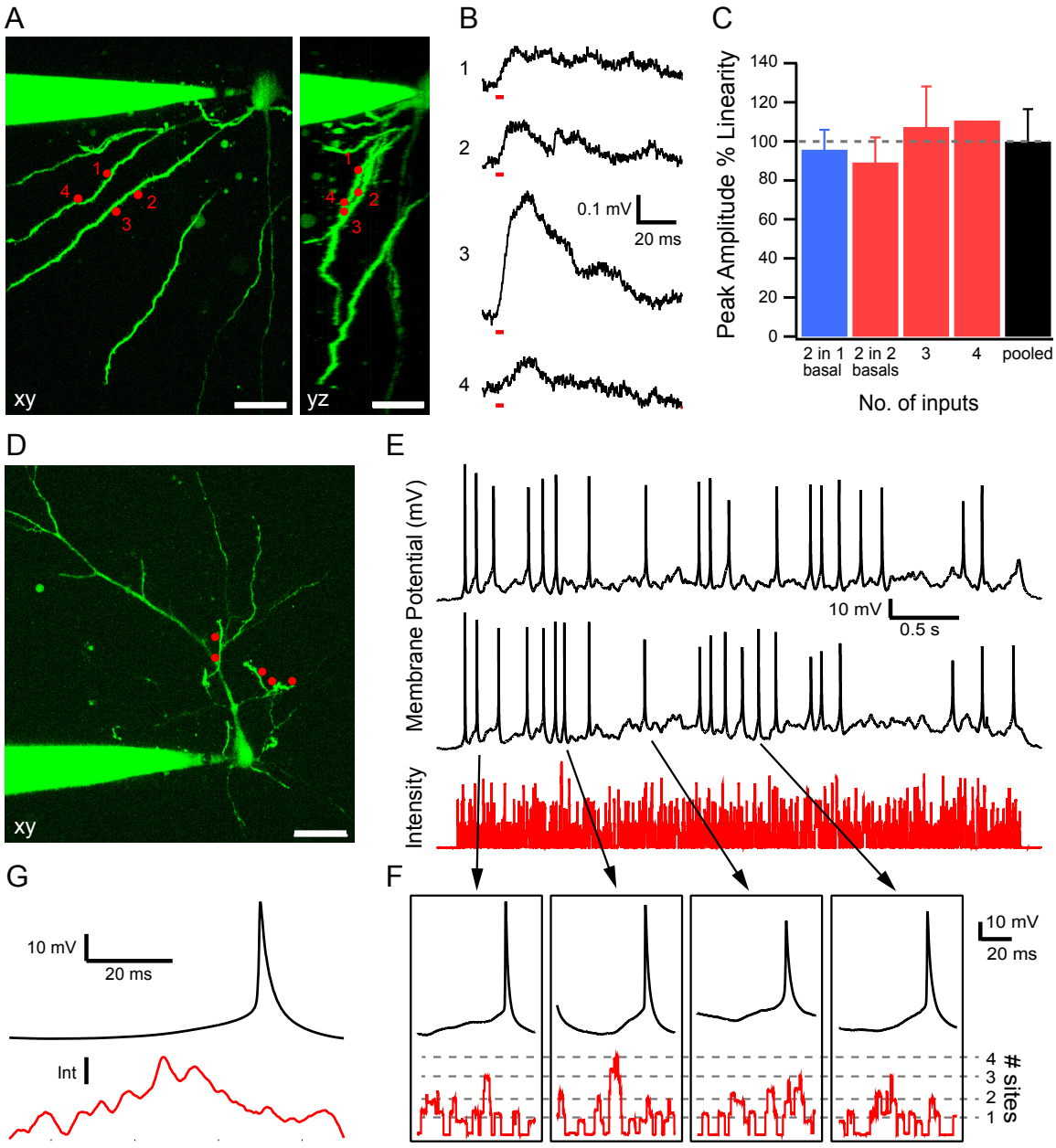

Figure 5.5: (Caption next page.)

Figure 5.5: Synaptic integration experiments. (**A**) Layer 5 pyramidal cell with uncaging sites in two planes 5 μm apart (1 and 2 are in one plane, 3 and 4 in another) as viewed in the xy and yz planes. Scale bar 25 μm. (**B**) Individual uncaging-evoked EPSPs obtained by turning ON stimulation sites in a static hologram one at a time with the DMD. Stimulus duration (3 ms) is indicated by red bars at the start of the EPSP. (**C**) Summary of results for different combinations of uncaging sites. Linearity is expressed as the ratio of the peak amplitudes of the measured compound EPSP and the arithmetic sum of individual EPSPs. Dashed line denotes linear summation (100%). Blue bar corresponds to within-branch summation; red, between-branch summation. Data are shown as mean $\pm$ s.e.m. for all combinations. (**D**) Layer 2/3 pyramidal cell with five uncaging sites situated along three apical oblique branches and all in a single plane. Scale bar 25 μm. (**E**) Representative membrane potential time courses generated by two repeats of the same train of random stimulus for uncaging glutamate at the sites in **D**. In the stimulus, the spatial selections and their time intervals are both random. The resting membrane potential at the soma was set to -55 mV. Several action potentials (APs) align in time triggered by the same uncaging patterns. Laser intensity in the sample plane is indicative of the number of simultaneously active stimulus sites. (**F**) Magnified view showing membrane potential (black) and laser intensity (red) for a time window from 60 ms before to 20 ms after the peak of the AP. (**G**) Mean membrane potential and laser intensity ($n = 53$ APs) from 60 ms preceding peak of AP to 20 ms after. AP is driven by a significant increase in laser intensity shortly ($\sim$23 ms) before its peak. These experiments were performed with Ann Go.

5.4 Discussion

We have shown that holographic projection with high-speed temporal gating via a DMD overcomes the 2D limitation of galvanometer-based laser scanning systems and the poor temporal resolution of SLM-based holographic projection systems for 2P uncaging of neurotransmitters. The DMD allows independent control of each uncaging spot in a SLM-generated photostimulation pattern and offers a convenient way to eliminate the zero and higher diffraction orders. This method offers unprecedented flexibility in the design of spatio-temporal (or 4D) light patterns for highly localised release of neurotransmitters. It opens up the possibility to study synaptic integration in 3D with high temporal resolution. Since holographic projection allows easy positioning of photostimulation sites along the dendritic arbour of neurons, this method enables integration between branches to be directly investigated. This is especially important since the extensive dendritic arbours of neurons are virtually never entirely in the same imaging plane.

This method can also be applied to the spatio-temporal control of neuronal activity which allows probing of neural coding, i.e. what kinds of spatio-temporal input patterns a neuron responds to. In addition, uncaging may be extended to neuronal populations. By generating a multi-cell holographic stimulation pattern and using the DMD to sequentially evoke suprathreshold 2P activation of neurons in a population, connections to a patched neuron can be determined. This facilitates a fast method for finding connected pairs, for instance. This multiplexing technique may also be used for population calcium imaging in the study of network activity [Ducros et al., 2013] and the interaction between different sub-networks. Another potential field of application for these 4D light patterns is optogenetics. By using sculptured light to activate specific subnetworks of genetically labeled neuronal populations, an even higher degree of selectivity can be achieved than is possible with traditional optogenetic approaches alone [Liu et al., 2012, Lovett-Barron et al., 2012].

Relation to other work The basic component of holographic projection is a phase-only liquid crystal (LC) SLM encoded with a computer-generated phase hologram. The response time of the LC is dependent on its phase retardation rate, which relates to the operating wavelength of the SLM ([Wu, 1986]. This response time is typically ∼10 ms, but addressing via computer video output further limits the temporal resolution to ∼30 ms. There have been several attempts to increase the response time of SLMs [Dayton et al., 2001, Kirby and Love, 2004], but no technique using spatially addressable SLMs has achieved multi-level phase-only modulation to perform a full OFF-ON-OFF cycle of the hologram at sub-millisecond timescales. High-speed hologram transition has recently been demonstrated using a device with an extended phase map of up to 4π and choosing the minimum route in phase shift for each

pixel in between transitions [Thalhammer et al., 2013]. This technique allows for one-way transitions of 1-3 ms. An iterative hologram optimisation routine is necessary to improve the diffraction efficiency with the reduced phase representation of the hologram. While this technique can potentially be applied to 4D photostimulation, changing the hologram introduces spurious light patterns during hologram transitions, which could result in unwanted uncaging. Although a high-speed shutter or an acousto-optic deflector can be used to turn OFF the light during transitions, the projection of zero and higher diffraction orders can still pose a potential issue when the hologram is ON especially when the iterative optimisation routine does not produce an efficient hologram for a specific stimulation pattern.

Holographic projection with binary phase modulations (0 and π) has been demonstrated recently for the study of neuronal circuits [Reutsky-Gefen et al., 2013]. SLMs employing ferro-electric LCs have fast response times ($\sim$0.5 ms). However, binary holograms produce mirror projections of equal light intensity in addition to the zero order. This reduces the power available for stimulation (after blocking zero order and mirror projection) to significantly less than 40%. While such a technique can well be applied for 1P excitation, either for optogenetics or uncaging, its low optical throughput can be an issue when applying the technique to 2P uncaging in 4D. Moreover, even for a fixed number of foci, global changes in the binary hologram impact the intensity level of each focus and could introduce variable 2P uncaging responses. Changing the number of foci necessitates dynamic control of the laser intensity affecting both 1P and 2P uncaging modes.

Our technique uniquely distinguishes itself from existing techniques in that it uses a conventional phase-only SLM with slow refresh rate combined with a DMD, which enables independent gating of the holographically projected multiple foci at high speeds. Here, the SLM first modulates the phase of the incoming laser beam to generate the desired multi-focal spatial profile before the DMD allows each focus to be individually turned ON or OFF. Thus, there is minimal loss of laser intensity compared to the method of using DMDs to remove unwanted light from a wide-field illumination to shape the excitation light [Bednarkiewicz et al., 2008, Zhu et al., 2012].

Future directions The DMD array size sets a minimum lateral distance between two uncaging sites for independent gating. For an array size of 15, the minimum distance is 6.5 μm. This is a soft limit as glutamate uncaging has a much narrower profile (0.8 ± 0.1 μm lateral FWHM) and considerable overlap between two DMD arrays is needed to induce 2P uncaging in the OFF site. However, we can further decrease this distance with a slight adjustment in the optical system. By replacing the FT lens (see

L_{FT} in Figure 5.1A) between the SLM and DMD with one with a shorter focal length, we can achieve smaller foci on the DMD and consequently require smaller DMD array sizes for gating. This, however, will increase the incident power density level on the DMD and will require high-tolerance mirror coatings to prevent damage.

Our system uses a DMD (DLP3000) from an evaluation module (DLP LightCrafter, Texas Instruments). We retained only the components in the module necessary to address the bare DMD via the video interface and removed the other components (e.g. light source and projection lenses). The DMD is electronically driven at 1440 Hz when delivering the uncaging binary pattern via the computer's digital video output. This rate can be increased up to 4 kHz (250 μs) when 96 frames are preloaded onto the onboard memory of the DMD's driver circuit but this would give a total of only 24 ms of stimulation. Alternatively, one can use more advanced DMD systems (e.g. DLP V-module, ViALUX), which are capable of switching rates of up to 22 kHz. One limitation in this work is the low damage threshold of the DMD component itself. Blockade of AMPA receptor desensitisation with cyclothiazide allowed us to reduce the laser intensity for uncaging. In the integration experiments (Figure 5.5), long pulse durations (3 ms) were utilised to further reduce laser intensity and minimise damage to the DMD with repetitive stimulation. Since it is not designed for use with high power light sources (e.g. lasers), illuminating the DMD for long periods with focused laser spots damages the device. Such a technical constraint could be overcome by custom fabricating DMDs with specific mirror coatings to tolerate higher power levels. In this work, the DMD was potentially stretched to its limits by positioning it in the Fourier plane where the holographically projected foci from the 2P laser were incident. Long sequences of spatio-temporal stimulation patterns are not possible with the current device due to photodamage of the array. Nonetheless, even with the limits of the current device it is apparent that the synergistic combination of SLM and DMD can be applied to the study of synaptic integration.

In summary, holographic projection using a SLM combined with high-speed temporal gating via a DMD allows the generation of random spatio-temporal stimulation patterns in 3D with sub-millisecond temporal resolution, and in this way offers unprecedented flexibility in the design of 4D light patterns for highly localised release of neurotransmitters. Implementing this approach opens up a wide range of prospects for the study of neuronal circuits.

Chapter 6

Operant conditioning of single neuron activity

6.1 Introduction

Up to this point, we have studied the biophysical and integrative properties of dendrites and seen how these enrichen the computations performed by single neurons. A shortfall however of these approaches however, is their *ex vivo* setting. How can we study integration *in vivo*, where neurons receive much more synaptic input and are under additional neuromodulatory drive [Destexhe et al., 2003, Seamans and Yang, 2004]? Furthermore, if we can modulate the neural activity what do we hope to learn about single neurons and their interaction with surrounding neurons *in vivo*? In Chapter 5 we discussed uncaging approaches for activating neurons by mimicking their synaptic input. Stimulation with electrodes or optogenetic modulation [Boyden et al., 2005] are two other approaches, however these methods all share a caveat in that they represent artificial means for modulating network activity.

Here we describe an operant conditioning task as an alternative approach to impose a constraint on neural activity *in vivo*, by presenting rewards only when a pre-defined pattern of neuronal activity occurs. Leveraging two-photon microscopy [Svoboda and Yasuda, 2006] and genetically-encoded calcium indicators [Chen et al., 2013b], we demonstrate operant conditioning of single neuron activity with simultaneous imaging of hundreds of neurons in the surrounding population. The behavioural paradigm we present is analogous to neuroprosthetic learning [Carmena, 2013] and shares similarities with a series of early studies successfully demonstrating operant conditioning of neural activity based on extracellular recording [Fetz, 1969, Fetz and Finocchio, 1971]. In these studies, the activity of single cortical neurons recorded by microelectrodes was conditioned by reinforcing elevated firing rates with delivery of a reward. More re-

cent developments in neuroprosthetic learning have included electrode recordings of neural activity from larger ensembles involving up to hundreds of neurons [Taylor et al., 2002, Carmena et al., 2003, Velliste et al., 2008] and imaging approaches to track neural activity in real-time [Clancy et al., 2014, Hira et al., 2014]. Drawing on these developments and to demonstrate the utility of our experimental paradigm, we relate the dynamics of single neurons undergoing operant conditioning to the activity of the surrounding population, and characterise how functional plasticity of the conditioned neuron is correlated with behavioural learning. In particular, we seek to determine whether learning is based solely on the activity of the single conditioned neuron, or whether many neurons in the network increase their activity during training. The work presented in this chapter was undertaken in collaboration with Diego Gutnisky (design and implementation of behavioural paradigm), with assistance from Nick Sofroniew (configuration of two-photon microscope), Simon Peron (image analysis), Vijay Iyer (ScanImage programming) and Bryan MacLennan (animal surgeries). All experiments and analyses reported were performed by the author.

6.2 Methods

Mice and water restriction

We used C57BL/6 mice, aged between 2 and 4 months old. Mice were housed separately in cages with bedding in a reverse light cycle room and kept under water restriction of 1-1.5 mL of water per day. The total water provided to mice each day was comprised of the water consumed during any behavioural sessions and supplemental water. The weight gained during behavioural sessions was used as an estimate of the volume of water consumed during the session and the amount of supplemental water provided was adjusted accordingly. All animal procedures were in compliance with protocols approved by the Janelia Farm Research Campus Institutional Animal Care and Use Committee.

Surgical procedures

Head post surgery was performed as previously described [O'Connor et al., 2010]. Mice were implanted with a titanium head post (22.5 mm length, 3.2 mm width) for head fixation and mounting in the behavioural apparatus. Mice were anaesthetised with isofluorane (1-2% by volume in O_2; SurgiVet, Smiths Medical) and maintained at 37°C on a thermal blanket (Harvard Apparatus). Marcaine (50 μL, 0.5%) was injected under the scalp prior to removal of the scalp and periosteum over the dorsal surface of the skull. A thin layer of cyanoacrylate adhesive (Krazy glue, Elmer's Products Inc.) was then applied to the skull. The head post was attached to the skull with dental acrylic (Jet Repair Acrylic, Land Dental Manufacturing, P/N 1223). Buprenorphine HCl (0.1 mg/kg, i.p.; Bedford Laboratories) was used for postoperative analgesia. Ketoprofen (5 mg/kg, s.c.; Fort Dodge Animal Health) was used at time of surgery postoperatively to reduce inflammation. Mice were allowed at least three days to recover from surgery before being placed on water restriction.

Cranial windows and viral injections

Cranial window surgery and viral injections were performed at the same time as head post surgery. A circular craniotomoy (2-3 mm diameter) was made above anterior lateral motor cortex (ALM; 1.5 mm lateral to midline, 2.5 mm anterior to bregma). AAV1 *syn*-GCaMP6f (Penn Vector Core #Av-1-PV2822) or AAV1 *syn*-GCaMP6s (Penn Vector Core #Av-1-PV2824) was injected using a home-made injector into ALM of anaesthetised mice. Injections were administered in 300 μm intervals on a 3×3 grid. 20 nL of virus was injected over 80 seconds at a depth of 450 μm at each injection site. A cranial window was then placed over the craniotomy. Both pyramidal and GABAergic neurons were labelled using this approach. Imaging and behavioural training started 2-3 weeks after window implantation and viral injection.

Data acquisition and experimental control

The entire experimental apparatus was coordinated in a real-time environment by BControl software (Z. Mainen, C. Brody, Cold Spring Harbor Laboratory, Cold Spring Harbor, NY, `http://brodywiki.princeton.edu/bcontrol/index.php/Main_Page`) on a real-time Linux system (`code.google.com/p/rt-fsm`). The behavioural control was implemented on a separate system by a MATLAB (Mathworks) graphic user interface (GUI) running on Windows XP, and communicated with the real-time system over Ethernet and additional interfaces with PCI-6229 and PCI-6713 data acquisition boards (National Instruments) using COMEDI drivers (`comedi.org`; [O'Connor et al., 2010]). The real-time system executed a module of C code at 6 kHz that read and wrote digital and analog voltages on the data acquisition boards for monitoring the sensors and controlling the actuators on the apparatus. Data was sent back from the real-time system to the MATLAB system for logging, refreshing the GUI at 4 Hz. The MATLAB GUI was also used to initiate and terminate sessions on the real-time system, trigger water delivery, and specify the trial type and structure.

Imaging and real-time analysis

The two-photon imaging system used has been described previously ([Huber et al., 2012]). A Ti-Sapphire laser (MaiTai-HP, Spectra Physics) tuned to 1000 nm was used for excitation. Microscope control and image acquisition were performed by *ScanImage* (`http://vidriotechnologies.com/` [Pologruto et al., 2003]) running on a Windows 7 machine. Imaging was performed through a 16 × 0.8 NA microscope objective (Nikon) and photons were detected using GaAsp photomultiplier tubes (10770PB-40, Hamamatsu). The microscope was equipped with a piezo focuser (Physik Instrumente) for positioning the objective in the z axis and a resonant-galvo module (Thorlabs) for scanning in the lateral xy dimensions. Together, these enabled fast multi-plane imaging. The field of view was 300 μm × 300 μm (512 × 512 pixels) over 3 planes separated by 25 μm in the z-axis, imaged at 7.8 Hz per plane. Average imaging power was <40 mW, measured at the back aperture of the objective.

Real-time image analysis was performed by C++ code and a GUI written in Qt (ReTiNA) running in parallel with ScanImage. To correct for brain motion, a simple real-time cross-correlation based image registration process using fast Fourier transforms was implemented. A reference image for image registration as well as region of interest (ROI) selection was obtained at the beginning of each behavioural session by aligning and stacking an image sequence obtained over a minute while the animal was actively behaving. Visually-identified soma were selected as ROIs, and semi-automated ROI segmentation was performed as in

[Chen et al., 2013b]. Once the reference image was obtained, images newly acquired in ScanImage were shuttled to ReTiNA in real-time by memory mapping for immediate registration. This approach also allowed the field of view from previous sessions to be easily relocated. Following registration, the neural activity in the pre-segmented ROIs was extracted. The calcium dynamics in the ROIs was estimated by $dF/F_0 = (F - F_0)/F_0$, where F was the instantaneous pixel intensity and F_0 was continually updated as a rolling moving average of the lowest 10% pixel values over the previous 5 minutes. The activity of one randomly-selected ROI was then logarithmically mapped to a sound frequency command that was immediately sent to an Arduino-based sound server.

Sound server

An Arduino Due microcontroller board was used to integrate the trial structure and ROI activity from the various systems and was responsible for producing an appropriate feedback sound signal. The Due was coupled to a direct digital synthesizer (DDS, AD9833, Analog Decives), which in turn generated a frequency input to a speaker. The Due received and integrated inputs from the real-time system via an analog voltage command, the MATLAB behaviour GUI system via Ethernet, and ReTiNA also via Ethernet. Together, these three inputs determined when and what frequency tone would be generated by the Due. The MATLAB behaviour system conveyed to the Due what type of behavioural trial was occurring, the real-time system indicated what the trial structure was and what the current stage of the trial was, while ReTiNA delivered the frequency command related to the ROI activity.

Spherical treadmill

We used the same spherical treadmill apparatus described previously [Sofroniew et al., 2014]. A smooth foam ball (Plasteel; 16 inch diameter, Ball no. 183), obtained in hollow halves with initial wall thickness of 19.5 $\pm$ 0.2 mm (weight 121.3 $\pm$ 0.5 g), was carved on the inside with a hot wire system (Hot Wire Foam Factory) to reduce the wall thickness to 3.79 $\pm$ 0.66 mm. The halves were then glued together with expanded polystyrene foam glue (Hot Wire Foam Factory; Foam Clu, no. 028B-8), giving a total weight of 82.5 g. The ball was elevated by 10 Ping-Pong balls (JOOLA Gold 3-Star 40 mm) in air cannons. Each air cannon consisted of a 1.577 inch diameter acrylic tube plugged at one end with acetyl resin base plate containing a tube fitting (McMaster Carr, no. 50745K15) for air flow. The ball was seated in a custom 19 inch diameter acrylic ribbed bowl with air cannons positioned around the lower half. One cannon was located beneath the ball, three cannons on a ring at latitude 60°S, and six on a ring at latitude 20°S. Airflow to the bottom cannon, the cannons at 60°S, and two groups of cannons at 20°S was controlled independently with regulators (McMaster Carr, nos. 3846K29 and 5627K511).

Ball tracking

The ball rotation was tracked using two cameras with chips that measure optic flow (Avago Technologies, ADNS-6090) and have a serial interface to a microcontroller (Atmel, ATMega644p; [Seelig et al., 2010]). The cameras were mounted on the ribbed bowl, one directly in front of the mouse and the other on the right. A 940 nm IR LED (Roithner, ELJ-940-629) was used to illuminate the surface of the ball in front of each camera. The optic flow was measured by each camera at 2 ms intervals and converted into a ball motion vector as previously described [Sofroniew et al., 2014].

Water delivery and lick detection

Water was delivered through a stainless steel tube (0.05 inch outer diameter; Small Parts, HTX-18H-36-10), and water flow was controlled using a solenoid valve (Lee Company, LHDA0533115H). The delivery port was attached to a 3D printed thermoplastic piece and could be positioned by a three-axis stepper motor system (Zaber 3X, NA11B30 and T-JOY3). Licks were detected by an electric detector that was triggered every time a lick completed a circuit [Slotnick, 2009].

Training and behavioural task

Training began after head post implantation surgery, recovery and >7 days of water restriction. Mice were initially handled over several days before being placed into the head-fixation apparatus. In some instances, brief sedation with isoflurane anaesthesia (2% for up to 2 minutes) was used to assist with head fixation. Training was progressive and consisted of four main stages (Figure 6.1A). The first stage involved free, periodic water delivery. The minimum period between successive openings of the water valve was 4 seconds, and was increased to 10 seconds as the mice became more familiar with the lickport. This stage typically lasted between 5 and 10 minutes. The second stage involved periodic water delivery paired with a reward cue. The period between successive water delivery was at least 10 seconds, and was increased up to 20 seconds. We progressed through to the third stage of training once mice licked frequently in response to water delivery. The next stage of training involved presentation of the reward cue and water delivery triggered by licking. Mice were required to lick within 2 seconds of the reward cue and the interval between reward cues was varied from 10 to 20 seconds. Population calcium imaging was commenced from the third stage of behavioural training. The same field of view was imaged across different sessions and days. At the start of each new session, between 20 and 40 neurons were randomly selected in addition to any neurons of interest from the previous session, and the activity of these neurons was monitored in real-time. When mice consistently responded to the reward cue, they were progressed

through to the fourth stage of training. These first three stages typically required one to three days of training.

The fourth stage of training involved providing additional auditory feedback during training. One neuron was randomly chosen from the pool of tracked neurons, based on a lack of observable licking- and movement-related activity, and then used for closed-loop conditioning training with auditory feedback. The structure of the conditioning training is depicted in Figure 6.1B. During the pre-trial period, the dF/F_0 activity of the neuron had to remain below a starting threshold otherwise the trial was aborted. The pre-trial period was followed by the response window, during which the animal was provided auditory feedback on the activity of the neuron. We converted the activity of this neuron to an auditory frequency based on the instantaneous value of the dF/F_0 signal (Figure 6.1C). The dF/F_0 signal was thresholded above and below (Figure 6.1C, top), and linearly mapped to a log-scale of frequency between 3 and 12 kHz (Figure 6.1C, bottom); thus the maximum variation in auditory frequency was two octaves. If the activity of the conditioned neuron increased beyond the reward threshold, the feedback was stopped and a reward cue was provided indicating the start of a brief reward window. A trial was successful if the mouse then licked for water during the reward window. Otherwise, the feedback was continued for up to 20 seconds before ceasing, indicating the end of an unsuccessful trial.

Additional control trials were interleaved with regular trials (probability 0.1 - 0.2) during the fourth stage of training once mice achieved intermediate performance. For random reward trials, no auditory feedback was provided and a reward cue was given at a random time during the response window. The provision of water reward was not contingent on the dF/F_0 trajectory. Random reward trials were included to assess the neural response to licking and reward delivery and also enabled *post hoc* verification that the target neuron was not licking related.

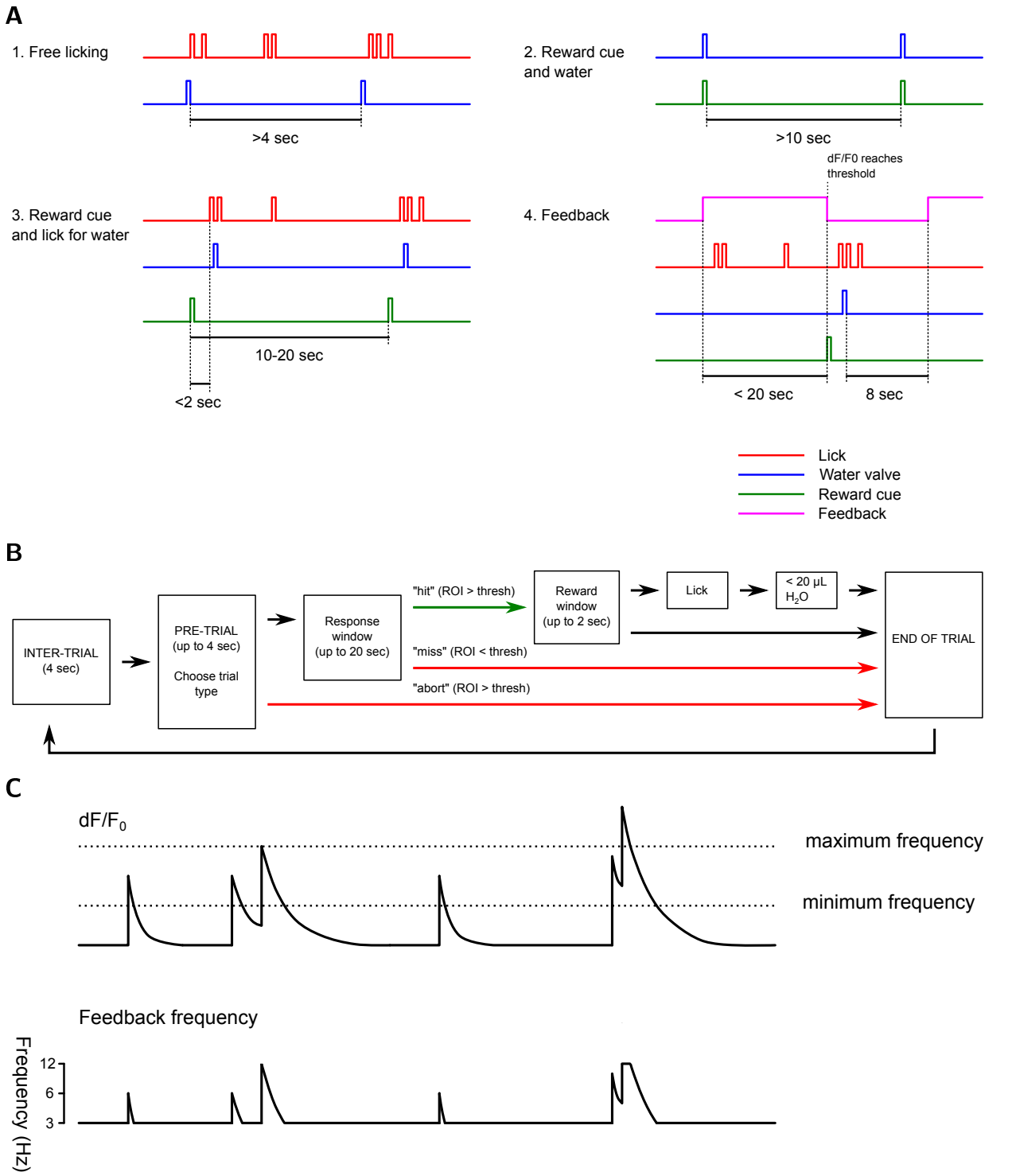

Figure 6.1: Behaviour training. (**A**) Stages of behavioural training. Animals were progressed through four different stages of behavioural training. During the first stage, animals were habituated to the behavioural apparatus (top left). Water was delivered periodically. Following this stage, water was delivered along with a reward cue (top right). During the third stage, a reward cue was provided and water delivery was triggered by licking in a short window after the reward cue (bottom left). The final stage involved closed-loop conditioning of a single neuron (bottom right). During the response window auditory feedback was provided indicating the level of activity of the conditioned neuron. The criterion for water reward was met when the dF/F_0 activity reached a given threshold. Level of coloured lines indicate the status (high or low) of the indicated parameter. (**B**) Block diagram showing sequence of events during feedback trials (see Methods for further details). (**C**) Conversion of dF/F_0 to an audio frequency. The dF/F_0 signal was thresholded above and below and logarithmically mapped to a frequency between 3 kHz and 12 kHz.

6.3 Results

Behavioural training

Our aim was to develop an imaging-based, closed-loop single neuron operant conditioning paradigm to study the dynamics of single neuron and population activity during behavioural learning. Water-deprived mice were head-fixed on a spherical treadmill and trained to voluntarily elevate the activity of a selected neuron in order to receive a water reward. Trials began after a period of activity in the selected neuron below the reward threshold. During this pre-trial 'catch' period, if the neuron activity reached the reward threshold and remained elevated above the threshold for one second the trial was aborted. No specific signal was provided to the mouse when this occurred, apart from lengthening of the effective inter-trial time. The beginning of each trial was marked by the onset of a continuous auditory signal, which provided feedback to the mouse as to the level of activity of the target neuron. Mice had up to 20 seconds from the onset of the feedback period to elevate the activity of the target neuron above the reward threshold (Figure 6.1B) (for details, see Methods). If the reward threshold was not reached during this period, the trial 'timed out' and the continuous auditory feedback was discontinued for the transition to a four second inter-trial period. When the neuron activity reached the reward threshold, the continuous auditory feedback was terminated and a different auditory tone was delivered to signal that a reward was available. Mice received a water reward if they licked within 2 seconds of the reward tone (a 'hit') but no reward was provided otherwise (a 'miss').

To assess the performance, we considered the proportion of hit trials as well as the duration of time taken during hit trials from onset of the feedback signal to the reward delivery (latency to reward). An increase in the proportion of correct trials concomitant with a reduction in the latency to reward was suggestive of learning (Figure 6.2A). In addition to these measures, we also calculated the rate of rewards received by combining the proportion of correct trials with the latency to reward (Figure 6.2B). We considered this composite measure of performance to be more reliable than either measure alone, since we observed sessions where the proportion of correct trials increased without a change in the latency to reward and similarly, other sessions where the latency to reward decreased without a change in the proportion of correct trials. Mice demonstrated an ability to rapidly increase their behavioural performance during individual sessions. The average behavioural performance for all animals showed a tendency for an increase in the reward rate in the first 15 minutes of feedback training (Figure 6.2C,D). However there was significant variability in performance from session to session, since the underlying sessions included those that showed no tendency of learning or improvement in performance, as well as

sessions that displayed strong signs of learning.

Licking and movement on the spherical treadmill

Having demonstrated that mice were quickly able to learn the task, we proceeded to characterise particular behaviours observed during learning. The reward apparatus contained circuitry to detect tongue contacts with the water port i.e. lick events [Slotnick, 2009]. As mice were head-fixed and positioned on a spherical treadmill, we were also able to monitor locomotion on the treadmill, which was reported as the rotational speed of the ball (see Methods for further details). We aligned these behaviours to the onset of feedback and compared the behavioural responses according to the trial outcome (hit or miss) (Figure 6.3). Average lick activity prior to sound onset was low but increased sharply when the feedback commenced. For hit trials, the activity showed two characteristics peaks. There was a sharp, initial response to sound onset, followed by a slower increase in licking corresponding to recipient of the water reward. For miss trials, the initial response to sound onset was also present, but since no reward was received, licking activity ceased after a few seconds. Average movement on the treadmill showed less variability between hit and miss trials and was relatively uniform through most of the trial period. However, at the instance of sound onset, there was a characteristic decrease in movement.

Response of the conditioned neuron

How does the target neuron response to operant conditioning evolve? In the representative example shown in Figure 6.4, the activity of the conditioned neuron is sporadic and unrelated to the timing of the feedback signal during early trials at the start of training (Figure 6.4A). With progression through the session, the target neuron becomes more consistently activated at the onset of the feedback. Furthermore, the response of the target neuron to feedback is more intense later in the session (Figure 6.4A) with a mean event rate 2 seconds after onset of feedback of 0.32 events/sec in the first 25% of trials compared to 0.72 events/sec in the last 25% of trials ($p < 0.05$). Comparing the activity of the target neuron between hit and miss trials (Figure 6.4B,C), the average elevation in activity at onset of feedback is significantly greater during hit trials, with mean area under the dF/F_0 curve of 0.56 for hit trials compared to 0.19 for miss trials ($p < 0.001$). Even on miss trials, the activity showed elevations after onset of feedback, but these did not meet the reward criterion. On both hit and miss trials, there was significant variation in the dF/F_0 amplitude and time course from trial to trial (shown by the shading in Figure 6.4C), despite the strong modulation of the target neuron on both hit and miss trials.

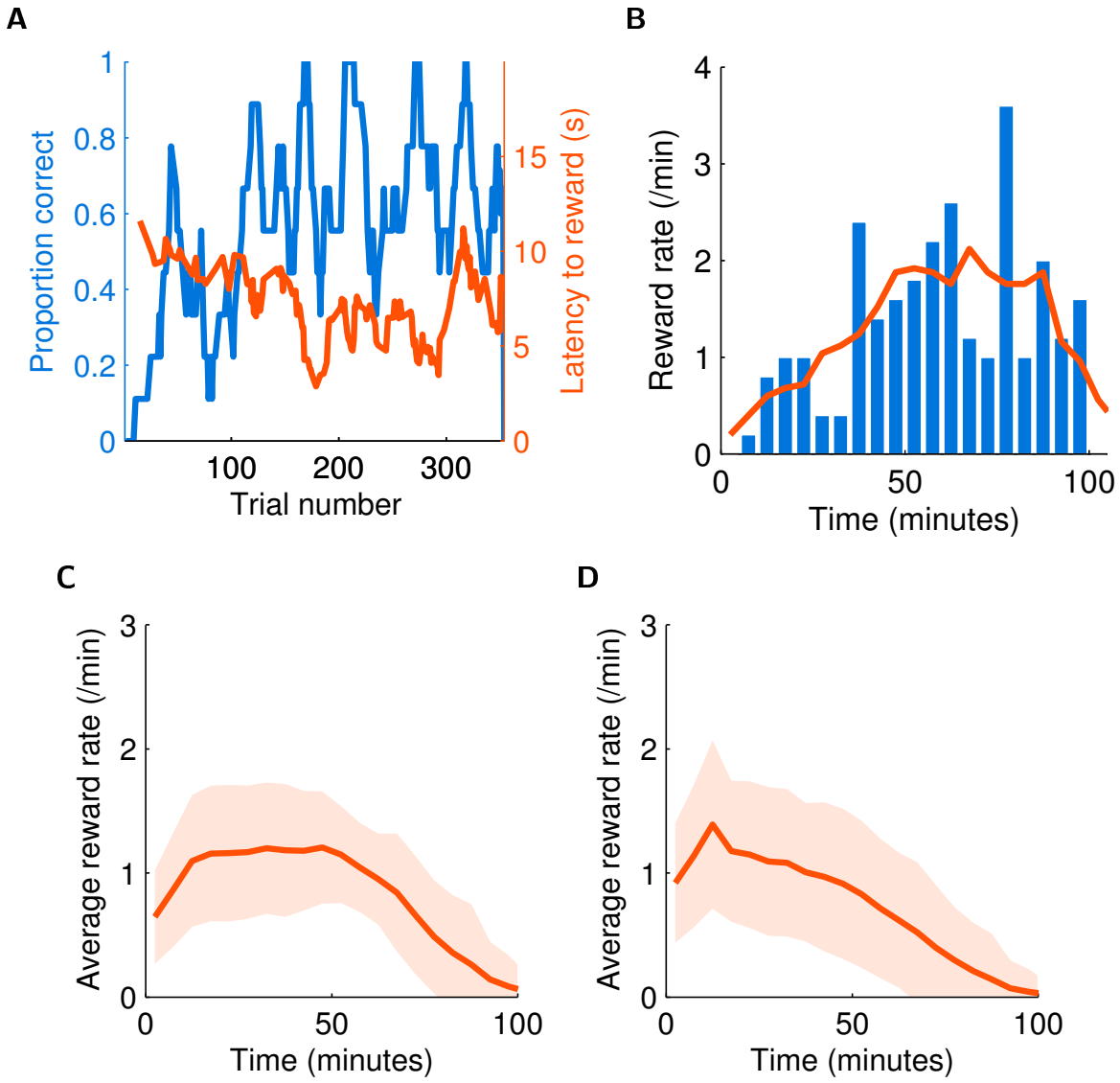

Figure 6.2: Behavioural performance improves with learning. (**A**) Example of behavioural performance during a single training session demonstrating how the proportion of trials correct (blue) increases and the latency to reward (red) decreases with behavioural training. (**B**) Example of the reward rate in a single training session, as a composite measure of behavioural performance combining the proportion of trials correct and the latency to reward. With training, the reward rate also increases. The histogram (blue) shows the average number of rewards in 5 minute bins and is overlaid by a smoothed reward rate (red). (**C**) The reward rate, as a composite measure of behavioural performance combining the proportion of trials correct and the latency to reward. The average behavioural performance is taken across multiple sessions in a single animal (n = 12 sessions). Shaded region indicates ± 1 standard deviation. (**D**) The average behavioural performance taken across multiple sessions showing learning in different animals (n = 29 sessions in four mice). Shaded region indicates ± 1 standard deviation.

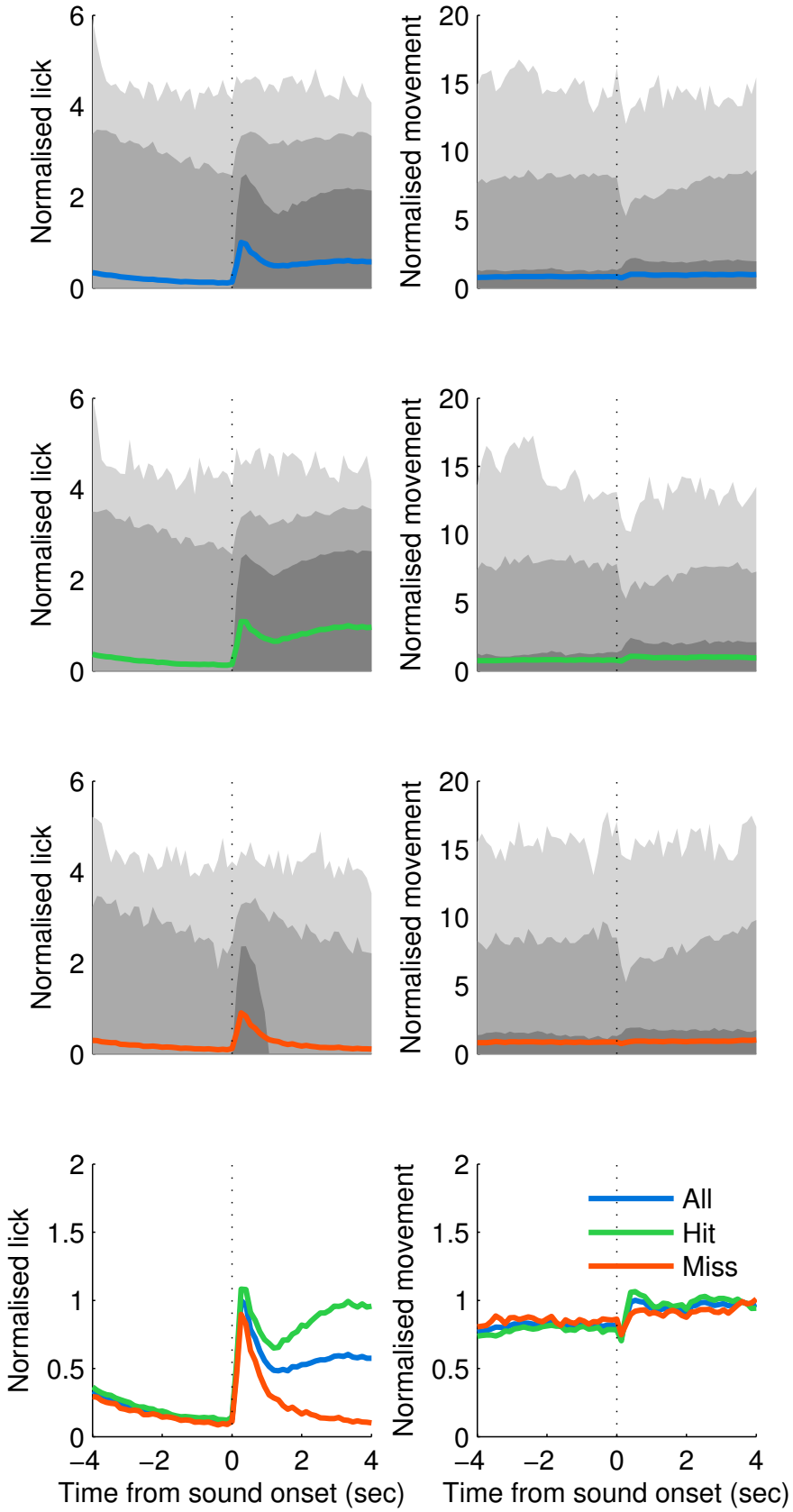

Figure 6.3: Characteristics of licking behaviour and locomotion on the spherical treadmill. The average normalised licking behaviour (left column) and movement on spherical treadmill (right column) are shown. Top row, all trials (n = 3652 trials); second row, hit trials (n = 2024 trials); third row, miss trials (n = 1628 trials); last row, mean traces The shaded regions represent percentile responses corresponding to the 16-84%-tile (dark grey), 5-95%-tile (medium grey) and 1-99%-tile (light grey).

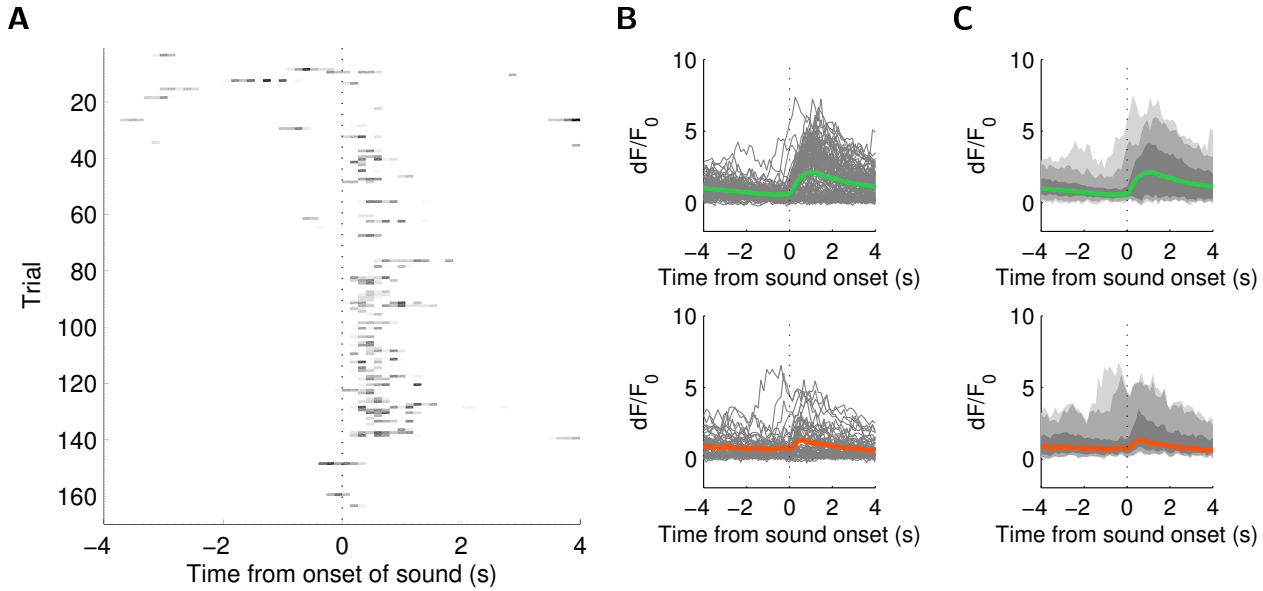

Figure 6.4: Activity of the target neuron reliably increases after onset of feedback. (**A**) Fluorescence activity of the conditioned neuron during progression of a training session. (**B**) Fluorescence activity of the conditioned neuron during *hit* (top, $n = 104$ trials) and *miss* (bottom, $n = 56$ trials) trials. Mean activity is shown in green (hit trials) or red (miss trials), individual trials are shown in grey. (**C**) Distribution of the dF/F_0 response of the target neuron. The shaded regions represent percentile responses corresponding to the 16-84%-tile (dark grey), 5-95%-tile (medium grey) and 1-99%-tile (light grey). Mean activity is shown in green (hit trials) or red (miss trials), individual trials are shown in grey.

Analysis of random reward trials

We observed a strong tendency for mice to start licking at the onset of feedback (Figure 6.3), which occurred together with an increase in the activity of the target neuron (Figure 6.4). The coincidence of these two events suggests there may be a association between licking and activity in the target neuron, which would be the case if the target neuron was lick-related. To delineate between a lick-related neural response and neural activity coincident with licking, in each session, we included a small proportion of trials involving random delivery of a reward cue and water reward in the absence of additional auditory feedback (Figure 6.5). For these trials, reward delivery was not contingent on the activity of the target neuron reaching the reward threshold (compare Figure 6.5A, top with Figure 6.5B, top), but was triggered by licking after presentation of the reward cue. Since no auditory feedback was provided to signal the commencement of the trial, mice did not anticipate the reward cue. In contrast to normal trials, where licking commenced before valve opening (Figure 6.5A, middle), in random reward trials mice only licked once the reward cue had been presented (Figure 6.5B, middle). In these trials, there was no increase in activity in the target neuron that is associated with licking, which demonstrates that the target neuron is not simply responding to licking. Additionally, for both normal trials and random reward trials, reward delivery was associated with a decrease in movement on the spherical treadmill (Figure 6.5A,B, middle). Taken together, these results show how random reward trials enable differentiation between lick-related responses triggered by onset of feedback and neural activity coincident with licking. Furthermore, these trials provide a means to verify that the target neuron is not lick-related.

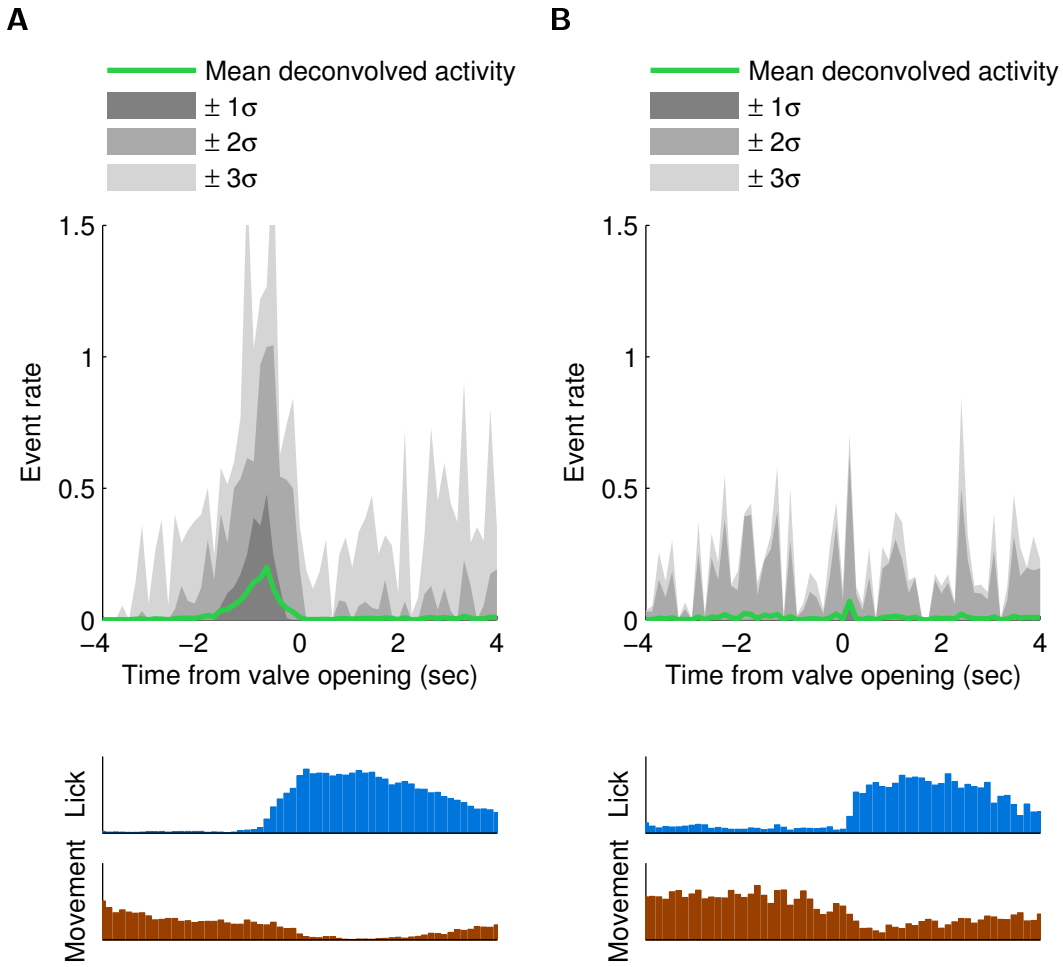

Figure 6.5: Random reward trials distinguish lick-related neural activity from activity coincident with licking. (**A**) Normal trials ($n = 154$) and (**B**) random reward trials ($n = 40$) showing the average activity of the target neuron (green) in an 8-second time window surrounding opening of the water valve (top). The shaded regions represent percentile responses corresponding to the 16-84%-tile (dark grey), 5-95%-tile (medium grey) and 1-99%-tile (light grey). Average licking (middle) and locomotion on the spherical treadmill (bottom) for corresponding trials are also shown.

Specificity of response in target neurons

We next investigated how much the neural activity is modulated by the onset of feedback. Since the training paradigm required the activity of the target neuron to be low prior to onset of feedback and elevated after onset of feedback in order for the animal to be rewarded, we defined a neuron's *responsiveness* as the ratio of its activity in the 2 seconds after to the activity in the 2 seconds before onset of feedback. We observed that in sessions where mice demonstrated strong evidence of learning, the responsiveness of the target neuron reached values significantly greater than one later in the session, even if early in the session the ratio was less than one when behavioural performance was poor (Figure 6.6A-C).

While the responsiveness of the conditioned neuron increases with training, how does it compare with the responsiveness of other neurons in the population? To investigate how specific the change in responsiveness was for the conditioned neuron, we ranked neurons by their responsiveness in comparison to other neurons in the population and assessed how the rank of the conditioned neuron varied with training. A lack of change in rank of the conditioned neuron with learning would suggest a global learning mechanism whereby a large proportion of neurons in the population is activated by feedback. On the other hand, an increase in rank is consistent with the view that operant conditioning specifically enhances activation of the conditioned neuron but does not rule out the neuron being part of a larger subpopulation that is also activated. We found that learning was associated with an increase in rank of the responsiveness of the conditioned neuron (Figure 6.6D). Such modulation of target neurons is consistent with the notion that conditioning led to specific activation of a subset of neurons and animals did not employ a global strategy for activating large numbers of neurons.

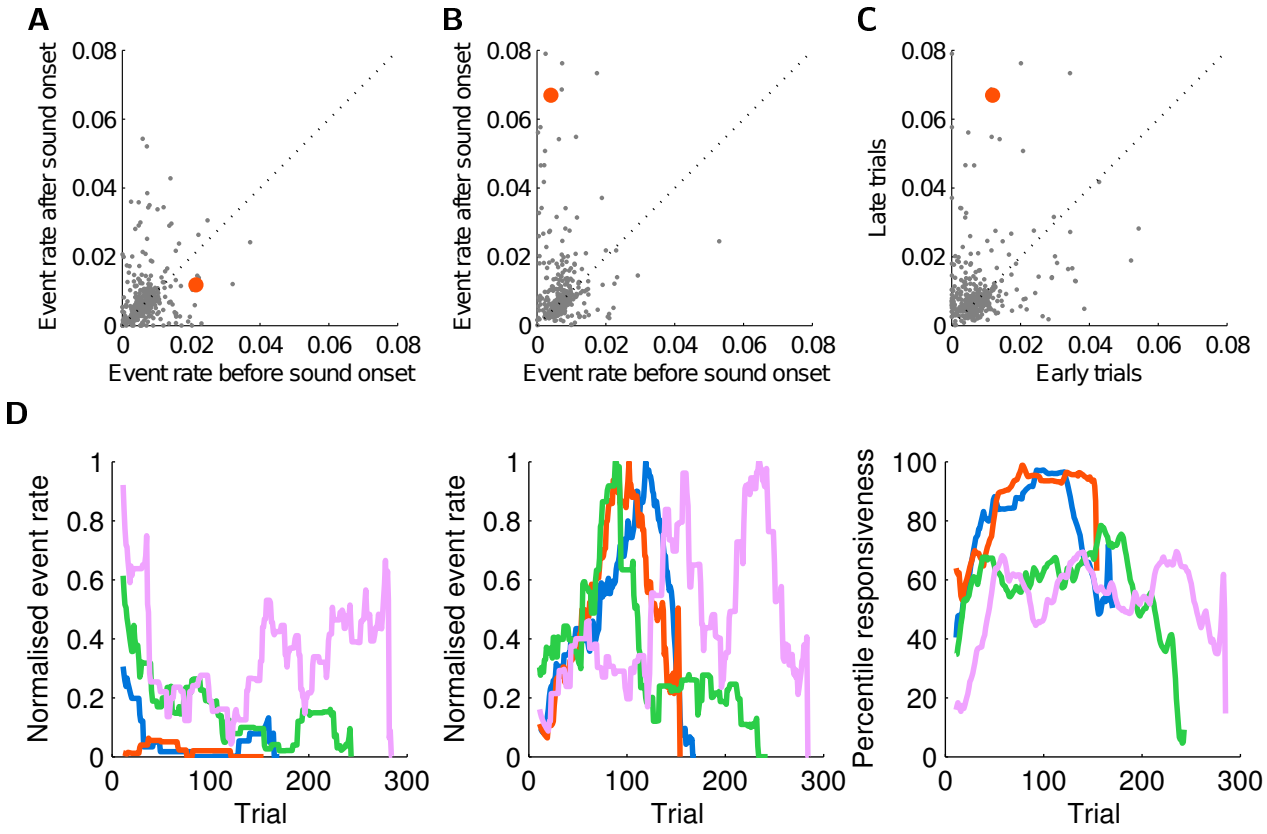

Figure 6.6: Responsiveness of the conditioned neuron increases with behavioural training. (**A**) Change in event rate of neurons in a time window 2 seconds before compared to 2 seconds after the onset of feedback during early trials in the learning session (first 20 trials). The mean event rate after onset of feedback is plotted against the mean event rate before onset of feedback. The conditioned neuron is denoted by red, all other neurons in grey ($n = 344$ neurons). (**B**) Change in event rate of neurons in a time window 2 seconds before compared to 2 seconds after the onset of feedback during late trials in the learning session (last 50 trials). The mean event rate after onset of feedback is plotted against the mean event rate before onset of feedback. The conditioned neuron is denoted by red, all other neurons in grey ($n = 344$ neurons). (**C**) Change in event rate in a time window 2 seconds after onset of feedback, early trials in the learning session compared to late trials. The mean event rate during late trials is plotted against the mean event rate during early trials. The conditioned neuron is denoted by red, all other neurons in grey ($n = 344$ neurons). (**D**) Change in rank responsiveness of the conditioned neuron ($n = 4$). Normalised average event rate of target neuron in the 2 seconds before (left) and after (middle) onset of feedback. With progress in the training session, the rank responsiveness of the conditioned neuron increases (right). Each colour represents a different conditioned neuron.

Diversity of responses in the population

We observed that while the activity of conditioned neurons was elevated at sound onset, the activity of other neurons in the population showed more variability (Figure 6.6). Some neurons also displayed elevations in their activity, while others showed no change in activity or even a reduction in activity at the onset of feedback. Based on these observations, we classified neurons into one of three groups depending on the relative change in activity during the 2 seconds before onset of feedback and during the 2 seconds after. Neurons whose average activity increased by at least 40% were classified as *activating* neurons, neurons whose average activity decreased by at least 40% were classified as *deactivating* neurons, while the remaining neurons were classified as *non-responsive* neurons (Figure 6.7B). We further separated the activity of these ensembles during hit and miss trials (Figure 6.7C-E). While the activity of the activating ensemble increased significantly more during hit trials (Figure 6.7C), the activity of the other two groups were similar during both hit and miss trials (Figure 6.7D,E). Since licking activity was also more vigorous during hit trials (Figure 6.3), the activating group may simply represent licking behaviour. Even with this classification, there was a degree of heterogeneity within the different groups, with respect to the precise timing of the changes in activity. For example, some neurons in the activating group showed very fast increases in activity after sound onset, while other neurons showed slower increases in activity (Figure 6.7F).

An important advantage of population calcium imaging is the ability to compare the spatial differences in the way neurons behave. Accordingly, we next set out to characterise the spatial relationship between the conditioned neuron and neurons in the three response categories described above. For each imaging volume, we binned the radial distance from the conditioned neuron and counted the number of neurons from each response category in each radial distance bin. Each radial distance bin is therefore represented by an annulus of fixed width, with inner and outer radii corresponding to the lower and upper limits, respectively, of the radial distance bin. Comparing the spatial distributions of neurons belonging to the different response categories, we observed a similar spatial distribution of neurons in each of the categories. For this analysis we did not normalise counts to the radial distance when estimating the density of neurons. The increase in probability of finding neurons further away from the conditioned neuron (Figure 6.7G) arises because the area of the annulus increases with the radial distance. While normalising for radial distance may allow comparisons between different fields of view and different animals, imaging conditions were not sufficiently uniform to enable such comparisons. For example, GCaMP6 expression displayed variation between animals, and the presence of blood vessels in the field of view also obscured visualisation of some neurons. Nevertheless, this analysis suggests that neural responses showed a homogeneous spatial

distribution, with no evidence of spatial clustering of responses.

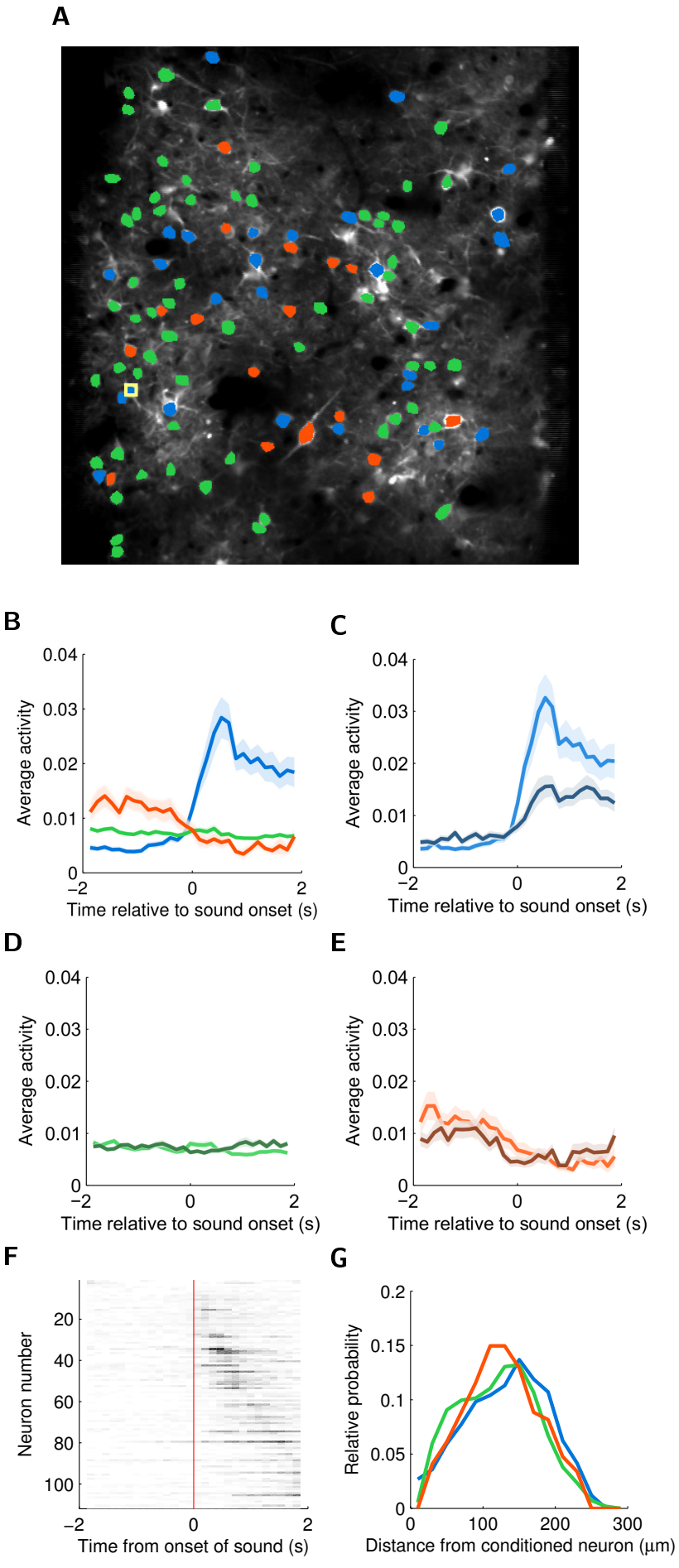

Figure 6.7: (Caption next page.)

Figure 6.7: Diversity of neural responses in the population. (**A**) Example imaging field showing ROIs shaded according to response group. Conditioned neuron indicated by yellow box. (**B**) Average fluorescence activity of the three response groups, activating ($n = 112$ neurons; blue), deactivating ($n = 49$ neurons; red), non-responsive ($n = 184$ neurons; green). Shaded error bars denote s.e.m. (**C**) Average fluorescence activity of activating neurons during hit (light blue) and miss (dark blue) trials ($n = 112$ neurons). Shaded error bars denote s.e.m. (**D**) Average fluorescence activity of non-responsive neurons during hit (light green) and miss (dark green) trials ($n = 49$ neurons). Shaded error bars denote s.e.m. (**E**) Average fluorescence activity of deactivating neurons during hit (light red) and miss (dark red) trials ($n = 184$ neurons). Shaded error bars denote s.e.m. (**F**) Average fluorescence activity of individual neurons in activating group. Neurons are sorted in ascending order of time to peak fluorescence. (**G**) Relative probability of finding a neuron from the three different groups versus the distance from the conditioned neuron.

Although we were imaging in ALM, an area involved in pre-motor planning for licking activities [Komiyama et al., 2010, Guo et al., 2014], other motor activities such as locomotion on the spherical treatmill were also represented in the neural activity (Figure 6.8A). Since we monitored both licking and movement on the treadmill, reported as the rotational speed of the treadmill, we were able to identify epochs of neural activity in some neurons that were distinctively correlated with physical behaviour (Figure 6.8A). Despite the clear correlations, it was also evident that neurons did not respond with absolute reliability during licking or movement epochs. When we calculated the correlation between the activity of individual neurons and both licking and running, we found a wide distribution of correlation strengths (Figure 6.8B). While some neurons were strongly correlated with either or both behaviours, many neurons in fact showed weak or negative correlations with behaviour.

To extend the analysis, we explored the temporal evolution of behavioural correlations during a training session. We evaluated a coincidence measure in several steps. We first normalised the licking and movement traces, as well as the dF/F_0 traces of all imaged neurons. To calculate the coincidence, for each time point we multiplied the normalised traces together and then applied a temporal smoothing filter using an exponential moving average (EMA) with a time constant of two minutes. For example, to obtain the coincidence with licking, for each neuron in the dataset the normalised dF/F_0 trace was multiplied with the normalised lick trace before the EMA was applied. In Figure 6.8C we show how the distribution of the coincidence measures across all neurons evolves during a training session. To compare how these coincidence measures evolve with training, we also ranked the target neuron against the rest of the population. As the target neuron is more robustly activated with training, the rank of dF/F_0-lick coincidence of the target increased throughout a session, while by comparison, dF/F_0-movement coincidence showed strong fluctuations through the training session and no clear trend. Across multiple animals, we observed a characteristic increase in dF/F_0-lick coincidence rank (Figure 6.8D, left) that remained elevated through to the end of the training session, even when behavioural performance had already deteriorated entirely by the latter stages of the session (Figure 6.8D, right). In contrast, dF/F_0-movement coincidence rank showed strong fluctuations throughout the session and did not follow any clear trends (Figure 6.8D, middle). This finding suggests that conditioning establishes and maintains a coupling between activity in target neurons and licking behaviour, even when motivation to perform for water reward diminishes by the end of training sessions.

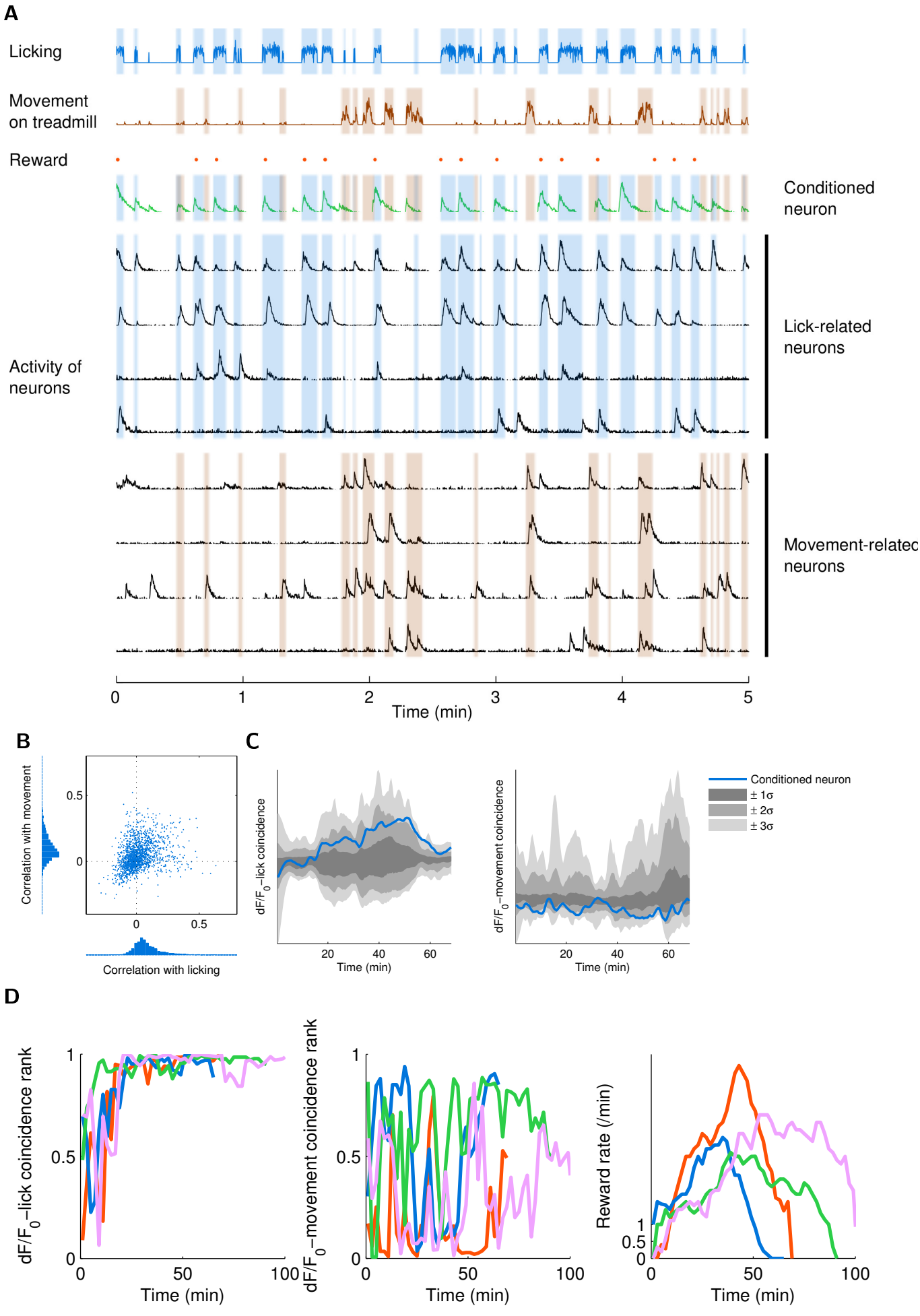

Figure 6.8: (Caption next page.)

Figure 6.8: Correlations of neural activity with movement and licking. (**A**) Example traces of licking and movement on the spherical treadmill, and the corresponding dF/F_0 traces (normalised by standard deviation) of the target neuron (green) and other selected neurons (black). (**B**) The activity of ROIs showed variable correlation with movement and licking ($n = 1651$ ROIs). (**C**) Examples showing how dF/F_0-lick coincidence (left) and dF/F_0-movement coincidence (right) vary during a single training session. The coincidence measure for the target neuron is shown in blue. The shaded regions represent percentile responses of the population, corresponding to the 16-84%-tile (dark grey), 5-95%-tile (medium grey) and 1-99%-tile (light grey) ($n = 345$ neurons). As the session progresses, the dF/F_0-lick coincidence of the conditioned neuron reaches values above the 95th percentile of the population, while the dF/F_0-movement coincidence does not reach the same upper extremes. (**D**) Evolution of the dF/F_0-lick (left) and movement (middle) coincidence rank of the conditioned neuron throughout a training session ($n = 4$ sessions from different animals). The dF/F_0-lick coincidence rank of the conditioned neuron increases during a training session and remains elevated until the end of the session (left). In contrast, the dF/F_0-movement coincidence rank of the conditioned neuron shows no clear trend. The reward rate during each of these sessions show a characteristic increase followed by a decrease as animals become satiated by the end of each session (right). Each colour corresponds to a different conditioned neuron.

6.4 Discussion

In this chapter we demonstrate an optical brain-machine interface for operant conditioning based on the activity of single neurons. Water-deprived mice were trained to voluntarily increase the activity of a selected neuron in order to receive a water reward. Mice showed the ability to quickly learn the behavioural task, reaching high rates of reward within 15 minutes of new training sessions. Modulation of activity showed specificity for target neurons, while the population response was much more heterogeneous. One of our most striking observation was an increase in lick-related correlations that persisted through to the end of training sessions. When compared with other neurons in the network, target neurons achieved and maintained very high ranks in the dF/F_0-lick coincidence measure, even when behavioural performance had deteriorated (Figure 6.8D). This observation suggests that the lick-related correlations were not simply due to licking behaviour being coincident with elevations in activity of the target neuron as part of the training paradigm, but that a functional coupling between the neuron's activity and licking was established from conditioning. These lick-related correlations in the target neuron can arise in one of two ways. The first is coupling of an unobserved motor behaviour, which the target neuron is related to, with licking behaviour. This represents learning to associate behaviours, and is not necessarily indicative of cortical plasticity. The second way is cortical plasticity and circuit reorganisation such that the target neuron becomes wired in with the circuit responsible for licking. In this case, dopaminergic neurotransmission triggered by water intake is a likely candidate mechanism that provides the reward signal for driving synaptic plasticity [Schultz, 1998, Schultz, 2013]. We are unable to distinguish between these two possibilities since our behavioural apparatus did not monitor motor activities apart from licking and locomotion. Nevertheless, two lines of evidence support a cortical plasticity hypothesis; the increase in lick-coincidence we observed was a common feature of learning across conditioned animals and, prior studies have demonstrated that pairing a reward signal with a sensory stimulus can induce plasticity of the receptive fields of primary sensory cortical neurons [Bao et al., 2001, Shuler and Bear, 2006, Goltstein et al., 2013]

The imaging was performed in the ALM cortex, a region involved in high-level control of licking behaviour [Komiyama et al., 2010] and preparatory motor activity [Guo et al., 2014]. In our imaging experiments, only a minority of neurons appeared directly correlated with licking or were correlated with movement running on the spherical treadmill. A caveat of imaging in a motor region is that it can be difficult to dissociate genuine learning of a novel pattern of neural activity from simple execution of an existing motor plan. To rule out the latter, selection of neurons for conditioning was based on an absence of correlation

with licking and movement on the spherical treadmill prior to behavioural training. Instead of conditioning single neuron activity, others have demonstrated conditioning paradigms involving more arbitrary patterns of neural activity that are unlikely to already exist in the natural repertoire of responses [Koralek et al., 2012, Clancy et al., 2014]. Such approaches also help to ensure that novel patterns of activity are being conditioned, rather than requiring the animal to reinforce a pre-existing pattern of activity.

While inclusion of random reward trials allowed us to verify the strength of the correlation between licking and the activity of the conditioned neuron, additional trial types that could be investigated include:

- Trials with no sound, to assess the rate of rewards achieved with baseline neural activity and the absence of auditory feedback to indicate the start of a new trial.
- Trials where no reward is provided when the target neuron reaches the reward threshold and the cue for reward is given. These trials will enable differentiation between the neural response for licking or reward expectation and response to reward delivery.
- Trials where the auditory feedback is held at a constant frequency and does not vary with the level of neural activity. These trials will allow assessment of the neural response to variable auditory feedback, and whether neural activity is dependent on the frequency of feedback.
- Trials where the auditory feedback is based on the dF/F_0 trajectory of a previous trial. For these trials, uncoupling of the feedback frequency from the instantaneous neural activity breaks the closed-loop structure of the trial and is expected to degrade the behavioural performance. Well-trained mice respond to increases in auditory frequency by licking in anticipation of reward since in normal trials, such increases in frequency are predictive of reward.

We observed signficant variability in behavioural performance from neuron to neuron. Some neurons responded to operant conditioning with a high degree of specificity, while other neurons showed no or little signs of learning. Why are some neurons trainable whereas others are not? On the one hand, animals are capable of learning a wide range of tasks, from moving computer cursors [Serruya et al., 2002, Taylor et al., 2002], manipulation of robotic arms with one or even 3 degrees of freedom [Chapin et al., 1999, Wessberg et al., 2000], to arbitrary modulation of ensemble activity [Koralek et al., 2012]. On the other hand, some behaviours are easier to learn than others [Krakauer and Mazzoni, 2011, Ranganathan et al., 2014]. Our observation that not all neurons are responsive to the learning paradigm are consistent with the notion that patterns of activity similar to existing patterns are easier to learn than patterns that

are orthogonal to the existing structure [Hwang et al., 2013, Sadtler et al., 2014]. However, it remains unclear if operant conditioning of novel patterns of activity can expand the repertoire of *innate* activity, and if so, the extent to and conditions under which this occurs.

Operant conditioning of neural activity opens up new avenues to explore the mechanisms underlying synaptic plasticity *in vivo*. Contemporary approaches for studying synaptic and spine plasticity *in vivo* have typically relied upon sensory stimulation or behavioural training and observation of structural or functional changes in spines and dendrites [Trachtenberg et al., 2002, Yang et al., 2009, Fu et al., 2012, Caroni et al., 2012, Cichon and Gan, 2015]. While it may be possible to extract the structural and functional correlates of neural plasticity by determining which neurons are reliably activated during the behaviour, such experimental paradigms themselves do not constrain the pattern of neural activity. In contrast, operant conditioning of neural activity involves reinforcement of specific patterns of activity and thereby allows a more direct investigation of post-synaptic plasticity in the target neuron or circuit. In this vein, operant conditioning of neural activity is an extension of earlier attempts to reproduce spike timing dependent plasticity (STDP) *in vivo* by various means, including pairing electrical stimulation or a post-synaptic spike with sensory input [Schuett et al., 2001, Jacob et al., 2007] and manipulating the spatio-temporal features of the sensory input to generate temporally precise patterns of cortical activity [Fu et al., 2002, Yao et al., 2004].

While unlikely to have immediate practical applications in the clinical domain, cellular imaging remains indispensable for studying the functional and structural adaptations underlying neuroprosthetic learning. Fluorescence imaging approaches offer several key advantages over electrical recordings, including the ability to unambiguously identify different neurons within a session and across multiple sessions thereby allowing chronic behavioural training over multiple days. In addition, this method affords the ability to investigate the precise spatial relationships between different neurons, and when combined with genetic approaches, the ability to label distinct neuronal subtypes. Additional advantages are afforded by our imaging configuration. The use of fast z-focusing enabled us to capture the activity of a large number of neurons; in many experiments, over 400 simultaneously. Furthermore, population imaging lends itself to a variety of complex analytical techniques for studying the interactions between neurons and ensemble behaviour including dimensionality reduction approaches [Cunningham and Byron, 2014], statistical modelling of population activity e.g. [Pillow et al., 2008], and investigations into the correlational structure of neuronal firing [Schneidman et al., 2006]. The analyses we have presented here are only a fraction of the analyses possible.

We utilised a simple real-time imaging analysis engine for real-time image registration and dF/F_0 estimation. Image registration was necessary to compensate for lateral motion artefacts, while in our hands, motion correction in the axial direction was not required [Chen et al., 2013a]. Our image registration algorithm itself employed fast Fourier transforms to estimate the cross-correlation matrix between the reference image and newly acquired images. This approach is much simpler and faster than previous methods fitting statistical models to the motion artefacts [Dombeck et al., 2007, Greenberg and Kerr, 2009], but was facilitated by the fast resonant-scanning hardware used in our imaging setup.

Beyond image registration, with incorporation of appropriate computing hardware (such as GPUs, and FPGAs) into the real-time processing engine, we expect it will be possible to undertake much more intensive procedures in real-time. These include, but are not limited to, sophisticated analyses of neural activity, model fitting, and eventually interfacing with a neuro-prosthetic device [Serruya et al., 2002, Velliste et al., 2008]. Furthermore, by coupling real-time analysis of neural activity with optogenetic control we envisage all-optical closed-loop control of neural activity, allowing the capacity to precisely control the activity of hundreds of neurons in real-time [Paluch-Siegler et al., 2015]. All-optical closed-loop optogenetic control of neural activity is made possible by combining the use of fluorescent reporters of neural activity (e.g. GCaMP6 [Chen et al., 2013b]) with optogenetic tools (e.g. ChR2 [Yizhar et al., 2011]) to enable feedback control of circuit activity. In Chapter 4 we demonstrated and discussed optical methods for achieving millisecond control of multiple neuron simultaneously and independently, which will push the limits of closed-loop optogenetic control even further. Closed-loop manipulation of neural activity by optical means allows interrogation of neurons and neural circuitry in the vein of 'control theory', with this approach already making progress in the clinical settings, for instance in the control of epilepsy [Paz et al., 2013, Krook-Magnuson et al., 2015]. Control strategies for closed-loop neuroprosthetic systems have been recently reviewed elsewhere [Wright et al., 2016] and these may offer alternative approaches for designing neuroprosthetic learning paradigms.

Chapter 7

General discussion

In this Chapter we synthesise our results and discuss broader implications of our findings. Throughout the thesis, we have explored the integrative properties and behaviour of single cortical neurons from a number of perspectives. We have employed multiple approaches and techniques, and we have attempted to exploit synergism through combinations of these. The core experimental techniques we have utilised were patch-clamp electrophysiology and two-photon imaging, applied both *in vitro* and *in vivo*, while numerical simulations have also contributed a large number of the results.

We set out in Chapter 2 to investigate the integration of synaptic inputs *in vivo*. Despite abundant evidence for the existence of supralinear dendritic mechanisms [Major et al., 2013], it remains unclear what *in vivo* conditions produce supralinear activity in dendrites and how such activity contributes to behaviour. Recent work has shown how sublinear dendritic processing can expand the computational power of neurons [Cazé et al., 2013, Tran-Van-Minh et al., 2015]. Our findings in Chapter 2 contribute to this body of work. We chose as our model system layer 2/3 pyramidal neurons in the binocular region of the mouse primary visual cortex, since this system offers a convenient means to investigate how pyramidal neurons *in vivo* integrate two separate streams of input i.e. the visual input from each eye. Whole-cell patch-clamp recordings revealed that binocular inputs were summated sublinearly, and that the degree of sublinearity was determined by the amplitude of the synaptic inputs and not by any particular feature of the visual stimulus used to drive the synaptic response. We explored the dendritic mechanisms underlying sublinear responses by supplementing these experiments with detailed neuron modelling. We first considered a range of scenarios involving excitatory inputs only, however, maximising the interactions between excitatory synapses by activating synapses close together in space or time could not produce the degree of sublinearity observed experimentally. Since balanced excitation and inhibition is a ubiquitous feature of cortical synaptic responses [Haider and McCormick, 2009], we subsequently investigated the

contribution of inhibitory inputs. Voltage-clamp recordings provided the experimental basis for our next series of simulations, and our experiments and simulations together confirmed that balanced excitation and inhibition was responsible for generating sublinear integration. However, what became apparent from these simulations was that we were unable to determine the location of the inhibitory inputs and could not distinguish betwee somatic versus dendritic inhibition. Voltage-clamp simulations also revealed marked differences in the excitatory and inhibitory synaptic drive required to match the experimental data, depending on whether inhibitory inputs were somatic or dendritic. This study raised a number of questions for future investigations, such as when and why cortical pyramidal neurons operate in a supralinear, sublinear or even linear fashion, and what are the consequences of this on behaviour including the impacts on perception and learning. In addition, this study highlighted problems with estimating excitatory and inhibitory conductances based on somatic voltage-clamp due to voltage- and space-clamp errors. This issue motivated the themes of the next two Chapters of the thesis.

In Chapter 3, we explored the capacity of the somatic voltage-clamp technique to estimate combined excitatory and inhibitory synaptic conductances. In contrast to Chapter 2, where we used a realistic neuron morphology in our simulations, in Chapter 3 we restricted our analysis to a simple, one- or two-compartment neuron model. This allowed us to extract the core features of voltage- and space-clamp errors and how they affect the estimation of synaptic conductances. Our findings extended previous results [Williams and Mitchell, 2008, Poleg-Polsky and Diamond, 2011] and in particular showed how space-clamp distortions affect the estimates of the temporal dynamics of synaptic conductance changes, by introducing anti-correlations between excitation and inhibition and exaggerating the estimated mismatch between excitation and inhibition when a real mismatch is present. This has important consequences on the interpretation of much of the literature concerning the temporal dynamics of excitatory and inhibitory conductance changes underlying spontaneous and evoked cortical activity, since the voltage-clamp technique has been the principle method for deriving these results [Haider and McCormick, 2009].

In Chapter 4, we explored the impact of somatic versus dendritic inhibition on the action potential output. The diversity of inhibitory interneurons in the cortex has driven many investigations into the roles of different interneuron subtypes including several that have considered how the subcellular location of inhibition regulates neuronal output [Wilson et al., 2012, Lee et al., 2012b, Atallah et al., 2012]. These studies, which utilised optogenetic manipulation of inhibitory interneurons, characterised the effect of inhibition according to how it transforms the neuron's input-output relationship but reached opposing conclusions. We attempted to reconcile these conflicting experimental studies with numerical simulations

and using a detailed multicompartmental model of a layer 2/3 pyramidal neuron with passive dendrites found that both somatic and dendritic inhibition can exert similar subtractive or divisive effects on the input-output relationship of the neuron. These simulations allow for unrestricted control of the stimulation parameters and conditions, and are not affected by experimental limitations of optogenetic systems such as non-specificity of ChR2 expression. In addition, they allowed us to explore a range of stimulation conditions that would be difficult to reproduce experimentally *in vitro* or *in vivo*. The effects observed depended on the stimulation conditions, such as whether current or conductance input was used to drive neuronal firing and whether the input was stationary or noisy. These results are especially intriguing in the context of our findings in Chapter 2 that somatic and dendritic inhibition could both underlie the sublinear summation observed experimentally, and suggest that other interneuron subtype-specific features of inhibition predominate over subcellular location in regulating the output of the postsynaptic target [Palmer et al., 2012a]. These include subtype-specific activity of inhibitory interneurons in a state-dependent and behaviour-dependent manner, as well as subtype-specific neuron-neuron connectivity that govern how neurons interact and influence each other.

While in these preceding chapters the emphasis was on the measurement and impact of synaptic inputs on neuronal output, in Chapter 5 we shifted our focus to developing a system that would allow arbitrary but precise stimulation of the dendritic tree in three dimensions (3D), and thereby enable us to directly interrogate the rules underlying integration of synaptic inputs by dendrites. To achieve this goal we designed a two-photon microscope that combined a spatial-light modulator with a digital micro-mirror device to perform holographic stimulation with high-speed temporal switching. This approach offers unprecedented flexibility in generating stimulation patterns for studying the rules governing synaptic integration. Using this system we mimicked excitatory synaptic activation in 3D with millisecond precision using glutamate uncaging. Such a system can be extended to other neurotransmitters including GABA, separately or in combination with each other, and could also be adapted for optogenetic stimulation. Furthermore, our system is not limited just to studying synaptic integration in individual neurons, but could be used for photo-stimulation across large neuronal populations. In summary, the applications range from mapping the subcellular distribution of synaptic inputs within single neurons [Petreanu et al., 2009], to mapping local connectivity [Shepherd, 2012] as well as long-range connections between different brain regions [Mao et al., 2011].

Ultimately, our focus on dendritic integration thus far has been driven by a desire to understand the contribution of single neurons to behaviour. To that end, in Chapter 6 we developed a real-time two-photon

microscope for imaging the fluorescence signal of the genetically-encoded calcium indicator GCaMP6 *in vivo* and performed real-time image registration and signal analysis. Using this system as an optical brain-machine interface, we designed a behavioural paradigm involving operant conditioning of single neuron activity. By expressing GCaMP6 in superficial neurons of the anterior lateral motor cortex area, a region known to be involved in motor planning [Komiyama et al., 2010, Guo et al., 2014], we demonstrated that mice had the ability to voluntarily modulate the activity of single target neurons, in some instances with relatively high specificity. The system we developed and behavioural paradigm we demonstrated provides a prototypical example of how an operator can modulate the activity of a subset of neurons in a specific manner *in vivo*. This is in contrast to more conventional approaches, such as presentation of sensory stimuli as in Chapter 2, which do not enforce specific temporal spiking patterns in arbitrary groups of neurons. The approach we take in Chapter 6 therefore offers the possibility of investigating phenomena *in vivo* that are dependent on spike-timing, such as dendritic integration and spike-timing dependent plasticity (STDP) [Sjöström et al., 2008] without resorting to artificial stimulation methods.

Much of the work in this thesis lies at the intersection of experiment, numerical simulations, and techniques development. These approaches complement each other in several ways. On the one hand, experimental results provide the foundations necessary to construct computational models. These models can be used to test hypotheses that are beyond experimental interrogation, as well as increase our understanding of the biophysical mechanism underlying the experimental observations. On the other hand, results produced from numerical simulations can inform, guide and provide hypotheses for future experimental work. We saw in Chapter 2 for example, the interplay between *in vivo* whole-cell recordings and simulations uncovered the critical contribution of inhibition to sublinear summation. Similarly, many of the simulations presented in Chapter 4 were built upon experimental results and conflicting ideas that arose from those experiments [Wilson et al., 2012, Lee et al., 2012b, Atallah et al., 2012]. In particular, our results reconciled these earlier studies and provided insights for future experiments. At the same time, the simulations we performed in Chapter 3 enabled us to rigorously explore the validity and limitations of experimental procedures relying on somatic voltage-clamp recordings which are affected by space-clamp errors in neurons with dendrites. New methods and techniques build on existing experimental approaches to drive progress, and often provide a means to cross from theoretical *in silico* simulations to real experimental data. This was the motivation for Chapters 5 and 6, where the systems and behavioural paradigms developed enable the detailed investigation of dendritic integration and single neuron behaviour *in vitro* and *in vivo*.

On that note, the pinnacle of dendritic integration research is reaching an understanding of how computations performed at the dendritic level contribute to behaviour. To attain this goal, we envisage that the investigation of dendritic function will continue to require a multi-faceted approach encompassing the experimental and theoretical domains. This includes examining the physiology of dendrites in detail, such as characterising the ion channels expressed in dendrites and their effects on the various phenomena exhibited by dendrites *in vitro* and *in vivo*, identification of the circuit elements involved in regulating these phenomena, such as inhibitory interneurons, a continued expansion of theoretical frameworks to understand the computations performed by dendrites and individual neurons, and ultimately the implementation of behavioural experiments that capture the physiology and computation in action. To this end, throughout the thesis we have strived to incorporate many of these elements in our quest to fully understand the neuronal basis of behaviour.

References

[Adams and Tsien, 1993] Adams, S. R. and Tsien, R. Y. (1993). Controlling cell chemistry with caged compounds. *Annual Review of Physiology*, 55(1):755–784.

[Agmon-Snir et al., 1998] Agmon-Snir, H., Carr, C. E., and Rinzel, J. (1998). The role of dendrites in auditory coincidence detection. *Nature*, 393(6682):268–272.

[Andermann et al., 2013] Andermann, M. L., Gilfoy, N. B., Goldey, G. J., Sachdev, R. N., Wölfel, M., McCormick, D. A., Reid, R. C., and Levene, M. J. (2013). Chronic cellular imaging of entire cortical columns in awake mice using microprisms. *Neuron*, 80(4):900–913.

[Anderson et al., 2000a] Anderson, J. S., Carandini, M., and Ferster, D. (2000a). Orientation tuning of input conductance, excitation, and inhibition in cat primary visual cortex. *Journal of Neurophysiology*, 84(2):909–926.

[Anderson et al., 2000b] Anderson, J. S., Lampl, I., Gillespie, D. C., and Ferster, D. (2000b). The contribution of noise to contrast invariance of orientation tuning in cat visual cortex. *Science*, 290(5498):1968–1972.

[Andreasen and Lambert, 1995] Andreasen, M. and Lambert, J. (1995). Regenerative properties of pyramidal cell dendrites in area CA1 of the rat hippocampus. *The Journal of Physiology*, 483(2):421–441.

[Anselmi et al., 2011] Anselmi, F., Ventalon, C., Bègue, A., Ogden, D., and Emiliani, V. (2011). Three-dimensional imaging and photostimulation by remote-focusing and holographic light patterning. *Proceedings of the National Academy of Sciences*, 108(49):19504–19509.

[Araya et al., 2006] Araya, R., Jiang, J., Eisenthal, K. B., and Yuste, R. (2006). The spine neck filters membrane potentials. *Proceedings of the National Academy of Sciences*, 103(47):17961–17966.

[Araya et al., 2007] Araya, R., Nikolenko, V., Eisenthal, K. B., and Yuste, R. (2007). Sodium channels amplify spine potentials. *Proceedings of the National Academy of Sciences*, 104(30):12347–12352.

[Ariav et al., 2003] Ariav, G., Polsky, A., and Schiller, J. (2003). Submillisecond precision of the input-output transformation function mediated by fast sodium dendritic spikes in basal dendrites of CA1 pyramidal neurons. *The Journal of Neuroscience*, 23(21):7750–7758.

[Armstrong, 2005] Armstrong, D. D. (2005). Neuropathology of Rett syndrome. *Journal of Child Neurology*, 20(9):747–753.

[Ascoli et al., 2008] Ascoli, G. A., Alonso-Nanclares, L., Anderson, S. A., Barrionuevo, G., Benavides-Piccione, R., Burkhalter, A., Buzsáki, G., Cauli, B., DeFelipe, J., Fairén, A., et al. (2008). Petilla terminology: nomenclature of features of gabaergic interneurons of the cerebral cortex. *Nature Reviews Neuroscience*, 9(7):557–568.

[Atallah et al., 2012] Atallah, B. V., Bruns, W., Carandini, M., and Scanziani, M. (2012). Parvalbumin-expressing interneurons linearly transform cortical responses to visual stimuli. *Neuron*, 73(1):159–170.

[Baloyannis, 2009] Baloyannis, S. (2009). Dendritic pathology in Alzheimer's disease. *Journal of the Neurological Sciences*, 283(1):153–157.

[Bao et al., 2001] Bao, S., Chan, V. T., and Merzenich, M. M. (2001). Cortical remodelling induced by activity of ventral tegmental dopamine neurons. *Nature*, 412(6842):79–83.

[Bar-Yehuda and Korngreen, 2008] Bar-Yehuda, D. and Korngreen, A. (2008). Space-clamp problems when voltage clamping neurons expressing voltage-gated conductances. *Journal of Neurophysiology*, 99(3):1127–36.

[Barlow et al., 1964] Barlow, H., Hill, R., and Levick, W. (1964). Retinal ganglion cells responding selectively to direction and speed of image motion in the rabbit. *The Journal of Physiology*, 173(3):377–407.

[Barlow and Levick, 1965] Barlow, H. and Levick, W. R. (1965). The mechanism of directionally selective units in rabbit's retina. *The Journal of Physiology*, 178(3):477–504.

[Bastrikova et al., 2008] Bastrikova, N., Gardner, G. A., Reece, J. M., Jeromin, A., and Dudek, S. M. (2008). Synapse elimination accompanies functional plasticity in hippocampal neurons. *Proceedings of the National Academy of Sciences*, 105(8):3123–3127.

[Becker et al., 1986] Becker, L., Armstrong, D., and Chan, F. (1986). Dendritic atrophy in children with Down's syndrome. *Annals of Neurology*, 20(4):520–526.

[Bédard et al., 2012] Bédard, C., Béhuret, S., Deleuze, C., Bal, T., and Destexhe, A. (2012). Oversampling method to extract excitatory and inhibitory conductances from single-trial membrane potential recordings. *Journal of Neuroscience Methods*, 210(1):3–14.

[Bednarkiewicz et al., 2008] Bednarkiewicz, A., Bouhifd, M., and Whelan, M. P. (2008). Digital micromirror device as a spatial illuminator for fluorescence lifetime and hyperspectral imaging. *Applied Optics*, 47(9):1193–1199.

[Bekkers, 2000] Bekkers, J. M. (2000). Distribution and activation of voltage-gated potassium channels in cell-attached and outside-out patches from large layer 5 cortical pyramidal neurons of the rat. *The Journal of Physiology*, 525(3):611–620.

[Bereshpolova et al., 2007] Bereshpolova, Y., Amitai, Y., Gusev, A. G., Stoelzel, C. R., and Swadlow, H. A. (2007). Dendritic backpropagation and the state of the awake neocortex. *The Journal of Neuroscience*, 27(35):9392–9399.

[Berger et al., 2001] Berger, T., Larkum, M. E., and Lüscher, H.-R. (2001). High I_h channel density in the distal apical dendrite of layer V pyramidal cells increases bidirectional attenuation of EPSPs. *Journal of Neurophysiology*, 85(2):855–868.

[Berger et al., 2003] Berger, T., Senn, W., and Lüscher, H.-R. (2003). Hyperpolarization-activated current I_h disconnects somatic and dendritic spike initiation zones in layer V pyramidal neurons. *Journal of Neurophysiology*, 90(4):2428–2437.

[Bernard et al., 2004] Bernard, C., Anderson, A., Becker, A., Poolos, N. P., Beck, H., and Johnston, D. (2004). Acquired dendritic channelopathy in temporal lobe epilepsy. *Science*, 305(5683):532–535.

[Bhatt et al., 2009] Bhatt, D. H., Zhang, S., and Gan, W.-B. (2009). Dendritic spine dynamics. *Annual Report of the Review of Physiology*, 71:261–282.

[Bi and Poo, 1998] Bi, G.-q. and Poo, M.-m. (1998). Synaptic modifications in cultured hippocampal neurons: dependence on spike timing, synaptic strength, and postsynaptic cell type. *The Journal of Neuroscience*, 18(24):10464–10472.

[Biel et al., 2009] Biel, M., Wahl-Schott, C., Michalakis, S., and Zong, X. (2009). Hyperpolarization-activated cation channels: from genes to function. *Physiological Reviews*, 89(3):847–885.

[Bittner et al., 2015] Bittner, K. C., Grienberger, C., Vaidya, S. P., Milstein, A. D., Macklin, J. J., Suh, J., Tonegawa, S., and Magee, J. C. (2015). Conjunctive input processing drives feature selectivity in hippocampal CA1 neurons. *Nature Neuroscience*, 18(8):1133–1142.

[Blank et al., 2003] Blank, T., Nijholt, I., Kye, M.-J., Radulovic, J., and Spiess, J. (2003). Small-conductance, Ca^{2+}-activated K^+ channel SK3 generates age-related memory and LTP deficits. *Nature Neuroscience*, 6(9):911–912.

[Blanpied and Ehlers, 2004] Blanpied, T. A. and Ehlers, M. D. (2004). Microanatomy of dendritic spines: emerging principles of synaptic pathology in psychiatric and neurological disease. *Biological Psychiatry*, 55(12):1121–1127.

[Bloodgood and Sabatini, 2007] Bloodgood, B. L. and Sabatini, B. L. (2007). Nonlinear regulation of unitary synaptic signals by CaV 2.3 voltage-sensitive calcium channels located in dendritic spines. *Neuron*, 53(2):249–260.

[Borg-Graham et al., 1998] Borg-Graham, L. J., Monier, C., and Fregnac, Y. (1998). Visual input evokes transient and strong shunting inhibition in visual cortical neurons. *Nature*, 393(6683):369–373.

[Boyden et al., 2005] Boyden, E. S., Zhang, F., Bamberg, E., Nagel, G., and Deisseroth, K. (2005). Millisecond-timescale, genetically targeted optical control of neural activity. *Nature Neuroscience*, 8(9):1263–1268.

[Branco et al., 2010] Branco, T., Clark, B. A., and Häusser, M. (2010). Dendritic discrimination of temporal input sequences in cortical neurons. *Science*, 329(5999):1671–1675.

[Branco and Häusser, 2010] Branco, T. and Häusser, M. (2010). The single dendritic branch as a fundamental functional unit in the nervous system. *Current Opinion in Neurobiology*, 20(4):494–502.

[Branco and Häusser, 2011] Branco, T. and Häusser, M. (2011). Synaptic integration gradients in single cortical pyramidal cell dendrites. *Neuron*, 69(5):885–892.

[Brecht et al., 2004] Brecht, M., Schneider, M., Sakmann, B., and Margrie, T. W. (2004). Whisker movements evoked by stimulation of single pyramidal cells in rat motor cortex. *Nature*, 427(6976):704–710.

[Buzsáki et al., 1983] Buzsáki, G., Vanderwolf, C. H., et al. (1983). Cellular bases of hippocampal eeg in the behaving rat. *Brain Research Reviews*, 6(2):139–171.

[Cafaro and Rieke, 2010] Cafaro, J. and Rieke, F. (2010). Noise correlations improve response fidelity and stimulus encoding. *Nature*, 468(7326):964–967.

[Cai et al., 2004] Cai, X., Liang, C. W., Muralidharan, S., Kao, J. P., Tang, C.-M., and Thompson, S. M. (2004). Unique roles of SK and Kv4.2 potassium channels in dendritic integration. *Neuron*, 44(2):351–364.

[Carmena, 2013] Carmena, J. M. (2013). Advances in neuroprosthetic learning and control. *PLoS Biology*, 11(5):e1001561.

[Carmena et al., 2003] Carmena, J. M., Lebedev, M. A., Crist, R. E., O'doherty, J. E., Santucci, D. M., Dimitrov, D. F., Patil, P. G., Henriquez, C. S., and Nicolelis, M. A. (2003). Learning to control a brain-machine interface for reaching and grasping by primates. *PLoS Biology*, 1(2):e42.

[Caroni et al., 2012] Caroni, P., Donato, F., and Muller, D. (2012). Structural plasticity upon learning: regulation and functions. *Nature Reviews Neuroscience*, 13(7):478–490.

[Carvalho and Buonomano, 2009] Carvalho, T. P. and Buonomano, D. V. (2009). Differential effects of excitatory and inhibitory plasticity on synaptically driven neuronal input-output functions. *Neuron*, 61(5):774–785.

[Cash and Yuste, 1998] Cash, S. and Yuste, R. (1998). Input summation by cultured pyramidal neurons is linear and position-independent. *The Journal of Neuroscience*, 18(1):10–15.

[Cash and Yuste, 1999] Cash, S. and Yuste, R. (1999). Linear summation of excitatory inputs by CA1 pyramidal neurons. *Neuron*, 22(2):383–394.

[Cazé et al., 2013] Cazé, R. D., Humphries, M., and Gutkin, B. (2013). Passive dendrites enable single neurons to compute linearly non-separable functions. *PLoS Computational Biology*, 9(2):e1002867.

[Chance et al., 2002] Chance, F. S., Abbott, L., and Reyes, A. D. (2002). Gain modulation from background synaptic input. *Neuron*, 35(4):773–782.

[Chapin et al., 1999] Chapin, J. K., Moxon, K. A., Markowitz, R. S., and Nicolelis, M. A. (1999). Real-time control of a robot arm using simultaneously recorded neurons in the motor cortex. *Nature Neuroscience*, 2(7):664–670.

[Chen et al., 2013a] Chen, J. L., Pfäffli, O. A., Voigt, F. F., Margolis, D. J., and Helmchen, F. (2013a). Online correction of licking-induced brain motion during two-photon imaging with a tunable lens. *The Journal of Physiology*, 591(19):4689–4698.

[Chen et al., 2013b] Chen, T.-W., Wardill, T. J., Sun, Y., Pulver, S. R., Renninger, S. L., Baohan, A., Schreiter, E. R., Kerr, R. A., Orger, M. B., Jayaraman, V., et al. (2013b). Ultrasensitive fluorescent proteins for imaging neuronal activity. *Nature*, 499(7458):295–300.

[Chen et al., 2011] Chen, X., Leischner, U., Rochefort, N. L., Nelken, I., and Konnerth, A. (2011). Functional mapping of single spines in cortical neurons *in vivo*. *Nature*, 475(7357):501–505.

[Cheng-Yu et al., 2009] Cheng-Yu, T. L., Poo, M.-M., and Dan, Y. (2009). Burst spiking of a single cortical neuron modifies global brain state. *Science*, 324(5927):643–646.

[Chia and Levene, 2009] Chia, T. H. and Levene, M. J. (2009). Microprisms for *in vivo* multilayer cortical imaging. *Journal of Neurophysiology*, 102(2):1310–1314.

[Chizhov et al., 2014] Chizhov, A. V., Malinina, E., Druzin, M., Graham, L. J., and Johansson, S. (2014). Firing clamp: a novel method for single-trial estimation of excitatory and inhibitory synaptic neuronal conductances. *Frontiers in Cellular Neuroscience*, 8(86).

[Chu et al., 2003] Chu, Z., Galarreta, M., and Hestrin, S. (2003). Synaptic interactions of late-spiking neocortical neurons in layer 1. *The Journal of Neuroscience*, 23(1):96–102.

[Cichon and Gan, 2015] Cichon, J. and Gan, W.-B. (2015). Branch-specific dendritic Ca^{2+} spikes cause persistent synaptic plasticity. *Nature*, 520(7546):180–185.

[Clancy et al., 2014] Clancy, K. B., Koralek, A. C., Costa, R. M., Feldman, D. E., and Carmena, J. M. (2014). Volitional modulation of optically recorded calcium signals during neuroprosthetic learning. *Nature Neuroscience*, 17(6):807–809.

[Coetzee et al., 1999] Coetzee, W. A., Amarillo, Y., Chiu, J., Chow, A., Lau, D., McCormack, T., Morena, H., Nadal, M. S., Ozaita, A., Pountney, D., et al. (1999). Molecular diversity of K^+ channels. *Annals of the New York Academy of Sciences*, 868(1):233–255.

[Coleman et al., 2009] Coleman, J., Law, K., and Bear, M. (2009). Anatomical origins of ocular dominance in mouse primary visual cortex. *Neuroscience*, 161(2):561 – 571.

[Cossart et al., 2001] Cossart, R., Dinocourt, C., Hirsch, J. C., Merchan-Perez, A., De Felipe, J., Ben-Ari, Y., Esclapez, M., and Bernard, C. (2001). Dendritic but not somatic GABAergic inhibition is decreased in experimental epilepsy. *Nature Neuroscience*, 4(1):52–62.

[Cruikshank et al., 2007] Cruikshank, S. J., Lewis, T. J., and Connors, B. W. (2007). Synaptic basis for intense thalamocortical activation of feedforward inhibitory cells in neocortex. *Nature Neuroscience*, 10(4):462–468.

[Cunningham and Byron, 2014] Cunningham, J. P. and Byron, M. Y. (2014). Dimensionality reduction for large-scale neural recordings. *Nature Neuroscience*, 17(11):1500–1509.

[Curtis et al., 2002] Curtis, J. E., Koss, B. A., and Grier, D. G. (2002). Dynamic holographic optical tweezers. *Optics Communications*, 207(1):169–175.

[Dal Maschio et al., 2010] Dal Maschio, M., Difato, F., Beltramo, R., Blau, A., Benfenati, F., and Fellin, T. (2010). Simultaneous two-photon imaging and photo-stimulation with structured light illumination. *Optics Express*, 18(18):18720–18731.

[Daria et al., 2009] Daria, V. R., Stricker, C., Bowman, R., Redman, S., and Bachor, H.-A. (2009). Arbitrary multisite two-photon excitation in four dimensions. *Applied Physics Letters*, 95(9):093701.

[Dayton et al., 2001] Dayton, D., Browne, S., Gonglewski, J., and Restaino, S. (2001). Characterization and control of a multielement dual-frequency liquid-crystal device for high-speed adaptive optical wavefront correction. *Applied Optics*, 40(15):2345–2355.

[DeFelipe et al., 2013] DeFelipe, J., López-Cruz, P. L., Benavides-Piccione, R., Bielza, C., Larrañaga, P., Anderson, S., Burkhalter, A., Cauli, B., Fairén, A., Feldmeyer, D., et al. (2013). New insights into the classification and nomenclature of cortical GABAergic interneurons. *Nature Reviews Neuroscience*, 14(3):202–216.

[Destexhe et al., 2001] Destexhe, A., Rudolph, M., Fellous, J.-M., and Sejnowski, T. J. (2001). Fluctuating synaptic conductances recreate *in vivo*-like activity in neocortical neurons. *Neuroscience*, 107(1):13–24.

[Destexhe et al., 2003] Destexhe, A., Rudolph, M., and Paré, D. (2003). The high-conductance state of neocortical neurons *in vivo*. *Nature Reviews Neuroscience*, 4(9):739–51.

[Dombeck et al., 2007] Dombeck, D. A., Khabbaz, A. N., Collman, F., Adelman, T. L., and Tank, D. W. (2007). Imaging large-scale neural activity with cellular resolution in awake, mobile mice. *Neuron*, 56(1):43–57.

[Doron et al., 2014] Doron, G., von Heimendahl, M., Schlattmann, P., Houweling, A. R., and Brecht, M. (2014). Spiking irregularity and frequency modulate the behavioral report of single-neuron stimulation. *Neuron*, 81(3):653–663.

[Douglas et al., 1988] Douglas, R. J., Martin, K. A., and Whitteridge, D. (1988). Selective responses of visual cortical cells do not depend on shunting inhibition. *Nature*, 332(6165):642–644.

[Ducros et al., 2013] Ducros, M., Houssen, Y. G., Bradley, J., de Sars, V., and Charpak, S. (2013). Encoded multisite two-photon microscopy. *Proceedings of the National Academy of Sciences*, 110(32):13138–13143.

[El-Boustani et al., 2014] El-Boustani, S., Wilson, N. R., Runyan, C. A., and Sur, M. (2014). El-boustani et al. reply. *Nature*, 508(7494):E3–E4.

[Emptage et al., 1999] Emptage, N., Bliss, T. V., and Fine, A. (1999). Single synaptic events evoke NMDA receptor–mediated release of calcium from internal stores in hippocampal dendritic spines. *Neuron*, 22(1):115–124.

[Engert and Bonhoeffer, 1999] Engert, F. and Bonhoeffer, T. (1999). Dendritic spine changes associated with hippocampal long-term synaptic plasticity. *Nature*, 399(6731):66–70.

[Enoki et al., 2002] Enoki, R., Namiki, M., Kudo, Y., and Miyakawa, H. (2002). Optical monitoring of synaptic summation along the dendrites of CA1 pyramidal neurons. *Neuroscience*, 113(4):1003–1014.

[Faber, 2010] Faber, E. L. (2010). Functional interplay between NMDA receptors, SK channels and voltage-gated Ca^{2+} channels regulates synaptic excitability in the medial prefrontal cortex. *The Journal of Physiology*, 588(8):1281–1292.

[Faber and Sah, 2003] Faber, E. L. and Sah, P. (2003). Calcium-activated potassium channels: multiple contributions to neuronal function. *The Neuroscientist*, 9(3):181–194.

[Fetz, 1969] Fetz, E. E. (1969). Operant conditioning of cortical unit activity. *Science*, 163(3870):955–958.

[Fetz and Finocchio, 1971] Fetz, E. E. and Finocchio, D. V. (1971). Operant conditioning of specific patterns of neural and muscular activity. *Science*, 174(4007):431–435.

[Fiala et al., 2002] Fiala, J. C., Spacek, J., and Harris, K. M. (2002). Dendritic spine pathology: cause or consequence of neurological disorders? *Brain Research Reviews*, 39(1):29–54.

[Fino et al., 2009] Fino, E., Araya, R., Peterka, D. S., Salierno, M., Etchenique, R., and Yuste, R. (2009). Rubi-glutamate: two-photon and visible-light photoactivation of neurons and dendritic spines. *Frontiers in Neural Circuits*, 3(2).

[Fiser et al., 2004] Fiser, J., Chiu, C., and Weliky, M. (2004). Small modulation of ongoing cortical dynamics by sensory input during natural vision. *Nature*, 431(7008):573–578.

[Froemke et al., 2005] Froemke, R. C., Poo, M.-m., and Dan, Y. (2005). Spike-timing-dependent synaptic plasticity depends on dendritic location. *Nature*, 434(7030):221–225.

[Fu et al., 2012] Fu, M., Yu, X., Lu, J., and Zuo, Y. (2012). Repetitive motor learning induces coordinated formation of clustered dendritic spines *in vivo*. *Nature*, 483(7387):92–95.

[Fu et al., 2002] Fu, Y.-X., Djupsund, K., Gao, H., Hayden, B., Shen, K., and Dan, Y. (2002). Temporal specificity in the cortical plasticity of visual space representation. *Science*, 296(5575):1999–2003.

[Fujita, 1968] Fujita, Y. (1968). Activity of dendrites of single Purkinje cells and its relationship to so-called inactivation response in rabbit cerebellum. *Journal of Neurophysiology*, 31(2):131–141.

[Gambino et al., 2014] Gambino, F., Pagès, S., Kehayas, V., Baptista, D., Tatti, R., Carleton, A., and Holtmaat, A. (2014). Sensory-evoked LTP driven by dendritic plateau potentials *in vivo*. *Nature*, 515(7525):116–119.

[Gasparini and Magee, 2006] Gasparini, S. and Magee, J. C. (2006). State-dependent dendritic computation in hippocampal CA1 pyramidal neurons. *The Journal of Neuroscience*, 26(7):2088–2100.

[Gasparini et al., 2004] Gasparini, S., Migliore, M., and Magee, J. C. (2004). On the initiation and propagation of dendritic spikes in CA1 pyramidal neurons. *The Journal of Neuroscience*, 24(49):11046–11056.

[Gillespie, 1996] Gillespie, D. T. (1996). Exact numerical simulation of the Ornstein-Uhlenbeck process and its integral. *Physical Review E*, 54(2):2084.

[Go et al., 2011] Go, M. A., Ng, P.-F., Bachor, H.-A., and Daria, V. R. (2011). Optimal complex field holographic projection. *Optics letters*, 36(16):3073–3075.

[Go et al., 2012] Go, M. A., Stricker, C., Redman, S., Bachor, H.-A., and Daria, V. R. (2012). Simultaneous multi-site two-photon photostimulation in three dimensions. *Journal of biophotonics*, 5(10):745–753.

[Goldberg et al., 2003] Goldberg, J. H., Tamas, G., and Yuste, R. (2003). Ca^{2+} imaging of mouse neocortical interneurone dendrites: Ia-type K^{+} channels control action potential backpropagation. *The Journal of Physiology*, 551(1):49–65.

[Golding et al., 1999] Golding, N. L., Jung, H.-y., Mickus, T., and Spruston, N. (1999). Dendritic calcium spike initiation and repolarization are controlled by distinct potassium channel subtypes in CA1 pyramidal neurons. *The Journal of Neuroscience*, 19(20):8789–8798.

[Golding and Spruston, 1998] Golding, N. L. and Spruston, N. (1998). Dendritic sodium spikes are variable triggers of axonal action potentials in hippocampal CA1 pyramidal neurons. *Neuron*, 21(5):1189–1200.

[Golding et al., 2002] Golding, N. L., Staff, N. P., and Spruston, N. (2002). Dendritic spikes as a mechanism for cooperative long-term potentiation. *Nature*, 418(6895):326–331.

[Golgi, 1873] Golgi, C. (1873). Sulla struttura della sostanza grigia del cervello. *Gazzetta Medica Italiana. Lombardia*, 33:244–246.

[Goltstein et al., 2013] Goltstein, P. M., Coffey, E. B., Roelfsema, P. R., and Pennartz, C. M. (2013). *In vivo* two-photon Ca^{2+} imaging reveals selective reward effects on stimulus-specific assemblies in mouse visual cortex. *The Journal of Neuroscience*, 33(28):11540–11555.

[Gray, 1959] Gray, E. (1959). Electron microscopy of synaptic contacts on dendrite spines of the cerebral cortex. *Nature*, 183(4675):1592–1593.

[Greenberg and Kerr, 2009] Greenberg, D. S. and Kerr, J. N. (2009). Automated correction of fast motion artifacts for two-photon imaging of awake animals. *Journal of Neuroscience Methods*, 176(1):1–15.

[Gulledge and Stuart, 2005] Gulledge, A. T. and Stuart, G. J. (2005). Cholinergic inhibition of neocortical pyramidal neurons. *The Journal of Neuroscience*, 25(44):10308–10320.

[Guo et al., 2014] Guo, Z. V., Li, N., Huber, D., Ophir, E., Gutnisky, D., Ting, J. T., Feng, G., and Svoboda, K. (2014). Flow of cortical activity underlying a tactile decision in mice. *Neuron*, 81(1):179–194.

[Guthrie et al., 1991] Guthrie, P. B., Segal, M., and Kater, S. (1991). Independent regulation of calcium revealed by imaging dendritic spines. *Nature*, 354(6348):76–80.

[Hagberg et al., 1983] Hagberg, B., Aicardi, J., Dias, K., and Ramos, O. (1983). A progressive syndrome of autism, dementia, ataxia, and loss of purposeful hand use in girls: Rett's syndrome: report of 35 cases. *Annals of Neurology*, 14(4):471–479.

[Haider et al., 2006] Haider, B., Duque, A., Hasenstaub, A. R., and McCormick, D. A. (2006). Neocortical network activity *in vivo* is generated through a dynamic balance of excitation and inhibition. *Journal of Neuroscience*, 26(17):4535–45.

[Haider et al., 2013] Haider, B., Häusser, M., and Carandini, M. (2013). Inhibition dominates sensory responses in the awake cortex. *Nature*, 493(7430):97–100.

[Haider and McCormick, 2009] Haider, B. and McCormick, D. A. (2009). Rapid neocortical dynamics: cellular and network mechanisms. *Neuron*, 62(2):171–189.

[Hammond et al., 2006] Hammond, R. S., Bond, C. T., Strassmaier, T., Ngo-Anh, T. J., Adelman, J. P., Maylie, J., and Stackman, R. W. (2006). Small-conductance Ca^{2+}-activated K^+ channel type 2

(SK2) modulates hippocampal learning, memory, and synaptic plasticity. *The Journal of Neuroscience*, 26(6):1844–1853.

[Harnett et al., 2015] Harnett, M. T., Magee, J. C., and Williams, S. R. (2015). Distribution and function of HCN channels in the apical dendritic tuft of neocortical pyramidal neurons. *The Journal of Neuroscience*, 35(3):1024–1037.

[Harnett et al., 2012] Harnett, M. T., Makara, J. K., Spruston, N., Kath, W. L., and Magee, J. C. (2012). Synaptic amplification by dendritic spines enhances input cooperativity. *Nature*, 491(7425):599–602.

[Harris and Stevens, 1988] Harris, K. M. and Stevens, J. (1988). Dendritic spines of rat cerebellar Purkinje cells: serial electron microscopy with reference to their biophysical characteristics. *The Journal of Neuroscience*, 8(12):4455–4469.

[Harris and Stevens, 1989] Harris, K. M. and Stevens, J. K. (1989). Dendritic spines of CA1 pyramidal cells in the rat hippocampus: serial electron microscopy with reference to their biophysical characteristics. *The Journal of Neuroscience*, 9(8):2982–2997.

[Hartline and Castelfranco, 2003] Hartline, D. K. and Castelfranco, A. M. (2003). Simulations of voltage clamping poorly space-clamped voltage-dependent conductances in a uniform cylindrical neurite. *Journal of Computational Neuroscience*, 14(3):253–269.

[Hasenstaub et al., 2005] Hasenstaub, A., Shu, Y., Haider, B., Kraushaar, U., Duque, A., and McCormick, D. A. (2005). Inhibitory postsynaptic potentials carry synchronized frequency information in active cortical networks. *Neuron*, 47(3):423–435.

[Häusser et al., 2000] Häusser, M., Spruston, N., and Stuart, G. J. (2000). Diversity and dynamics of dendritic signaling. *Science*, 290(5492):739–744.

[Häusser et al., 1995] Häusser, M., Stuart, G., Racca, C., and Sakmann, B. (1995). Axonal initiation and active dendritic propagation of action potentials in substantia nigra neurons. *Neuron*, 15(3):637–647.

[Helmchen et al., 1999] Helmchen, F., Svoboda, K., Denk, W., and Tank, D. W. (1999). *In vivo* dendritic calcium dynamics in deep-layer cortical pyramidal neurons. *Nature Neuroscience*, 2(11):989–996.

[Hering and Sheng, 2001] Hering, H. and Sheng, M. (2001). Dentritic spines: structure, dynamics and regulation. *Nature Reviews Neuroscience*, 2(12):880–888.

[Heron et al., 2007] Heron, S. E., Scheffer, I. E., Berkovic, S. F., Dibbens, L. M., and Mulley, J. C. (2007). Channelopathies in idiopathic epilepsy. *Neurotherapeutics*, 4(2):295–304.

[Higgs et al., 2006] Higgs, M. H., Slee, S. J., and Spain, W. J. (2006). Diversity of gain modulation by noise in neocortical neurons: regulation by the slow afterhyperpolarization conductance. *The Journal of Neuroscience*, 26(34):8787–8799.

[Higley and Contreras, 2006] Higley, M. J. and Contreras, D. (2006). Balanced excitation and inhibition determine spike timing during frequency adaptation. *The Journal of Neuroscience*, 26(2):448–457.

[Higley and Sabatini, 2008] Higley, M. J. and Sabatini, B. L. (2008). Calcium signaling in dendrites and spines: practical and functional considerations. *Neuron*, 59(6):902–913.

[Hinton et al., 1991] Hinton, V., Brown, W., Wisniewski, K., and Rudelli, R. (1991). Analysis of neocortex in three males with the fragile x syndrome. *American Journal of Medical Genetics*, 41(3):289–294.

[Hira et al., 2014] Hira, R., Ohkubo, F., Masamizu, Y., Ohkura, M., Nakai, J., Okada, T., and Matsuzaki, M. (2014). Reward-timing-dependent bidirectional modulation of cortical microcircuits during optical single-neuron operant conditioning. *Nature Communications*, 5(5551).

[Hochbaum et al., 2014] Hochbaum, D. R., Zhao, Y., Farhi, S. L., Klapoetke, N., Werley, C. A., Kapoor, V., Zou, P., Kralj, J. M., Maclaurin, D., Smedemark-Margulies, N., et al. (2014). All-optical electrophysiology in mammalian neurons using engineered microbial rhodopsins. *Nature Methods*, 11(8):825–33.

[Hofer et al., 2009] Hofer, S. B., Mrsic-Flogel, T. D., Bonhoeffer, T., and Hübener, M. (2009). Experience leaves a lasting structural trace in cortical circuits. *Nature*, 457(7227):313–317.

[Hoffman et al., 1997] Hoffman, D. A., Magee, J. C., Colbert, C. M., and Johnston, D. (1997). K^+ channel regulation of signal propagation in dendrites of hippocampal pyramidal neurons. *Nature*, 387(6636):869–875.

[Holtmaat and Svoboda, 2009] Holtmaat, A. and Svoboda, K. (2009). Experience-dependent structural synaptic plasticity in the mammalian brain. *Nature Reviews Neuroscience*, 10(9):647–658.

[Holtmaat et al., 2005] Holtmaat, A. J., Trachtenberg, J. T., Wilbrecht, L., Shepherd, G. M., Zhang, X., Knott, G. W., and Svoboda, K. (2005). Transient and persistent dendritic spines in the neocortex *in vivo*. *Neuron*, 45(2):279–291.

[Houchin, 1973] Houchin, J. (1973). Procion yellow electrodes for intracellular recording and staining of neurones in the somatosensory cortex of the rat. *The Journal of Physiology*, 232(2):67–69.

[Houweling and Brecht, 2008] Houweling, A. R. and Brecht, M. (2008). Behavioural report of single neuron stimulation in somatosensory cortex. *Nature*, 451(7174):65–68.

[Howard et al., 2005] Howard, A., Tamas, G., and Soltesz, I. (2005). Lighting the chandelier: new vistas for axo-axonic cells. *Trends in Neurosciences*, 28(6):310–316.

[Howarth et al., 2014] Howarth, M., Walmsley, L., and Brown, T. (2014). Binocular integration in the mouse lateral geniculate nuclei. *Current Biology*, 24(11):1241–1247.

[Huber et al., 2012] Huber, D., Gutnisky, D., Peron, S., O'Connor, D., Wiegert, J., Tian, L., Oertner, T., Looger, L., and Svoboda, K. (2012). Multiple dynamic representations in the motor cortex during sensorimotor learning. *Nature*, 484(7395):473–478.

[Hwang et al., 2013] Hwang, E. J., Bailey, P. M., and Andersen, R. A. (2013). Volitional control of neural activity relies on the natural motor repertoire. *Current Biology*, 23(5):353–361.

[Irwin et al., 2000] Irwin, S. A., Galvez, R., and Greenough, W. T. (2000). Dendritic spine structural anomalies in fragile-x mental retardation syndrome. *Cerebral Cortex*, 10(10):1038–1044.

[Irwin et al., 2001] Irwin, S. A., Patel, B., Idupulapati, M., Harris, J. B., Crisostomo, R. A., Larsen, B. P., Kooy, F., Willems, P. J., Cras, P., Kozlowski, P. B., et al. (2001). Abnormal dendritic spine characteristics in the temporal and visual cortices of patients with fragile-x syndrome: a quantitative examination. *American Journal of Medical Genetics*, 98(2):161–167.

[Isaacson and Scanziani, 2011] Isaacson, J. S. and Scanziani, M. (2011). How inhibition shapes cortical activity. *Neuron*, 72(2):231–243.

[Isomura et al., 2002] Isomura, Y., Fujiwara-Tsukamoto, Y., Imanishi, M., Nambu, A., and Takada, M. (2002). Distance-dependent Ni^{2+}-sensitivity of synaptic plasticity in apical dendrites of hippocampal CA1 pyramidal cells. *Journal of Neurophysiology*, 87(2):1169–1174.

[Jacob et al., 2007] Jacob, V., Brasier, D. J., Erchova, I., Feldman, D., and Shulz, D. E. (2007). Spike timing-dependent synaptic depression in the *in vivo* barrel cortex of the rat. *The Journal of Neuroscience*, 27(6):1271–1284.

[Jaubert-Miazza et al., 2005] Jaubert-Miazza, L., Green, E., Lo, F.-S., Bui, K., Mills, J., and Guido, W. (2005). Structural and functional composition of the developing retinogeniculate pathway in the mouse. *Visual Neuroscience*, 22(5):661–676.

[Jerng et al., 2004] Jerng, H. H., Pfaffinger, P. J., and Covarrubias, M. (2004). Molecular physiology and modulation of somatodendritic A-type potassium channels. *Molecular and Cellular Neuroscience*, 27(4):343–369.

[Jia et al., 2010] Jia, H., Rochefort, N. L., Chen, X., and Konnerth, A. (2010). Dendritic organization of sensory input to cortical neurons *in vivo*. *Nature*, 464(7293):1307–1312.

[Jiang et al., 1998] Jiang, M., Lee, C. L., Smith, K. L., and Swann, J. W. (1998). Spine loss and other persistent alterations of hippocampal pyramidal cell dendrites in a model of early-onset epilepsy. *The Journal of Neuroscience*, 18(20):8356–8368.

[Jiang et al., 2015] Jiang, X., Shen, S., Cadwell, C. R., Berens, P., Sinz, F., Ecker, A. S., Patel, S., and Tolias, A. S. (2015). Principles of connectivity among morphologically defined cell types in adult neocortex. *Science*, 350(6264):aac9462.

[Jiang et al., 2013] Jiang, X., Wang, G., Lee, A. J., Stornetta, R. L., and Zhu, J. J. (2013). The organization of two new cortical interneuronal circuits. *Nature Neuroscience*, 16(2):210–218.

[Jones and Stuart, 2013] Jones, S. L. and Stuart, G. J. (2013). Different calcium sources control somatic versus dendritic SK channel activation during action potentials. *The Journal of Neuroscience*, 33(50):19396–19405.

[Joyner et al., 1975] Joyner, R. W., Moore, J. W., and Ramón, F. (1975). Axon voltage-clamp simulations. III. postsynaptic region. *Biophysical Journal*, 15(1):37.

[Kamondi et al., 1998] Kamondi, A., Acsády, L., and Buzsáki, G. (1998). Dendritic spikes are enhanced by cooperative network activity in the intact hippocampus. *The Journal of Neuroscience*, 18(10):3919–3928.

[Kampa and Stuart, 2006] Kampa, B. M. and Stuart, G. J. (2006). Calcium spikes in basal dendrites of layer 5 pyramidal neurons during action potential bursts. *The Journal of Neuroscience*, 26(28):7424–7432.

[Kantevari et al., 2010] Kantevari, S., Matsuzaki, M., Kanemoto, Y., Kasai, H., and Ellis-Davies, G. C. (2010). Two-color, two-photon uncaging of glutamate and GABA. *Nature Methods*, 7(2):123–125.

[Kasai et al., 2010] Kasai, H., Fukuda, M., Watanabe, S., Hayashi-Takagi, A., and Noguchi, J. (2010). Structural dynamics of dendritic spines in memory and cognition. *Trends in Neurosciences*, 33(3):121–129.

[Katona et al., 2012] Katona, G., Szalay, G., Maák, P., Kaszás, A., Veress, M., Hillier, D., Chiovini, B., Vizi, E. S., Roska, B., and Rózsa, B. (2012). Fast two-photon in vivo imaging with three-dimensional random-access scanning in large tissue volumes. *Nature Methods*, 9(2):201–208.

[Kaufmann and Moser, 2000] Kaufmann, W. E. and Moser, H. W. (2000). Dendritic anomalies in disorders associated with mental retardation. *Cerebral Cortex*, 10(10):981–991.

[Kepecs and Fishell, 2014] Kepecs, A. and Fishell, G. (2014). Interneuron cell types are fit to function. *Nature*, 505(7483):318–326.

[Kim and Hoffman, 2008] Kim, J. and Hoffman, D. A. (2008). Potassium channels: newly found players in synaptic plasticity. *The Neuroscientist*, 14(3):276–86.

[Kirby and Love, 2004] Kirby, A. and Love, G. (2004). Fast, large and controllable phase modulation using dual frequency liquid crystals. *Optics Express*, 12(7):1470–1475.

[Kitamura et al., 2008] Kitamura, K., Judkewitz, B., Kano, M., Denk, W., and Häusser, M. (2008). Targeted patch-clamp recordings and single-cell electroporation of unlabeled neurons *in vivo*. *Nature Methods*, 5(1):61–67.

[Klausberger et al., 2003] Klausberger, T., Magill, P. J., Márton, L. F., Roberts, J. D. B., Cobden, P. M., Buzsáki, G., and Somogyi, P. (2003). Brain-state-and cell-type-specific firing of hippocampal interneurons *in vivo*. *Nature*, 421(6925):844–848.

[Kleindienst et al., 2011] Kleindienst, T., Winnubst, J., Roth-Alpermann, C., Bonhoeffer, T., and Lohmann, C. (2011). Activity-dependent clustering of functional synaptic inputs on developing hippocampal dendrites. *Neuron*, 72(6):1012–1024.

[Koch et al., 1983] Koch, C., Poggio, T., and Torre, V. (1983). Nonlinear interactions in a dendritic tree: localization, timing, and role in information processing. *Proceedings of the National Academy of Sciences*, 80(9):2799–2802.

[Koester and Sakmann, 1998] Koester, H. J. and Sakmann, B. (1998). Calcium dynamics in single spines during coincident pre-and postsynaptic activity depend on relative timing of back-propagating action potentials and subthreshold excitatory postsynaptic potentials. *Proceedings of the National Academy of Sciences*, 95(16):9596–9601.

[Kole et al., 2007a] Kole, M. H., Bräuer, A. U., and Stuart, G. J. (2007a). Inherited cortical HCN1 channel loss amplifies dendritic calcium electrogenesis and burst firing in a rat absence epilepsy model. *The Journal of Physiology*, 578(2):507–525.

[Kole et al., 2007b] Kole, M. H., Letzkus, J. J., and Stuart, G. J. (2007b). Axon initial segment Kv1 channels control axonal action potential waveform and synaptic efficacy. *Neuron*, 55(4):633–647.

[Kole et al., 2006] Kole, M. H. P., Hallermann, S., and Stuart, G. J. (2006). Single I_h channels in pyramidal neuron dendrites: properties, distribution, and impact on action potential output. *Journal of Neuroscience*, 26(6):1677–87.

[Kole et al., 2008] Kole, M. H. P., Ilschner, S. U., Kampa, B. M., Williams, S. R., Ruben, P. C., and Stuart, G. J. (2008). Action potential generation requires a high sodium channel density in the axon initial segment. *Nature Neuroscience*, 11(2):178–86.

[Komai et al., 2006] Komai, S., Denk, W., Osten, P., Brecht, M., and Margrie, T. W. (2006). Two-photon targeted patching (TPTP) *in vivo*. *Nature Protocols*, 1(2):647–652.

[Komiyama et al., 2010] Komiyama, T., Sato, T. R., O'Connor, D. H., Zhang, Y.-X., Huber, D., Hooks, B. M., Gabitto, M., and Svoboda, K. (2010). Learning-related fine-scale specificity imaged in motor cortex circuits of behaving mice. *Nature*, 464(7292):1182–1186.

[Koralek et al., 2012] Koralek, A. C., Jin, X., Long II, J. D., Costa, R. M., and Carmena, J. M. (2012). Corticostriatal plasticity is necessary for learning intentional neuroprosthetic skills. *Nature*, 483(7389):331–335.

[Korngreen and Sakmann, 2000] Korngreen, A. and Sakmann, B. (2000). Voltage-gated K^+ channels in layer 5 neocortical pyramidal neurones from young rats: subtypes and gradients. *The Journal of Physiology*, 525(3):621–639.

[Kovalchuk et al., 2000] Kovalchuk, Y., Eilers, J., Lisman, J., and Konnerth, A. (2000). NMDA receptor-mediated subthreshold Ca^{2+} signals in spines of hippocampal neurons. *The Journal of Neuroscience*, 20(5):1791–1799.

[Krakauer and Mazzoni, 2011] Krakauer, J. W. and Mazzoni, P. (2011). Human sensorimotor learning: adaptation, skill, and beyond. *Current Opinion in Neurobiology*, 21(4):636–644.

[Krook-Magnuson et al., 2015] Krook-Magnuson, E., Armstrong, C., Bui, A., Lew, S., Oijala, M., and Soltesz, I. (2015). *In vivo* evaluation of the dentate gate theory in epilepsy. *The Journal of Physiology*, 593(10):2379–2388.

[Krueppel et al., 2011] Krueppel, R., Remy, S., and Beck, H. (2011). Dendritic integration in hippocampal dentate granule cells. *Neuron*, 71(3):512–528.

[Kuczewski et al., 2008] Kuczewski, N., Porcher, C., Ferrand, N., Fiorentino, H., Pellegrino, C., Kolarow, R., Lessmann, V., Medina, I., and Gaiarsa, J.-L. (2008). Backpropagating action potentials trigger dendritic release of bdnf during spontaneous network activity. *The Journal of Neuroscience*, 28(27):7013–7023.

[Kwan and Dan, 2012] Kwan, A. C. and Dan, Y. (2012). Dissection of cortical microcircuits by single-neuron stimulation *in vivo*. *Current Biology*, 22(16):1459–1467.

[Lai and Jan, 2006] Lai, H. C. and Jan, L. Y. (2006). The distribution and targeting of neuronal voltage-gated ion channels. *Nature Reviews Neuroscience*, 7(7):548–562.

[Lampl et al., 1999] Lampl, I., Reichova, I., and Ferster, D. (1999). Synchronous membrane potential fluctuations in neurons of the cat visual cortex. *Neuron*, 22(2):361–374.

[Lang et al., 2004] Lang, C., Barco, A., Zablow, L., Kandel, E. R., Siegelbaum, S. A., and Zakharenko, S. S. (2004). Transient expansion of synaptically connected dendritic spines upon induction of hippocampal long-term potentiation. *Proceedings of the National Academy of Sciences*, 101(47):16665–16670.

[Lansky et al., 2006] Lansky, P., Sanda, P., and He, J. (2006). The parameters of the stochastic leaky integrate-and-fire neuronal model. *Journal of Computational Neuroscience*, 21(2):211–223.

[Lansky et al., 2010] Lansky, P., Sanda, P., and He, J. (2010). Effect of stimulation on the input parameters of stochastic leaky integrate-and-fire neuronal model. *Journal of Physiology-Paris*, 104(3):160–166.

[Larkum et al., 1999a] Larkum, M. E., Kaiser, K., and Sakmann, B. (1999a). Calcium electrogenesis in distal apical dendrites of layer 5 pyramidal cells at a critical frequency of back-propagating action potentials. *Proceedings of the National Academy of Sciences*, 96(25):14600–14604.

[Larkum et al., 2009] Larkum, M. E., Nevian, T., Sandler, M., Polsky, A., and Schiller, J. (2009). Synaptic integration in tuft dendrites of layer 5 pyramidal neurons: a new unifying principle. *Science*, 325(5941):756–760.

[Larkum et al., 2004] Larkum, M. E., Senn, W., and Lüscher, H.-R. (2004). Top-down dendritic input increases the gain of layer 5 pyramidal neurons. *Cerebral Cortex*, 14(10):1059–1070.

[Larkum et al., 1999b] Larkum, M. E., Zhu, J. J., and Sakmann, B. (1999b). A new cellular mechanism for coupling inputs arriving at different cortical layers. *Nature*, 398(6725):338–341.

[Larkum et al., 2001] Larkum, M. E., Zhu, J. J., and Sakmann, B. (2001). Dendritic mechanisms underlying the coupling of the dendritic with the axonal action potential initiation zone of adult rat layer 5 pyramidal neurons. *The Journal of Physiology*, 533(2):447–466.

[Lavzin et al., 2012] Lavzin, M., Rapoport, S., Polsky, A., Garion, L., and Schiller, J. (2012). Nonlinear dendritic processing determines angular tuning of barrel cortex neurons in vivo. *Nature*, 490(7420):397–401.

[Lecoq et al., 2014] Lecoq, J., Savall, J., Vučinić, D., Grewe, B. F., Kim, H., Li, J. Z., Kitch, L. J., and Schnitzer, M. J. (2014). Visualizing mammalian brain area interactions by dual-axis two-photon calcium imaging. *Nature Neuroscience*, 17(12):1825–1829.

[Lee et al., 2012a] Lee, D., Lin, B.-J., and Lee, A. K. (2012a). Hippocampal place fields emerge upon single-cell manipulation of excitability during behavior. *Science*, 337(6096):849–853.

[Lee et al., 2014] Lee, S.-H., Kwan, A. C., and Dan, Y. (2014). Interneuron subtypes and orientation tuning. *Nature*, 508(7494):E1–E2.

[Lee et al., 2012b] Lee, S.-H., Kwan, A. C., Zhang, S., Phoumthipphavong, V., Flannery, J. G., Masmanidis, S. C., Taniguchi, H., Huang, Z. J., Zhang, F., Boyden, E. S., et al. (2012b). Activation of specific interneurons improves V1 feature selectivity and visual perception. *Nature*, 488(7411):379–383.

[Liesener et al., 2000] Liesener, J., Reicherter, M., Haist, T., and Tiziani, H. (2000). Multi-functional optical tweezers using computer-generated holograms. *Optics Communications*, 185(1):77–82.

[Lin et al., 2008] Lin, M. T., Luján, R., Watanabe, M., Adelman, J. P., and Maylie, J. (2008). SK2 channel plasticity contributes to LTP at schaffer collateral–CA1 synapses. *Nature Neuroscience*, 11(2):170–177.

[Linden, 1999] Linden, D. J. (1999). The return of the spike: postsynaptic action potentials and the induction of LTP and LTD. *Neuron*, 22(4):661–666.

[Liu et al., 2012] Liu, X., Ramirez, S., Pang, P. T., Puryear, C. B., Govindarajan, A., Deisseroth, K., and Tonegawa, S. (2012). Optogenetic stimulation of a hippocampal engram activates fear memory recall. *Nature*, 484(7394):381–385.

[Llinás and Hess, 1976] Llinás, R. and Hess, R. (1976). Tetrodotoxin-resistant dendritic spikes in avian Purkinje cells. *Proceedings of the National Academy of Sciences*, 73(7):2520–2523.

[Llinás et al., 1968] Llinás, R., Nicholson, C., Freeman, J. A., and Hillman, D. E. (1968). Dendritic spikes and their inhibition in alligator Purkinje cells. *Science*, 160(3832):1132–1135.

[Llinás and Sugimori, 1980] Llinás, R. and Sugimori, M. (1980). Electrophysiological properties of *in vitro* purkinje cell dendrites in mammalian cerebellar slices. *The Journal of Physiology*, 305(1):197–213.

[London and Häusser, 2005] London, M. and Häusser, M. (2005). Dendritic computation. *Annual Review of Neuroscience*, 28:503–532.

[London et al., 2010] London, M., Roth, A., Beeren, L., Häusser, M., and Latham, P. E. (2010). Sensitivity to perturbations *in vivo* implies high noise and suggests rate coding in cortex. *Nature*, 466(7302):123–127.

[Longordo et al., 2013] Longordo, F., To, M.-S., Ikeda, K., and Stuart, G. J. (2013). Sublinear integration underlies binocular processing in primary visual cortex. *Nature Neuroscience*, 16(6):714–723.

[Lörincz et al., 2002] Lörincz, A., Notomi, T., Tamás, G., Shigemoto, R., and Nusser, Z. (2002). Polarized and compartment-dependent distribution of HCN1 in pyramidal cell dendrites. *Nature Neuroscience*, 5(11):1185–1193.

[Losonczy and Magee, 2006] Losonczy, A. and Magee, J. C. (2006). Integrative properties of radial oblique dendrites in hippocampal CA1 pyramidal neurons. *Neuron*, 50(2):291–307.

[Lovett-Barron et al., 2012] Lovett-Barron, M., Turi, G. F., Kaifosh, P., Lee, P. H., Bolze, F., Sun, X.-H., Nicoud, J.-F., Zemelman, B. V., Sternson, S. M., and Losonczy, A. (2012). Regulation of neuronal input transformations by tunable dendritic inhibition. *Nature Neuroscience*, 15(3):423–430.

[Ludwig et al., 1998] Ludwig, A., Zong, X., Jeglitsch, M., Hofmann, F., and Biel, M. (1998). A family of hyperpolarization-activated mammalian cation channels. *Nature*, 393(6685):587–591.

[Ludwig and Pittman, 2003] Ludwig, M. and Pittman, Q. J. (2003). Talking back: dendritic neurotransmitter release. *Trends in Neurosciences*, 26(5):255–261.

[Ludwig et al., 2002] Ludwig, M., Sabatier, N., Bull, P. M., Landgraf, R., Dayanithi, G., and Leng, G. (2002). Intracellular calcium stores regulate activity-dependent neuropeptide release from dendrites. *Nature*, 418(6893):85–89.

[Lüscher et al., 1997] Lüscher, C., Jan, L. Y., Stoffel, M., Malenka, R. C., and Nicoll, R. A. (1997). G protein-coupled inwardly rectifying K^+ channels (GIRKs) mediate postsynaptic but not presynaptic transmitter actions in hippocampal neurons. *Neuron*, 19(3):687–695.

[Lutz et al., 2008] Lutz, C., Otis, T. S., DeSars, V., Charpak, S., DiGregorio, D. A., and Emiliani, V. (2008). Holographic photolysis of caged neurotransmitters. *Nature Methods*, 5(9):821–827.

[Magee, 1998] Magee, J. C. (1998). Dendritic hyperpolarization-activated currents modify the integrative properties of hippocampal CA1 pyramidal neurons. *The Journal of Neuroscience*, 18(19):7613–7624.

[Magee, 1999] Magee, J. C. (1999). Dendritic I_h normalizes temporal summation in hippocampal CA1 neurons. *Nature Neuroscience*, 2(6):508–514.

[Magee and Carruth, 1999] Magee, J. C. and Carruth, M. (1999). Dendritic voltage-gated ion channels regulate the action potential firing mode of hippocampal CA1 pyramidal neurons. *Journal of Neurophysiology*, 82(4):1895–1901.

[Magee et al., 1995] Magee, J. C., Christofi, G., Miyakawa, H., Christie, B., Lasser-Ross, N., and Johnston, D. (1995). Subthreshold synaptic activation of voltage-gated Ca^{2+} channels mediates a localized Ca^{2+} influx into the dendrites of hippocampal pyramidal neurons. *Journal of Neurophysiology*, 74(3):1335–1342.

[Magee and Johnston, 1995] Magee, J. C. and Johnston, D. (1995). Synaptic activation of voltage-gated channels in the dendrites of hippocampal pyramidal neurons. *Science*, 268(5208):301–304.

[Magee and Johnston, 1997] Magee, J. C. and Johnston, D. (1997). A synaptically controlled, associative signal for hebbian plasticity in hippocampal neurons. *Science*, 275(5297):209–213.

[Mainen et al., 1999] Mainen, Z. F., Malinow, R., and Svoboda, K. (1999). Synaptic calcium transients in single spines indicate that NMDA receptors are not saturated. *Nature*, 399(6732):151–155.

[Majewska et al., 2000] Majewska, A., Brown, E., Ross, J., and Yuste, R. (2000). Mechanisms of calcium decay kinetics in hippocampal spines: role of spine calcium pumps and calcium diffusion through the spine neck in biochemical compartmentalization. *The Journal of Neuroscience*, 20(5):1722–1734.

[Major et al., 2013] Major, G., Larkum, M. E., and Schiller, J. (2013). Active properties of neocortical pyramidal neuron dendrites. *Annual Review of Neuroscience*, 36:1–24.

[Maletic-Savatic et al., 1999] Maletic-Savatic, M., Malinow, R., and Svoboda, K. (1999). Rapid dendritic morphogenesis in CA1 hippocampal dendrites induced by synaptic activity. *Science*, 283(5409):1923–1927.

[Mao et al., 2011] Mao, T., Kusefoglu, D., Hooks, B. M., Huber, D., Petreanu, L., and Svoboda, K. (2011). Long-range neuronal circuits underlying the interaction between sensory and motor cortex. *Neuron*, 72(1):111–123.

[Margrie et al., 2003] Margrie, T. W., Meyer, A. H., Caputi, A., Monyer, H., Hasan, M. T., Schaefer, A. T., Denk, W., and Brecht, M. (2003). Targeted whole-cell recordings in the mammalian brain *in vivo*. *Neuron*, 39(6):911–918.

[Markram et al., 1997] Markram, H., Lübke, J., Frotscher, M., and Sakmann, B. (1997). Regulation of synaptic efficacy by coincidence of postsynaptic APs and EPSPs. *Science*, 275(5297):213–215.

[Markram and Sakmann, 1994] Markram, H. and Sakmann, B. (1994). Calcium transients in dendrites of neocortical neurons evoked by single subthreshold excitatory postsynaptic potentials via low-voltage-activated calcium channels. *Proceedings of the National Academy of Sciences*, 91(11):5207–5211.

[Markram et al., 2004] Markram, H., Toledo-Rodriguez, M., Wang, Y., Gupta, A., Silberberg, G., and Wu, C. (2004). Interneurons of the neocortical inhibitory system. *Nature Reviews Neuroscience*, 5(10):793–807.

[Martina et al., 2000] Martina, M., Vida, I., and Jonas, P. (2000). Distal initiation and active propagation of action potentials in interneuron dendrites. *Science*, 287(5451):295–300.

[Matsuzaki et al., 2001] Matsuzaki, M., Ellis-Davies, G. C., Nemoto, T., Miyashita, Y., Iino, M., and Kasai, H. (2001). Dendritic spine geometry is critical for AMPA receptor expression in hippocampal CA1 pyramidal neurons. *Nature Neuroscience*, 4(11):1086–1092.

[Matsuzaki et al., 2004] Matsuzaki, M., Honkura, N., Ellis-Davies, G. C., and Kasai, H. (2004). Structural basis of long-term potentiation in single dendritic spines. *Nature*, 429(6993):761–766.

[Medini, 2011] Medini, P. (2011). Layer-and cell-type-specific subthreshold and suprathreshold effects of long-term monocular deprivation in rat visual cortex. *The Journal of Neuroscience*, 31(47):17134–17148.

[Mehaffey et al., 2005] Mehaffey, W. H., Doiron, B., Maler, L., and Turner, R. W. (2005). Deterministic multiplicative gain control with active dendrites. *The Journal of Neuroscience*, 25(43):9968–9977.

[Mehta, 2004] Mehta, M. R. (2004). Cooperative LTP can map memory sequences on dendritic branches. *Trends in Neurosciences*, 27(2):69–72.

[Migliore et al., 2004] Migliore, M., Messineo, L., and Ferrante, M. (2004). Dendritic I_h selectively blocks temporal summation of unsynchronized distal inputs in ca1 pyramidal neurons. *Journal of Computational Neuroscience*, 16(1):5–13.

[Migliore and Shepherd, 2002] Migliore, M. and Shepherd, G. M. (2002). Emerging rules for the distributions of active dendritic conductances. *Nature Reviews Neuroscience*, 3(5):362–70.

[Milburn et al., 1989] Milburn, T., Matsubara, N., Billington, A. P., Udgaonkar, J. B., Walker, J. W., Carpenter, B. K., Webb, W. W., Marque, J., and Denk, W. (1989). Synthesis, photochemistry, and biological activity of a caged photolabile acetylcholine receptor ligand. *Biochemistry*, 28(1):49–55.

[Miles et al., 1996] Miles, R., Tóth, K., Gulyás, A. I., Hájos, N., and Freund, T. F. (1996). Differences between somatic and dendritic inhibition in the hippocampus. *Neuron*, 16(4):815–823.

[Milojkovic et al., 2005a] Milojkovic, B., Wuskell, J., Loew, L., and Antic, S. (2005a). Initiation of sodium spikelets in basal dendrites of neocortical pyramidal neurons. *The Journal of Membrane Biology*, 208(2):155–169.

[Milojkovic et al., 2005b] Milojkovic, B. A., Radojicic, M. S., and Antic, S. D. (2005b). A strict correlation between dendritic and somatic plateau depolarizations in the rat prefrontal cortex pyramidal neurons. *The Journal of Neuroscience*, 25(15):3940–3951.

[Mitchell and Silver, 2003] Mitchell, S. J. and Silver, R. A. (2003). Shunting inhibition modulates neuronal gain during synaptic excitation. *Neuron*, 38(3):433–445.

[Monier et al., 2008] Monier, C., Fournier, J., and Frégnac, Y. (2008). *In vitro* and *in vivo* measures of evoked excitatory and inhibitory conductance dynamics in sensory cortices. *Journal of Neuroscience Methods*, 169(2):323–65.

[Muir-Robinson et al., 2002] Muir-Robinson, G., Hwang, B. J., and Feller, M. B. (2002). Retinogeniculate axons undergo eye-specific segregation in the absence of eye-specific layers. *The Journal of Neuroscience*, 22(13):5259–5264.

[Müller and Connor, 1991] Müller, W. and Connor, J. A. (1991). Dendritic spines as individual neuronal compartments for synaptic Ca^{2+} responses. *Nature*.

[Mulley et al., 2003] Mulley, J. C., Scheffer, I. E., Petrou, S., and Berkovic, S. F. (2003). Channelopathies as a genetic cause of epilepsy. *Current Opinion in Neurology*, 16(2):171–176.

[Multani et al., 1994] Multani, P., Myers, R., Blume, H., Schomer, D., and Sotrel, A. (1994). Neocortical dendritic pathology in human partial epilepsy: a quantitative golgi study. *Epilepsia*, 35(4):728–736.

[Murayama and Larkum, 2009] Murayama, M. and Larkum, M. E. (2009). Enhanced dendritic activity in awake rats. *Proceedings of the National Academy of Sciences*, 106(48):20482–20486.

[Murayama et al., 2009] Murayama, M., Pérez-Garci, E., Nevian, T., Bock, T., Senn, W., and Larkum, M. E. (2009). Dendritic encoding of sensory stimuli controlled by deep cortical interneurons. *Nature*, 457(7233):1137–1141.

[Murphy and Miller, 2003] Murphy, B. K. and Miller, K. D. (2003). Multiplicative gain changes are induced by excitation or inhibition alone. *The Journal of Neuroscience*, 23(31):10040–10051.

[Nägerl et al., 2004] Nägerl, U. V., Eberhorn, N., Cambridge, S. B., and Bonhoeffer, T. (2004). Bidirectional activity-dependent morphological plasticity in hippocampal neurons. *Neuron*, 44(5):759–767.

[Nevian et al., 2007] Nevian, T., Larkum, M. E., Polsky, A., and Schiller, J. (2007). Properties of basal dendrites of layer 5 pyramidal neurons: a direct patch-clamp recording study. *Nature Neuroscience*, 10(2):206–214.

[Nevian and Sakmann, 2006] Nevian, T. and Sakmann, B. (2006). Spine Ca^{2+} signaling in spike-timing-dependent plasticity. *The Journal of Neuroscience*, 26(43):11001–11013.

[Ngo-Anh et al., 2005] Ngo-Anh, T. J., Bloodgood, B. L., Lin, M., Sabatini, B. L., Maylie, J., and Adelman, J. P. (2005). SK channels and NMDA receptors form a Ca^{2+}-mediated feedback loop in dendritic spines. *Nature Neuroscience*, 8(5):642–649.

[Nikolenko et al., 2008] Nikolenko, V., Watson, B. O., Araya, R., Woodruff, A., Peterka, D. S., and Yuste, R. (2008). SLM microscopy: scanless two-photon imaging and photostimulation with spatial light modulators. *Frontiers in Neural Circuits*, 2.

[Nimchinsky et al., 2002] Nimchinsky, E. A., Sabatini, B. L., and Svoboda, K. (2002). Structure and function of dendritic spines. *Annual Review of Physiology*, 64(1):313–353.

[Noguchi et al., 2011] Noguchi, J., Nagaoka, A., Watanabe, S., Ellis-Davies, G. C., Kitamura, K., Kano, M., Matsuzaki, M., and Kasai, H. (2011). *In vivo* two-photon uncaging of glutamate revealing the structure–function relationships of dendritic spines in the neocortex of adult mice. *The Journal of Physiology*, 589(10):2447–2457.

[Notomi and Shigemoto, 2004] Notomi, T. and Shigemoto, R. (2004). Immunohistochemical localization of I_h channel subunits, HCN1–4, in the rat brain. *Journal of Comparative Neurology*, 471(3):241–276.

[O'Connor et al., 2010] O'Connor, D. H., Clack, N. G., Huber, D., Komiyama, T., Myers, E. W., and Svoboda, K. (2010). Vibrissa-based object localization in head-fixed mice. *The Journal of Neuroscience*, 30(5):1947–1967.

[Ohtsuki et al., 2012] Ohtsuki, G., Piochon, C., Adelman, J. P., and Hansel, C. (2012). SK2 channel modulation contributes to compartment-specific dendritic plasticity in cerebellar Purkinje cells. *Neuron*, 75(1):108–120.

[Ohzawa and Freeman, 1986a] Ohzawa, I. and Freeman, R. D. (1986a). The binocular organization of complex cells in the cat's visual cortex. *Journal of Neurophysiology*, 56(1):243–259.

[Ohzawa and Freeman, 1986b] Ohzawa, I. and Freeman, R. D. (1986b). The binocular organization of simple cells in the cat's visual cortex. *Journal of Neurophysiology*, 56(1):221–242.

[Okun and Lampl, 2008] Okun, M. and Lampl, I. (2008). Instantaneous correlation of excitation and inhibition during ongoing and sensory-evoked activities. *Nature Neuroscience*, 11(5):535–537.

[Oláh et al., 2009] Oláh, S., Füle, M., Komlósi, G., Varga, C., Báldi, R., Barzó, P., and Tamás, G. (2009). Regulation of cortical microcircuits by unitary GABA-mediated volume transmission. *Nature*, 461(7268):1278–1281.

[Palima and Daria, 2006] Palima, D. and Daria, V. R. (2006). Effect of spurious diffraction orders in arbitrary multifoci patterns produced via phase-only holograms. *Applied Optics*, 45(26):6689.

[Palima and Daria, 2007] Palima, D. and Daria, V. R. (2007). Holographic projection of arbitrary light patterns with a suppressed zero-order beam. *Applied Optics*, 46(20):4197.

[Palmer et al., 2012a] Palmer, L., Murayama, M., and Larkum, M. (2012a). Inhibitory regulation of dendritic activity *in vivo*. *Frontiers in Neural Circuits*, 6(26).

[Palmer et al., 2012b] Palmer, L. M., Schulz, J. M., Murphy, S. C., Ledergerber, D., Murayama, M., and Larkum, M. E. (2012b). The cellular basis of $GABA_B$-mediated interhemispheric inhibition. *Science*, 335(6071):989–993.

[Palmer et al., 2014] Palmer, L. M., Shai, A. S., Reeve, J. E., Anderson, H. L., Paulsen, O., and Larkum, M. E. (2014). NMDA spikes enhance action potential generation during sensory input. *Nature Neuroscience*, 17(3):383–390.

[Palmer and Stuart, 2009] Palmer, L. M. and Stuart, G. J. (2009). Membrane potential changes in dendritic spines during action potentials and synaptic input. *The Journal of Neuroscience*, 29(21):6897–6903.

[Paluch-Siegler et al., 2015] Paluch-Siegler, S., Mayblum, T., Dana, H., Brosh, I., Gefen, I., and Shoham, S. (2015). All-optical bidirectional neural interfacing using hybrid multiphoton holographic optogenetic stimulation. *Neurophotonics*, 2(3):031208.

[Papagiakoumou et al., 2010] Papagiakoumou, E., Anselmi, F., Bègue, A., de Sars, V., Glückstad, J., Isacoff, E. Y., and Emiliani, V. (2010). Scanless two-photon excitation of channelrhodopsin-2. *Nature Methods*, 7(10):848–854.

[Parks and Rubel, 1975] Parks, T. N. and Rubel, E. W. (1975). Organization and development of brain stem auditory nuclei of the chicken: organization of projections from n. magnocellularis to n. laminaris. *Journal of Comparative Neurology*, 164(4):435–448.

[Paz et al., 2013] Paz, J. T., Davidson, T. J., Frechette, E. S., Delord, B., Parada, I., Peng, K., Deisseroth, K., and Huguenard, J. R. (2013). Closed-loop optogenetic control of thalamus as a tool for interrupting seizures after cortical injury. *Nature Neuroscience*, 16(1):64–70.

[Penzes et al., 2011] Penzes, P., Cahill, M. E., Jones, K. A., VanLeeuwen, J.-E., and Woolfrey, K. M. (2011). Dendritic spine pathology in neuropsychiatric disorders. *Nature Neuroscience*, 14(3):285–293.

[Pérez-Garci et al., 2013] Pérez-Garci, E., Larkum, M. E., and Nevian, T. (2013). Inhibition of dendritic Ca^{2+} spikes by $GABA_B$ receptors in cortical pyramidal neurons is mediated by a direct gi/o-$\beta\gamma$-subunit interaction with Cav1 channels. *The Journal of Physiology*, 591(7):1599–1612.

[Peters and Kaiserman-Abramof, 1970] Peters, A. and Kaiserman-Abramof, I. R. (1970). The small pyramidal neuron of the rat cerebral cortex. the perikaryon, dendrites and spines. *American Journal of Anatomy*, 127(4):321–355.

[Petersen et al., 2003] Petersen, C. C. H., Hahn, T. T. G., Mehta, M., Grinvald, A., and Sakmann, B. (2003). Interaction of sensory responses with spontaneous depolarization in layer 2/3 barrel cortex. *Proceedings of the National Academy of Sciences*, 100(23):13638–13643.

[Petreanu et al., 2009] Petreanu, L., Mao, T., Sternson, S. M., and Svoboda, K. (2009). The subcellular organization of neocortical excitatory connections. *Nature*, 457(7233):1142–1145.

[Pettit et al., 1997] Pettit, D. L., Wang, S. S.-H., Gee, K. R., and Augustine, G. J. (1997). Chemical two-photon uncaging: a novel approach to mapping glutamate receptors. *Neuron*, 19(3):465–471.

[Pfeffer et al., 2013] Pfeffer, C. K., Xue, M., He, M., Huang, Z. J., and Scanziani, M. (2013). Inhibition of inhibition in visual cortex: the logic of connections between molecularly distinct interneurons. *Nature Neuroscience*, 16(8):1068–1076.

[Pillow et al., 2008] Pillow, J. W., Shlens, J., Paninski, L., Sher, A., Litke, A. M., Chichilnisky, E., and Simoncelli, E. P. (2008). Spatio-temporal correlations and visual signalling in a complete neuronal population. *Nature*, 454(7207):995–999.

[Poirazi et al., 2003] Poirazi, P., Brannon, T., and Mel, B. W. (2003). Pyramidal neuron as two-layer neural network. *Neuron*, 37(6):989–999.

[Poleg-Polsky and Diamond, 2011] Poleg-Polsky, A. and Diamond, J. S. (2011). Imperfect space clamp permits electrotonic interactions between inhibitory and excitatory synaptic conductances, distorting voltage clamp recordings. *PloS One*, 6(4):e19463.

[Pologruto et al., 2003] Pologruto, T. A., Sabatini, B. L., and Svoboda, K. (2003). Scanimage: flexible software for operating laser scanning microscopes. *BioMedical Engineering OnLine*, 2(1):13.

[Polsky et al., 2004] Polsky, A., Mel, B. W., and Schiller, J. (2004). Computational subunits in thin dendrites of pyramidal cells. *Nature Neuroscience*, 7(6):621–627.

[Poolos and Johnston, 2012] Poolos, N. P. and Johnston, D. (2012). Dendritic ion channelopathy in acquired epilepsy. *Epilepsia*, 53(s9):32–40.

[Poolos et al., 2002] Poolos, N. P., Migliore, M., and Johnston, D. (2002). Pharmacological upregulation of h-channels reduces the excitability of pyramidal neuron dendrites. *Nature Neuroscience*, 5(8):767–774.

[Pospischil et al., 2009] Pospischil, M., Piwkowska, Z., Bal, T., and Destexhe, A. (2009). Extracting synaptic conductances from single membrane potential traces. *Neuroscience*, 158(2):545–552.

[Pospischil et al., 2007] Pospischil, M., Piwkowska, Z., Rudolph, M., Bal, T., and Destexhe, A. (2007). Calculating event-triggered average synaptic conductances from the membrane potential. *Journal of Neurophysiology*, 97(3):2544–2552.

[Pospischil et al., 2008] Pospischil, M., Toledo-Rodriguez, M., Monier, C., Piwkowska, Z., Bal, T., Frégnac, Y., Markram, H., and Destexhe, A. (2008). Minimal Hodgkin-Huxley type models for different classes of cortical and thalamic neurons. *Biological Cybernetics*, 99(4-5):427–41.

[Pouille and Scanziani, 2001] Pouille, F. and Scanziani, M. (2001). Enforcement of temporal fidelity in pyramidal cells by somatic feed-forward inhibition. *Science*, 293(5532):1159–1163.

[Pouille et al., 2013] Pouille, F., Watkinson, O., Scanziani, M., and Trevelyan, A. J. (2013). The contribution of synaptic location to inhibitory gain control in pyramidal cells. *Physiological Reports*, 1(5).

[Prescott and De Koninck, 2003] Prescott, S. A. and De Koninck, Y. (2003). Gain control of firing rate by shunting inhibition: roles of synaptic noise and dendritic saturation. *Proceedings of the National Academy of Sciences*, 100(4):2076–2081.

[Rall, 1959] Rall, W. (1959). Branching dendritic trees and motoneuron membrane resistivity. *Experimental Neurology*, 1(5):491–527.

[Rall, 1964] Rall, W. (1964). Theoretical significance of dendritic trees for neuronal input-output relations. *Neural Theory and Modeling*, pages 73–97.

[Rall et al., 1995] Rall, W., Segev, I., Rinzel, J., and Shepherd, G. M. (1995). *The theoretical foundation of dendritic function: selected papers of Wilfrid Rall with commentaries*. MIT press.

[Ranganathan et al., 2014] Ranganathan, R., Wieser, J., Mosier, K. M., Mussa-Ivaldi, F. A., and Scheidt, R. A. (2014). Learning redundant motor tasks with and without overlapping dimensions: facilitation and interference effects. *The Journal of Neuroscience*, 34(24):8289–8299.

[Reddy et al., 2008] Reddy, G. D., Kelleher, K., Fink, R., and Saggau, P. (2008). Three-dimensional random access multiphoton microscopy for functional imaging of neuronal activity. *Nature Neuroscience*, 11(6):713–720.

[Restani et al., 2009] Restani, L., Cerri, C., Pietrasanta, M., Gianfranceschi, L., Maffei, L., and Caleo, M. (2009). Functional masking of deprived eye responses by callosal input during ocular dominance plasticity. *Neuron*, 64(5):707–718.

[Reutsky-Gefen et al., 2013] Reutsky-Gefen, I., Golan, L., Farah, N., Schejter, A., Tsur, L., Brosh, I., and Shoham, S. (2013). Holographic optogenetic stimulation of patterned neuronal activity for vision restoration. *Nature Communications*, 4:1509.

[Robinson and Siegelbaum, 2003] Robinson, R. B. and Siegelbaum, S. A. (2003). Hyperpolarization-activated cation currents: from molecules to physiological function. *Annual Review of Physiology*, 65(1):453–480.

[Rochefort and Konnerth, 2012] Rochefort, N. L. and Konnerth, A. (2012). Dendritic spines: from structure to *in vivo* function. *EMBO Reports*, 13(8):699–708.

[Rothman et al., 2009] Rothman, J. S., Cathala, L., Steuber, V., and Silver, R. A. (2009). Synaptic depression enables neuronal gain control. *Nature*, 457(7232):1015–1018.

[Rudolph and Destexhe, 2003] Rudolph, M. and Destexhe, A. (2003). Characterization of subthreshold voltage fluctuations in neuronal membranes. *Neural Computation*, 15(11):2577–2618.

[Rudolph et al., 2004] Rudolph, M., Piwkowska, Z., Badoual, M., Bal, T., and Destexhe, A. (2004). A method to estimate synaptic conductances from membrane potential fluctuations. *Journal of Neurophysiology*, 91(6):2884–2896.

[Rudy et al., 2011] Rudy, B., Fishell, G., Lee, S., and Hjerling-Leffler, J. (2011). Three groups of interneurons account for nearly 100% of neocortical gabaergic neurons. *Developmental Neurobiology*, 71(1):45–61.

[Sabatini and Svoboda, 2000] Sabatini, B. L. and Svoboda, K. (2000). Analysis of calcium channels in single spines using optical fluctuation analysis. *Nature*, 408(6812):589–593.

[Sadtler et al., 2014] Sadtler, P. T., Quick, K. M., Golub, M. D., Chase, S. M., Ryu, S. I., Tyler-Kabara, E. C., Byron, M. Y., and Batista, A. P. (2014). Neural constraints on learning. *Nature*, 512(7515):423–426.

[Sah, 1996] Sah, P. (1996). Ca^{2+}-activated K^{+} currents in neurones: types, physiological roles and modulation. *Trends in Neurosciences*, 19(4):150–154.

[Sakmann and Neher, 1984] Sakmann, B. and Neher, E. (1984). Patch clamp techniques for studying ionic channels in excitable membranes. *Annual Review of Physiology*, 46(1):455–472.

[Sanchez-Vives and McCormick, 2000] Sanchez-Vives, M. V. and McCormick, D. A. (2000). Cellular and network mechanisms of rhythmic recurrent activity in neocortex. *Nature Neuroscience*, 3(10):1027–1034.

[Santoro and Tibbs, 1999] Santoro, B. and Tibbs, G. R. (1999). The HCN gene family: molecular basis of the hyperpolarization-activated pacemaker channels. *Annals of the New York Academy of Sciences*, 868(1):741–764.

[Scanziani and Häusser, 2009] Scanziani, M. and Häusser, M. (2009). Electrophysiology in the age of light. *Nature*, 461(7266):930–9.

[Schiller et al., 2000] Schiller, J., Major, G., Koester, H. J., and Schiller, Y. (2000). NMDA spikes in basal dendrites of cortical pyramidal neurons. *Nature*, 404(6775):285–289.

[Schiller et al., 1997] Schiller, J., Schiller, Y., Stuart, G., and Sakmann, B. (1997). Calcium action potentials restricted to distal apical dendrites of rat neocortical pyramidal neurons. *The Journal of Physiology*, 505(3):605–616.

[Schneidman et al., 2006] Schneidman, E., Berry, M. J., Segev, R., and Bialek, W. (2006). Weak pairwise correlations imply strongly correlated network states in a neural population. *Nature*, 440(7087):1007–1012.

[Schuett et al., 2001] Schuett, S., Bonhoeffer, T., and Hübener, M. (2001). Pairing-induced changes of orientation maps in cat visual cortex. *Neuron*, 32(2):325–337.

[Schultz, 1998] Schultz, W. (1998). Predictive reward signal of dopamine neurons. *Journal of Neurophysiology*, 80(1):1–27.

[Schultz, 2013] Schultz, W. (2013). Updating dopamine reward signals. *Current Opinion in Neurobiology*, 23(2):229–238.

[Schulz and Scholz, 1991] Schulz, E. and Scholz, B. (1991). Neurohistological findings in the parietal cortex of children with chromosome aberrations. *Journal fur Hirnforschung*, 33(1):37–62.

[Schwarz et al., 2010] Schwarz, C., Hentschke, H., Butovas, S., Haiss, F., Stüttgen, M. C., Gerdjikov, T. V., Bergner, C. G., and Waiblinger, C. (2010). The head-fixed behaving rat-procedures and pitfalls. *Somatosensory & Motor Research*, 27(4):131–148.

[Seamans and Yang, 2004] Seamans, J. K. and Yang, C. R. (2004). The principal features and mechanisms of dopamine modulation in the prefrontal cortex. *Progress in Neurobiology*, 74(1):1–58.

[Seelig et al., 2010] Seelig, J. D., Chiappe, M. E., Lott, G. K., Dutta, A., Osborne, J. E., Reiser, M. B., and Jayaraman, V. (2010). Two-photon calcium imaging from head-fixed drosophila during optomotor walking behavior. *Nature Methods*, 7(7):535–540.

[Serruya et al., 2002] Serruya, M. D., Hatsopoulos, N. G., Paninski, L., Fellows, M. R., and Donoghue, J. P. (2002). Brain-machine interface: Instant neural control of a movement signal. *Nature*, 416(6877):141–142.

[Shadlen and Newsome, 1998] Shadlen, M. N. and Newsome, W. T. (1998). The variable discharge of cortical neurons: Implications for connectivity, computation, and information coding. *Journal of Neuroscience*, 18(10):3870–3896.

[Shah et al., 2004] Shah, M. M., Anderson, A. E., Leung, V., Lin, X., and Johnston, D. (2004). Seizure-induced plasticity of h channels in entorhinal cortical layer III pyramidal neurons. *Neuron*, 44(3):495–508.

[Shepherd, 2012] Shepherd, G. M. (2012). Circuit mapping by ultraviolet uncaging of glutamate. *Cold Spring Harbor Protocols*, 2012(9):998–1004.

[Shu et al., 2003a] Shu, Y., Hasenstaub, A., Badoual, M., Bal, T., and McCormick, D. A. (2003a). Barrages of synaptic activity control the gain and sensitivity of cortical neurons. *The Journal of Neuroscience*, 23(32):10388–10401.

[Shu et al., 2006] Shu, Y., Hasenstaub, A., Duque, A., Yu, Y., and McCormick, D. A. (2006). Modulation of intracortical synaptic potentials by presynaptic somatic membrane potential. *Nature*, 441(7094):761–765.

[Shu et al., 2003b] Shu, Y., Hasenstaub, A., and McCormick, D. A. (2003b). Turning on and off recurrent balanced cortical activity. *Nature*, 423(6937):288–293.

[Shuler and Bear, 2006] Shuler, M. G. and Bear, M. F. (2006). Reward timing in the primary visual cortex. *Science*, 311(5767):1606–1609.

[Silberberg and Markram, 2007] Silberberg, G. and Markram, H. (2007). Disynaptic inhibition between neocortical pyramidal cells mediated by martinotti cells. *Neuron*, 53(5):735–746.

[Silver et al., 2003] Silver, R. A., Lübke, J., Sakmann, B., and Feldmeyer, D. (2003). High-probability uniquantal transmission at excitatory synapses in barrel cortex. *Science*, 302(5652):1981–1984.

[Simmons et al., 1995] Simmons, M. L., Terman, G. W., Gibbs, S. M., and Chavkin, C. (1995). L-type calcium channels mediate dynorphin neuropeptide release from dendrites but not axons of hippocampal granule cells. *Neuron*, 14(6):1265–1272.

[Sivyer and Williams, 2013] Sivyer, B. and Williams, S. R. (2013). Direction selectivity is computed by active dendritic integration in retinal ganglion cells. *Nature Neuroscience*, 16(12):1848–1856.

[Sjöström et al., 2008] Sjöström, P. J., Rancz, E. A., Roth, A., and Häusser, M. (2008). Dendritic excitability and synaptic plasticity. *Physiological Reviews*, 88(2):769–840.

[Slotnick, 2009] Slotnick, B. (2009). A simple 2-transistor touch or lick detector circuit. *Journal of the Experimental Analysis of Behavior*, 91(2):253–255.

[Smith and Rubel, 1979] Smith, D. J. and Rubel, E. W. (1979). Organization and development of brain stem auditory nuclei of the chicken: dendritic gradients in nucleus laminaris. *Journal of Comparative Neurology*, 186(2):213–239.

[Smith et al., 2013] Smith, S. L., Smith, I. T., Branco, T., and Häusser, M. (2013). Dendritic spikes enhance stimulus selectivity in cortical neurons *in vivo*. *Nature*, 503(7474):115–120.

[Sofroniew et al., 2014] Sofroniew, N. J., Cohen, J. D., Lee, A. K., and Svoboda, K. (2014). Natural whisker-guided behavior by head-fixed mice in tactile virtual reality. *The Journal of Neuroscience*, 34(29):9537–9550.

[Somogyi and Klausberger, 2005] Somogyi, P. and Klausberger, T. (2005). Defined types of cortical interneurone structure space and spike timing in the hippocampus. *The Journal of Physiology*, 562(1):9–26.

[Somogyi et al., 1998] Somogyi, P., Tamás, G., Lujan, R., and Buhl, E. H. (1998). Salient features of synaptic organisation in the cerebral cortex. *Brain Research Reviews*, 26(2-3):113–135.

[Somogyl, 1995] Somogyl, P. (1995). Synchronization of neuronal activity in hippocampus by individual gabaergic interneurons. *Nature*, 378:2.

[Spruston, 2008] Spruston, N. (2008). Pyramidal neurons: dendritic structure and synaptic integration. *Nature Reviews Neuroscience*, 9(3):206–21.

[Spruston et al., 1993] Spruston, N., Jaffe, D. B., Williams, S. H., and Johnston, D. (1993). Voltage- and space-clamp errors associated with the measurement of electrotonically remote synaptic events. *Journal of Neurophysiology*, 70:781–781.

[Spruston et al., 1995] Spruston, N., Schiller, Y., Stuart, G., and Sakmann, B. (1995). Activity-dependent action potential invasion and calcium influx into hippocampal CA1 dendrites. *Science*, 268(5208):297–300.

[Stackman et al., 2002] Stackman, R. W., Hammond, R. S., Linardatos, E., Gerlach, A., Maylie, J., Adelman, J. P., and Tzounopoulos, T. (2002). Small conductance Ca^{2+}-activated K^{+} channels modulate synaptic plasticity and memory encoding. *The Journal of Neuroscience*, 22(23):10163–10171.

[Steriade et al., 1993] Steriade, M., Nunez, A., and Amzica, F. (1993). A novel slow (< 1 hz) oscillation of neocortical neurons *in vivo*: depolarizing and hyperpolarizing components. *The Journal of Neuroscience*, 13(8):3252–3265.

[Stotler, 1953] Stotler, W. (1953). An experimental study of the cells and connections of the superior olivary complex of the cat. *Journal of Comparative Neurology*, 98(3):401–431.

[Strauss et al., 2004] Strauss, U., Kole, M. H., BraÈuer, A. U., Pahnke, J., Bajorat, R., Rolfs, A., Nitsch, R., and Deisz, R. A. (2004). An impaired neocortical I_h is associated with enhanced excitability and absence epilepsy. *European Journal of Neuroscience*, 19(11):3048–3058.

[Stuart et al., 1993] Stuart, G., Dodt, H., and Sakmann, B. (1993). Patch-clamp recordings from the soma and dendrites of neurons in brain slices using infrared video microscopy. *Pflügers Archiv*, 423(5-6):511–518.

[Stuart and Häusser, 1994] Stuart, G. and Häusser, M. (1994). Initiation and spread of sodium action potentials in cerebellar Purkinje cells. *Neuron*, 13(3):703–712.

[Stuart and Sakmann, 1995] Stuart, G. and Sakmann, B. (1995). Amplification of EPSPs by axosomatic sodium channels in neocortical pyramidal neurons. *Neuron*, 15(5):1065–1076.

[Stuart et al., 1997a] Stuart, G., Schiller, J., and Sakmann, B. (1997a). Action potential initiation and propagation in rat neocortical pyramidal neurons. *The Journal of Physiology*, 505(3):617–632.

[Stuart et al., 2008] Stuart, G., Spruston, N., and Häusser, M. (2008). *Dendrites*. Oxford University Press New York.

[Stuart et al., 1997b] Stuart, G., Spruston, N., Sakmann, B., and Häusser, M. (1997b). Action potential initiation and backpropagation in neurons of the mammalian CNS. *Trends in Neurosciences*, 20(3):125–131.

[Stuart and Häusser, 2001] Stuart, G. J. and Häusser, M. (2001). Dendritic coincidence detection of EPSPs and action potentials. *Nature Neuroscience*, 4(1):63–71.

[Stuart et al., 1994] Stuart, G. J., Sakmann, B., et al. (1994). Active propagation of somatic action potentials into neocortical pyramidal cell dendrites. *Nature*, 367(6458):69–72.

[Stuart and Spruston, 2015] Stuart, G. J. and Spruston, N. (2015). Dendritic integration: 60 years of progress. *Nature Neuroscience*, 18(12):1713–1721.

[Sturgill and Isaacson, 2015] Sturgill, J. F. and Isaacson, J. S. (2015). Somatostatin cells regulate sensory response fidelity via subtractive inhibition in olfactory cortex. *Nature Neuroscience*, 18(4):531–535.

[Suetsugu and Mehraein, 1980] Suetsugu, M. and Mehraein, P. (1980). Spine distribution along the apical dendrites of the pyramidal neurons in down's syndrome. *Acta neuropathologica*, 50(3):207–210.

[Svoboda et al., 1996] Svoboda, K., Tank, D. W., Denk, W., et al. (1996). Direct measurement of coupling between dendritic spines and shafts. *Science*, 272(5262):716–719.

[Svoboda and Yasuda, 2006] Svoboda, K. and Yasuda, R. (2006). Principles of two-photon excitation microscopy and its applications to neuroscience. *Neuron*, 50(6):823–839.

[Swann et al., 2000] Swann, J. W., Al-Noori, S., Jiang, M., and Lee, C. L. (2000). Spine loss and other dendritic abnormalities in epilepsy. *Hippocampus*, 10(5):617–625.

[Takahashi et al., 2012] Takahashi, N., Kitamura, K., Matsuo, N., Mayford, M., Kano, M., Matsuki, N., and Ikegaya, Y. (2012). Locally synchronized synaptic inputs. *Science*, 335(6066):353–356.

[Takashima et al., 1981] Takashima, S., Becker, L. E., Armstrong, D. L., and Chan, F. (1981). Abnormal neuronal development in the visual cortex of the human fetus and infant with Down's syndrome. a quantitative and qualitative Golgi study. *Brain Research*, 225(1):1–21.

[Takechi et al., 1998] Takechi, H., Eilers, J., and Konnerth, A. (1998). A new class of synaptic response involving calcium release in dendritic spines. *Nature*, 396(6713):757–760.

[Tan et al., 2011] Tan, A. Y., Brown, B. D., Scholl, B., Mohanty, D., and Priebe, N. J. (2011). Orientation selectivity of synaptic input to neurons in mouse and cat primary visual cortex. *The Journal of Neuroscience*, 31(34):12339–12350.

[Taylor et al., 2002] Taylor, D. M., Tillery, S. I. H., and Schwartz, A. B. (2002). Direct cortical control of 3D neuroprosthetic devices. *Science*, 296(5574):1829–1832.

[Taylor and Vaney, 2002] Taylor, W. R. and Vaney, D. I. (2002). Diverse synaptic mechanisms generate direction selectivity in the rabbit retina. *The Journal of Neuroscience*, 22(17):7712–7720.

[Thalhammer et al., 2013] Thalhammer, G., Bowman, R. W., Love, G. D., Padgett, M. J., and Ritsch-Marte, M. (2013). Speeding up liquid crystal SLMs using overdrive with phase change reduction. *Optics Express*, 21(2):1779–1797.

[Toni et al., 1999] Toni, N., Buchs, P.-A., Nikonenko, I., Bron, C., and Muller, D. (1999). LTP promotes formation of multiple spine synapses between a single axon terminal and a dendrite. *Nature*, 402(6760):421–425.

[Trachtenberg et al., 2002] Trachtenberg, J. T., Chen, B. E., Knott, G. W., Feng, G., Sanes, J. R., Welker, E., and Svoboda, K. (2002). Long-term *in vivo* imaging of experience-dependent synaptic plasticity in adult cortex. *Nature*, 420(6917):788–794.

[Tran-Van-Minh et al., 2015] Tran-Van-Minh, A., Cazé, R. D., Abrahamsson, T., Cathala, L., Gutkin, B. S., and DiGregorio, D. A. (2015). Contribution of sublinear and supralinear dendritic integration to neuronal computations. *Frontiers in Cellular Neuroscience*, 9(67).

[Treue and Trujillo, 1999] Treue, S. and Trujillo, J. C. M. (1999). Feature-based attention influences motion processing gain in macaque visual cortex. *Nature*, 399(6736):575–579.

[Tsay et al., 2007] Tsay, D., Dudman, J. T., and Siegelbaum, S. A. (2007). HCN1 channels constrain synaptically evoked Ca^{2+} spikes in distal dendrites of CA1 pyramidal neurons. *Neuron*, 56(6):1076–1089.

[Tsay and Yuste, 2002] Tsay, D. and Yuste, R. (2002). Role of dendritic spines in action potential backpropagation: a numerical simulation study. *Journal of Neurophysiology*, 88(5):2834–2845.

[Tzounopoulos and Stackman, 2003] Tzounopoulos, T. and Stackman, R. (2003). Enhancing synaptic plasticity and memory: A role for small-conductance Ca^{2+}-activated K^{+} channels. *The Neuroscientist*, 9(6):434–439.

[Uhlenbeck and Ornstein, 1930] Uhlenbeck, G. E. and Ornstein, L. S. (1930). On the theory of the Brownian motion. *Physical Review*, 36(5):823.

[Vacher et al., 2008] Vacher, H., Mohapatra, D. P., and Trimmer, J. S. (2008). Localization and targeting of voltage-dependent ion channels in mammalian central neurons. *Physiological Reviews*, 88(4):1407–1447.

[Varga et al., 2011] Varga, Z., Jia, H., Sakmann, B., and Konnerth, A. (2011). Dendritic coding of multiple sensory inputs in single cortical neurons *in vivo*. *Proceedings of the National Academy of Sciences*, 108(37):15420–15425.

[Velliste et al., 2008] Velliste, M., Perel, S., Spalding, M. C., Whitford, A. S., and Schwartz, A. B. (2008). Cortical control of a prosthetic arm for self-feeding. *Nature*, 453(7198):1098–1101.

[Velte and Miller, 1996] Velte, T. and Miller, R. (1996). Computer simulations of voltage clamping retinal ganglion cells through whole-cell electrodes in the soma. *Journal of Neurophysiology*, 75(5):2129–2143.

[Vergara et al., 1998] Vergara, C., Latorre, R., Marrion, N. V., and Adelman, J. P. (1998). Calcium-activated potassium channels. *Current Opinion in Neurobiology*, 8(3):321–329.

[Vetter et al., 2001] Vetter, P., Roth, A., and Häusser, M. (2001). Propagation of action potentials in dendrites depends on dendritic morphology. *Journal of Neurophysiology*, 85(2):926–937.

[Vogalis et al., 2003] Vogalis, F., Storm, J. F., and Lancaster, B. (2003). SK channels and the varieties of slow after-hyperpolarizations in neurons. *European Journal of Neuroscience*, 18(12):3155–3166.

[Voigt et al., 2008] Voigt, B. C., Brecht, M., and Houweling, A. R. (2008). Behavioral detectability of single-cell stimulation in the ventral posterior medial nucleus of the thalamus. *The Journal of Neuroscience*, 28(47):12362–12367.

[Wang and Augustine, 1995] Wang, S. S.-H. and Augustine, G. J. (1995). Confocal imaging and local photolysis of caged compounds: dual probes of synaptic function. *Neuron*, 15(4):755–760.

[Wang et al., 2000] Wang, S. S.-H., Denk, W., and Häusser, M. (2000). Coincidence detection in single dendritic spines mediated by calcium release. *Nature Neuroscience*, 3(12):1266–1273.

[Watanabe et al., 2002] Watanabe, S., Hoffman, D. A., Migliore, M., and Johnston, D. (2002). Dendritic K^+ channels contribute to spike-timing dependent long-term potentiation in hippocampal pyramidal neurons. *Proceedings of the National Academy of Sciences*, 99(12):8366–8371.

[Waters and Helmchen, 2004] Waters, J. and Helmchen, F. (2004). Boosting of action potential backpropagation by neocortical network activity *in vivo*. *The Journal of Neuroscience*, 24(49):11127–11136.

[Waters et al., 2003] Waters, J., Larkum, M., Sakmann, B., and Helmchen, F. (2003). Supralinear Ca^{2+} influx into dendritic tufts of layer 2/3 neocortical pyramidal neurons *in vitro* and *in vivo*. *The Journal of Neuroscience*, 23(24):8558–8567.

[Waters et al., 2005] Waters, J., Schaefer, A., and Sakmann, B. (2005). Backpropagating action potentials in neurones: measurement, mechanisms and potential functions. *Progress in Biophysics and Molecular Biology*, 87(1):145–70.

[Wehr and Zador, 2003] Wehr, M. and Zador, A. M. (2003). Balanced inhibition underlies tuning and sharpens spike timing in auditory cortex. *Nature*, 426(6965):442–446.

[Wendling et al., 2002] Wendling, F., Bartolomei, F., Bellanger, J., and Chauvel, P. (2002). Epileptic fast activity can be explained by a model of impaired GABAergic dendritic inhibition. *European Journal of Neuroscience*, 15(9):1499–1508.

[Wessberg et al., 2000] Wessberg, J., Stambaugh, C. R., Kralik, J. D., Beck, P. D., Laubach, M., Chapin, J. K., Kim, J., Biggs, S. J., Srinivasan, M. A., and Nicolelis, M. A. (2000). Real-time prediction of hand trajectory by ensembles of cortical neurons in primates. *Nature*, 408(6810):361–365.

[White et al., 1995] White, J. A., Sekar, N., and Kay, A. R. (1995). Errors in persistent inward currents generated by space-clamp errors: a modeling study. *Journal of Neurophysiology*, 73(6):2369–2377.

[Wieboldt et al., 1994] Wieboldt, R., Ramesh, D., Carpenter, B. K., and Hess, G. P. (1994). Synthesis and photochemistry of photolabile derivatives of gaba for chemical kinetic investigations of the gaba receptor in the millisecond time region. *Biochemistry*, 33(6):1526–1533.

[Williams and Mitchell, 2008] Williams, S. R. and Mitchell, S. J. (2008). Direct measurement of somatic voltage clamp errors in central neurons. *Nature Neuroscience*, 11(7):790–8.

[Williams and Stuart, 1999] Williams, S. R. and Stuart, G. J. (1999). Mechanisms and consequences of action potential burst firing in rat neocortical pyramidal neurons. *The Journal of Physiology*, 521(2):467–482.

[Williams and Stuart, 2000] Williams, S. R. and Stuart, G. J. (2000). Site independence of EPSP time course is mediated by dendritic I_h in neocortical pyramidal neurons. *Journal of Neurophysiology*, 83(5):3177–3182.

[Williams and Stuart, 2002] Williams, S. R. and Stuart, G. J. (2002). Dependence of EPSP efficacy on synapse location in neocortical pyramidal neurons. *Science*, 295(5561):1907–10.

[Wilson et al., 2012] Wilson, N. R., Runyan, C. A., Wang, F. L., and Sur, M. (2012). Division and subtraction by distinct cortical inhibitory networks *in vivo*. *Nature*, 488(7411):343–348.

[Wisniewski, 1990] Wisniewski, K. (1990). Down syndrome children often have brain with maturation delay, retardation of growth, and cortical dysgenesis. *American Journal of Medical Genetics*, 37(S7):274–281.

[Wolfe et al., 2010] Wolfe, J., Houweling, A. R., and Brecht, M. (2010). Sparse and powerful cortical spikes. *Current Opinion in Neurobiology*, 20(3):306–312.

[Womack and Khodakhah, 2004] Womack, M. D. and Khodakhah, K. (2004). Dendritic control of spontaneous bursting in cerebellar Purkinje cells. *The Journal of Neuroscience*, 24(14):3511–3521.

[Wong and Prince, 1978] Wong, R. and Prince, D. (1978). Participation of calcium spikes during intrinsic burst firing in hippocampal neurons. *Brain research*, 159(2):385–390.

[Wong et al., 1979] Wong, R., Prince, D., and Basbaum, A. (1979). Intradendritic recordings from hippocampal neurons. *Proceedings of the National Academy of Sciences*, 76(2):986–990.

[Woodruff et al., 2010] Woodruff, A. R., Anderson, S. A., and Yuste, R. (2010). The enigmatic function of chandelier cells. *Frontiers in Neuroscience*, 4(201).

[Wright et al., 2016] Wright, J., Macefield, V. G., van Schaik, A., and Tapson, J. C. (2016). A review of control strategies in closed-loop neuroprosthetic systems. *Frontiers in Neuroscience*, 10:312.

[Wu, 1986] Wu, S.-T. (1986). Phase retardation dependent optical response time of parallel-aligned liquid crystals. *Journal of Applied Physics*, 60(5):1836–1838.

[Xu et al., 2012] Xu, N.-l., Harnett, M. T., Williams, S. R., Huber, D., O'Connor, D. H., Svoboda, K., and Magee, J. C. (2012). Nonlinear dendritic integration of sensory and motor input during an active sensing task. *Nature*, 492(7428):247–251.

[Xu et al., 2009] Xu, T., Yu, X., Perlik, A. J., Tobin, W. F., Zweig, J. A., Tennant, K., Jones, T., and Zuo, Y. (2009). Rapid formation and selective stabilization of synapses for enduring motor memories. *Nature*, 462(7275):915–919.

[Yang et al., 2009] Yang, G., Pan, F., and Gan, W.-B. (2009). Stably maintained dendritic spines are associated with lifelong memories. *Nature*, 462(7275):920–924.

[Yang et al., 2011] Yang, S., Papagiakoumou, E., Guillon, M., de Sars, V., Tang, C.-M., and Emiliani, V. (2011). Three-dimensional holographic photostimulation of the dendritic arbor. *Journal of Neural Engineering*, 8(4):046002.

[Yao et al., 2004] Yao, H., Shen, Y., and Dan, Y. (2004). Intracortical mechanism of stimulus-timing-dependent plasticity in visual cortical orientation tuning. *Proceedings of the National Academy of Sciences*, 101(14):5081–5086.

[Yasuda et al., 2003] Yasuda, R., Sabatini, B. L., and Svoboda, K. (2003). Plasticity of calcium channels in dendritic spines. *Nature Neuroscience*, 6(9):948–955.

[Yasumatsu et al., 2008] Yasumatsu, N., Matsuzaki, M., Miyazaki, T., Noguchi, J., and Kasai, H. (2008). Principles of long-term dynamics of dendritic spines. *The Journal of Neuroscience*, 28(50):13592–13608.

[Yizhar et al., 2011] Yizhar, O., Fenno, L. E., Davidson, T. J., Mogri, M., and Deisseroth, K. (2011). Optogenetics in neural systems. *Neuron*, 71(1):9–34.

[Yuan and Chen, 2006] Yuan, L.-L. and Chen, X. (2006). Diversity of potassium channels in neuronal dendrites. *Progress in Neurobiology*, 78(6):374–389.

[Yuste and Bonhoeffer, 2004] Yuste, R. and Bonhoeffer, T. (2004). Genesis of dendritic spines: insights from ultrastructural and imaging studies. *Nature Reviews Neuroscience*, 5(1):24–34.

[Yuste and Denk, 1995] Yuste, R. and Denk, W. (1995). Dendritic spines as basic functional units of neuronal integration. *Nature*, 375(6533):682–684.

[Yuste et al., 1999] Yuste, R., Majewska, A., Cash, S. S., and Denk, W. (1999). Mechanisms of calcium influx into hippocampal spines: heterogeneity among spines, coincidence detection by NMDA receptors, and optical quantal analysis. *The Journal of Neuroscience*, 19(6):1976–1987.

[Yuste et al., 2000] Yuste, R., Majewska, A., and Holthoff, K. (2000). From form to function: calcium compartmentalization in dendritic spines. *Nature Neuroscience*, 3(7):653–659.

[Zahid et al., 2010] Zahid, M., Vélez-Fort, M., Papagiakoumou, E., Ventalon, C., Angulo, M. C., and Emiliani, V. (2010). Holographic photolysis for multiple cell stimulation in mouse hippocampal slices. *PLoS One*, 5(2):e9431.

[Zhang et al., 2014] Zhang, Y., Bonnan, A., Bony, G., Ferezou, I., Pietropaolo, S., Ginger, M., Sans, N., Rossier, J., Oostra, B., LeMasson, G., et al. (2014). Dendritic channelopathies contribute to neocortical and sensory hyperexcitability in fmr1-/y mice. *Nature Neuroscience*, 17(12):1701–1709.

[Zhou et al., 2004] Zhou, Q., Homma, K. J., and Poo, M.-m. (2004). Shrinkage of dendritic spines associated with long-term depression of hippocampal synapses. *Neuron*, 44(5):749–757.

[Zhu et al., 2012] Zhu, P., Fajardo, O., Shum, J., Schärer, Y.-P. Z., and Friedrich, R. W. (2012). High-resolution optical control of spatiotemporal neuronal activity patterns in zebrafish using a digital micromirror device. *Nature Protocols*, 7(7):1410–1425.

[Ziburkus and Guido, 2006] Ziburkus, J. and Guido, W. (2006). Loss of binocular responses and reduced retinal convergence during the period of retinogeniculate axon segregation. *Journal of Neurophysiology*, 96(5):2775–2784.

[Zuo et al., 2005] Zuo, Y., Lin, A., Chang, P., and Gan, W.-B. (2005). Development of long-term dendritic spine stability in diverse regions of cerebral cortex. *Neuron*, 46(2):181–189.